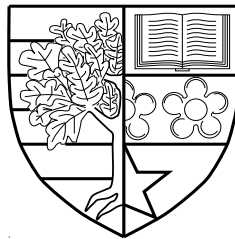


Statistical Millimeter Wave Channel Modelling For 5G and Beyond

by

Yi Tan



Submitted for the degree of Doctor of Philosophy

at

Heriot-Watt University

School of Engineering and Physical Sciences

December 2019

The copyright in this thesis is owned by the author. Any quotation from the thesis or use of any of the information contained in it must acknowledge this thesis as the source of the quotation or information.

Abstract

Millimetre wave (mmWave) wireless communication is one of the most promising technologies for the fifth generation (5G) wireless communication networks and beyond. The very broad bandwidth and directional propagation are the two features of mmWave channels. In order to develop the channel models properly reflecting the characteristics of mmWave channels, the in-depth studies of mmWave channels addressing those two features are required. In this thesis, three mmWave channel models and one beam alignment scheme are proposed related to those two features.

First, for studying the very broad bandwidth feature of mmWave channels, we introduce an averaged power delay profile (APDP) method to estimate the frequency stationarity regions (FSRs) of channels. The frequency non-stationary (FnS) properties of channels are found in the data analysis. A FnS model is proposed to model the FnS channels in both the sub-6 GHz and mmWave frequency bands and cluster evolution in the frequency domain is utilised in the implementation of FnS model.

Second, for studying the directional propagation feature of mmWave channels, we develop an angular APDP (A-APDP) method to study the planar angular stationarity regions (ASRs) of directional channels (DCs). Three typical directional channel impulse responses (D-CIRs) are found in the data analysis and light-of-sight (LOS), non-LOS (NLOS), and outage classes are used to classify those DCs. A modified Saleh-Valenzuela (SV) model is proposed to model the DCs. The angular domain cluster evolution is utilised to ensure the consistency of DCs.

Third, we further extend the A-APDP method to study the spherical-ASRs of DCs. We model the directional mmWave channels by three-state Markov chain that consists of LOS, NLOS, and outage states and we use stationary model, non-stationary model, and “null” to describe the channels in each Markov state according to the estimated ASRs. Then, we propose to use joint channel models to simulate the instantaneous directional mmWave channels based on the limiting distribution of Markov chain.

Finally, the directional propagated mmWave channels when the Tx and Rx in motion is addressed. A double Gaussian beams (DGBs) scheme for mobile-to-mobile (M2M) mmWave communications is proposed. The connection ratios of directional mmWave channels in each Markov state are studied.

Dedicated to my loving family and dear colleagues

Acknowledgement

My greatest appreciation goes to my primary supervisor Prof. Cheng-Xiang Wang for giving me the golden opportunity to do research. I would like to gratefully acknowledge his invaluable and patient guidance in all the researches toward my doctoral study and writing this thesis. Without his precious support, it would not be possible to accomplish this work. My sincere thanks must go to my secondary supervisors Prof. George Goussetis for his advice and his generosity to give me access to the research facilities in his laboratory. I am also very grateful to visiting researcher Prof. Qiuming Zhu from Nanjing University of Aeronautics and Astronautics for the discussions and cooperation of original papers.

I would like to express my heartfelt gratitude to my colleagues Carlos Lopez, Yu Fu, Ahmed Al-Kinani, Qianru Zhou, Liang Gong, and the visiting researchers from China Zhou Li, Prof. Minzheng Li, Yu Liu, Weijun Xing, Yuhan Ruan, Rui Zhang, Liyang Zhang, Rui Feng, Lu Bai, and Ji Bian in the Advanced Wireless Technologies (AWiTec) Lab. It was my pleasure to work with you and made progress together. Your friendship and kindness also made my stay in Edinburgh an enjoyable experience.

I also would like to thank EU H2020 Marie Skłodowska-Curie ITN project Innovative Architectures, Wireless Technologies and Tools for High Capacity and Sustainable 5G Ultra-Dense Cellular Networks (5Gwireless, No. 641985) for the financial support and well-organized training activities of international communication and cooperation. My special thanks go to Beatriz Bedia and Ana Ruiz for their kindly help during my four months secondment in TTI, Santander, Spain.

Last but not least, my great gratefulness to my wife Jingxuan Zhu and my daughter Olivia Weizhen Tan for their company and constant support. I also give my best wishes to my mother Bin He, my father Laixiao Tan, my sister Yan Huang, brother-in-law Ji Liu, other family members, and my British friends Vince Gray and Angela Gray. Thank you for all of their understanding and unconditional assistance.

Yi Tan

Edinburgh UK, December 2019

Research Thesis Submission

Please note this form should be bound into the submitted thesis.

Name:	Yi Tan		
School:	School of Engineering & Physical Sciences		
Version: <i>(i.e. First, Resubmission, Final)</i>	Final	Degree Sought:	Ph.D. degree

Declaration

In accordance with the appropriate regulations I hereby submit my thesis and I declare that:

1. The thesis embodies the results of my own work and has been composed by myself
2. Where appropriate, I have made acknowledgement of the work of others
3. The thesis is the correct version for submission and is the same version as any electronic versions submitted*.
4. My thesis for the award referred to, deposited in the Heriot-Watt University Library, should be made available for loan or photocopying and be available via the Institutional Repository, subject to such conditions as the Librarian may require
5. I understand that as a student of the University I am required to abide by the Regulations of the University and to conform to its discipline.
6. I confirm that the thesis has been verified against plagiarism via an approved plagiarism detection application e.g. Turnitin.

ONLY for submissions including published works

Please note you are only required to complete the Inclusion of Published Works Form (page 2) if your thesis contains published works)

7. Where the thesis contains published outputs under Regulation 6 (9.1.2) or Regulation 43 (9) these are accompanied by a critical review which accurately describes my contribution to the research and, for multi-author outputs, a signed declaration indicating the contribution of each author (complete)
8. Inclusion of published outputs under Regulation 6 (9.1.2) or Regulation 43 (9) shall not constitute plagiarism.

* Please note that it is the responsibility of the candidate to ensure that the correct version of the thesis is submitted.

Signature of Candidate:	<i>Tan Yi</i>	Date:	18 Dec. 2019
-------------------------	---------------	-------	--------------

Submission

Submitted By <i>(name in capitals)</i> :	YI TAN
Signature of Individual Submitting:	<i>Tan Yi</i>
Date Submitted:	18 Dec. 2019

For Completion in the Student Service Centre (SSC)

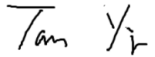
Limited Access	Requested	Yes	No	Approved	Yes	No
<i>E-thesis Submitted (mandatory for final theses)</i>						
Received in the SSC by <i>(name in capitals)</i> :				Date:		

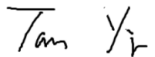
Inclusion of Published Works

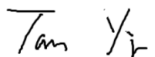
Please note you are only required to complete the Inclusion of Published Works Form if your thesis contains published works under Regulation 6 (9.1.2)

Declaration

This thesis contains one or more multi-author published works. In accordance with Regulation 6 (9.1.2) I hereby declare that the contributions of each author to these publications is as follows:

Citation details	Y. Tan, C.-X. Wang, Q. Zhu, Z. Zhang, Z. Wang, J. Huang, and R. Feng, "A novel beamforming scheme for mobile-to-mobile millimeter wave communications," in <i>Proc. WSA'18</i> , Bochum, Germany, Mar. 2018.
Author 1	Data analysis, proposing the channel model, and simulations.
Author 2	Supervising all the research related works.
Signature:	
Date:	18 Dec. 2019

Citation details	Y. Tan, J. Huang, R. Feng, and C.-X. Wang, "A study of angular stationarity of 5G millimeter wave channels," in <i>Proc. ISWCS'18 Workshop</i> , Bologna, Italy, Aug. 2017.
Author 1	Data analysis, proposing the channel model, and simulations.
Author 2	Provide channel measurement data. Give suggestions to improve the manuscript.
Signature:	
Date:	18 Dec. 2019

Citation details	Y. Tan, C.-X. Wang, J. . Nielsen, and G. F. Pedersen, "Comparison of stationarity regions for wireless channels from 2GHz to 30 GHz," in <i>Proc. IWCMC'17</i> , Invited Paper, Valencia, Spain, Jun. 2017.
Author 1	Data analysis, proposing the channel model, and simulations.
Author 2	Supervising all the research related works.
Signature:	
Date:	18 Dec. 2019

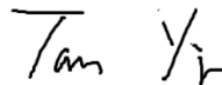
Please included additional citations as required.

Declaration of Authorship

I, [Yi Tan](#), declare that this thesis titled, 'Statistical Millimetre Wave Channel Modelling For 5G And Beyond' and the work presented in it is my own. I confirm that this work submitted for assessment is my own and is expressed in my own words. Any uses made within it of the works of other authors in any form (e.g., ideas, equations, figures, text, tables, codes) are properly acknowledged at any point of their use. A list of the references employed is included.

- This work was done wholly or mainly while in candidature for a research degree at this University.
- Where any part of this thesis has previously been submitted for a degree or any other qualification at this University or any other institution, this has been clearly stated.
- Where I have consulted the published work of others, this is always clearly attributed.
- Where I have quoted from the work of others, the source is always given. With the exception of such quotations, this thesis is entirely my own work.
- I have acknowledged all main sources of help.
- Where the thesis is based on work done by myself jointly with others, I have made clear exactly what was done by others and what I have contributed myself.

Signed:



Date: December 2019

Contents

Abstract	i
Acknowledgement	iv
Declaration of Authorship	v
List of Figures	xi
List of Tables	xv
Abbreviations	xvi
Symbols	xix
1 Introduction	1
1.1 Background	1
1.1.1 The 5G Wireless Communication Systems and Beyond	1
1.1.2 The Brief of MmWave Communication	3
1.2 Motivation	6
1.3 Contributions	7
1.4 Original Publications	9
1.5 Thesis Organisation	10
2 Millimetre Wave Channel Modelling: Literature Review	13
2.1 Introduction	13
2.2 The Categories of Channel Models	14
2.2.1 Deterministic Channel Model	15
2.2.2 Stochastic Channel Models	15
2.2.3 Hybrid Channel Models	18
2.3 Modelling of MmWave Channels	18
2.3.1 Standard MmWave Channel Models	19

2.3.1.1	IEEE 802.11ad & IEEE 802.15.3c	20
2.3.1.2	METIS	20
2.3.1.3	MmMagic	21
2.3.1.4	3GPP models, above 6 GHz	22
2.3.2	Specific Characteristics of MmWave Channels	23
2.3.2.1	Frequency Dependent Characteristics	23
2.3.2.2	Path loss and Oxygen Absorption	24
2.3.2.3	Penetration Loss and Blockage	25
2.3.3	Directionality of MmWave Channels	25
2.3.3.1	NYU Wireless Models	26
2.3.4	Studies of Vehicular/Mobile MmWave Channels	27
2.4	MmWave Channel Measurements	28
2.4.1	Principle of Wide-Band Channel Sounding	28
2.4.2	MmWave Channel Sounder	29
2.4.3	A Short Brief of MmWave Channel Measurement Campaigns	31
2.5	Research Gap	31
2.6	Summary	35

3	Frequency non-Stationarity and Frequency non-Stationary Channel Modelling	36
3.1	Introduction	36
3.1.1	Contributions	39
3.2	Stationarity Regions in Time, Frequency, and Spatial Domains	40
3.2.1	APDP Method Applied in Time Domain	41
3.2.2	APDP Method Applied in Spatial Domain	42
3.2.3	APDP Method Applied in Frequency Domain	42
3.2.3.1	Case 1: Averaging on Snapshots	43
3.2.3.2	Case 2: Averaging on Antenna Array	45
3.3	Channel Measurements and Data Analysis	46
3.3.1	Channel Measurements and Data Processing	46
3.3.2	FSR Analysis	48
3.3.3	Variation of Statistical Properties of Channels	51
3.3.3.1	Statistical Property of Channel in Frequency Domain	54
3.3.3.2	Variation of FCFs of Sub-Band Channels	54
3.4	A FnS Channel model	54
3.4.1	FnS Channel Modelling	55
3.4.2	Cluster Evolution in Frequency Domain	56
3.4.3	Statistical Parameters of Measured Sub-Band Channels	58
3.4.3.1	Parameters Estimation	58
3.4.3.2	Trends of Statistical Parameters	59
3.5	Generation of FnS Channel Coefficient	60
3.5.1	Generation of One Sub-Band Channel Coefficient	60
3.5.2	Cluster Evolution	62
3.5.3	Adding Up Sub-Band Channels	62

3.5.4	Implementation Details	64
3.6	Validation of FnS Channel Model	65
3.6.1	Simulation of FnS Channels	65
3.6.2	Fading of Simulated FnS channels	67
3.7	Summary	69
4	Planar Angular Stationarity and Directional MmWave Channel Modelling	71
4.1	Introduction	71
4.1.1	Contributions	74
4.2	Channel Measurements and Data Analysis	75
4.2.1	Angular Stationarity	75
4.2.2	MmWave Channel Measurements	77
4.2.3	Three Typical D-CIRs in the LOS Case	78
4.2.4	Two Typical D-CIRs in the NLOS Case	84
4.2.5	Study of Spatial Stationarity Based on Directional MmWave Channels	84
4.3	A New Modelling of Directional MmWave Channels	85
4.3.1	Three Classes of DCs	85
4.3.2	Inhomogeneity of MmWave Channel Environment	87
4.3.3	Directional MmWave Channel Model	88
4.3.4	Cluster Evolution in The Angular Domain	90
4.3.5	No Cluster Drifts in Different DCs	92
4.3.6	Estimation of Statistical Parameters	93
4.4	Generation of Channel Coefficients	97
4.4.1	Generation of First DC's Channel Coefficient/D-CIR	97
4.4.2	Generate Other DCs' Channel Coefficients by Cluster Evolution	99
4.4.3	Implementation Details of Channel Coefficient Generation	99
4.4.4	Generate Omni-Directional Channel Coefficient	101
4.5	Simulation and Validation	101
4.5.1	Verification of DCs in the LOS Class	101
4.5.2	Verification of DCs in the NLOS Class	102
4.5.3	Verification of Omni-CIRs	104
4.6	Summary	105
5	Spherical Angular Stationarity and Modelling Directional MmWave Channels by Markov States	107
5.1	Introduction	107
5.1.1	Contributions	108
5.2	ASRs of Directional Channels	109
5.2.1	S-ASRs of Directional Channel	110
5.3	Channel Measurements and Data Analysis	112
5.3.1	MmWave Channel Measurements	112
5.3.2	Data Analysis of LOS Case	112

5.3.3	Three Types of D-CIRs in the LOS Case	113
5.3.4	Two Types of D-CIRs in the NLOS Case	116
5.4	Three-State Markov Chain of Directional MmWave Channels	117
5.4.1	Three Markov States of Directional MmWave Channels	117
5.4.2	Transition Matrix and Limiting Distribution of Three-State Markov Chain	118
5.4.3	State Transition Characteristics of Directional MmWave Channel in the LOS Case	119
5.4.4	State Transition Characteristics of Directional MmWave Channel in the NLOS Case	120
5.5	Joint Channel Models	121
5.5.1	Procedure of Modelling Directional MmWave Channels	121
5.5.2	Stationary and Non-Stationary Channel Models	123
5.5.2.1	LOS State Stationary Channel Model	124
5.5.2.2	NLOS State Non-Stationary Channel Model	124
5.5.3	Estimation of Statistical Parameters	125
5.5.3.1	Parameter Estimations	126
5.5.3.2	Implementation Details	129
5.5.4	Channel Coefficients Generation Based on Stationary Channel Model	130
5.5.4.1	Implementation Details Based on Stationary Channel Model	132
5.5.5	Channel Coefficients Generation Based on Non-Stationary Channel Model	132
5.5.5.1	Implementation Details Based on Non-Stationary Channel Model	133
5.6	Simulation and Validation of Stationary and Non-Stationary Models	133
5.6.1	Verification of LOS State Stationary Model	134
5.6.2	Verification of NLOS State Non-Stationary Model	134
5.7	Summary	135
6	Mobile-to-Mobile Directional MmWave Channels Based on A Novel Beamforming Scheme	138
6.1	Introduction	138
6.1.1	Contributions	139
6.2	Double Gaussian Beams Communication	139
6.2.1	Gaussian Beam	140
6.2.2	DGBs Communication Scheme	141
6.3	Markov States MmWave Channels	142
6.3.1	Three Markov States DGBs Channels	143
6.3.2	Channel Measurement and Three Markov States Measured Channels	143
6.3.2.1	Three Markov States Measured Channels	144
6.4	Study and Comparison of Connection Ratios	145

6.4.1	Connection Ratios of Markov States DGBs Channels	146
6.4.1.1	Synchronised DGBs Channels	147
6.4.1.2	Asynchronised DGBs Channels	150
6.4.2	Connection Ratios of Markov States Measured mmWave Channels	151
6.4.3	Comparison of Connection Ratios	151
6.5	Summary	152
7	Conclusions and Future Work	154
7.1	Summary of Results	154
7.1.1	Frequency Non-Stationary MmWave Channel Models	154
7.1.2	Directional MmWave Channel Models	155
7.1.3	A Novel Beamforming Scheme for Mobile-to-Mobile Millimetre Wave Communications	157
7.2	Future Research Directions	158
7.2.1	Frequency non-Stationarity and Consistency of 5G Wireless Chan- nels	158
7.2.2	Modelling Directional MmWave Channels	159
7.2.3	Double Gaussian Beams MmWave Communication Scheme	162
A	Usage of Stationarity Regions of Wireless Channels	163
A.1	Data of Measured Channels Over a Few Stationarity Regions	163
A.2	Only Use Data Within One Stationarity Region	164
A.3	Stationarity in the time, frequency, spatial, and angular domains	164
B	Radiation Pattern of Commercial Standard Horn Antenna	166
	References	168

List of Figures

1.1	Attenuation vs. frequencies.	4
1.2	Omni-directional propagation to directional propagation.	5
2.1	Categories of channel models.	14
2.2	Standard channel models and their family history.	17
2.3	Comparison of 5G channel models.	19
2.4	Sounding principle of a time-variant wireless channel.	29
2.5	Categories of channel sounder structures.	30
2.6	Baseband components + RF components channel sounding system.	30
3.1	Sliding windows of APDPs moving along the time axis.	40
3.2	FSRs of the channel in high frequencies and low frequencies in the same environment.	43
3.3	Sliding-windows of sub-APTFs moving along the frequency axis (we denote $P_H(t, f')$ as the $\overline{P_H}(t, f')$ before averaging).	44
3.4	Floorplan of the channel measurements in the basements.	47
3.5	Approximation of linear antenna subarrays.	47
3.6	The FSRs of the channels, NLOS scenario: (a) correlation coefficients of the sub-APTFs and (b) stationary bandwidth vs. ASLs.	48
3.7	Correlation coefficients of the sub-APTFs in the LOS scenario.	49
3.8	Estimated MPCs in some of the sub-band channels from 2 to 4 GHz (LOS scenario).	51
3.9	Estimated MPCs in the sub-band channels from 28 to 30GHz (LOS scenario).	51
3.10	The FCFs of the sub-band channels, NLOS scenario: (a) within 2–4 GHz band and (b) within 28–30 GHz band.	53
3.11	Cluster evolution in the frequency domain.	55
3.12	Tidal variation, as a metaphor to explain the cluster evolution in the frequency domain.	56
3.13	Example of adding up two sub-band channels as one FnS channel.	63
3.14	Frequency consistent simulated sub-band CIRs, 28–30 GHz band.	65
3.15	FnS channels, NLOS scenario, 28–30 GHz band: (a) simulated FnS-CIR and (b) measured FnS-CIR.	66

3.16	FCF approximations, NLOS scenario: (a) 2–4 GHz band, (b) 14–16 GHz band, and (c) 28–30 GHz band.	68
3.17	FCF approximations with 10 clusters in each simulated sub-band channel, NLOS scenario, 28–30 GHz band.	69
4.1	A-APDP method.	76
4.2	(a) Layout of an indoor office environment and definition of DCs in the LOS case and (b) sounder testbed.	77
4.3	(a) Angular correlation coefficients between the APDP at azimuth angle $\phi = 0^\circ$ and the APDPs at other azimuth angles and (b) estimated ASRs on the azimuth plane with 90° elevation angle in the LOS case (ASL = 0.8), and (c) estimated ASRs based on (b) with different ASL levels from 0.4 to 0.9.	79
4.4	(a) RMS DSs and (b) K-factors estimated by the measured D-CIRs on the azimuth plane with the 90° elevation angle in the LOS case.	80
4.5	Three typical D-CIRs on the azimuth plane with 90° elevation angle based on the PPG levels in the LOS case.	81
4.6	Three typical D-CIRs in the LOS case: (a) D-CIR of Type 1, (b) D-CIR of Type 2, and (c) D-CIR of Type 3.	82
4.7	The DCs in the LOS and NLOS classes in the LOS case.	85
4.8	D-CIR $h^D(\tau)$ can be modelled as the sum of responses from the scatterers at (ϕ_l, τ_l) with amplitudes $a_l(\phi_l, \tau_l)$ in the angle range of a Rx beam.	87
4.9	The modeling parameters of modified SV model.	89
4.10	(a) PDF of cluster excess delay and (b) cluster power decay rate estimated based on the D-CIRs in the NLOS class in the LOS case.	94
4.11	(a) PDF of ray excess delay and (b) ray power decay rate estimated based on the D-CIRs in the NLOS class in the LOS case.	95
4.12	The normal distributed FCPRs estimated based on the D-CIRs in the NLOS class in the LOS case.	96
4.13	The log-normal distributed cluster decay rates (normal distributed values in dB) estimated based on the D-CIRs in the NLOS class in the LOS case.	96
4.14	A group of simulated D-CIRs of DCs in the LOS class.	102
4.15	(a) Comparison of the CDF of RMS DSs between the simulated DCs and measured DCs and (b) comparison of the correlation coefficients between the simulated DCs and the measured DCs on the azimuth plane with 90° elevation angle in the LOS class in the LOS case.	103
4.16	(a) Comparison of the CDF of RMS DSs between the simulated DCs and measured DCs and (b) comparison of the correlation coefficients between the simulated DCs and the measured DCs on the azimuth plane with 90° elevation angle in the largest group of NLOS class in the LOS case.	104
4.17	One simulated omni-CIR compared with one measured omni-CIR.	105

5.1	A-APDP method in the spherical coordinate system: (a) turning sliding windows and (b) apex angle and S-ASR.	110
5.2	(a) Spherical angular correlation coefficients against azimuth and elevation angles in the LOS case and (b) estimated S-ASRs of mmWave channels in all directions (ASL = 0.8).	113
5.3	PPGs of D-CIRs in all directions in the LOS case.	114
5.4	RMS DSs estimated by D-CIRs in all directions in the LOS case. . . .	114
5.5	K-factors estimated by D-CIRs in all directions in the LOS case. . . .	115
5.6	PPGs of D-CIRs in all directions in the NLOS case.	116
5.7	Procedure of modelling directional mmWave channels.	122
5.8	(a) PDF of inter-cluster excess delay and (b) inter-cluster power decay rate based on the D-CIRs in the LOS state in the LOS case.	126
5.9	(a) PDF of intra-cluster/ray excess delay and (b) intra-cluster/ray power decay rate based on the D-CIRs in the LOS state in the LOS case.	127
5.10	The normal distributed FCPRs estimated based on the D-CIRs in the NLOS state.	128
5.11	The log-normal distributed inter-cluster decay rates (data in dB follow normal distribution) estimated based on the D-CIRs in the NLOS state.	128
5.12	(a) One simulated LOS state D-PDP $h^{D,LOS}(\tau)$ and (b) the comparison of the CDFs of RMS DSs between the simulated D-CIRs and the measured D-CIRs, LOS state, LOS case.	135
5.13	(a) One simulated NLOS state D-PDP $h^{D,NLOS}(\tau)$, and (b) the comparison of the CDFs of RMS DSs between the simulated D-CIRs and the measured D-CIRs, NLOS state, LOS case.	136
6.1	The transverse energy intensity of a beam follows Gaussian distribution. There is a torch at up-right corner, the transverse energy intensity at the down-right corner, and the transverse energy intensity profile at the left hand side.	140
6.2	Construction of one Gaussian beam based on beamforming technology.	140
6.3	DGBs channels.	141
6.4	Estimated ASRs of mmWave channel from D-CIRs in different azimuth angles, ASL is 0.8.	144
6.5	Angular separated three typical D-CIRs in three Markov states (Tx rotates and Rx hold still).	144
6.6	DGBs channels in the located case.	146
6.7	DGBs channels in the dislocated case (shifting distance is d).	146
6.8	The DGBs overlapping area for both the located and dislocated cases. .	147
6.9	Synchronised DGBs channels (swing ranges $\psi_{Tx} = \psi_{Rx} = 60^\circ$, length of vertical positioned slim object is 1 m, distance between Tx and Rx is 10 m, and the shifting distance d is 2 m for the dislocated case). . . .	147
6.10	Synchronised DGBs channels (swing ranges $\psi_{Tx} = \psi_{Rx} = 60^\circ$, length of vertical positioned slim object is 3 m, distance between Tx and Rx is 10 m, and the shifting distance d is 2 m for the dislocated case). . . .	148

6.11	Synchronised DGBs channels (swing ranges $\psi_{Tx} = \psi_{Rx} = 60^\circ$, length of vertical positioned slim object is 1 m, distance between Tx and Rx is 10 m, and the shifting distance d is 4 m for the dislocated case). . . .	148
6.12	Both synchronised and asynchronised DGBs channels (swing range $\psi_{Tx} = \psi_{Rx} = 60^\circ$, length of vertical positioned slim object is 1m, distance between Tx and Rx is 10 m, and the shifting distance d is 2 m for the dislocated case): (a) LOS states, and (b) NLOS states.	150
7.1	Directional dependent stationary distance for mmWave channels.	159
7.2	Split the channel environment into parts.	161
A.1	The distorted estimation of channel.	164
A.2	Stationarity studies of mmWave channels.	165

List of Tables

2.1	Brief of mmWave channel measurements	32
3.1	Size of FSRs in a NLOS scenario.	47
3.2	Parameters of sub-band channels (NLOS scenario, 2–4 GHz).	58
3.3	Parameters of sub-band channels (NLOS scenario, 28–30 GHz).	58
4.1	Estimated Statistical Parameters in LOS Case.	93
4.2	Specific Statistical Parameters in LOS Case.	93
5.1	The numbers of state transitions in the LOS case.	119
5.2	Statistical parameters of both LOS state and NLOS state (LOS case). .	125

Abbreviations

3GPP	Third Generation Partnership Project
4G	Fourth Generation
5G	Fifth Generation
5GCM	5G Channel Model for bands up to 100 GHz
5GPPP	5G Infrastructure Public Private Partnership
6G	Sixth Generation
ACF	Autocorrelation Function
AoA	Angle of Arrival
AoD	Angle of Departure
ASL	Allowance of the Similarity Level
ASR	Angular Stationarity Region
A-APDP	Angular Averaged Power Delay Profile
APDP	Averaged Power Delay Profile
APTF	Average Power Transfer Function
AS	Angular Spread
A2X	Air-to-Everything
COST	European Cooperative in Science and Technology
CCF	Cross-Correlation Function
CDF	Cumulative Distribution Function
CBSM	Correlation Based Stochastic Model
DC	Directional Channel

D-CIR	Directional Channel Impulse Response
DGBs	Double Gaussian Beams
D2D	Device-to-Device
D-PDP	Directional Power Delay Profile
DS	Delay Spread
eMBB	Evolved Mobile Broadband
FCF	Frequency Correlation Function
FCPR	First Cluster Power Ratio
FFT	Fast Fourier Transformation
FnS	Frequency non Stationary
FS	Frequency Stationary
FSR	Frequency Stationarity Region
GBSM	Geometry Based Stochastic Model
GSCM	Geometry Based Stochastic Channel Model
HF	High Frequency
HST	High-Speed Train
HO	Homogeneous Channel
IEEE	Institute of Electrical and Electronics Engineers
i.i.d.	Independent and Identically Distributed
IMT	International Mobile Telecommunication
ITU	International Telecommunication Union
ITU-R	ITU Radiocommunication Sector
LTE	Long Term Evolution
LTE-A	LTE-Advanced
LF	Low Frequency
LMS	Land Mobile-Satellite
LOS	Line-of-Sight
LSP	Large-Scale Parameters
mmWave	Millimetre Wave
mMTC	Massive Machine-Type Communications
mmMagic	mm-Wave based Mobile Radio Access Network

for 5G Integrated Communications

METIS	Mobile and wireless communications Enablers for Twenty-twenty Information Society
MIMO	Multiple-Input Multiple-Output
MU-MIMO	Multi-User MIMO
M2M	Mobile-to-Mobile
MPC	Multi-Path Component
NR	New Radio
NLOS	Non-LOS
omni-CIR	Omni-Directional CIR
P-ASR	Planar Angular Stationarity Region
PDP	Power Delay Profile
PDF	Probability Density Function
PPG	Peak Power Gain
PTF	Power Transfer Function
PPG	Peak Power Gain
QuaDRiGa	QUAsi Deterministic RadIo channel GenerAtor
RMS	Root Mean Square
S-ASR	Spherical Angular Stationarity Region
SV	Saleh-Valenzuela
ToA	Time of Arrival
UCA	Uniform Circular Array
URLLC	Ultra-Reliable and Low-Latency Communications
UWB	Ultra-Wide Band
V2V	Vehicle-to-Vehicle
V2X	Vehicle-to-Everything
V2I	Vehicle-to-infrastructure
VLC	Visible Light Communication
WINNER	Wireless World Initiative New Radio
WSS	Wide Sense Stationary

Symbols

a_l	amplitude of cluster
$a_{l,m}$	amplitude of intra-cluster rays
$c(t, \Delta t)$	correlation coefficients in time domain
$c(f', \Delta f)$	correlation coefficients in frequency domain
$c(\phi, \Delta \phi)$	angular correlation coefficient
$C[\cdot]$	covariance operator
d	shifting distance (Chapter 6)
d_t	stationarity interval (stationarity region in the time domain)
d_f	stationarity bandwidth (stationarity region in the frequency domain)
d_ϕ	angular stationary interval (stationarity region in the angular domain)
d_{sep}	angular separation interval (Chapter 5)
$\exp[\cdot]/\exp(\cdot)$	exponential operator
$E\{\cdot\}$	statistical expectation
f_{co}	centre frequency of the o sub-band channels
$\mathcal{F}^{-1}[\cdot]$	inverse Fourier transformation
$h(t_i, \tau)$	(omni-directional) channel impulse response
$H(t_i, f)$	(omni-directional) channel transfer function
$\mathbf{h}(\tau)$	(omni-directional) FnS channel impulse response (Chapter 3)
$h^{\text{sub}}(\tau, f_{co})$	(omni-directional) impulse response of the o sub-band

	channel (Chapter 3)
$h^D(\phi_i, \tau)$	directional channel impulse response (Chapter 4)
$h^D(\phi_i, \theta_j, \tau)$	directional channel impulse response (Chapter 5)
$h^D(\tau)$	directional channel impulse response (short notation, Chapter 4, 5, and 6)
$h^{D,LOS}(\tau)$	directional channel impulse response in the LOS class/state
$h^{D,NLOS}(\tau)$	directional channel impulse response in the NLOS class/state
$h^{\text{Omni-d}}(\tau)$	omni-directional channel impulse response (Chapter 4)
K	LOS Rician factor
K_{c1}	first cluster power ratio (FCPR)
\tilde{K}_{c1}	normal distributed FCPR
$\ln(\cdot)$	logarithm operator
o	sub-band channel index
O'	number of sub-band channels one cluster survives / number of D-CIRs one cluster survives (Chapter 4)
p	successful connection ratio between the Tx and Rx (Chapter 6)
$P_h(t_i, \tau)$	(omni-directional) instantaneous PDP
$P_H(t_i, f)$	(omni-directional) instantaneous PTF
$\overline{P}_h(t, \tau)$	average PDP of n -snapshots
$\overline{P}_H(t, f)$	average PTF along time axis
$\overline{P}_H(r, f)$	average PTF along spatial axis
$P_h^D(\phi_i, \tau)$	directional PDP (Chapter 4)
$P_h^D(\phi_i, \theta_j, \tau)$	directional PDP (Chapter 5)
$\overline{P}_h^D(\phi, \tau)$	average PDP of n D-CIRs (Chapter 4)
$\overline{P}_h^D(\phi, \theta_j, \tau)$	average PDP of n D-CIRs (Chapter 5)
$P_l(f_{co})$	normalised inter-cluster power
P_{survival}	survival probabilities of the clusters
P^1	probability of one-step transition matrix
P^n	n -step transition matrix
$\text{pdf}(\cdot)$	probability density function (PDF)
$r_\tau(f_{co})$	delay distribution proportionality factor

R_H	frequency correlation function (FCF)
t	time
$V[\cdot]$	variance operator
$[\cdot]^*$	conjugate operator

Greek:

$\beta_{l,m}$	random phases of intra-cluster rays
γ	intra-cluster ray power decay rate / flashing rate (Chapter 6)
Γ	inter-cluster power decay rate
$\tilde{\Gamma}$	log-normal distributed inter-cluster power decay rate
Δf	frequency difference
Δt	time difference
$\Delta\phi$	azimuth angle difference
ϵ_{τ_1}	compensation of delay interval between the first cluster and the rest of the clusters
θ	azimuth angle / beamwidth (Chapter 6)
$\theta_l(f_{co})$	inter-cluster angle
$\theta_{l,m}(f_{co})$	intra-cluster angle, ray angle
$\theta_l^{\text{mean}}(f_{co})$	mean angle of cluster
λ	rate parameter used to define survival probability
μ_k	mean of normal distributed FCPRs
π	limiting distribution
ρ	apex angle
σ_k	variance of normal distributed FCPRs
$\sigma_{\tau}(f_{co})$	delay spread
$\sigma_{\theta}(f_{co})$	standard deviation of inter-cluster angle
τ_l	delay of the l th Cluster
$\tau_{l,m}$	relative delay of the m th ray within the l th Cluster
$\tau_l(f_{co})$	inter-cluster delay

$\tau_{l,m}(f_{co})$	intra-cluster delay, ray delay
ψ	swing range (Chapter 6)
Ω	stationary solid angle (spherical angular stationarity region, Chapter 5)

Chapter

1

Introduction

1.1 Background

1.1.1 The 5G Wireless Communication Systems and Beyond

Driven by new service innovations and new innovative applications, the demand for data traffic is greatly increased for the fifth generation (5G) wireless communication systems and beyond [1]. In order to meet these service demands, the telecommunication industry is converging on a common set of 5G requirements compared to the fourth generation (4G) network that the 5G network should achieve 1000 times the system capacity, 10 times the spectral efficiency, energy efficiency and data rate, and 25 times the average cell throughput. The aim of 5G is “*to connect the entire world and achieve seamless and ubiquitous communications between anybody, anything, wherever they are, whenever they need, by whatever electronic devices/services/networks they wish*” [2]. The International Telecommunication Union (ITU) has classified 5G mobile network services into three categories as the envision of 5G: Evolved mobile broadband (eMBB), Ultra-reliable and low-latency communications (URLLC), and Massive machine-type communications (mMTC) [3]–[5]. With such great perspective, the fundamental and radical paradigm-shift of our traditional 4G Long Term Evolution

(LTE)/LTE-Advanced (LTE-A) wireless communication system is inevitable. The development of 5G leads to an overall re-thinking of cellular operational principles and architectures, network topologies, transmission technologies, and the analysis, design and optimisation methodologies.

In the networks upgrading of previous generations, both the access and core network are generally deployed at the same time. For the aim of 5G that connecting the entire world, the 5G network will be deployed with existing networks, such as the 4G LTE system. The standalone (SA) operation of 5G system and the non-standalone (NSA) integrated elements of different generations in different configurations are both under research and development [6]. The 3GPP has defined both a new 5G core (5GC) network and a new radio access technology called 5G new radio (NR) [6]. The specification of NR is subdivided into two frequency bands, FR1 is below 6 GHz band and FR2 is millimetre wave (mmWave) frequency band [7]. The development for the features and performance specifications of 5G continues. The academia and industry are working very closely towards the standardization of 5G around 2020. New fundamentals have been selected and formalized into standards in Release-15 (Phase 1) and Release-16 (Phase 2) by 3GPP [8]. Release-16 is in the middle of the specification development, aiming at freezing the physical layer part by March 2020. More 5G system enhancements will be set in Release-17, which is under development, scheduled for delivery in 2021.

The researches towards 5G are multi-fold. The approaches to enhance capacity/-data rate are mainly in the directions of more antenna, more bandwidth, and more cells. Correspondingly, massive multi-input-multi-output (MIMO) technology, mm-Wave technology, and network densification are the most promising technologies to meet the requirements of 5G mobile communication networks [2], [9] and very fruitful research results have been published both from academia and industry. There are other research areas related to 5G, such as visible light communications, network slicing [10], software-defined networks [11], full-duplex Communications [12], spatial modulation [13], network coding (polar coding [14]), new waveform (generalized frequency division multiplexing, refer to GFDM) [15], wireless caching [16], cloud and

virtualisation technologies, energy efficiency, etc. In the industry, development of 5G is being led by companies like Intel [17] and Qualcomm [18], Lenovo [19], Nokia [20], Huawei [21], Ericsson [22], and Samsung [23], etc. By the fall of 2018, the operators, such as AT&T, Verizon, and T-Mobile in the USA, EE in the U.K., Elisa in Finland, Vodafone in Spain, KT, LG U+, and SK Telecom in Korea, have announced the 5G trials and network launch plans start from the end of 2018 [24]. In the summer of 2019, the first commercial 5G networks in U.K. has been launched [25], and China has issued the 5G frequency licenses to the main operators for initializing the construction of commercial 5G networks [26].

With the perspective of intelligent societies based on wireless communication systems in the future, recent advances in machine learning infused with network edge intelligence is pushing the researches into the sixth generation (6G) wireless communication systems. The latest insights and innovations from industry and academia on 5G and beyond has been presented and discussed in the first 6G summit, Levi Lapland, Finland, which paves the road for the coming of 6G [27].

1.1.2 The Brief of MmWave Communication

The mobile data traffic of smartphones and tablets has grown 4,000-fold over the past 10 years since 2005 [28]. If this trend continues, the traffic will globally reach 30.6 Exabyte (10^{18} bytes) per month by 2020 [29]. One approach to enhance the capacity/data rate is more bandwidth. ITU radio communication sector (ITU-R) reported about 2 GHz spectrum requirements to accommodate such service demand at latest in 2020 [30]. It is obvious that this bandwidth is not available in the frequency bands used in current 4G mobile communications. The industry is looking at new spectrum in the range up to 100 GHz or higher, i.e., mmWave frequency range. It has been shown that the spectrum around up to 30 GHz and higher frequency range is much less crowded. There are about 1 GHz bandwidth resource available in 28 GHz and 38 GHz bands and 7 GHz bandwidth resource available in 60 GHz band (unlicensed) [31].

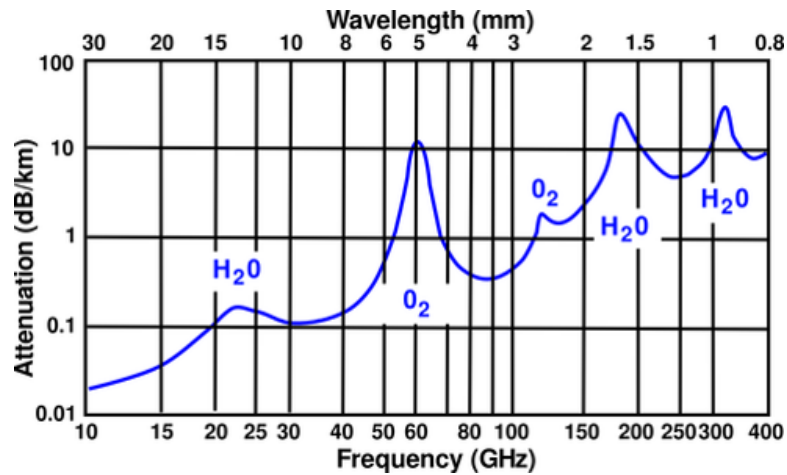


FIGURE 1.1: Attenuation vs. frequencies.

The studies from academia [32]–[34] and ITU-R have shown the feasibility of mm-Wave mobile cellular networks and the technical feasibility of international mobile telecommunication (IMT) in bands above 6 GHz [35]. 3GPP NR specification [7] has addressed the frequency range from 6 GHz to 100 GHz and bandwidth up to 400 MHz in mmWave communication. ITU-R selected candidate bands between 24.25 GHz and 86 GHz for IMT 2020, namely 5G cellular networks in 2015 [36]. Standardization activities for 5G have been kicked-off in ITU-R [37] and in 3GPP [38]. The envision [1], [29], [39] for 5G mmWave communication does not only include scenarios and the applications supported by current 4G communication, it also includes the new applications within the scope of eMBB, mMTC, and URLLC [40], such as vehicle-to-vehicle/infrastructure/everything (V2V/V2I/V2X) communication [41], [42], device-to-device (D2D) communication [43], mmWave air-to-everything (A2X) [44], high speed railway [45], shot-latency gaming and remote control [46], mmWave localization [47], mmWave WiFi [40], etc. Though there are some discussions about the health effect of mmWave communication [48], [49], the academia and industry are working closely together to bring mmWave communication to reality.

Ultra-high speed access and backhaul systems can be formed by using mmWave spectrum together with network densification and massive MIMO [50]. The advantages are that mmWave signals have much shorter wave length. The antennas array with a large number of antenna elements can be packed within a compact size [32], [51] and the applications with large antenna arrays in the future mobile networks can be

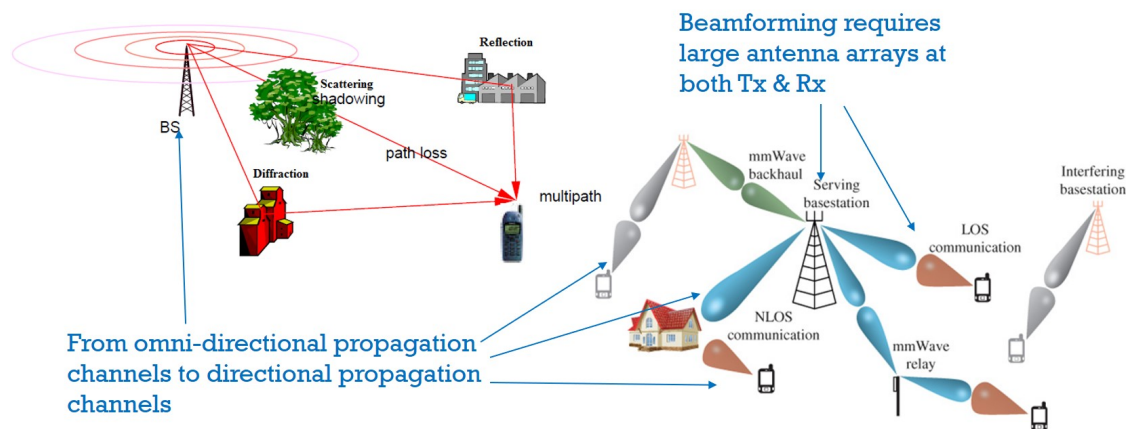


FIGURE 1.2: Omni-directional propagation to directional propagation.

greatly enriched [52], [53]. Also, the beamforming technology based on large antenna arrays generates beams with narrow beamwidths. This enables higher security communication against eavesdropping/jamming and the reuse of spectrum in space [54].

There are many challenges in the design of mmWave communication systems. The high attenuation is the biggest issue of transmitting signals at mmWave frequencies. For example, in Fig. 1.1, the attenuation at 60 GHz is more than 100 times larger than those below 10 GHz. In order to compensate the high attenuation, beamforming technology based on large antenna array is considered as an enabling technology in mmWave communication [55] as shown in Fig. 1.2. In [56], the investigation has shown that by using beamforming technologies [55] and other means to compensate the high attenuation, the mmWave communication over a few hundreds of meters or even a few kilometers is possible. However, controlling each antenna element of a large antenna array by a separate radio frequency (RF) chain is very complex, and the high-frequency power amplifiers (PAs) and RF chains with large bandwidth are very expensive and power consuming [57]. The redesign of corresponding RF/signal processing techniques is required, and the spectral efficiency and energy consumption/hardware cost need to be balanced [58].

Moreover, the radiation patterns with narrow main beams and side lobes are complicated to implement in practise (main beam gain is not constant) [54], especially, in beam misalignment cases during mmWave communications. Therefore, a robust alignment scheme of the Tx and Rx beams is required, and channel state feedback

and management to support directional beam search/steering will be vital [59], [60]. The state-of-the-art researches in this area are mainly as follows: adaptive beamforming [61], [62], hybrid antenna array [63], two layers of beam alignment [64], [65], beam switching [66], dual connectivity [67], beam training [68], intelligent beam search and tracking algorithms [69], etc.

1.2 Motivation

The very broad bandwidth and directional propagation are the main features of mmWave channels. The radio propagation mechanism and the channel characteristics of mmWave channels change dramatically from those of well-known conventional 3G/4G channels. Though plenty of mmWave channel measurements in different scenarios have been performed, the results of propagation properties, such as attenuation, the blocking effect, the large scale fading, delay spread (DS), and angle of arrival/angle of departure (AoA/AoD), etc., have been adopted in the latest developed standard mmWave channel models. However, those research results are mainly the expansion of former 3G/4G standard models by adding new additional components and extending the frequency range of channel models to mmWave frequencies. In this case, some important mmWave channel properties may be overlooked following the inertia of classic approaches of channel models. An overall re-think of the mechanism in modelling mmWave channels is required.

For a thorough understanding of the mmWave channels, the studies of stationarity properties of mmWave channels are fundamental in the data analysis and modelling of mmWave channels. On one hand, the advantage of mmWave communications is the very broad bandwidth. The properties of a mmWave channel with broad bandwidth can be non-stationary in the frequency domain. On the other hand, the directional propagation properties of mmWave channel can also introduce another dimension of non-stationarity in the angular domain [70] due to the inhomogeneous channel environment. Currently, the non-stationarity in the time and spatial domains were investigated in the latest developed mmWave channel models, such as Quadriga [71]

and [72], [73]. The non-stationarity studies in the frequency and angular domains are rarely seen in the literature and current standard mmWave channel models.

In recent studies, there are plenty of beamforming alignment schemes proposed in the literature to support the Tx and Rx movement in mmWave communication [74]. The general mmWave channel properties may change due to using beam alignment schemes (beam behaviours), and the new channel characteristics of mobile-type mmWave channels according to various beam alignment schemes needed to be supported by standard channel models. Currently, the studies of mmWave channel properties affected by the beam alignment schemes are not sufficient, and the standard channel models have not included the properties of mobile-type mmWave channels according to various beam alignment schemes.

The motivation of researches during my Ph.D. study is to develop mmWave channel models which are able to model the key channel characteristics of mmWave channels with very broad bandwidth and directional propagation features. The development of those models is based on the data analysis of channel measurements and the stationarity studies of measured mmWave channels in the frequency and angular domains. The motivation also includes the studies of mmWave channels when Tx/Rx is in motion. It is based on the beam alignment scheme proposed in this thesis.

1.3 Contributions

The key contributions of the thesis are summarised as follows:

- Review recent advances on mmWave channel measurements, summarise and classify recent advances on existing stochastic models for mmWave channels.

Researches on a frequency non-stationarity and frequency non-stationary channel modelling

- Further develop the averaged power delay profile (APDP) methods, which enables to study the stationarity regions of channels in the frequency domain.

- Study the frequency non-stationary (FnS) properties of channels based on the measurements data. The variations of statistical parameters within the bandwidths of FnS channels are addressed.
- Propose a novel FnS channel model for the channels with very broad bandwidths in both the sub-6 GHz and mmWave frequency bands. Ensure the frequency consistency of sub-band channels by cluster evolution in the frequency domain.

Researches on angular stationarity and directional mmWave channel modelling

- Develop an angular APDP (A-APDP) method to estimate the angular stationarity regions (ASRs) of channels in the angular domain.
- Three classes, namely, the light-of-sight (LOS), Non-LOS (NLOS), and outage classes, are utilised to classify the mmWave directional channels (DCs) based on measured directional channel impulse responses (D-CIRs).
- Propose a modified SV model to model the DCs in both LOS and NLOS classes. The consistency of DCs is ensured by cluster evolution in the angular domain.
- Synthesize the omni-directional CIR (omni-CIR) by DCs.
- Propose to model the directional mmWave channels by a Markov chain with three Markov states.
- Propose joint channel models to simulate the instantaneous directional mmWave channels based on the limiting distribution of Markov chain. The joint channel models include a stationary channel model, a non-stationary channel model, and “zero” model.

Researches on mobile-to-mobile directional mmWave channels based on a novel beam-forming scheme

- Proposing a double Gaussian beams (DGBs) scheme for mobile-to-mobile mm-Wave communication.

- Using three Markov states to model the instantaneous directional mmWave channel under DGBs scheme.
- The connection ratios of each Markov state is studied.

1.4 Original Publications

This Ph.D. project has led to the following (potential) publications:

Refereed Journals Papers

1. **Y. Tan**, C.-X. Wang, J. Ø. Nielsen, G. F. Pedersen, and Q. Zhu, “A Novel Frequency Non-Stationary Channel Model for 5G and Beyond¹,” *IEEE Access* 2019 (submitted for publication).
2. **Y. Tan**, C.-X. Wang, Q. Zhu, J. Huang, R. Feng, J. Bian, W. Zhong, and J. Yang , “A Novel GBSM For Wireless Directional MmWave Channels²,” *IEEE Trans. Commun.*, 2019 (to be submitted).
3. **Y. Tan**, C.-X. Wang, J. Huang, R. Feng, J. Bian, and Q. Zhu, “Modeling Directional Millimeter Wave Wireless Channels by Markov States²,” *IEEE Trans. Wireless Commun.*, 2019 (to be submitted).
4. Q. Zhu, Y. Yang, C.-X. Wang, **Y. Tan**, J. Sun, X. Chen, and W. Zhong, “Spatial correlations of a 3D non-stationary MIMO channel model with 3D antenna arrays and 3D arbitrary trajectories,” *IEEE Wireless Commun. Lett.*, vol. 8, no. 2, pp. 512-515, Apr. 2019.

¹The related contents have been recorded in the bi-monthly reports in 1st Quarter 2017 and 1st yearly report of EU H2020 Marie Skłodowska-Curie ITN project 5Gwireless, No. 641985. A video presentation can be found from [www.youtube.com](https://www.youtube.com/watch?v=5dcrFRjHroo&list=PLDxu3M0DpVdF9iqaKpMSN4oMM5Pf4zlv0&index=18): Complementary Courses - Day 1 - ESRs giving presentations - Yi Tan (<https://www.youtube.com/watch?v=5dcrFRjHroo&list=PLDxu3M0DpVdF9iqaKpMSN4oMM5Pf4zlv0&index=18>)

²The related contents have been recorded in the bi-monthly reports and yearly reports in 2017 and 2018 of EU H2020 Marie Skłodowska-Curie ITN project 5Gwireless, No. 641985.

5. Q. Zhu, Y. Yang, X. Chen, **Y. Tan**, Y. Fu, C.-X. Wang, and W. Li, “A novel 3D non-stationary vehicle-to-vehicle channel model and its spatial-temporal correlation properties,” *IEEE Access*, vol. 6. pp. 43633–43643, Jul. 2018
6. Q. Zhu, H. Li, Y. Fu, C.-X. Wang, **Y. Tan**, X. Chen, and Q. Wu, “A novel 3D non-stationary MIMO channel simulator and hardware emulator,” *IEEE Trans. Commun.*, vol. 66, no. 9, pp. 3865–3878, Sept. 2018.

Refereed Conferences Papers

1. **Y. Tan**, C.-X. Wang, Q. Zhu, Z. Zhang, Z. Wang, J. Huang, and R. Feng, “A novel beamforming scheme for mobile-to-mobile millimeter wave communications,” in *Proc. WSA ’18*, Bochum, Germany, Mar. 2018.
2. **Y. Tan**, J. Huang, R. Feng, and C.-X. Wang, “A study of angular stationarity of 5G millimeter wave channels,” in *Proc. ISWCS’18 Workshop*, Bologna, Italy, Aug. 2017.
3. **Y. Tan**, C.-X. Wang, J. Ø. Nielsen, and G. F. Pedersen, “Comparison of stationarity regions for wireless channels from 2GHz to 30 GHz,” in *Proc. IWCMC’17*, Invited Paper, Valencia, Spain, Jun. 2017.
4. W. Qi, J. Huang, J. Sun, **Y. Tan**, C.-X. Wang, and X. Ge, “Measurements and modeling of human blockage effects for multiple millimeter wave bands,” in *Proc. IWCMC’17*, Valencia, Spain, Jun. 2017.
5. R. Feng, J. Huang, J. Sun, **Y. Tan**, C.-X. Wang, and S. Zhou, “Spatial cross-correlation properties of mmWave massive MIMO channels,” in *Proc. IEEE/CIC ICC’17*, Invited Paper, Qingdao, China, Oct. 2017.

1.5 Thesis Organisation

Chapter 2 provides the literature review on the stochastic models for mmWave fading channels in the standard. The studies of two key features of mmWave channels, very broad bandwidth and directional propagation, in the current literature will be briefed,

as well as the studies of vehicular/mobile mmWave channels. In the end, the principle of channel measurement and recent advances on mmWave channel measurements will be reviewed.

Chapter 3 relates to the studies of frequency non-stationarity and frequency non-stationary channel modelling. It forms the main body of journal paper “a novel frequency non-stationary channel model for 5G and beyond.” This chapter first introduces the APDP method and shows the FSR studies of channels based on the measurement data. Then, it proposes a FnS channels models for modelling the channels in both sub-6 GHz and mmWave frequency bands. The studies in this chapter relate to the features of very broad bandwidth of mmWave channels.

Chapter 4 relates to the studies of planar angular stationarity and directional mmWave channel modelling. It forms the main body of journal paper “a novel GBSM for wireless directional mmWave channels.” This chapter first introduces the A-APDP method and shows the planar ASR studies of channels based on the measurement data. Then, it proposes to model the directional mmWave channels based on the classification of LOS, NLOS, and Null classes. The studies in this chapter relate to the feature of directional propagated mmWave channels.

Chapter 5 relates to the studies of spherical angular stationarity and modelling directional mmWave channels based on Markov states. It forms the main body of journal paper “modeling directional mmWave channels based on Markov states.” This chapter first further develops the A-APDP method and shows the spherical ASR studies of channels based on the measurement data. Then, it proposes to model the directional mmwave channels based on Markov states. The studies in this chapter also relate to the feature of directional mmWave channels.

Chapter 6 relates to the studies of mobile-to-mobile directional mmWave channels based on a novel beamforming scheme. It forms the main body of conference paper “a novel beamforming scheme for mobile-to-mobile millimetre wave communications.” This chapter proposes a DGBs scheme used in mmWave communications when both Tx and Rx are in motion (beam alignment is required). The focus of this chapter is

the connection ratios of directional mmWave channels in each Markov state when the DGBs scheme is applied.

Chapter 7 is the conclusions of the works in this thesis. It also points out the potential future works in mmWave channel modelling.

Chapter 2

Millimetre Wave Channel Modelling: Literature Review

2.1 Introduction

The wireless radio channels are the transmission medium to convey the information signals from Tx and Rx. The researches in this area play a fundamental role in the radio system design because all the studies in wireless communication areas are aiming to overcome the “bad” effects on the signals that are caused by the radio channels. The channel measurements and channel models are the methods to study the radio channels. The channel characteristics are analysed and estimated based on the channel measurement data, and they are modelled as references for system-level designs and evaluations. For the conventional 3G/4G wireless channels, the working frequencies are mainly below 6 GHz. For the mmWave channels, we consider the working frequencies are above 6 GHz and up to 100 GHz or even higher [55], [75].

The study of mmWave channels is a very hot topic. There are many universities, research institutes, and companies working in this field. We can find quite a few survey papers published in recent years [40], [54], [75], [76]. The contents in this chapter relate to the background information and general idea of mmWave channel

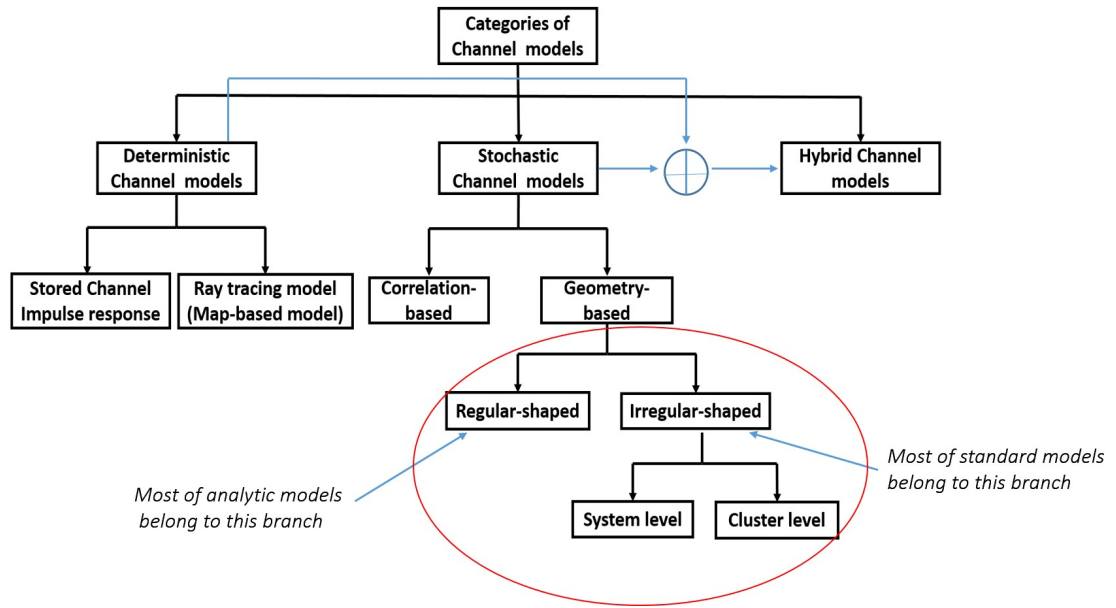


FIGURE 2.1: Categories of channel models.

measurement and modelling. Those can be considered as a reference/baseline for the research topics in this thesis.

In this chapter, the categories of channel models are introduced first. Then, the standard mmWave channel models and the latest development of mmWave channels are introduced. In the following, the background of channel measurements, channel sounders, and a short brief of mmWave channel measurements campaigns are introduced.

2.2 The Categories of Channel Models

The wireless channel models can be generally divided into three categories as in Fig. 2.1. The methods used in the development of those models can be sorted as (1) Deterministic channel model, (2) Stochastic channel model, and (3) Hybrid channel model (combined stochastic model and map-based model).

2.2.1 Deterministic Channel Model

The typical deterministic channel models are site-specific models as one main branch in Fig. 2.1. It can be further resolved as (1) restored impulse responses and (2) ray tracing models. Restored impulse responses are acquired from channel measurements, they are the most direct way to present the wireless channels. All the channel measurement data recorded in the literature can be considered as this type of channel model. The ray tracing models are also recorded in form of channel impulse responses, which are acquired from the deterministic solution of Maxwell's equations or some approximations based on the geographical and morphological information of certain wireless scenarios [77]. Ray tracing models are used to complement time-consuming and expensive measurement campaigns in the investigation of propagation characteristics, coverage, and system performance [78]–[80]. Though with the drawback that large computational efforts are required and the results are inherently less accurate, ray tracing models have been recognised as reliable tools to simulate accurate mmWave channel properties [81], [82]. This type of channel model method has been used as part of standard channel models, such as IEEE 802.15.3c [83], IEEE 802.11ad [84], MiWEBA [85], METIS [39], etc.

2.2.2 Stochastic Channel Models

Stochastic channel models, as another main branch in Fig. 2.1, have been developed for the purpose of fast system-level simulations (compare with ray tracing models) [54]. They are the most widely used channel models in the system level simulation. They are not designed to correctly predict the impulse response in one specific location, but they can be used to predict the probability density function (PDF) over a large area [77]. This kind of models relies on statistical observations of the channels with various measurements in different typical scenarios. The distributions of various channel characteristics are estimated from measurements. Stochastic channel model can be generally divided into two categories further: (1) correlation-based stochastic channel

model (CBSM or CSCM) and (2) geometry-based stochastic channel model (GBSM or GSCM).

The CBSM channel model describes the MIMO characteristics by correlation matrices. Its merit is the lower computational complexity compared with the channel models in other categories. It is widely used by system-level performance simulations. The well-known and widely used Kronecker model and Weichselberger model belong to this category [86]. The difference between those two models is that the Kronecker model considers the Tx and Rx are not mutually correlated, but the Weichselberger model could well present the joint correlation between Tx and Rx.

The GBSM channel models are more accurate than CBSM channel models, but they are much more computational complex. There are mainly two types of GBSM: (1) regular-shape based GBSM and (2) irregular-shape based GBSM. Most of the regular-shape based GBSMs are analytical models, such as the Clarke model [87] and those in [73], [88]–[91]. Typically, the scatters of the channels are distributed based on a geometrical shape, such as ring, ellipse, etc. with certain distribution density functions. In such an approach of modelling, all the channel parameters can be tracked and calculated geometrically. The feature of such models is that the reference models of regular-shape based GBSM are the mathematical channel models based on the geometric calculation, and the approximation methods, such as exact Doppler, the L_p -norm method (LPNM), etc., are often used in the simulation model to approximate the reference models. Compared with that, in the irregular-shape based GBSM, the positions of scatterers are following certain distributions and they are randomly located rather than located on a geometric shape in irregular-shape based GBSMs. The parameters used in the simulation models are estimated based on the data of real channel measurements in different scenarios. Therefore, most of the standard channel models are in this category, such as WINNER II/+ [92], [93], QuaDRiGa [71], COST2100 [94], etc., as well as mmWave channel models, such as 3GPP [95], METIS [39], mmMagic [29], 5GCM [1]. Note that, follow the stochastic model branch in Fig. 2.1, the irregular-shape based GBSM can be further divided into two branches: (1) system-level approach (most fast fading models of standard

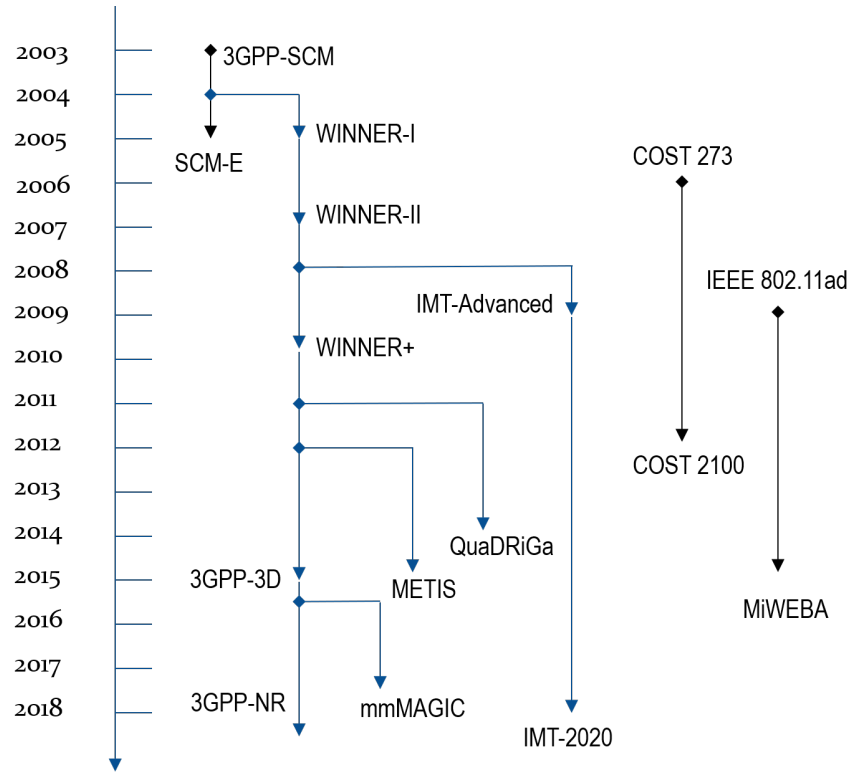


FIGURE 2.2: Standard channel models and their family history.

models), (2) cluster-level approach (used in COST2100). More details can be found in [96].

Stochastic channel models are in constant development to adapt to the new features of wireless communication systems. From the topology in Fig. 2.2 [54], we can see that the leading research of channel models is following the developing line of 3GPP-SCM (SCM stands for spatial channel model) [97], WINNER-I/II/+ [92], [93], and then 3GPP-3D [98], and 3GPP-NR [95]. Those models have covered most of the aspects of wireless channels in various scenarios, which include network layout, the large-scale and small-scale parameters, channel scenario transition (channel segment, drop and time evolution), etc. Some Matlab codes are also available for reference from the websites of those projects. As to the other developing lines, they are not all-inclusive channel models, but they are prone to be developed for specific applications/scenarios of wireless communication, or using other approaches to better model the properties of wireless channels in certain aspects. For example, COST 2100 [94] focuses on

multi-user, distributed MIMO, and moving Tx/Rx scenarios in the 4G communication system. ¹

2.2.3 Hybrid Channel Models

There is a combined stochastic and deterministic channel modelling approach, which is called a hybrid channel model in METIS [39], as the third main branch of channel models in Fig. 2.1. Normally, in the procedure of modelling the channel, the locations of the base stations (BSs) and the user equipment (UE) have to be fixed on a map first. The path loss (PL) and shadowing are calculated based on the map, and random shadowing objects can be generated based on ray tracing modelling method, which explained in Section 2.2.1. Then, all other calculations are done by the stochastic model [39]. Hybrid modelling approach takes the merits from both the deterministic and stochastic models, and it is widely accepted in the modelling of mmWave channels. In the mmMagic project, it extends the existing QuaDRiGa channel model [71] by using the deterministic channel approach in the simulations [29], [99].

2.3 Modelling of MmWave Channels

European Commission is funding the projects about 5G communication within the perspective of Horizon 2020. The 5G infrastructure public private partnership (5GPPP) [100] is taking Europe's leadership in standardizing 5G communications and the research of mmWave channels is one of the most important areas. The mmWave channel models developed inherit the spirit of WINNER family models and have included most of the aspects of mmWave channels in different scenarios. The methodologies, such as the stochastic channel modelling approach, ray tracing modelling approach, and the hybrid modelling approach, as shown in Fig. 2.1, are all adopted in the development of those models, such as 5GCM, IEEE 802.11ay [101], IMT 2020 [102], and New York University (NYU) wireless models [103]. The researches in this area are leading by

¹Note that the description of developing lines of channel models are excerpts from [54].

Feature	COST 2100	MiWEBA	QuaDRiGa	METIS		MCHFB	3GPP	mmMAGIC
				stochastic	map-based			
Frequency range (GHz)	-	57-66	0.45-6	up to 70	up to 100	0.5-100	6-100	10-80
Bandwidth	-	-	100 MHz	100 MHz < 6 GHz, 1 GHz @ 60 GHz	10 % of the centre frequency	100 MHz < 6 GHz, 2 GHz > 6 GHz	10 % of the centre frequency	2 GHz
Support massive-MIMO	-	yes	yes	no	yes	limited	yes	yes
Support spherical wavefront	no	yes	yes	no	yes	no	no	yes
Support dual mobility	no	yes	no	limited	yes	no	yes	no
Support 3D (elevation)	yes	yes	yes	yes	yes	yes	yes	yes
Support mmW	no	yes	no	partly	yes	yes	yes	yes
Dynamic modeling	yes	limited	yes	no	yes	yes	yes	yes
Spatial consistency	yes	yes	limited	shadow fading only	yes	limited	yes	limited

FIGURE 2.3: Comparison of 5G channel models.

Prof. Theodore S. Rappaport in NYU [81], [104]–[106] and the researchers in Samsung Electron., Co., Ltd. [55]. The universities and the companies that are also working on mmWave channel models are Lund University [31], [107], University of Texas [108], Electron. & Telecommun. Res. Inst (ETRI) South Korea [109], [110], HWU [111], Intel Corp. [112]–[115], Huawei Technologies Co., Ltd. [116], etc.

2.3.1 Standard MmWave Channel Models

There are quite a few standard channel models support mmWave channel scenarios. From Fig. 2.3 [117], we can see that MiWEBA, METIS, MCHFB (5GCM), 3GPP, mmMagic models can be used to model mmWave channels. In the comparison among those models based on the corresponding materials, we can find that there are some common channel measurements and modelling methods in different standard models, because those models are developed in parallel and the partners belong to one project also actively contribute to other projects. For example, the mmMagic project partners also contribute to 3GPP and IMT 2020 projects. However, each individual model

has unique contributions. The status/expectation of existing information on high-frequency channels can be found in the 3GPP-NR document “Study on channel model for frequency spectrum above 6 GHz” [95]. In this section, we only brief some highly cited standard mmWave channel models.

2.3.1.1 IEEE 802.11ad & IEEE 802.15.3c

IEEE 802.11ad [84] and IEEE 802.15.3c [83] models are the previously proposed mm-Wave channel models at 60 GHz frequency range. IEEE 802.11ad is a 3D model and IEEE 802.15.3c is a 2D model. They were developed for different channel scenarios. IEEE 802.11ad focuses on the modelling of the channels in WLAN (wireless local area networks) scenarios, such as conference room, living room, and cubicle environment. IEEE802.15.3c focuses on the modelling of the channels in WPAN (wireless personal area networks) scenarios, such as residential, office, library, desktop, and kiosk. Those models are all rooted in the cluster-ray modelling approach which is similar to that of Saleh-Valenzuela (SV) model [118], [119] and the amplitudes and the delays are described by certain statistical distributions. Though they were both developed based on the statistical parameters estimated from the measurements and ray tracing were used in the modelling, but they are not exactly the same as the hybrid METIS model regarding their modelling methodologies. For example, empirical statistical distributions are wildly used in the modelling of cluster delays and angles, etc. in the IEEE 802.11ad which is called “quasi-deterministic” model [120].

2.3.1.2 METIS

METIS channel models inherit the spirit of common channel model, such as WINNER family models. The models are developed based on extensive literature reviews, massive data analysis of real measurements, and ray tracing simulations. The models developed are for overall 5G scenarios, which includes the characteristics of both massive MIMO channels and mmWave channels. METIS also classify the overall modelling methods by map-based models, stochastic models, and hybrid models. This is

very instructive for later developed channel models. The user needs to make the selection if the target propagation scenario can be modelled with more than one modelling methods. The model choice depends on the frequency range, accuracy, computational complexity, and simulation time (which depends mostly on the simulated system like the number of BSs and UEs). The key results of the METIS channel model investigations can be found from the specification in [39].²

In the comparison of METIS models, the map-based models are the most complete models covering most of the test cases, propagation scenarios, and the desired frequency range. Map-based mmWave channel models addressed the frequency range up to 100 GHz and the bandwidths of mmWave channels up to 10% of the centre frequency can be supported. The stochastic model suits best to urban macro and micro cell environments, including the outdoor to outdoor (O2O) and outdoor to indoor (O2I) scenarios. The hybrid model is a combination of both. It can be considered as a flexible and scalable framework to meet diverse channel modelling/simulation requirements [39].²

2.3.1.3 MmMagic

The mmMAGIC channel model is a geometry based stochastic model (GSCM/GBSM) comprised of baseline modelling framework and additional features that extend its accuracy and applicability. The features of model are the studies of ground reflection and blockage effects, building penetration loss, support of large bandwidths and large antenna arrays, and spatial consistency. There are more than 20 channel measurement campaigns conducted in various scenarios, such as UMi street canyon, UMi open square, office, airport check-in area and outdoor-to-indoor, across the frequency bands from below 6 GHz to up to 100 GHz (close the gap between the traditional cellular frequencies and mmWave frequencies). Specific measurements were performed to study the specular and diffused scattering, the impact of the ground reflection and blockage, and the frequency-dependent channel characteristics.³

²Note that the marked contents are excerpts from METIS [39].

Specifically, a blockage model based on METIS work has been developed based on Kirchhoff's diffraction formula and verified in the real measurements. The spatial consistency modelling procedure, which was initiated by 3GPP, has been investigated. A grid-based GSCM (partly based on METIS), using time-variant angles and cluster death and birth as the UE is moving, has been proposed. It is also an important feature to evaluate mobility and beam tracking. The small-scale fading characteristics caused by the diffused signal components have been investigated in the measurements related to the surface roughness of various building materials.³

2.3.1.4 3GPP models, above 6 GHz

The 3GPP models are general channel models which inherit the modelling methods used since the development of WINNER family models. It is a system-level channel model including all aspects of channel characteristics of all related large-scale and small-scale parameters. It also includes the time/cluster delay line (TDL/CDL) models for the convenience of link level evaluations, and the channel model calibration is filed to provide a baseline for all the industry and academia institutes in the development of 3GPP channel simulators. For the latest development 3GPP model, that support the modelling of channels above 6 GHz, is normally called 3GPP-NR. The details of model objectives can be found from the specification in [95].

In 3GPP NR, there are stochastic models and map-based hybrid models developed to support mmWave channels. The scenarios the stochastic models support include urban micro (UMi)-street canyon and urban macro (UMa), UMii-open square, indoor-office, indoor- shopping mall, and rural macro (RMa). Except for modelling the channel characteristics related to path loss, LOS probability, penetration, fast fading (small-scale model), etc., the specific characteristics of mmWave channels are modelled by adding additional components, such as oxygen absorption, blockage, correlation modelling for multi-frequency simulations. The map-based hybrid models are composed of a deterministic model (based on METIS work) and a corresponding

³Note that the marked contents are excerpts from mmMagic final report [29]. A subset of the proposed mmMAGIC features is implemented in QuaDRiGa v2.0 [71].

stochastic model mentioned before. By introducing a digital map into the simulation, it can be used for the evaluation and prediction of system performance taking the impacts of environmental structures and materials into consideration.⁴

2.3.2 Specific Characteristics of MmWave Channels

Since the working frequencies of mmWave channels are above 6 GHz (could up to 100 GHz or higher), there are some specific channel characteristics that are different from those of former conventional 3G/4G channels. In the standard mmWave channel models, the specific mmWave channel characteristics are introduced by additional components, such as those in chapter 7.6 of 3GPP-NR [95]: oxygen absorption (frequencies between 53 and 67 GHz), blockage effects, etc. Due to the limit of the thesis, we only make a summary on some of the important specific characteristics of mmWave channels investigated in the standard mmWave channel models.

2.3.2.1 Frequency Dependent Characteristics

In order to model the channel characteristics over the range of 6 GHz to 100 GHz working frequencies, the frequency dependent parameters are introduced into the standard channel models. For example, in 3GPP-NR [95], antenna patterns, array geometries, system centre frequency and bandwidth, oxygen absorption, cluster powers, delay spread, and angular spreads are all considered frequency dependent. As well as 5GCM version 2.0 [1], it provides significant updates to large-scale and small-scale parameter modelling, including a newly proposed clustering algorithm and models, which capture frequency dependent parameters.

In the modelling of mmWave channels with multiple frequencies, for example, transmitting signals at both low frequency (LF) and high frequency (HF) channels, the studies of consistency and correlation between them are required. The correlation coefficient is used as the metric to study the correlation of signals in time/spatial

⁴Note that the marked contents are excerpts from 3GPP, more details can be found in [95].

domains, etc. The consistency of channel can be considered as an overall description of correlations for each large-scale parameter, cluster specific parameter, and ray specific parameter of channels [95]. Similar studies have been done in frequency domain for multiple frequency channels. Currently, the consistency of multiple frequency bands channels in a heterogeneous network has been investigated by a ray tracing model in 5GCM [1]. The inter-frequency correlation of LSPs has been studied in IMT 2020 [102]. The frequency dependent channel behaviour and outline a simulation strategy to generate multi-band frequency dependent channels have been studied in [121].

2.3.2.2 Path loss and Oxygen Absorption

The Friis transmission formula is generally used in free-space transmission [32], [54]. It can also be used to approximately describe the power of received signal in non-free-space propagation as well. For example, finding a suitable value of n that can approximately describes the path loss based on the measurement data [54]. According to Friis transmission formula, the path loss of mmWave signals is much higher than that of the signals below 6 GHz if all other conditions including the antenna gains are the same. The rain attenuation and atmospheric/molecular/oxygen absorption increase the path loss and limit the communication range [122], [123]. The mechanical resonance frequencies of gaseous molecules also coincide with the mmWave signals and the important absorption peaks occur at 24 and 60 GHz [124].

Based on the measurements in 5GCM [1], it is shown that for the mmWave bands below 100 GHz, the attenuation was dominated by oxygen absorption, where the peak is around 60 GHz. In mmMagic [29], up to 4 dB loss caused by oxygen absorption for 1 m distance based on NLOS channel measurements between Tx and Rx was record. In 3GPP [95], the oxygen absorption varies according to frequency. The modelling of oxygen absorption between 53 GHz and 67 GHz can follow the Table 7.6.1-1 in [95], and there is no oxygen absorption in the frequencies below and above.

2.3.2.3 Penetration Loss and Blockage

As the carrier frequencies increase, the propagation behaviour of mmWave signals is more like optical propagation [125]. In general, they have high penetration loss and they are very sensitive to the blockage by walls and other objects [1]. In the studies of NLOS transmission, it has shown reasonable reflection loss and high diffraction loss. We also find that metal and concrete walls cause high penetration loss and heavy foliage cause severe shadowing loss [54]. Strong variation of the penetration loss depends on the window material composition were observed in mmMagic [29]. The material-dependent penetration loss models were developed separately in 3GPP and the low penetration and high penetration models were developed for O2I scenarios [95].

Plenty of channel measurements related to blockage were performed in standard channel models, such as mmMagic [29] and 5GCM. In 5GCM [1], two categories of blockage are considered: dynamic blockage and geometry-induced blockage. The dynamic blockage is caused by moving objects (i.e., cars, people). The effect is a transient additional loss on the paths that intercepted by the moving object. The geometry-induced blockage is a static property or object of the environment that block the signal paths. In 3GPP-NR [95], the blockage model is an add-on feature (developed in a component). It models the blockage effect by A and B models. A model adopts a stochastic method and B model adopts a geometric method for capturing human and vehicular blocking. Other approaches of modelling blockage can be found in [126] and literature.

Note that, the path loss measurements in urban areas often include the loss caused by trees and other vegetation in UMa and UMi case. It is important not to account for foliage losses twice in the channel model [1].

2.3.3 Directionality of MmWave Channels

Beamforming is used as an enabling technology for the 5G mmWave communications [2], [32], [55], [75], [89], [127]–[129]. Both the transmitter (Tx) and receiver

(Rx) use physical beams during the communication and the beams are required to be aligned to each other. This is one of the main features of mmWave channels mentioned previously. In this case, the transmitted signals only interact with the objects in the transmission direction between the Tx and Rx in the environment. The statistical properties of directional mmWave wireless channels can be directional dependent, which related to the inhomogeneity of the channel environment. At the moment, the descriptions of directional properties of mmWave channels can be found in newly developed channel models, such as the directional path loss channel models in mm-MAGIC, [130], [131], the super-resolved directional channel model in METIS [39], and NYU Wireless Models.

2.3.3.1 NYU Wireless Models

Based on extensive propagation measurements carried out from 2011 through 2015, NYU has proposed a statistical spatial channel model (SSCM) that break the conventional means of modelling the small-scale parameters of directional mmWave channels in standard mmWave channel models. In the model, the temporal and spatial/angular statistical descriptions of channels were firstly separated in the modelling of mmWave channels and the generation steps of angular dependent channel coefficients were introduced [132]–[135].

The SSCM is developed using the time cluster–spatial lobe (TCSL) approach. Based on the existing 3GPP model, the spatial lobes has been added by additional model parameters: directional RMS lobe angular spreads [132]. The SSCM can be used to generates both the omni-directional and directional multipath parameters of the channels between the TX and RX over a local area. The framework of TCSL can better reproduce the temporal and angular statistics of measured directional mmWave channels (using directional antennas) [136] and can more practically reflect the properties of mmWave channels in reality.⁵

⁵Note that the marked contents are excerpts from [132].

2.3.4 Studies of Vehicular/Mobile MmWave Channels

MmWave communication has been widely accepted to be used in 5G vehicular communication and mobile-device-type communication, such as D2D, V2V, M2M, vehicle-to-everything (V2X) and air-to-everything (A2X) [137]. Since using beamforming technology at both Tx and Rx, if the Tx or Rx moves or rotates during the communication, the beams will be misaligned and the communication can be broken if there is no robust solution to re-align the beams. Therefore, the physical alignment of Tx and Rx beams is one of the biggest challenges in the mobile-type mmWave communication. The studies about the impact of user mobility on mmWave communications can be found in [138]. Two layers of beam alignment [64], [65], beam switching [66], beam training [68], intelligent beam search tracking algorithms [69], and other beam alignment schemes have been developed. In cases of using beam alignment schemes in the mmWave communication, the modelling of mmWave channels facing new challenges that how to correctly model channel characteristics under those various beam alignment schemes need to be studied.

At the moment, there are researches of vehicular mmWave channels based on the similar approaches of studying conventional vehicular channels in 3G/4G systems, such as the studies of small-scale in-vehicle mmWave reflections [125], the modelling of UT mobility and UT rotation in 3GPP [95], and a newly proposed general 5G channel model [89]. We can also find the studies related to the directional vehicular mmWave channels and mobile-type mmWave channels related to various beam alignment in the literature. In [139], [140], the characteristics of directional vehicular mmWave channels were studied. In [141], the change of channel characteristics, especially the relationship between coherence time and beamwidth, was studied when using beam alignment schemes. The beam alignment schemes among vehicles and vehicles to infrastructures were suggested in [74], [142]–[145], and the corresponding channel characteristics were addressed.

2.4 MmWave Channel Measurements

Channel sounders are designed for channel measurements. As the system design becomes more complex, the requirements of channel sounding devices have been through three stages: be able to measure field strength in the 1960s; be able to measure impulse responses, i.e., delay dispersion (wideband systems); be able to measure (double) directional impulse responses since the 1990s (multi-antenna systems/MIMO) [77]. Nowadays, in order to measure 5G wireless channels, the sounders used for measuring the directional impulse responses have been further developed with the extension to support large antenna-array (Massive MIMO) and mmWave frequencies.

2.4.1 Principle of Wide-Band Channel Sounding

According to [77], [146], sounding the wireless channel can be considered as using a delta function $\delta(t)$ to excite a system and analysing the impulse response. It is very difficult to create an impulse to measure the wireless channels, due to generating an impulse equal to generating a signal with infinite bandwidth. So, it is very common to using signal processing technologies to approximate the impulse in reality. Using pseudo-noise (PN)-sequence sounding signals to measure the channels by correlative sounder [77] and using OFDM sounding signals to measure the transfer function of channels in the frequency domain [147] are designed to fulfil such purpose.

In a time-variant system (Rx or Tx is in motion), the repetition period T_{rep} of the sounding pulse is fundamentally important. In Fig. 2.4, we consider the channel response to an excitation pulse as one “snapshot” (sample) $h(t, \tau)$ of the channel. In order to track the changes of channel, the repetition time T_{rep} to take these snapshots must be smaller than the time the channel changes $\frac{1}{2 \times v_{max}}$ [77]. Similar to using the Nyquist sampling rate (minimum sampling rate) to sample a signal with a band-limited spectrum, a Nyquist temporal sampling rate needs to be satisfied taking the snapshots of a time-variant channel with a band-limited Doppler spectrum. Therefore, the repetition time T_{rep} , which can be considered as temporal sampling frequency,

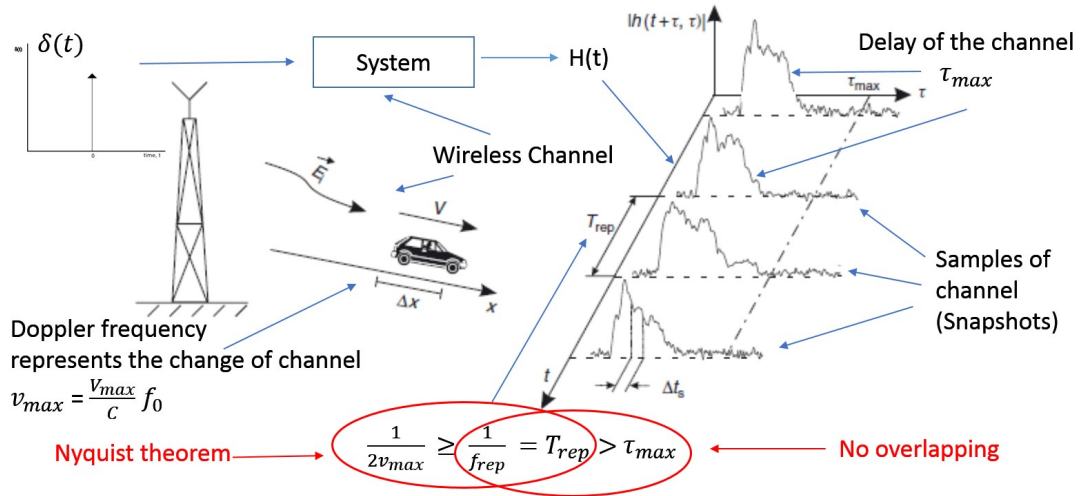


FIGURE 2.4: Sounding principle of a time-variant wireless channel.

must be twice the maximum Doppler frequency (based on the Doppler spectrum of channel) [77]. Furthermore, the repetition time T_{rep} must be larger than the maximum excess delay of channel τ_{max} for avoiding the overlapping of the impulse responses from the consecutive excitation pulses.⁶

2.4.2 MmWave Channel Sounder

Generally, there are two types of channel sounders: (1) vector network analyser (VNA) + antenna/antenna-array, and (2) baseband components + RF components, which forms a typical RF signal transmission system, see figures 2.5 and 2.6. The first type of sounders measures the channels in the frequency domain, and it can only measure the time-invariant (static) channel scenarios, which are normally indoor channel environments. The second type of sounders are correlative sounders (see previous section) and OFDM channel sounders, which measures the wireless channels in time and frequency domain respectively. The advantage is that it can measure the time-variant channels of both indoor and outdoor scenarios, such as V2V, machine-to-machine (M2M) scenarios. More details can be found in Chapter 8 of Molisch's book [77].

⁶Note that the marked contents are excerpts from [77].

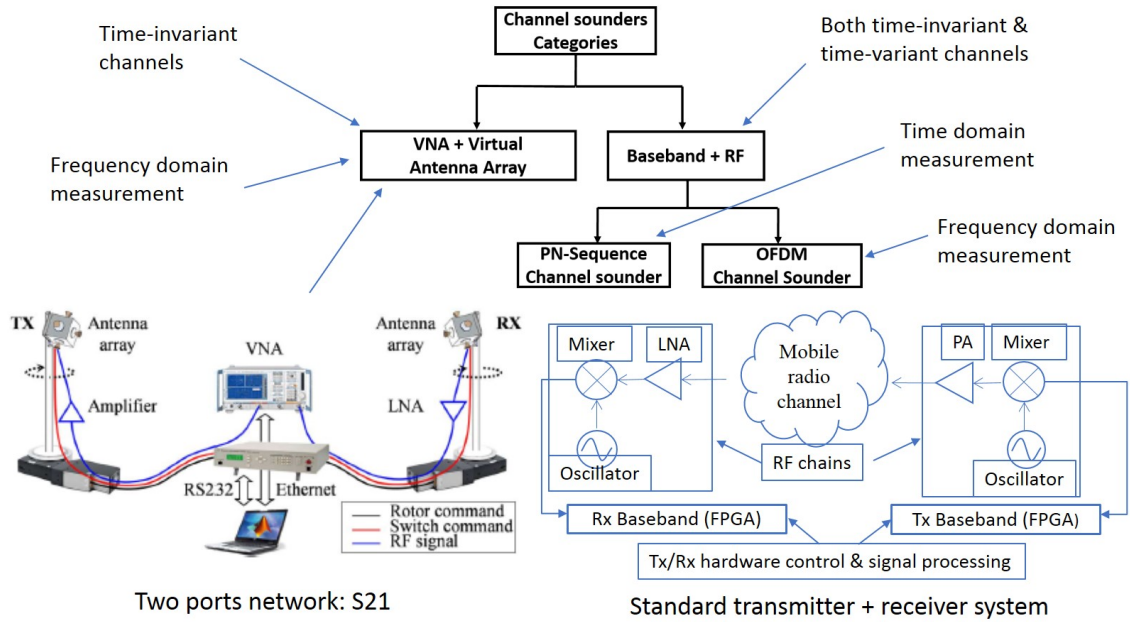


FIGURE 2.5: Categories of channel sounder structures.

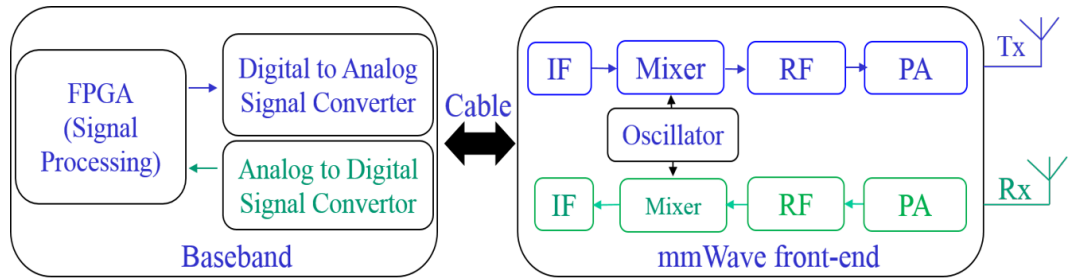


FIGURE 2.6: Baseband components + RF components channel sounding system.

In the mmWave channel measurements, the first type of sounders has been widely used by universities and research institutes due to low cost [107]. As the requirement of measuring time-variant mmWave channels, there are more universities and companies have started to develop the second type of sounders, and more and more research results have been published based on those sounders in the literature, such as the channel measurements from NYU [32], Technische Universität Ilmenau [148], [149], Fraunhofer Heinrich Hertz Institute [150], Electron. & Telecommun. Res. Inst (ETRI) South Korea [151], as well as the channel measurements from companies R&S, Keysight [152], Nutaq, etc. In addition, some companies are offering the channel measurement solutions to the research institutes who have difficulties to build the sounder by themselves and willing to buy channel sounder directly.

However, the current mmWave channel sounder are not suitable to measure the vehicular/mobile mmWave channels when the Tx and Rx are moving. When both Tx and Rx use omni-directional antennas, the high attenuation limits the mmWave communication to a very short distance. The vehicular/mobile communication can drop off frequently, the channel measurements can not be done. When both Tx and Rx use beamforming or horn antennas, a robust beam alignment scheme need to be implemented in the channel sounder. Though there are plenty of studies related to the beam alignment schemes as mentioned previously, implementation of them are not easy. This is one of the biggest challenges for mmWave channel sounders.

2.4.3 A Short Brief of MmWave Channel Measurement Campaigns

There are numerous mmWave channel measurements have been performed in recent years. The characteristics of mmWave channels have been well reported in the literature. Table 2.1 list some typical mmWave channel measurement campaigns at different frequencies (from below mmWave frequencies 2–4 GHz to 86 GHz) for different scenarios, which includes indoor office, library, outdoor street canyon, Urban environment etc. in different cities (Edinburgh, New York, Berlin, Jinan China, etc.). More measurements results and the overview of mmWave channel measurement campaigns can be found in [54], [75] and the related literature. Due to the limit of this thesis, we do not show them.

2.5 Research Gap

The very broad bandwidth is the merit of using mmWave communication. For example, mmWave channel measurements with 4 GHz bandwidth were used in METIS [39], [168]. Within such broad bandwidths of mmWave channels, we expect that the frequency stationarity assumption does not always hold for mmWave channels as those were studied in the ultra-wide band (UWB) channel below 10 GHz [169]. This is a

TABLE 2.1: Brief of mmWave channel measurements

Frequency (GHz)	Scenario	Site	Parameters	Ref.
2-4, 14-16, 28-30	Indoor base-ment	Aalborg	Frequency and spatial stationarity regions	[153]
11, 16, 28, and 38	Indoor office	Jinan	Power delay profile, delay spread, angular spread, power azimuth/elevation profile, and cluster evolution	[127]
15, 60	Outdoor to indoor	Stockholm	Penetration loss and delay spread	[29]
28	Indoor, a five-story building	New York	Path loss, angular spread, and delay spread	[154]
28	Indoor laboratory	Edinburgh	Power delay profile, power angle profile, and delay spread	[111]
28	Urban	Daejeon	Path loss, delay spread, angular spread, angle of arrival, and angle of departure	[155], [156]
38	Outdoor, urban environment	New York	Path loss, delay spread, and outage study.	[157]
38	Street canyon, corner scenarios, outdoor to indoor	Aalborg	Reflection, scattering, diffraction, transmission, and polarization	[158]
40	Indoor laboratory	Dallas	Penetration loss and reflectivity	[159]
41,82	Street canyon	Berlin	Large-scale parameters, time evolution, and frequency dependence	[29]
45	Indoor conference room, living room	Nanjing	Antenna beamwidth and large-scale fading	[160]
60	Indoor office	Jinan	Power delay profile, delay spread, angular spread, power azimuth/elevation profile	[161]
60	Indoor and outdoor	Durham,	Path loss, delay spread, and MIMO capacity	[162]
60	Urban outdoor	Berlin	Path loss, time evolution, and human body shadowing	[163]
61-65	Hospital environments	Helsinki	Path loss and delay spread	[164]
61-63	Indoor conference room	Lund	delay, direction of departure, direction of arrival, delay spread and direction spread	[107]
62.5	Indoor living room	Sendai	Received power, angle of departure, and angle of arrival	[165]
72	Indoor office	Shanghai	Angular spreads and directional dispersion	[166]
81-86	Roof-to-street and street canyon	Helsinki	Impulse response, frequency response, and delay	[167]

problem when utilizing mmWave communications in the environments such as factories, warehouses, mines of coal/metals, chemistry laboratories, etc., where the sizes of objects are comparable to the wavelengths of mmWave signals. However, in the current standard mmWave channel models [29], [39], [83]–[85] and those mmWave channel models developed recently [32], [107], [132], [170]–[172], the channel parameters were normally considered as frequency stationary (FS). Though there is one component developed to support large antenna array and large bandwidth in standard channel models, the criterion to determine the large bandwidth is not directly related to the FnS properties of channels. For example, if we transmit signals with 150 MHz bandwidth at 2 GHz (centre frequency) by an antenna (array) with 1 m aperture, its bandwidth is smaller than the criteria $c/D = 300$ MHz. This criteria is used to determine if the bandwidth can be treated as a large bandwidth (where c is speed of light and D is the aperture of antenna). While, it is considered as a FnS channel according to the results in Section 3.3. The FnS property clearly needs to be further studied. Furthermore, the study of frequency dependent channel with broad bandwidth, i.e., frequency stationarity, is also required. For example, the multi-band OFDM system is widely accepted for UWB communications [173]. The multi-band OFDM technologies can also be used to generate a mmWave sounder signal with very broad bandwidth. It is possible to model each of narrow-band OFDM channels, but we cannot simply combine them. The frequency-dependent statistical parameters of those multi-band channels and the modelling of frequency-consistent multi-band channels need to be studied.

Highly directional transmitted signals are used in mmWave communications for compensating high attenuation. Such signals only experience a part of the whole channel environment and this is another key feature of mmWave communication. In the standard mmWave channels, the studies of mmWave channels inherit the approaches of studying the conventional 3G/4G channels. Model the whole omni-directional channel first, then, obtain the directional mmWave channels by multiplying the directional antenna patterns or by applying the beamforming technology on the antenna arrays at both the Tx and Rx. However, the channel environment is inhomogeneous in different directions in reality. The objects, such as building, trees, vehicles, human,

etc., contribute differently to the statistical properties of channel in different directions. In the standard channel models, the approach used to generate the directional channels lacks in-depth analysis on the inhomogeneity of wireless environment at the moment. The whole environment is considered as a homogeneous environment and it is described with same statistical property. The different properties of directional mmWave channels cannot be properly represented. For example, we have tried to use the Quadriga model [71] to generate the directional mmWave channels based on the scenario configurations from mmMagic/3GPP in Quadriga's archive with different beamwidths of the antenna beams, different rotating azimuth angles, and different mmMagic/3GPP channel parameters. We found that the comparison of estimated statistical parameters between the simulations and measured data, such as the cluster number, the value of RMS delay spread and their distributions (in chapter IV and V) are quite different. The reason could be that the standard mmWave channel models using the estimated parameters based on the whole channel cannot really represent the properties of directional mmWave channels due to the inhomogeneity of environment. Therefore, further studies about the directionality of mmWave channels are needed.

There are quite a few beam alignment schemes that have been developed for mmWave communications where beamforming technology is applied at both Tx and Rx, such as adaptive beamforming [61], [62], dual connectivity [67], intelligent beam search and tracking algorithms [69], etc. Consequently, modelling the mmWave channels facing new challenges that how to correctly model the characteristics of mobile-type mmWave channels based on various beam alignment schemes. So, the researches in this field are twofold, both the beam alignment scheme and the changes of channel characteristics caused by the beam alignment scheme need to be studied at the same time. In the latest studies, the beam alignment schemes developed require the system-level controls from protocol and application layers. They are relatively complicated to be implemented. Meanwhile, further studies related to the channel characteristics affected by using beams and applying beam alignment schemes in the mmWave communication, such as beamwidth impact [141], are required. There is still a lot of work needs to be done.

2.6 Summary

This chapter has categorized wireless channel models as deterministic channel model, stochastic channel model, and hybrid channel models. It also categorized the standard mmWave channel models as geometry-based stochastic channel models. After that, we have first reviewed the features of some standard channel models and their emphasis in the modelling of mmWave channel properties have been briefed. We have also reviewed the specific characteristics of mmWave channels that are different from conventional 3G/4G channels. Second, we have reviewed the current studies about the directionality of mmWave channels, and the NYU models have been briefed. Then, the current beam alignment schemes developed for mmWave communications have been briefed and the studies of vehicular and mobile mmWave channels have been addressed. In the end of this chapter, the mmWave channel sounders have been introduced and a brief of the mmWave channel measurements have been listed based on [54]. In summary, the studies of mmWave channels were not sufficient enough, there are still quite a few open topics.

Chapter 3

Frequency non-Stationarity and Frequency non-Stationary Channel Modelling

3.1 Introduction

MmWave communication technology is one of the most promising candidates for the 5G wireless networks and even beyond 5G (B5G) [2], [75]. There are about 7 GHz bandwidth resource available in 60 GHz band (unlicensed) and 1 GHz bandwidth resource available in 28 GHz and 38 GHz bands [31]. In current mmWave channel measurements, channel sounding signals with 500 MHz or even broader bandwidths are normally utilised [55], [132], [174]. With such large bandwidths, the propagation properties of mmWave channels can be very different from those of channels in the 4G communication systems.

The stationarity study of wireless channels plays a fundamental role in the analysis of channel measurements and channel modelling. Wide-sense stationary (WSS) channels were introduced in [175], and the stationarity assumptions in the time, frequency, and spatial domains can be found in [77], [176]. In the WINNER II/+ [92], [93], ITU-R [177], and 3GPP [95] channel models, the concept of segments and drops were used to define the “quasi-stationary” periods, during which the channels satisfy the WSS assumption. In QuaDRiGa [71], COST 2100 [94], and recently developed channel

models based on WINNER+, [129], [178], time evolution was used in the study of channel non-stationarities in the time domain, based on the trajectory of a mobile terminal and birth-death processes. Similarly, time evolution was also used in the modelling of high-speed train (HST) and vehicle-to-vehicle (V2V) channels [90], [179]–[182]. In the study of massive multiple-input and multiple-output (MIMO) channels, it was shown that the cluster powers vary over the large antenna array [127], [183]. The spatial stationary assumption does not hold for the whole large antenna array. The modelling of spatial-variation over large antenna arrays was suggested for the COST 2100 channel model based on the modification of visibility region (VR) [184]. A newly developed novel massive MIMO channel model in [185] addressed the spatial non-stationarity along the antenna axis. In [72], [73], [89], birth-death processes were proposed to model both the temporal and spatial non-stationarities of channels in a similar manner. More related research results can be found in [91].

IEEE 802.15.4a ultra-wide band (UWB) channel model can support up to 2 GHz bandwidths [169]. Due to the fact that the wavelengths of sounding signals used in channel measurements are comparable to the sizes of objects in the environment, the fundamental propagation processes such as reflection and diffraction are frequency dependent within UWB channels [186]. Since the frequency stationarity assumption does not hold for the whole bandwidth, UWB channels can be considered as frequency non-stationary (FnS) channels. In [174], the frequency-selective propagation phenomena of mmWave channels were found. In [187], the results of root mean square (RMS) delay spread (DS) and angle spread (AS) were shown to be frequency dependent within 6 GHz bandwidth, i.e., 2–8 GHz. MmWave channels normally have comparable bandwidths to those of UWB channels. In METIS [39], [168], mmWave channel measurements with 4 GHz bandwidth were used. Map-based mmWave channel models addressed the frequency range up to 100 GHz and the bandwidths of mmWave channels up to 10% of the centre frequency can be supported. We can expect that the frequency stationarity assumption does not always hold for mmWave channels within such broad bandwidths. This can happen when utilizing mmWave communications in the environments such as factories, warehouses, mines of coal/metals, chemistry laboratories, etc., where the sizes of objects are comparable to the wavelengths of

mmWave signals. In the ray tracing models of mmMAGIC [29], we can also find that the diffuse scattering at mmWave frequencies was studied based on the similar concern that the sizes of objects are comparable to the wavelengths of mmWave signals. However, in the current standard mmWave channel models, such as IEEE 802.15.3c [83], IEEE 802.11ad [84], MiWEBA [85], mmMAGIC, METIS, and those mmWave channel models developed recently [32], [107], [132], the channel parameters were normally considered as frequency stationary (FS).

In the development of 5G channel models, the general studies of frequency dependent channel parameters can be found in 5GCM [1] and latest 3GPP [95] channel models. We can observe the drift of channel parameters within a few consecutive GHz frequency interval in both the sub-6 GHz and mmWave frequency ranges. In the latest 3GPP, IMT 2020 [102], and 5GCM models, a new component was developed to support the advanced simulation of massive MIMO channels with large bandwidths and large antenna arrays. If the bandwidth is greater than the ratio of speed of light over maximum antenna aperture, the channel coefficient generation step related to modelling clusters is updated to model individual rays. This implies that the WSS assumption may not hold for the channels with large bandwidths and large antenna arrays. However, that criterion is not suitable to determine the FnS properties and it cannot be used to model the FnS channels. Since broad bandwidth resource is the main merit of using mmWave frequencies in 5G communications, the studies about the FnS properties of mmWave channels are required.

In this chapter, we first introduce an APDP method to study the stationarities of channels in the time, frequency, and spatial domains. We apply it in the study of frequency stationarity regions (FSRs) of channels in both the sub-6 GHz and mmWave frequency bands based on real channel measurements. This part of the work is similar to that in [153]. In current work, a further data analysis is carried out showing the FnS properties of measured channels. Then, a general FnS channel model is proposed to model the FnS channels.

3.1.1 Contributions

The contributions of this chapter are summarized as follows.

- The channel measurements in both sub-6 GHz and mmWave frequency bands were performed in a basement environment. The FSRs of channels in three bands are compared and the FnS properties are found. The variation of statistical parameters within the bandwidth of FnS channels is illustrated. The phenomenon of frequency-non-stationarity is shown.
- A novel FnS channel model is proposed to model the channels in both the sub-6 GHz and mmWave frequency bands. In the model, the FnS channel is split into a few FS sub-band channels, modelled one by one, and combined into one FnS channel. Thus, this model also explains the differences between the wideband FS and FnS channels.
- For easy implementation, the modelling of first sub-band channel is similar to that of the 3GPP model. The rest of sub-band channels are modelled based on the cluster evolution in the frequency domain. Due to the inherent nature of stochastic channel models, the consistency issues of simulated channels in temporal and spatial domains were raised in [71] and [188]. Using the frequency domain cluster evolution can avoid the similar issue happening in the frequency domain. It ensures the frequency consistency of simulated sub-band channels.

The remainder of chapter is organized as follows. Section 3.2 introduces an APDP method to estimate the stationarity regions in time, frequency, and spatial domains. The data analysis of frequency stationarity based on real channel measurements is shown in Section 3.3. In Section 3.4, a FnS channel model is proposed to model the FnS properties of the measured channels in both sub-6 GHz and mmWave frequency bands. The details of generating the FnS channel coefficients can be found in Section 3.5. The validation of the proposed FnS channel model is shown in Section 3.6. Finally, conclusions are drawn in Section 3.7.

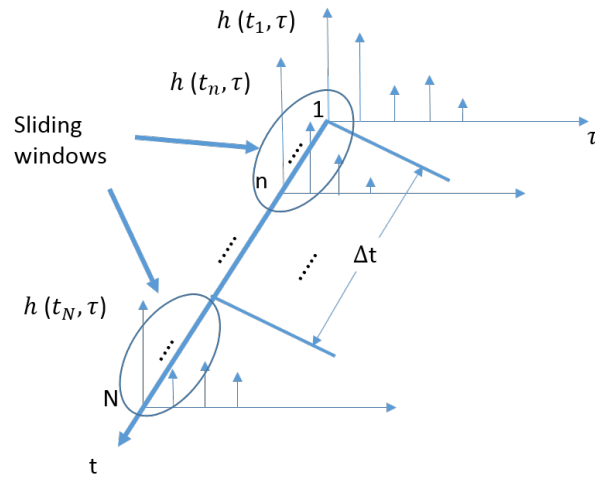


FIGURE 3.1: Sliding windows of APDPs moving along the time axis.

3.2 Stationarity Regions in Time, Frequency, and Spatial Domains

As mentioned in the motivation of this thesis in Section 1.2, in order to improve the mmWave channel models, the stationarity study of mmWave channels is fundamental. In this chapter, we first introduce the method to study the stationarity region of channels. Then, the non-stationary channel model based on the results of stationarity studies will be proposed.

Currently, the APDP method [189] and covariance matrix distance (CMD) method [190]–[192] are generally used to estimate the stationarity regions of channels in the time and spatial domains. Though the CMD method can be used to estimate the stationarity region in the frequency domain, the channel correlation based on antenna arrays is required in the calculation. Compared with that, the APDP method does not have such limit. Therefore, we choose to use APDP method in the thesis. We extend the former APDP method in [189] that was used to study the stationarity regions of the channels in the time and spatial domains to the frequency domain.

3.2.1 APDP Method Applied in Time Domain

For a 1×1 wideband wireless channel, we define $h(t_i, \tau)$ as a channel impulse response (CIR). Then the instantaneous power delay profile (PDP) $P_h(t_i, \tau) = |h(t_i, \tau)|^2$ can be seen as a snapshot of the channel at specific time $t_i, i = 1, 2, \dots, N$, and we assume there are N snapshots in total as Fig. 3.1. We define $\overline{P}_h(t, \tau)$ as

$$\overline{P}_h(t, \tau) = \frac{1}{n} \sum_{i=1}^n |h(t_i, \tau)|^2 \quad (3.1)$$

to present the average PDP of n -snapshots ($n \ll N$) in one sliding window on the time axis t , and define $\overline{P}_h(t + \Delta t, \tau)$ as another APDP of n -snapshots as it moves forward along the time axis t with a distance of Δt . Where t is the average time of t_i . It can be consider as the middle t_i in the sliding window. The correlation coefficient between the APDPs is defined as

$$c(t, \Delta t) = \frac{\int \overline{P}_h(t, \tau) \overline{P}_h(t + \Delta t, \tau) d\tau}{\max\{\int \overline{P}_h(t, \tau)^2 d\tau, \int \overline{P}_h(t + \Delta t, \tau)^2 d\tau\}}. \quad (3.2)$$

If the correlation coefficients $c(t, \Delta t)$ between the APDPs are all higher than the allowance of the similarity level (ASL) [153] tc_{ASL} , then the stationary interval d_t is defined as the stationarity region in the time domain

$$d_t = \max\{\Delta t \mid c(t, \Delta t) \geq tc_{ASL}\}. \quad (3.3)$$

We assume that the n -snapshots used to calculate the APDPs are within a very small interval that is much smaller than the stationary region. Using the larger value of $\int \overline{P}_h(t, \tau)^2 d\tau$ and $\int \overline{P}_h(t + \Delta t, \tau)^2 d\tau$ in the denominator of (3.2) is to assure the correlation coefficient is smaller than 1 when using the real measurement data in the calculation. Because the errors may be introduced in the measurements and those can invalid the equation to calculate the correlation coefficient (may larger than “1”, for example) in the book [193]. Note that Δt can be both positive and negative.

In practise, if an ensemble of CIRs measured at different time points within a time interval satisfy the WSS assumption, we consider them are within one stationarity region [194], and the statistical parameters of channel in such time interval can be estimated. This is not the same as the coherence time interval that those CIRs within can be considered approximately the same [77]. The ASL is the threshold to determine the size of stationarity region. We may consider it as the worst tolerable inaccuracy from the systematic level point of view, where the performance of communication systems is predicted based on the wireless channel models. Since each channel environment is unique, the ASL level need to be carefully chosen for each single wireless channel environment. Therefore, it is difficult to suggest an uniform verdict on the value of ASL at the moment. It can depend on personal judgement in the data analysis of each individual environment.

3.2.2 APDP Method Applied in Spatial Domain

Since the channel sounder samples the channel by impulses at both discrete times and discrete space as long as the Nyquist sampling frequency is satisfied (mentioned in Section 2.4.1), analogously, the definition of stationarity region in the spatial domain can be a logical-shift from time domain. The calculation of stationarity region in the spatial domain is very similar to that in the time domain. The sliding window moves along spatial axis (along the antenna array) instead of time axis, whilst other procedures maintain the same. For a $N \times 1$ wideband wireless channel scenario, we replace t by r and replace Δt by Δr in (3.1) to (3.3).

3.2.3 APDP Method Applied in Frequency Domain

In Fig. 3.2, two cluster-maps are used to represent the two different FSRs of same channel (environment). One is at high frequencies and the other one is at low frequencies. Within each of the FSR, the statistical parameters of channel does not change. However, those are different between two FSRs. If the bandwidth of a channel is broad

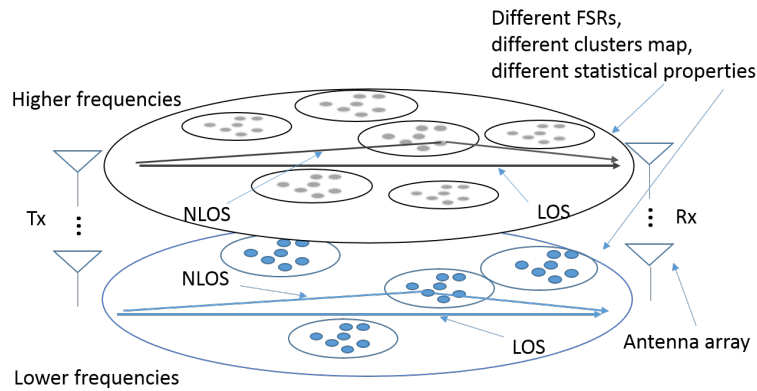


FIGURE 3.2: FSRs of the channel in high frequencies and low frequencies in the same environment.

enough to cover both the FSRs in the high frequencies and low frequencies, then, such channel is considered as a FnS channel. For example, the fundamental propagation processes such as reflection and diffraction are frequency-dependent within the bandwidths of UWB channels, because the wavelengths of sounding signals used in channel measurements are comparable to the sizes of objects in the environment [186]. There are also rich studies of frequency-dependent statistical parameters within the bandwidth of UWB channels (including the frequency range below 6 GHz) [169]. This means that UWB channels have covered more than one FSRs. Similar explanation of such phenomenon can be found in [195].

The proposed APDP method used in estimating the FSRs is an extension of the APDP method [189] used in estimating the stationarity regions in the time and spatial domains.

3.2.3.1 Case 1: Averaging on Snapshots

For a 1×1 wideband wireless channel, we define $H(t_i, f)$ as channel transfer function (Fourier transformation of $h(t_i, \tau)$). Then the instantaneous power transfer function (PTF) of the channel $P_H(t_i, f) = |H(t_i, f)|^2$ can also represent a snapshot of the channel at specific time t_i , $i = 1, 2, \dots, N$. We assume there are N snapshots in total as Fig. 3.3, and the bandwidth of each snapshot consists of M frequency points.

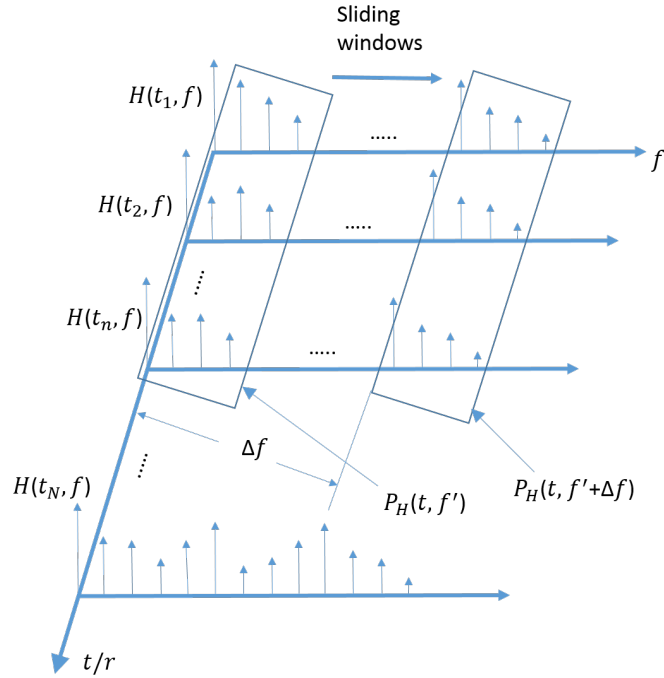


FIGURE 3.3: Sliding-windows of sub-APTFs moving along the frequency axis (we denote $P_H(t, f')$ as the $\overline{P}_H(t, f')$ before averaging).

First, we average the PTF of n -snapshots along time axis t as the average PTF (APTF), which can be expressed as

$$\overline{P}_H(t, f) = \frac{1}{n} \sum_{i=1}^n |H(t_i, f)|^2 \quad (3.4)$$

where t is the average time of t_i . Second, we define m -frequency-points sub-APTF ($m \ll M$) as $\overline{P}_H(t, f')$ in one sliding window on the frequency axis f , and define another m -frequency-points sub-APTF $\overline{P}_H(t, f' + \Delta f)$ as it moves forward along the frequency axis f with a distance of Δf . In order to avoid misunderstanding, we define f' as the frequencies within the sliding-windows. The correlation coefficient between the sub-APTFs is defined as

$$c(f, \Delta f) = \frac{\int \overline{P}_H(t, f') \overline{P}_H(t, f' + \Delta f) df'}{\max\{\int \overline{P}_H(t, f')^2 df', \int \overline{P}_H(t, f' + \Delta f)^2 df'\}}. \quad (3.5)$$

If the correlation coefficients $c(f, \Delta f)$ between the sub-APTFs are all higher than the ASL $f c_{ASL}$, then the stationary bandwidth d_f is defined as the stationarity region in

the frequency domain, i.e. FSR

$$d_f = \max\{\Delta f \mid c(f, \Delta f) \geq f c_{ASL}\}. \quad (3.6)$$

Likewise, we assume that the sub-APTFs are within a bandwidth that is much smaller than the stationary bandwidth.

Note that the n -snapshots selected in the first step should be within one stationarity region in the time domain (may need to estimate the stationarity interval first by the equations mentioned in last section 3.2.1 since all the stationarity conditions need to be met in time, frequency, and spatial domains when studying a channel). For the sub-APTFs in (3.5), we can consider them as imaginary FS-CIRs with much narrower bandwidths after Fourier transforming them to the time domain. However, in Section 3.2.1 and 3.2.2, the complete CIRs should be used since the transmitted signals in reality can be FnS and it is required to estimate the channel properties based on the FnS sounding signals used in the channel measurement.

3.2.3.2 Case 2: Averaging on Antenna Array

For a $N \times 1$ wireless channel scenario, such as using vector network analyser (VNA) to measure a time-invariant channel environment based on virtual antenna array methodology [196], we calculate PTF based on antenna arrays instead. Here we define $P_H(r_i, f) = |H(r_i, f)|^2$ as the PTF, and r_i is the antenna position along “ r -axis” as in Fig. 3.3. Compared with case 1, the APTF should be denoted as

$$\overline{P}_H(r, f) = \frac{1}{n} \sum_{i=1}^n |H(r_i, f)|^2. \quad (3.7)$$

The first step is now changed to average the PTFs based on the CIRs measured by an n -antenna subarray. Then the second step and the following are the same.

Similarly, the n -antenna subarray used to calculate the APTF should be selected within one stationary region in spatial domain (see the reason in the last the Section).

3.3 Channel Measurements and Data Analysis

3.3.1 Channel Measurements and Data Processing

The channel measurements were performed in a big and empty indoor basement environment [197]. The channel sounder consists of a VNA and a large virtual uniform circular array (UCA) with the radius 0.5 m. The channel was measured in a sub-6 GHz frequency band of 2–4 GHz, and two mmWave frequency bands of 14–16 GHz and 28–30 GHz. There are 750 frequency points within each of the frequency bands (frequency interval is 2.67 MHz). The area of the basement was 7.85 m \times 7.71 m as in Fig. 3.4. Two bi-conical antennas with a frequency range from 2–30 GHz were used at both Tx and Rx each. Their radiation patterns are omni-directional on the horizontal plane. One antenna was fixed at about 1 m height at the Tx side. The other one was moved along the trajectory of the virtual UCA at 1 m height at the Rx side. The whole UCA consists of 720 virtual antennas, and the distance between each two adjacent virtual antenna positions was 0.0044 m (less than $\lambda/2$ at 30 GHz). Both line-of-sight (LOS) and non-LOS (NLOS) scenarios were measured, and a metal board was placed between Tx and Rx for the NLOS scenario.

Note that we choose using virtual antenna array over real antenna array for lowering the cost of channel sounder and reducing the correlation among real antennas. It is also a widely used channel measurement method [196] to study the channels in different standard channel models. For example, it is not possible to use 720 real antennas to measure the channel at the same time in reality considering the aforementioned channel measurement. Also note that the interval between each two consecutive antenna elements of an antenna array should be about half wavelength (not much larger or smaller than half wavelength) in order to reduce the side lobes and maintain a narrow radiation pattern. Otherwise, the directivity of beam decreases and unexpected multipath components in ambiguous direction of arrival [169] can receive in the channel measurements.

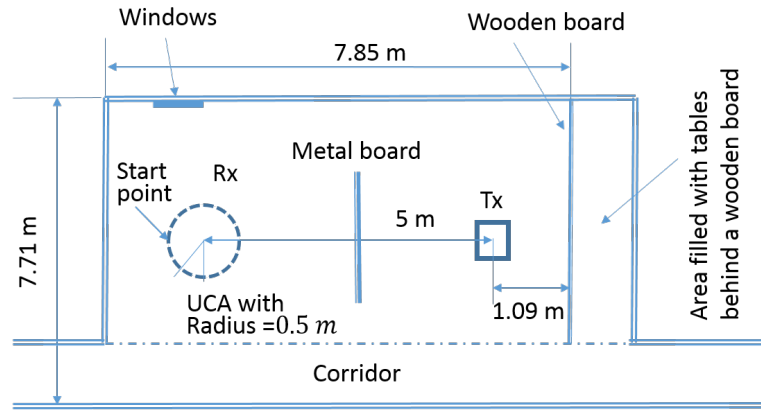


FIGURE 3.4: Floorplan of the channel measurements in the basements.

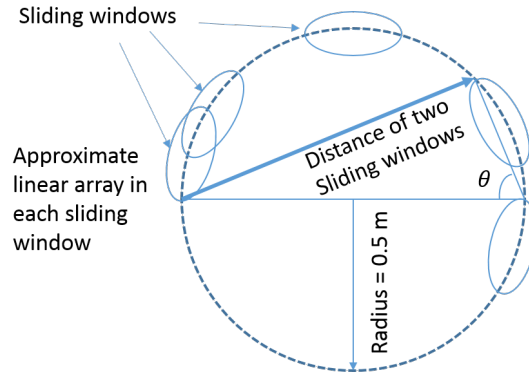
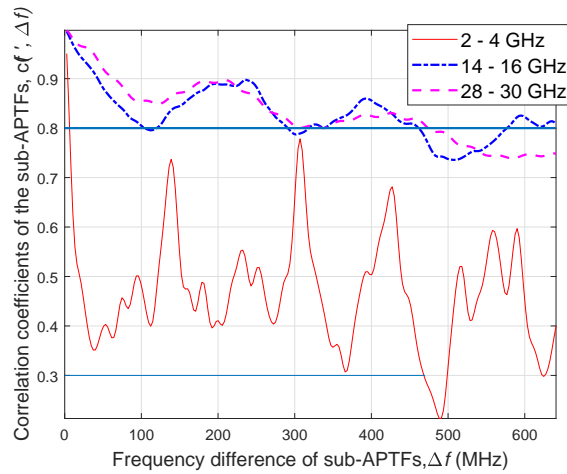


FIGURE 3.5: Approximation of linear antenna subarrays.

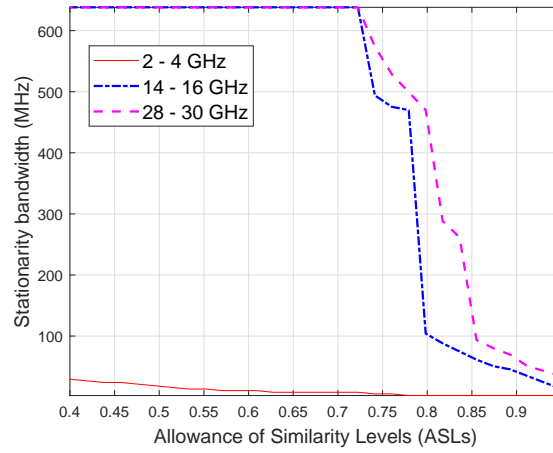
TABLE 3.1: Size of FSRs in a NLOS scenario.

Frequency bands (GHz)	Size of FSRs in MHz for ASL = 0.5	Size of FSRs in MHz for ASL = 0.8
2–4	18.69	2.67
14–16	638.13	104.13
28–30	638.13	285.29

Since the Rayleigh distance [127] of the whole UCA is beyond 200 meters (at 30 GHz), in the data analysis, 16 consecutive virtual antennas are chosen as the virtual linear subarray within each sliding window along half of the virtual UCA as in Fig. 3.5. The size of virtual linear subarray is approximately 0.07 m. The Rayleigh distance of it is considered shorter than the distance between Tx and Rx. To avoid the duplication in the content, more details of data processing can be found in Section 3.3.3 and Section 3.4.



(a)



(b)

FIGURE 3.6: The FSRs of the channels, NLOS scenario: (a) correlation coefficients of the sub-APTFs and (b) stationary bandwidth vs. ASLs.

3.3.2 FSR Analysis

The calculation of frequency correlation coefficients was based on the APDP method applied in the frequency domain: averaging on antenna array as in Section 3.2.3.2. In order to reduce fluctuation in the results, the bandwidths of sub-APTFs in the sliding windows were 5% of the centre frequency in each of the frequency bands for all the results shown below. The results were consistent with those calculated when using a narrower bandwidth. The 5% bandwidth is assumed smaller than the FSRs of channels in all three bands.

In the estimation of the FSRs based on Fig. 3.6a, we read the value from the x -axis

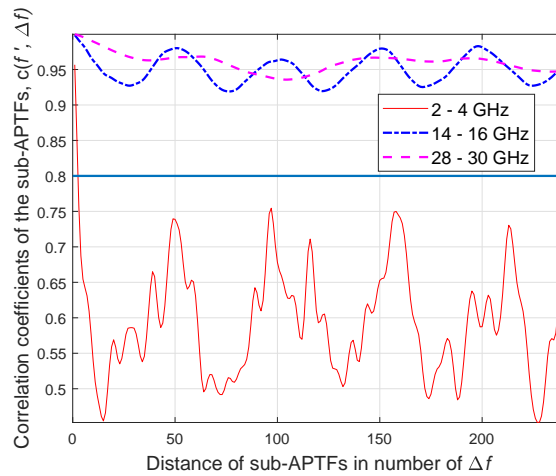


FIGURE 3.7: Correlation coefficients of the sub-APTFs in the LOS scenario.

as the stationary bandwidth (FSR) when the correlation coefficients cross the ASL level for the first time. Given $ASL = 0.8$ as an example, it is clear that the stationary bandwidths in 14–16 GHz and 28–30 GHz bands are larger than those in 2–4 GHz band. In Fig. 3.6b, we illustrate the stationary bandwidths of all three bands for the ASLs from 0.4 to 0.95. It shows that the FSRs in 14–16 GHz and 28–30 GHz bands are much larger than that in 2–4 GHz band. The results shown are based on the averaging of first virtual linear subarray of the virtual UCA (16 virtual antennas out of 720). The FSRs based on other virtual linear subarrays around the whole UCA are also calculated, and the comparable estimation results between the 14–16 GHz band and 28–30 GHz band are found. However, all the estimated FSRs in mmWave frequency bands are much larger than those in sub-6 GHz frequency band for different ASLs. This is an important baseline for the data analysis and modelling in the rest of chapter.

WINNER II channel models support 100 MHz system bandwidth, which is considered within one FSR. The FSR found in the 2–4 GHz band for the $ASL = 0.5$ is 18.69 MHz, which is much smaller, see Table 3.1. One reason could be that the ASL chosen is too high. Another reason could be that the sizes of scatterers in the basement is closer to the wavelengths of the frequencies in 2–4 GHz bands, such as the wall, ceiling, and windows, etc. (if the sizes of the objects in the channel are more comparable to the length of wavelength, the statistics of channel become more various). We can find

that the frequency-dependent scattering and reflection coefficients become smaller as the frequency goes higher in [39], [169]. Therefore, the sounding signals in lower frequencies are more interactive with the objects in this scenario. This also explains that the correlation coefficients are much larger in 14–16 GHz and 28–30 GHz bands than those in 2–4 GHz band in Fig. 3.6a. We can also observe that, for example, the correlation coefficients of sub-APTFs in 2–4 GHz band are all higher than 0.3 for the stationary bandwidth within 467.25 MHz in Fig. 3.6a, i.e., the FSR is 467.25 MHz based on the $ASL=0.3$. Though this bandwidth seems too large, but for this specific scenario, it could be a reasonable size of FSR for 2–4 GHz band.

For the LOS scenario, the correlation coefficients of 14–16 GHz and 28–30 GHz frequency bands are very similar at very high values as in Fig. 3.7. It is difficult to find an ASL to determine which frequency band has larger stationary bandwidth. The reason could be that the attenuation per meter of signals increases dramatically as the frequency goes higher. Therefore, the LOS component becomes more dominant in the measured CIRs at higher frequencies. The ratios of LOS component over NLOS components, i.e., K-factors [77], [176], are estimated based on the APDPs obtained from the first virtual linear subarray (similar results from other virtual linear subarrays). The K-factor in 2–4 GHz band is about 3 dB, it is about 12 dB in 14–16 GHz band and about 15 dB in 28–30 GHz band. It makes sense that the LOS component is more dominant in the measured CIRs in the 14–16 GHz and 28–30 GHz bands and the correlation coefficients estimated from those two bands mainly reflect the LOS component itself.

We notice that the FSRs (stationary bandwidths) are not linearly proportional to the centre frequency in each measured frequency band. We can see that in both Fig. 3.6a and Fig. 3.7, the correlation coefficients of sub-APTFs are very close together for the 14-16 GHz and 28-30 GHz bands. Since the FSRs are determined from the correlation coefficients of sub-APTFs by given ASLs, the FSRs are the same in the 14-16 GHz band and in the 28-30 GHz band based on the results shown in Fig. 3.6b and Table 3.1, especially when the given ASL is smaller than approximately 0.72. The sizes of FSRs in different frequencies are not similar to that of defining the coherence bandwidth

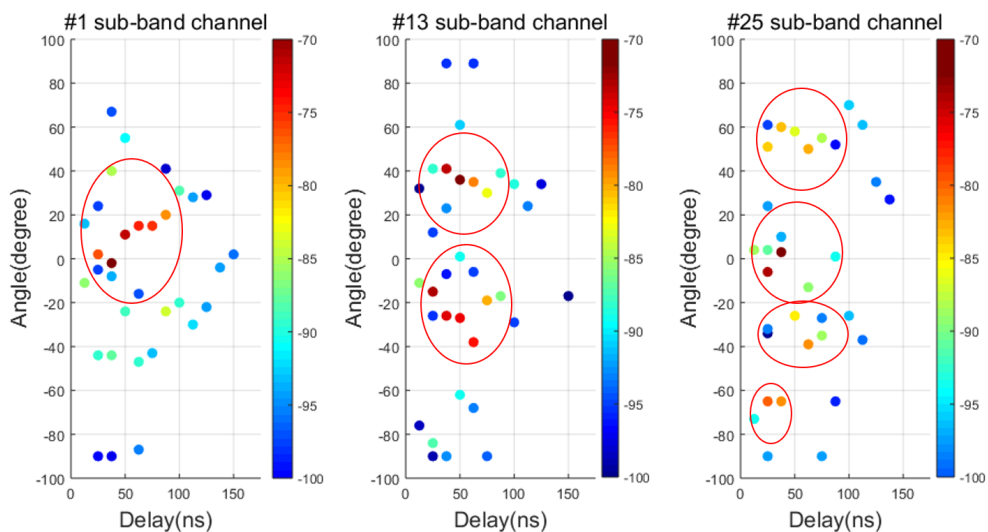


FIGURE 3.8: Estimated MPCs in some of the sub-band channels from 2 to 4 GHz (LOS scenario).

(fractal bandwidth), 10% of the centre frequency (rule of thumb), within which the channel is approximately considered frequency flat [198].

3.3.3 Variation of Statistical Properties of Channels

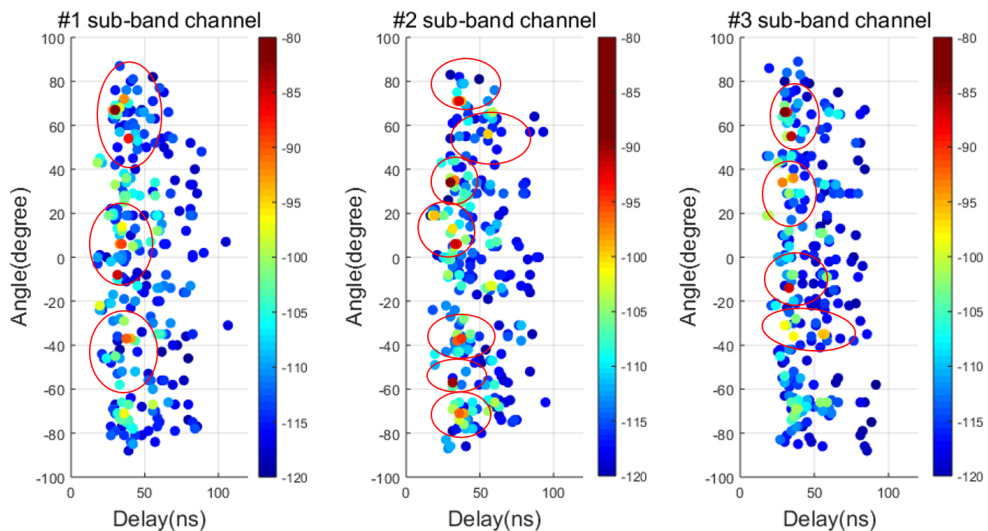


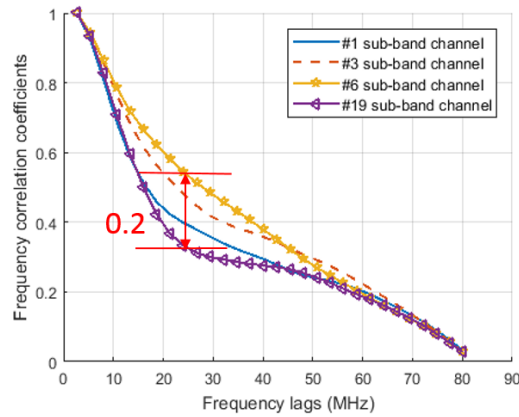
FIGURE 3.9: Estimated MPCs in the sub-band channels from 28 to 30GHz (LOS scenario).

Since the estimated FSRs are smaller than 2 GHz for the channels in those three frequency bands, the WSS assumption is only valid within one FSR, not the whole

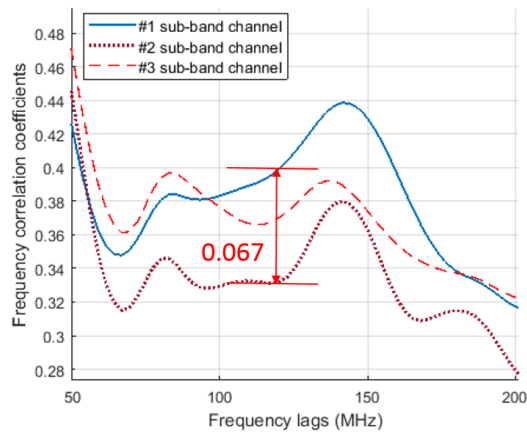
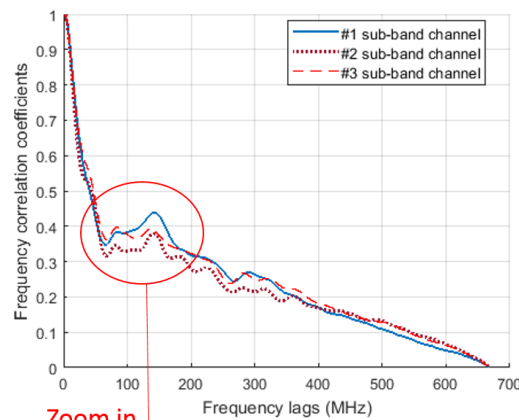
bandwidth of 2 GHz. Therefore, those channels should be considered as FnS. For the convenience, we equally split the bandwidth of 2–4 GHz band into 25 sub-bands, each with 80.1 MHz bandwidth (30 frequency points $\times \Delta f$, $\Delta f = 2.67$ MHz). We also equally split the bandwidth of 28–30 GHz band into 3 sub-bands, each with 667.5 MHz bandwidth (250 frequency points). The (stationary) bandwidths of the sub-band channels chosen are close to those of the standard channel models, such as WINNER II (100 MHz in sub-6 GHz bands) and METIS (500 MHz or larger in mmWave bands).

We choose 30 dB and 40 dB dynamic range of the sub-band CIRs in 2–4 GHz and in 14–16/28–30 GHz frequency bands, respectively. SAGE [199], [200] is used in the estimation of azimuth angle of arrival (AoA), time of arrival (ToA), and amplitude of multi-path components (MPCs) in each sub-band channels based on the first 16-virtual linear subarray. We estimate 35 MPCs from the sub-band channels within 2–4 GHz band, and 250 MPCs from those within 28–30 GHz band (the number of estimated MPCs are comparable to those in [107], [201]). The results are illustrated in Fig. 3.8 and Fig. 3.9. By virtual judgement, we can circle the clusters based on the MPCs with strongest powers in red colour. We can observe clearly different delays and angles of the MPCs with higher powers in Fig. 3.8, and slightly differences of those in Fig. 3.9. The MPCs of sub-band channels based on other 16 virtual linear subarrays are also estimated. Similar phenomenon was found. We do not show them here for conciseness purposes.

Note that it shows a larger gap before the first estimated cluster in Fig. 3.9 than that in Fig. 3.8. However, the excess delay before first arrival MPC in 2–4 GHz band should be comparable to that in 28–30 GHz band. The reason can be that the duration of delay bins in the impulse responses of sub-bands within 2–4 GHz ($1/80.1$ MHz) are much larger than those in the sub-bands within 28–30 GHz ($1/667.5$ MHz), which are determined by the bandwidths of the sub-bands channels mentioned in the beginning of this section. Since the estimated clusters are always located in the middle of delay bin, the estimated excess delay of first MPC in the first large delay bin of an impulse response in 2–4 GHz band looks like much shorter. The delay bin duration of the



(a)



(b)

FIGURE 3.10: The FCFs of the sub-band channels, NLOS scenario: (a) within 2–4 GHz band and (b) within 28–30 GHz band.

impulse responses in 28–30 GHz band is much smaller than that in 2–4 GHz band, the estimated excess delay of first arrival MPC can be more accurately estimated in 28–30 GHz band, and the excess delay of first arrival MPC (half duration of delay bin) looks longer.

3.3.3.1 Statistical Property of Channel in Frequency Domain

Autocorrelation function is normally used to present the statistical property of wireless channel in the time domain [77], [88]. In the frequency domain, frequency correlation function (FCF) can be used to represent the statistical properties of channels. Similarly, the FCF can be defined as

$$R_H(f_1; f_2) = E\{H^*(f_1)H(f_2)\} \quad (3.8)$$

where $H(f)$ is transfer function (Fourier transformation of CIR), and $[\cdot]^*$ and $E\{\cdot\}$ are conjugate operator and expectation operator, respectively.

3.3.3.2 Variation of FCFs of Sub-Band Channels

The FCFs of sub-band channels are shown in Fig. 3.10. The FCFs of selected sub-band channels within the 2–4 GHz band are apparently different in Fig. 3.10a (only shown the most different ones) and the maximum difference is 0.2. The FCFs of sub-band channels within the 28–30 GHz band are slightly different to each other and the maximum difference is 0.067. This is consistent with the MPC estimations in Fig. 3.8 and Fig. 3.9. Note that the results here can be an explanation about the higher values of correlation coefficients in mmWave frequency bands in Fig. 3.6a.

3.4 A FnS Channel model

To the best of our knowledge, the current standard channel models are not suitable to model the measured FnS channels described previously. Though the UWB channel models [186], [202] are FnS channel models, but they do not address the 14–16 GHz and 28–30 GHz frequency bands. However, the methodology of modelling the channel is totally different from 3GPP model. In addition, they are highly complex. Therefore, we propose a general FnS channel model and it can be used to model the channels in both the sub-6 GHz and mmWave frequency bands.

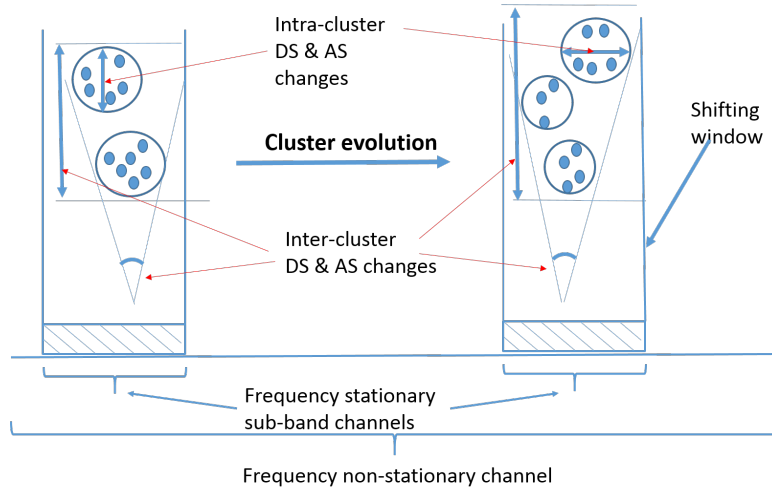


FIGURE 3.11: Cluster evolution in the frequency domain.

3.4.1 FnS Channel Modelling

Given a static FnS wireless channel with the bandwidth covers a few FSRs, we assume that there is a shifting window in the frequency domain with the bandwidth covering only one FSR, and it moves over each FS sub-band channel within such FnS channel. Assume that the whole FnS channel is the sum of all sub-band channels, in case the sub-band channels are non-overlapping to each other, it can be written as

$$\mathbf{h}(\tau) = \sum_{o=1}^O \mathcal{F}^{-1}[\delta(f - f_{co})]h^{\text{sub}}(\tau, f_{co}) \quad (3.9)$$

where there are O sub-band channels, $o = 1, 2, \dots, O$, f_{co} denoting the centre frequency $f_{c1}, f_{c2}, \dots, f_{cO}$ of sub-band channel, and $\mathcal{F}^{-1}[\cdot]$ is the inverse Fourier transformation.

For each sub-band channel, i.e., a wideband channel [77], it can be modelled as

$$\begin{aligned} h^{\text{sub}}(\tau, f_{co}) &= \sum_{l=1}^L \sum_{m=1}^M a_{l,m}(f_{co}) \exp(j\beta_{l,m}) \\ &\times \delta(\tau - \tau_l(f_{co}) - \tau_{l,m}(f_{co})) \\ &\times \delta(\theta - \theta_l(f_{co}) - \theta_{l,m}(f_{co})) \end{aligned} \quad (3.10)$$

where we assume there are L clusters and M rays in each cluster, $l = 1, 2, \dots, L$, $m = 1, 2, \dots, M$. The amplitude of ray is denoted as $a_{l,m}(f_{co})$. The inter-cluster delay

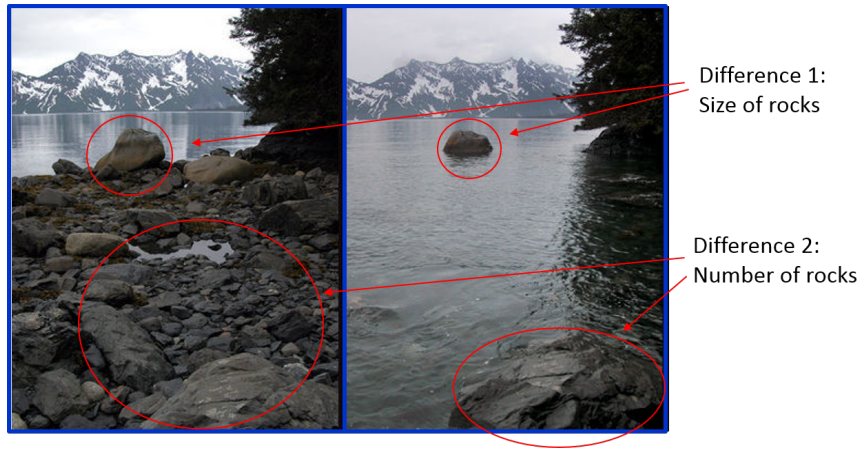


FIGURE 3.12: Tidal variation, as a metaphor to explain the cluster evolution in the frequency domain.

and angle are denoted as $\tau_l(f_{co})$ and $\theta_l(f_{co})$. Due to scattering, reflection, etc. as the rays travel through the channel, $\exp(j\beta_{l,m})$ represents the random phases of rays and $\beta_{l,m}$ is uniformly distributed, $\beta_{l,m} \sim \text{Uni}[-\pi, \pi]$.

Note that we can also let the sub-band channels overlap to each other. This is also suitable for the proposed model. However, the modelling workload will increase in this case. For conciseness purposes, we do not discuss this case.

3.4.2 Cluster Evolution in Frequency Domain

It is not realistic neither efficient to model each sub-band channel according to 3GPP model individually and add them up as one FnS channel based on (3.9). Therefore, a novel frequency domain cluster evolution is proposed for the implementation of FnS model as shown in Fig. 3.11. It describes the relationship among those sub-band channels, and maintains each two consecutive sub-band channels at a reasonable similarity level. This also assures the frequency consistency of sub-band channels, i.e., the similarity level of simulated sub-band channels is as close as possible to that of the sub-band channels found in the measurement data analysis.

Tidal variation can be used as a metaphor to describe the cluster evolution in the frequency domain as Fig. 3.12. We assume that the high tide and low tide situations

represent two estimated cluster-maps of two sub-band channels. There are two categories of differences we can observe from the high tide and low tide situations: the size of rocks and the number of rocks. Those are used to describe the cluster differences in two consecutive sub-band channels in the frequency domain cluster evolution.

The idea is based on that a cluster is a bunch of estimated MPCs, which represent the interaction between the transmitting signals and a bunch of correlated scatterers (objects). They are defined and modelled with reasonable discrepancies based on the frequency and bandwidth of channel. The proposed algorithm of cluster evolution in the frequency domain is similar to the birth-death processes used in [72], [73], [89]. However, we simply use cluster survival rate instead of the cluster birth rate and death rate as follows:

- Track the survival probability of each single cluster by

$$P_{\text{survival}} = \exp(-\lambda O') \quad (3.11)$$

when it evolves from one sub-band channel into another one. The rate parameter is denoted by λ , and O' is the number of sub-band channels one cluster survives.

- Pre-define the number of clusters for all sub-band channels by trend. When the clusters evolve to another sub-band channel, only generate new clusters to substitute the dead or if the number of clusters increases.
- In a new sub-band channel, use the updated inter-cluster parameters by the trends when generating new cluster. Update all the intra-cluster parameters of the clusters by the trends.

Note that it is primary to consider the cluster evolution in the frequency domain for a static channel. For the time-variant channels, which consists of a few or many snapshots, the cluster evolution in the frequency domain can be processed snapshot by snapshot since each snapshot is considered as a static channel.

TABLE 3.2: Parameters of sub-band channels (NLOS scenario, 2–4 GHz).

Parameters	Mean	Maximum
(Inter-cluster) DSs, $\sigma_\tau(f_{co})$ (ns)	15.516	22.263
Standard deviation of ray delays (ns)	46	74.78
Standard deviation of inter-cluster angles, $\sigma_\theta(f_{co})$ ($^\circ$)	49.59	63.5877
Standard deviation of intra-cluster ray angles ($^\circ$)	6.6874	9.6

TABLE 3.3: Parameters of sub-band channels (NLOS scenario, 28–30 GHz).

Parameters	Mean	Maximum
(Inter-cluster) DSs, $\sigma_\tau(f_{co})$ (ns)	7.865	9.395
Standard deviation of ray delays (ns)	12.567	14.827
Standard deviation of inter-cluster angles, $\sigma_\theta(f_{co})$ ($^\circ$)	49.67	51.185
Standard deviation of intra-cluster ray angles ($^\circ$)	8.26	8.817

3.4.3 Statistical Parameters of Measured Sub-Band Channels

3.4.3.1 Parameters Estimation

As described in Section 3.3.3 to split the 2 GHz band into sub-band channels, we estimated the MPCs of each sub-band. For each FnS CIR, it consist of delay/frequency 750 points. We split the 2–4 GHz band (750 frequency points) into 25 sub-band channels (each having 30 frequency points) and split the 28–30 GHz band (750 frequency points) into 3 sub-band channels (each having 250 frequency points). The numbers of clusters estimated by K-mean [203] are different in different sub-band channels due to the FnS property within 2 GHz bandwidth. We then apply visual judgement on the estimated clusters in each sub-band channels. We determine 7 clusters for each sub-band channel within the 2–4 GHz band and 10 clusters for each sub-band channel within the 28–30 GHz band, which are the highest reasonably estimated cluster numbers from those 30 sub-band channels within 2–4 GHz band and 3 sub-band channels within 28–30 GHz band. It enables us to capture the cluster properties of all the sub-band channels in different frequencies. The procedure for the parameter estimations of all the sub-band channels can be described by the pseudo code as below:

- 1: Determine the stationary bandwidth of sub-band channels, and equally split the FnS channel into FS sub-band channels according to the FSR;
 - 2: **while** ($o < \text{number of sub-band channels}$) **do**
 - 3: Estimate the delay, angle and the amplitude of the MPCs in current sub-band channel by SAGE;
 - 4: Cluster the MPCs;
 - 5: Estimate the inter-cluster and intra-cluster parameters;
 - 6: **end while**
 - 7: Find out the statistics of the inter-cluster and intra-cluster parameters of all sub-band channels.
-

The statistics of inter-cluster and intra-cluster parameters of all the sub-band channels are illustrated in Table 3.2 and Table 3.3. Due to that it is similar to estimate the parameters from the 14-16 GHz measurement data and for the compact of content, we do not show the results.

Note that the parameters in the tables were estimated based on one channel measurement campaign. They are unique and considered as a deterministic description of such radio environmental [77] (as well as survival probability [73]). We do not recommend to use those parameters in the prediction of the characteristics of channels in other environments. Much more works are required to determine the channel parameters used in this purpose and we leave it in the future at the moment. In addition, there are specially developed ToA/AoA algorithms that are used in the parameter estimation of UWB channels [169], [204], [205]. We expect that some of the algorithms could be used in the parameter estimations of FnS mmWave channels. However, further studies are required to verify the feasibility of them and we leave it in the future.

3.4.3.2 Trends of Statistical Parameters

The trends of statistical parameters through all the sub-band channels need to be estimated and those are the key factors in the implementation of FnS model. In [187],

the trends of (inter-cluster) AS and DS among sub-band channels, within 6 GHz bandwidth, were described as exponential functions (similar trends are used in the 5GCM and latest 3GPP channel models in the study of the frequency dependent parameters from 1 GHz to 100 GHz). However, due to limited number of sub-band channels available for data analysis in our cases, we can only observe the variation of those statistical parameters among sub-band channels (i.e., along frequency axis). We do not show them for conciseness purposes. However, we gave the mean and maximum value of those statistical parameters in Table 3.2 and Table 3.3. Since it is not sufficient to find the exact trends of them, we use linear trends instead, from the mean to the maximum.

3.5 Generation of FnS Channel Coefficient

3.5.1 Generation of One Sub-Band Channel Coefficient

In this section, a revised 3GPP simulation model is used to describe each of the sub-band channels, and this model is suitable in the implementation of cluster evolution in the frequency domain.

Step 1: Generate random delays based on exponential distribution as

$$\tau'_l(f_{co}) = -r_\tau(f_{co})\sigma_\tau(f_{co})\ln(X_l) \quad (3.12)$$

where $r_\tau(f_{co})$ is the delay distribution proportionality factor, $\sigma_\tau(f_{co})$ is the DS (inter-cluster DS as well), $\ln(\cdot)$ is natural logarithm, and X_l is the random number following uniform distribution, $X_l \sim \text{Uni}(0, 1)$. Normalise delays $\tau'_l(f_{co})$ by subtracting the minimum delay and aligning them in descending order. Then we get the inter-cluster delays $\tau_l(f_{co})$ as

$$\tau_l(f_{co}) = \text{sort}(\tau'_l(f_{co}) - \min(\tau'_l(f_{co}))). \quad (3.13)$$

Step 2: The inter-cluster powers are generated as

$$P'_l(f_{co}) = \exp(-\tau_l(f_{co}) \frac{r_\tau(f_{co}) - 1}{r_\tau(f_{co}) \sigma_\tau(f_{co})}) \quad (3.14)$$

$$P_l(f_{co}) = \frac{P'_l(f_{co})}{\sum_{l=1}^L P'_l(f_{co})} \quad (3.15)$$

where $P'_l(f_{co})$ is the random power follows exponential delay distribution, $P_l(f_{co})$ is the normalised inter-cluster power, which is the square of $a_{l,m}(f_{co})$ in (3.10). Note that there is no shadowing in the model, since we focus on the small-scale parameters.

Step 3: Inter-cluster angles are generated as

$$\theta_l(f_{co}) = \theta_l^{\text{mean}}(f_{co}) + \sigma_\theta(f_{co}) Z_l \quad (3.16)$$

where the mean angle of cluster and standard deviation of inter-cluster angles are denoted by $\theta_l^{\text{mean}}(f_{co})$ and $\sigma_\theta(f_{co})$. The random number Z_l follows standard normal distribution, $Z_l \sim \text{N}(0, 1)$.

Step 4: In order to make the cluster evolution possible in the frequency domain, we modify the description of rays in the 3GPP model. We introduce certain variables in the modelling of rays and we let the ray powers also follow exponential distributions as cluster powers. In the generations of intra-cluster parameters, such as delay of ray $\tau_{l,m}(f_{co})$, amplitude of ray $a_{l,m}(f_{co})$, and angle of ray $\theta_{l,m}(f_{co})$, we simply use intra-cluster parameters (for example in Table 3.2 and Table 3.3) to substitute the corresponding inter-cluster parameters in (3.12)–(3.16), except that we use standard deviation of ray delays to substitute $\sigma_\tau(f_{co})$ in (3.12). The sum of rays powers within one cluster should be equal to the power of such cluster, i.e., $P_l(f_{co}) = \sum_{m=1}^M P_{l,m}(f_{co})$, $P_{l,m}(f_{co})$ is the ray power.

Step 5: Scale the intra-cluster parameters based on inter-cluster parameters (for example, based on the generated inter-cluster powers in difference delays in *Step 2*) and sum up the ray powers (complex numbers) as the cluster powers. Finally, the sub-band channel coefficient can be generated as described in (3.10).

In the LOS case: Similar to 3GPP and ITU-R models, the sub-band channel coefficient in LOS case is the combination of a single LOS ray and a scale-downed NLOS channel coefficient generated above. Note that this generation method explains the data analysis results in Fig. 3.7.

3.5.2 Cluster Evolution

In the implementation of FnS channel model, we only generated the channel coefficient of first sub-band channel as described above. After that, we apply the frequency domain cluster evolution in the generation of the rest of sub-band channel coefficients according to the description in Section 3.4.3.2. For general purpose of the model, we suggest using trends to describe 5 frequency-dependent parameters in the frequency domain cluster evolution procedure. Those 5 parameters are (inter-cluster) DSs, standard deviation of inter-cluster angles, standard deviation of ray delays, standard deviation of intra-cluster ray angles, and number of clusters in each sub-band channels.

Based on the limited data, we choose to describe four parameters by linear trends in the model from the mean value to the maximum value as in Table 3.2 and Table 3.3. We do not use the linear trend for the number of clusters in the sub-band channels since we do not have enough data to prove the trend. We fix the cluster number for all sub-band channels instead.

3.5.3 Adding Up Sub-Band Channels

Once all the sub-band channel coefficients are generated, we add them up as one FnS channel coefficient. The idea is similar to the working principle of VNA in appendix IV.A.4 of [202]. The relationship of frequency/delay intervals and frequency/delay points, that are used to describe the sub-band channels in the time and frequency domains, can be simply regulated as those in fast Fourier transformation (FFT) [146]. However, the adding-up step is a straightforward combination of sub-band channels

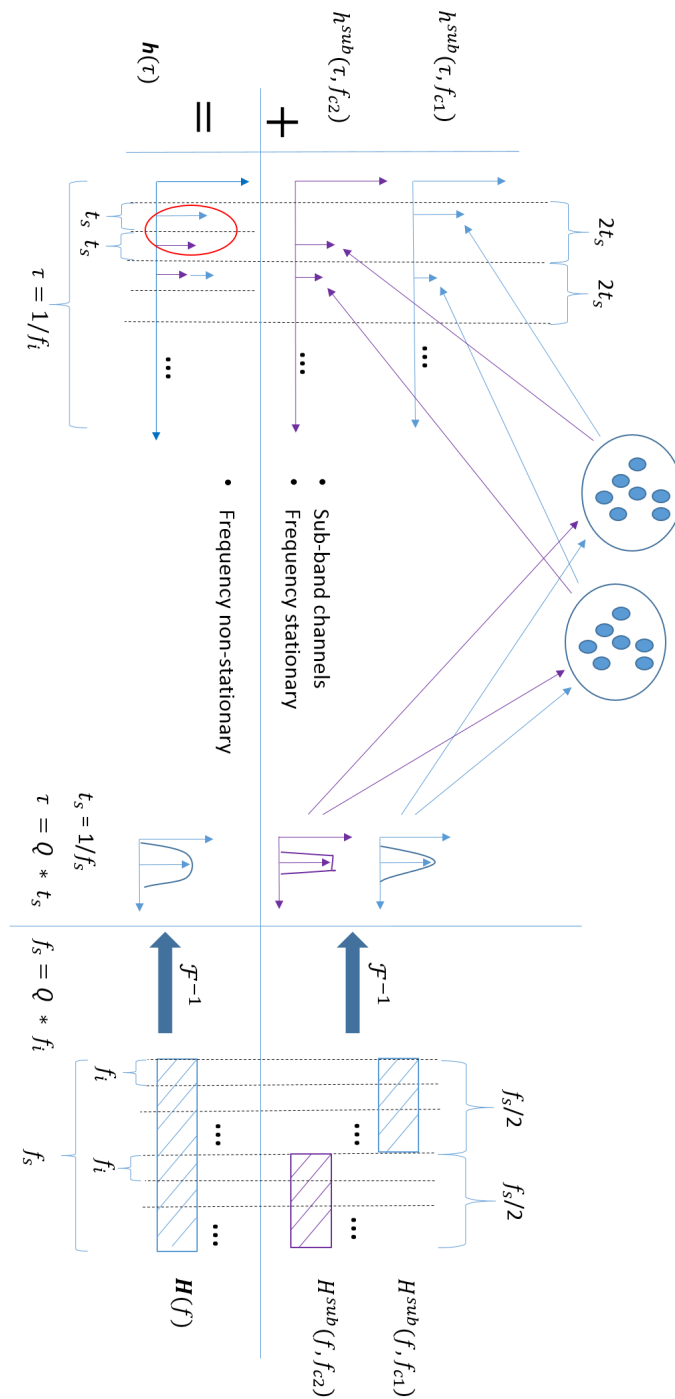


FIGURE 3.13: Example of adding up two sub-band channels as one FnS channel.

either in the frequency domain or in the time domain. Note that there is no Fourier transformation involved.

Fig. 3.13 is an example of adding up two sub-band channels. Similarly, we can add up more sub-band channels in the same manner. In the frequency domain (on the

right hand side of the figure), the bandwidth of FnS sounding signal $\mathbf{H}(f)$ is f_s Hz, and it consists of Q frequency points that with equal frequency interval of f_i Hz. We split $\mathbf{H}(f)$ into two sub-band sounding signals $H^{\text{sub}}(f, f_{c1})$ and $H^{\text{sub}}(f, f_{c2})$ with equal bandwidths of $Q/2$ frequency points while keeping the frequency interval as f_i Hz. Then, we Fourier transform those sub-band sounding signals into the time domain, and transmit them through the same static environment. In the time domain (on the left hand side of the figure), each delay bin of sub-band CIRs $h^{\text{sub}}(\tau, f_{c1})$ and $h^{\text{sub}}(\tau, f_{c2})$ is $2t_s$ ns ($t_s = 1/f_s$), and the lengths of $h^{\text{sub}}(\tau, f_{c1})$ and $h^{\text{sub}}(\tau, f_{c2})$ are both τ ns ($\tau = 1/f_i$). After adding them up, each delay bin of of FnS-CIRs $\mathbf{h}(\tau)$ is t_s ns, and the length of $\mathbf{h}(\tau)$ is still τ ns.

Fig. 3.13 also shows the main difference between the FS and FnS channels in the channel modelling. The power amplitude in each delay bin of FS-CIR relate to one cluster, vice versa. While the powers in a few delay bins of FnS-CIR could relate to the same cluster.

3.5.4 Implementation Details

The procedure of generating the FnS channel coefficient can be described as the pseudo code below:

- 1: Determine the number of sub-band channels, the number of clusters in each sub-band channel, and the number of rays within each cluster;
- 2: Determine the trends of (inter-cluster) DS and AS, and the intra-cluster DS and AS for all the sub-band channels;
- 3: **if** (first sub-band channel) **then**
- 4: Generate the first sub-band channel coefficient according to Section 3.5.1, and save the delay, angle and power of each cluster;
- 5: **else**
- 6: **while** ($o < \text{number of sub-band channels}$) **do**

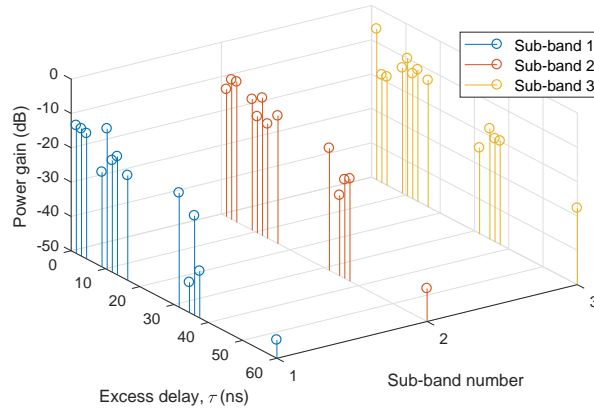


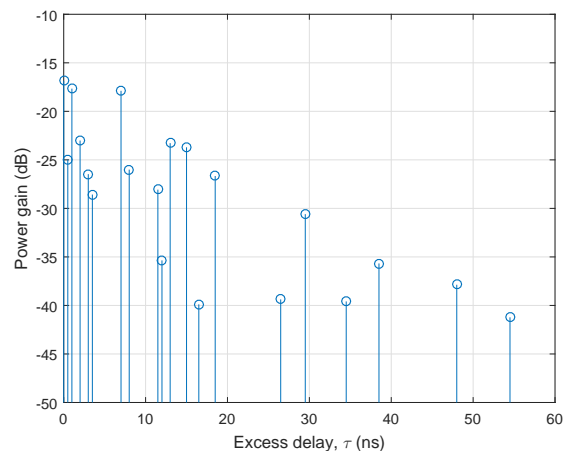
FIGURE 3.14: Frequency consistent simulated sub-band CIRs, 28–30 GHz band.

- 7: Track and calculate the cluster survival probability by (3.11) for each single cluster when it evolves to current sub-band channel;
 - 8: Once one cluster dies or the cluster number increases, generate a new cluster with the (inter-cluster) ASs and DSs following the trends. If the cluster survives, keep the cluster delay, angle, and power in the current sub-band channel;
 - 9: Update all intra-cluster ASs and DSs by trends;
 - 10: Regenerate intra-cluster delays, powers, and angles of each cluster;
 - 11: Generate the current sub-band channel coefficient;
 - 12: **end while**
 - 13: **end if**
 - 14: Adding up all the sub-band channel coefficients as in Section 3.5.3.
-

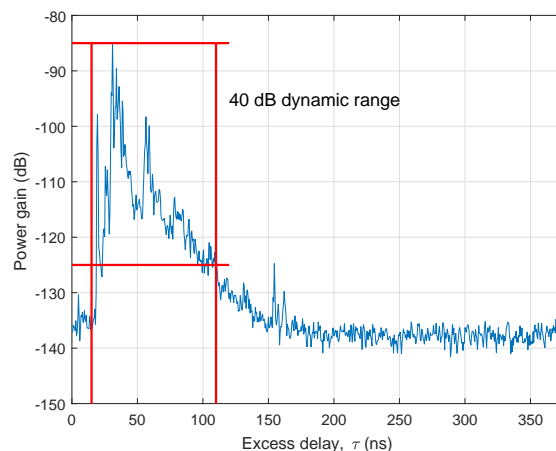
3.6 Validation of FnS Channel Model

3.6.1 Simulation of FnS Channels

In the simulation, the parameters used in the generation of first sub-band channel coefficient are the mean values in Table 3.2 and Table 3.3. In the procedure of cluster evolution in the frequency domain, the linear trends of those parameters are used, from the mean values to the max values. However, we do not use trends for the numbers of



(a)



(b)

FIGURE 3.15: FnS channels, NLOS scenario, 28–30 GHz band: (a) simulated FnS-CIR and (b) measured FnS-CIR.

clusters against sub-band channels in our cases. We fixed the number of clusters to 20 and number of rays within each cluster to 20 for all sub-band channels. Fig. 3.14 shows the sub-band CIRs from one simulation. The cross-correlation coefficients among the sub-band CIRs are between 0.785 and 0.8545. In Fig. 3.15a, one simulated FnS-CIR for the channel in 28–30 GHz band is shown. It represents the measured FnS-CIR within 40 dB dynamic range in Fig. 3.15b. We can observe more obvious clusters in the simulation than those in the data. The absolute gain levels of simulated CIR, in the range of $[-50 \text{ } -10]$ dB, are normalised values. It can be scaled by large-scale parameters, then, it can be close to the gain levels of measured CIR, in the range of $[-150 \text{ } -80]$ dB, in Fig. 3.15b. However, we only focus on the small-scale parameter and

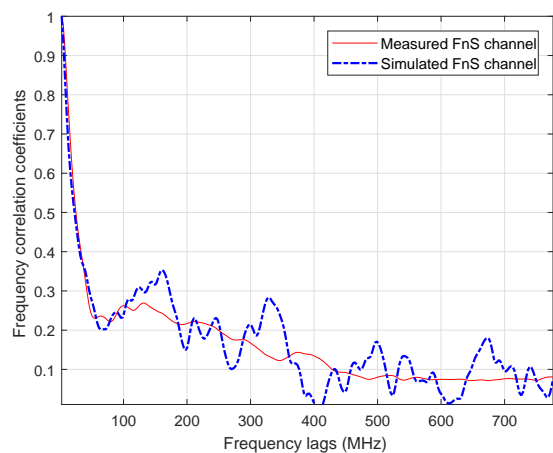
we keep the gain levels of simulated CIR as normalised values.

The measured FnS channels were used as the references in the validation of FnS channel model. We used the FCF of simulated FnS channel to approximate the FCF of measured FnS channel by optimisation. During the frequency domain cluster evolution process, we only changed the cluster survival probability and the initial values of the random numbers, X_l and Z_l in (3.12) and (3.16). We notice that for a good approximation, the cluster survival rates λ in (3.11) found by optimisation algorithm were between 0.05 and 0.1 in the sub-band channels within the 2–4 GHz band, and between 0.025 and 0.05 in those within the 28–30 GHz band. We also found that the clusters can survive 1–15 sub-band channels (25 in total) within the 2–4 GHz band in the cluster evolution. Since there are only 3 sub-band channels within the 28–30 GHz band, the clusters survived for all 1–3 sub-band channels were observed. The results of approximations can be found in Fig. 3.16. We can see that the simulations could follow the measured data in all the 2–4 GHz, 14–16 GHz, and 28–30 GHz bands.

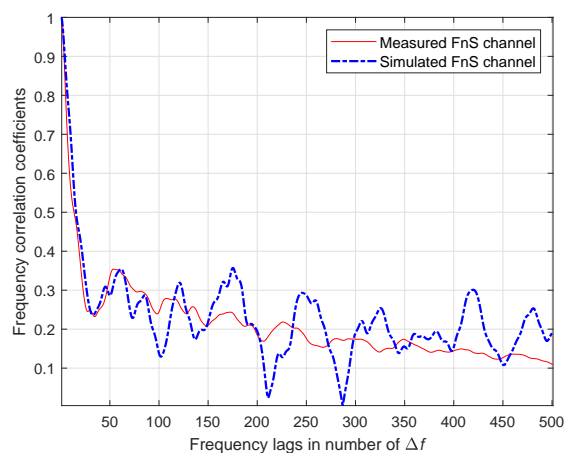
Note that we use 20 clusters in each sub-band channels based on observation during simulations. We found that the simulation results are good enough to approximate the data. If we change the number of clusters to other values, such as 10 (in Section 3.4.3, the estimated cluster number is 10 based on the data), the FCF approximation results are similar. However, the FCFs of simulated FnS channels are generally fluctuating with larger deviation surrounding the FCFs of measured FnS channels in 28–30 GHz band as shown in Fig. 3.17.

3.6.2 Fading of Simulated FnS channels

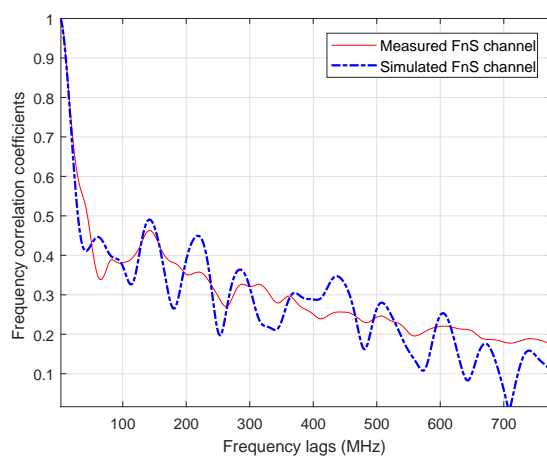
In the literature, the UWB channel models address the FnS channels [202]. The Nakagami- m distribution [206], [207] was used to describe the signal amplitudes of UWB channels and the estimated m -values were close to 1. Since the proposed FnS channel model can be used to model UWB channels, we expect that the signal amplitudes of simulated FnS channels also follow Nakagami- m distributions. However,



(a)



(b)



(c)

FIGURE 3.16: FCF approximations, NLOS scenario: (a) 2–4 GHz band, (b) 14–16 GHz band, and (c) 28–30 GHz band.

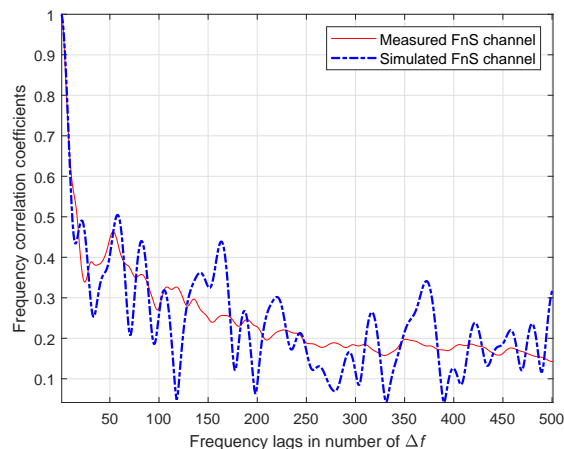


FIGURE 3.17: FCF approximations with 10 clusters in each simulated sub-band channel, NLOS scenario, 28–30 GHz band.

we do not use m values to affect the performance of the propose FnS model. The m values are estimated based on massive generated FnS CIRs, which is similar to estimating the statistical parameters based on the real channel measurement data.

We run FnS channel model 50,000 times working in the 28–30 GHz band for NLOS case. In order to increase the chance that the cluster powers of sub-band FS-CIRs can fall into the same delay bin of FnS-CIR when adding up the sub-band channels, we increase the number of clusters in the sub-band channels to 60 (20 clusters was used formerly).

3.7 Summary

A more general APDP method has been introduced to determine the stationarity regions of channels in the time, frequency, and spatial domains. It is an extension of the former APDP method used to study the stationarities of channels in time and spatial domains. We have applied this method to an empty basement channel measurements in a sub-6 GHz frequency band 2–4 GHz and two mmWave frequency bands 14–16 GHz and 28–30 GHz. We have found that the FSRs of channels in the mmWave frequency bands are larger than those in the sub-6 GHz frequency band.

We have also addressed the FnS properties of channels in all the measured frequency bands.

To the best of our knowledge, the current standard channel models are not suitable for modelling the measured FnS channels in our case. Therefore, we have proposed a novel FnS channel model that is suitable to model the channels in both the sub-6 GHz and mmWave frequency bands. In this model, the FnS channel is split into a few FS sub-band channels, modelled one by one, and combined as one FnS channel again. The cluster evolution in the frequency domain is the key to implement this model (if there are many sub-band channels) and it also ensures the frequency consistency of simulated sub-band channels. In the verification of FnS channel model, the FCFs of the simulated FnS channels and measured FnS channels have been compared. It has shown that the simulations can successfully approximate the data in both the 2–4 GHz and 28–30 GHz frequency bands.

Chapter 4

Planar Angular Stationarity and Directional MmWave Channel Modelling

4.1 Introduction

In previous chapter, the studies related to the very broad bandwidth features of mmWave channels have been described. Those works reveal the FnS properties of mmWave channels and a FnS channel model has been developed for modelling the FnS channels. In this chapter and followings, the study focus of mmWave channels changes to the directional propagation feature of mmWave channels.

The beamforming technology is a key technology to enable mmWave communications for the 5G wireless networks and even B5G [2], [55], [75], [89], [127]–[129], [180]–[182]. It is used at both the Tx and Rx sides and the physical alignment of Tx and Rx beams is required in the communication. In this case, a transmitted mmWave signal only experiences a part of the whole (channel) environment. Due to the inhomogeneous wireless channel environment in different directions, the objects contributing to the channel characteristics of DCs can be very different and the statistical properties of those DCs can be different as well. For example, in mmWave channel measurements [32], [127], [161], the measured D-CIRs (use rotating horn antenna) were diverse in different directions, so were the estimated stochastic parameters of them.

In the study of massive multiple-input and multiple-output (MIMO) channels, if the aperture of antenna arrays is larger than the spatial stationary distance, the wide sense stationary (WSS) assumption in space, i.e., homogeneous channel (HO) over several tens of the coherence distance [176], [208], does not hold [127], [183]. This phenomenon has been well studied in the standard channel models [1], [39], [95] and other literature [2], [72], [73], [184], [197]. In the studies of mmWave channels, considering the difference of the stochastic properties of DCs caused by the inhomogeneity of environment, the WSS assumption also does not hold over the space occupied by a few DCs. The questions are raised on how to define the stationarity upon DCs and how to estimate it. However, the topics related to those questions are rarely seen in the literature.

In the standard mmWave channel models, such as METIS [39], 3GPP [95], 5GCM [1], and mmMAGIC [29], the modelling of whole mmWave channel environments were firstly developed. Then, by multiplying the directional antenna patterns or by applying the beamforming technology to the antenna arrays at both the Tx and Rx, the directional mmWave channels were obtained. In the above-mentioned approach of modelling directional mmWave channels, the characteristics of whole omni-directional channel were modelled without an in-depth analysis of the inhomogeneity of environment. The statistical property of the whole channel in different directions are all the same. The models based on such an approach cannot properly represent the properties of directional mmWave channels in different angles. In the state-of-the-art studies of mmWave channels, the directionality is one of the research topics. In [132]–[135], the temporal and spatial (angular) statistical descriptions of mmWave channels were separated in the channel models. In mmMAGIC [29] and [130], [131], the directional path loss channel models were studied. In [209], [210], beam domain channel models were used to study the multicarrier multiuser MIMO (MU-MIMO) systems and mmWave massive MIMO systems. However, the stationarity study of directional mmWave channels, as a fundamental study of directionality, can be hardly found in the literature and the property studies of directional mmWave channels are still not sufficient.

The consistency is very important in the development of stochastic channel models. In the time domain, if the channel environment does not change significantly as time goes by, the CIRs measured at one fixed position in such an environment are correlated. The time evolution was thus suggested to ensure the consistency of simulated channels in WINNER II/+ [92], [93] and QuaDRiGa [71] implemented it based on the trajectories of mobile terminals. Spatial consistency was considered in the development of standard 5G channel models. Since 5G communication system consists of various types of links (channels) that co-exist in the same area, it requires that the channel evolves smoothly without discontinuities between different link types and in the situation when the Tx and Rx move or turn [211]. The components related to spatial consistency were included in METIS, latest 3GPP, 5GCM, and other standard 5G channel models. METIS [39] suggested modelling the consistent large-/small-scale parameters, such as power, angular properties, polarization state, etc., based on geometric locations of the first and last bounce scatterers of each path (Tx-to-scatterer and scatterer-to-Rx), birth-death process, and visibility regions of clusters. In the frequency domain, the inter-frequency correlation of large-scale parameters (LSPs) was included in IMT 2020 [102]. The consistency and correlation between the Low frequency (LF) and high frequency (HF) channels were investigated by a ray tracing model and the consistency among the channels of multiple frequency bands was studied in the 5G heterogeneous network [212]. Similarly, the consistency needs to be considered in the modelling of adjacent directional mmWave channels.

In this chapter, we first introduce an A-APDP method to study the angular stationarity regions (ASRs) of channels. We estimate the ASRs and other statistical parameters based on the measured D-CIRs in 60 GHz band from an office environment and three typical D-CIRs are found in the data analysis. This part of the work is similar to our former study in [70]. Then, we define the DCs based on the beamwidth of Tx/Rx beams and we use three classes to classify the DCs according to those three typical D-CIRs. We propose to model the DCs by a modified Saleh-Valenzuela (SV) model [118] and the cluster evolution in the azimuth domain is used to generate the consistent channel coefficients of DCs.

4.1.1 Contributions

The contributions of this chapter are as follows.

- An A-APDP method is introduced to estimate the ASRs of channels in the angular domain (azimuth angles). It is an extension of the stationarity studies of channels in the time, frequency, and spatial domains in [153].
- Three typical D-CIRs are found based on the estimated ASRs, root mean square (RMS) delay spreads (DSs), K-factors, and peak power gains (PPGs) in the data analysis of mmWave channel measurements in an office environment. The results reveal the inhomogeneity of mmWave channels in different angles.
- We define the directional mmWave channels based on the beamwidth of Tx/Rx beam used in the mmWave channel measurements. We split the small-scale mmWave channel around Tx into a few DCs according to the measured D-CIRs and utilise three classes, namely, the light-of-sight (LOS), Non-LOS (NLOS), and outage classes, to classify those DCs.
- A modified SV model is proposed to model the DCs in both LOS and NLOS classes. The model does not include the angular information of clusters and it is much less complex compared with the former developed mmWave channel models.
- Cluster evolution in the angular domain is introduced to generate the channel coefficients of all DCs in the LOS and NLOS classes along with 360° azimuth angles. It ensures the consistency of DCs. After that, the omni-directional CIR (omni-CIR) of the whole channel can be synthesized.

The rest of this chapter is organized as follows. In Section 4.2, an A-APDP method is introduced to estimate the ASRs of channels. Then, we apply it in the data analysis of time-invariant mmWave channel measurements in an office environment and three typical D-CIRs are found. In Section 4.3, the DCs are defined and three classes are utilised to classify those DCs. A modified SV model is proposed to model the DCs

in both LOS and NLOS classes and the cluster evolution along the azimuth angles is introduced to ensure the consistency of simulated DCs. In Section 4.4, the channel coefficient generation procedure of DCs are explained. The simulation and validation of the proposed SV model can be found in Section 4.5. Finally, conclusions are drawn in Section 4.6.

4.2 Channel Measurements and Data Analysis

4.2.1 Angular Stationarity

The APDP method in the last chapter (as well as in [153]) was used as a metric to determine the stationarity regions of channels in the time, frequency, and spatial domains. It extended the former studies of stationarity regions of channels from the time and spatial domains [189] to the frequency domain. Since the horn antenna or beamforming technologies are widely used in the mmWave communications, the directional mmWave channels between Tx and Rx only reflect a part of the whole environment [32], [39], [213] and the properties of them in different directions/angles can be dramatically different due to the inhomogeneity of environment. The stationarity study of directional mmWave channels is fundamental. In order to study the inhomogeneity of environment and the relationship among directional mmWave channels, the APDP method can be further extended to study the stationarity regions of channels in the angular domain. In this chapter, an A-APDP method is introduced.

For a beam aligned directional wireless channel between the Tx and Rx, we define $h^D(\phi_i, \tau)$ as a D-CIR measured by Rx at azimuth angle $\phi_i, i = 1, 2 \dots n$, τ is the excess delay. Then, the directional power delay profile (D-PDP) is defined as $P_h^D(\phi_i, \tau) = |h^D(\phi_i, \tau)|^2$ correspondingly. Assume that there are N D-CIRs in total as in Fig. 4.1, we define $\overline{P_h^D}(\phi, \tau)$ as

$$\overline{P_h^D}(\phi, \tau) = \frac{1}{n} \sum_{i=1}^n |h^D(\phi_i, \tau)|^2 \quad (4.1)$$

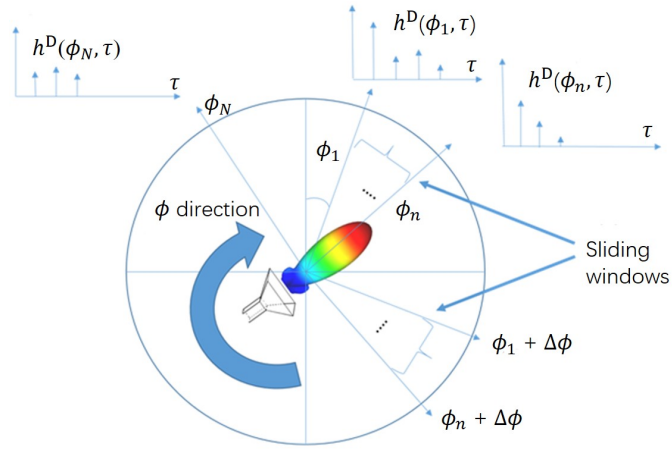


FIGURE 4.1: A-APDP method.

to present the APDP of n D-CIRs ($n \ll N$) in one sliding window on azimuth axis ϕ , and we define another APDP $\overline{P}_h^D(\phi + \Delta\phi, \tau)$ of n D-CIRs in the sliding window as it moves along the azimuth axis ϕ with a distance of $\Delta\phi$. The angular correlation coefficient between the two APDPs is defined as

$$c(\phi, \Delta\phi) = \frac{\int \overline{P}_h^D(\phi, \tau) \overline{P}_h^D(\phi + \Delta\phi, \tau) d\tau}{\max\{\int \overline{P}_h^D(\phi, \tau)^2 d\tau, \int \overline{P}_h^D(\phi + \Delta\phi, \tau)^2 d\tau\}} \quad (4.2)$$

and d_ϕ determines the angular stationary interval as the ASRs, if the angular correlation coefficients $c(\phi, \Delta\phi)$ between the APDPs are all higher than the ASL, i.e.,

$$d_\phi = \max\{\Delta\phi \mid c(\phi, \Delta\phi) \geq ac_{ASL}\}. \quad (4.3)$$

The n D-CIRs used to calculate the APDPs are in a very small interval that we assume is much smaller than the angular stationary interval. Using the larger value of $\int \overline{P}_h^D(\phi, \tau)^2 d\tau$ and $\int \overline{P}_h^D(\phi + \Delta\phi, \tau)^2 d\tau$ in the denominator of (4.2) is to assure the correlation coefficient is smaller than 1 when using real measurement data (some inaccuracy may be introduced in the measurement). Note that $\Delta\phi$ can be both positive and negative.

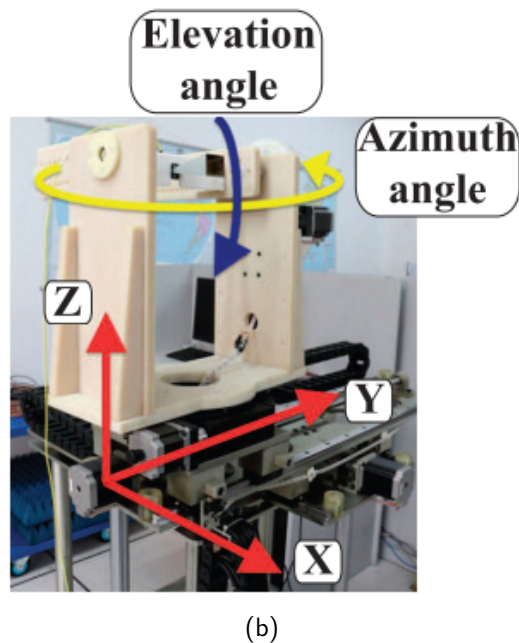
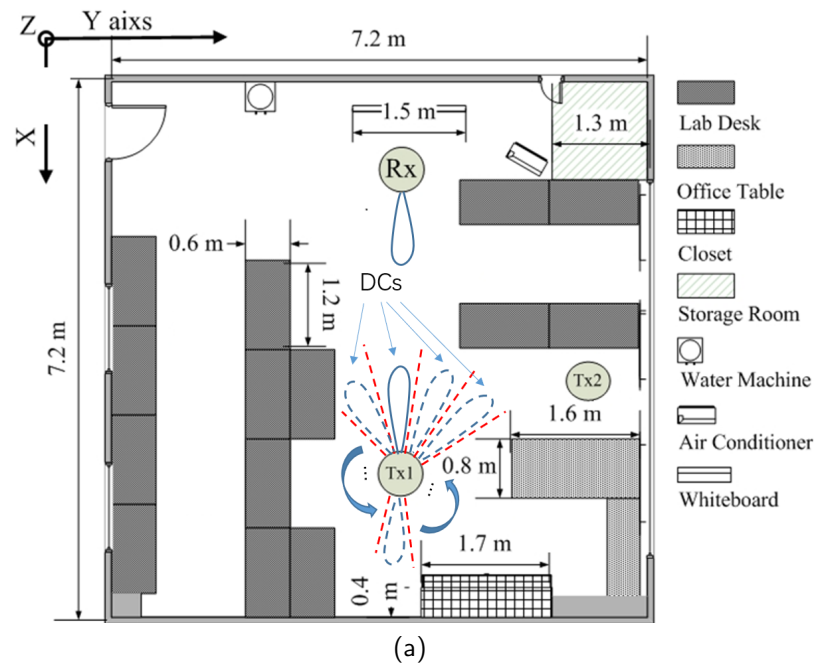


FIGURE 4.2: (a) Layout of an indoor office environment and definition of DCs in the LOS case and (b) sounder testbed.

4.2.2 MmWave Channel Measurements

The mmWave channel measurements were conducted in a time-invariant indoor office in Shandong University, China [70], [161]. Keysight N5227A vector network analyser (VNA) and Keysight E8257D signal generator were used [161] in the measurements.

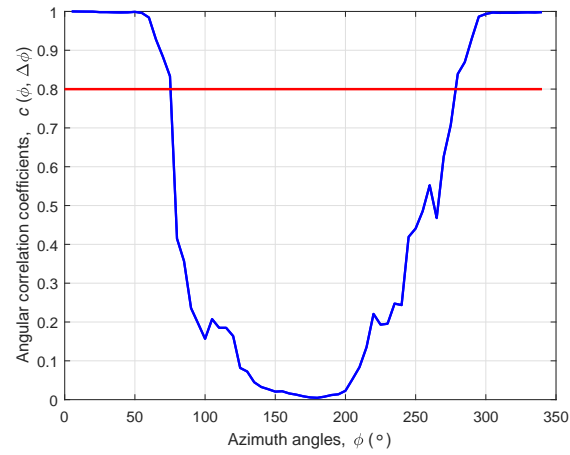
The output power of signal generator was 13 dBm and the intermediate frequency (IF) filter bandwidth of VNA was 1 kHz. The measured frequency range was from 59 to 61 GHz, and there were totally 401 frequency sweep points. The corresponding delay resolution was 0.5 ns. The standard horn antennas with 25 dBi gain and 10° 3-dB beamwidth at 60 GHz were used in both Tx and Rx. The radiation pattern can be found in Appendix B. They were both placed at a height of 1.6 m. The Tx1 and Tx2 positions were chosen for LOS and NLOS cases (measurements) respectively as in Fig. 4.2a. For each Tx position, the directional antenna (RDA)-based method was used in the measurement and the sounder testbed was used as shown in Fig. 4.2b [161]. The Tx antenna rotated from 0° to 355° in azimuth angles, and rotated from 30° to 150° in elevation angles. The rotation step was 5° in both azimuth and elevation angles. While, the Rx horn antenna was held still pointing to the Tx all the time. We also used omni-directional antenna at those two Tx positions with the same setup measuring the omni-directional channels.

Note that, in the data analysis, the measured D-CIRs are the focus. The measured omni-CIRs are only used in the end of Section 4.5 for verification purpose.

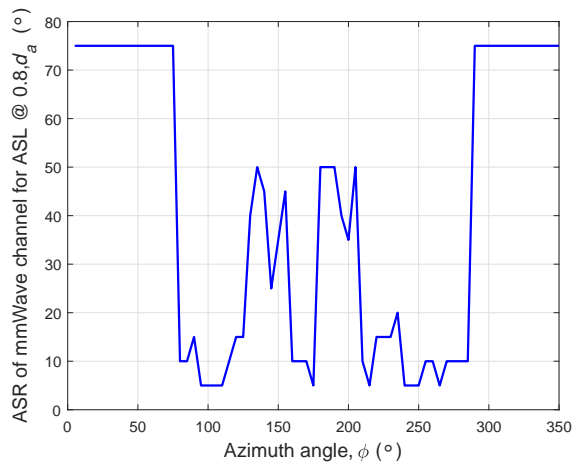
4.2.3 Three Typical D-CIRs in the LOS Case

On the azimuth plane with 90° elevation angle, the angular correlation coefficients between the APDP at azimuth angle $\phi = 0^\circ$ and the APDPs at other azimuth angles are shown in Fig. 4.3a. We assume $ASL = 0.8$, and the estimated ASR of channel at $\phi = 0^\circ$ is about 75° . We have also estimated all the ASRs of channel based on the D-CIRs at different azimuth angles as in Fig. 4.3b. We choose $ASL = 0.8$ as well, and we can observe that the ASRs of such mmWave channel are in the range from 5° to 75° . Due to the D-CIRs measured in different azimuth angles were impacted by the different propagation situations of channel, the estimated ASRs in different directions reflect the inhomogeneity of channel environment.

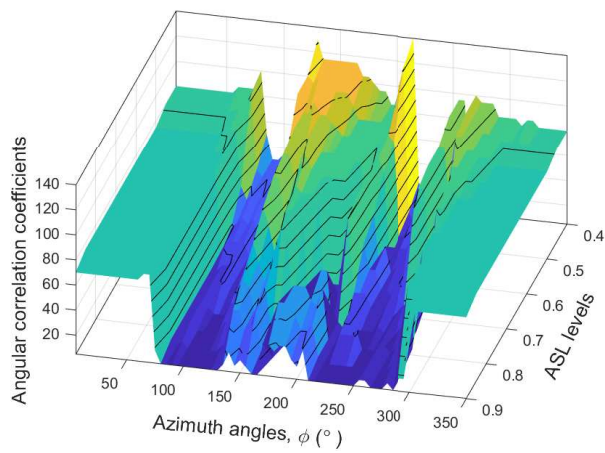
In Fig. 4.3c, we estimate all the ASRs of channel by different ASL levels from 0.4 to 0.9 based on the angular correlations coefficients at different azimuth angles on the



(a)

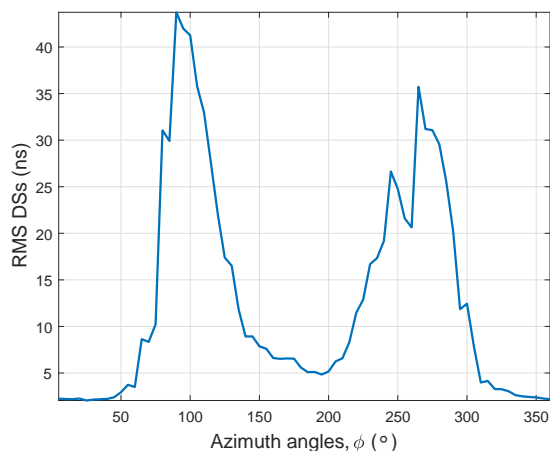


(b)

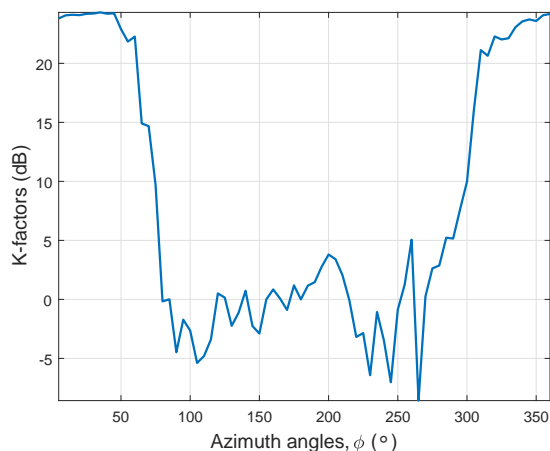


(c)

FIGURE 4.3: (a) Angular correlation coefficients between the APDP at azimuth angle $\phi = 0^\circ$ and the APDPs at other azimuth angles and (b) estimated ASRs on the azimuth plane with 90° elevation angle in the LOS case ($ASL = 0.8$), and (c) estimated ASRs based on (b) with different ASL levels from 0.4 to 0.9.



(a)



(b)

FIGURE 4.4: (a) RMS DSs and (b) K-factors estimated by the measured D-CIRs on the azimuth plane with the 90° elevation angle in the LOS case.

azimuth plane with 90° elevation angle. We can see that the estimated ASRs in the directions with azimuth angles $[0^\circ 85^\circ]$ and $[280^\circ 350^\circ]$ are very large, those in the directions with azimuth angles $[85^\circ 130^\circ]$ and $[220^\circ 280^\circ]$ are very small. furthermore, all of them do not change much. The reason can be that the D-CIRs received in those directions contain strong LOS component (NLOS components can be ignored) or NLOS components with very weak powers (two ultimate cases). The affect of channel environment on the sounding signals which represented by NLOS components can be ignored. The estimated ASRs in the directions with other azimuth angles change a lot as the ASL level becomes smaller. The reason can be that the D-CIRs received in those directions contain the NLOS components with strong powers, the affect of

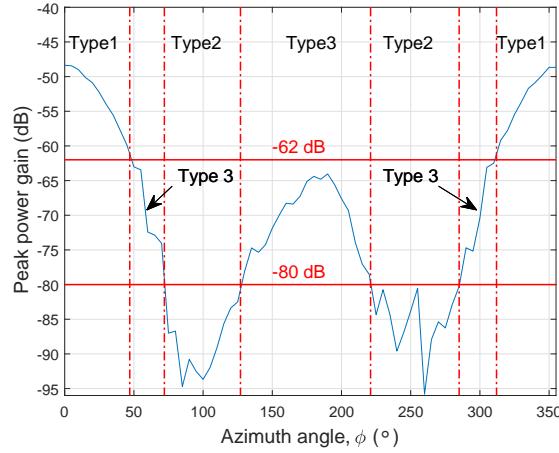
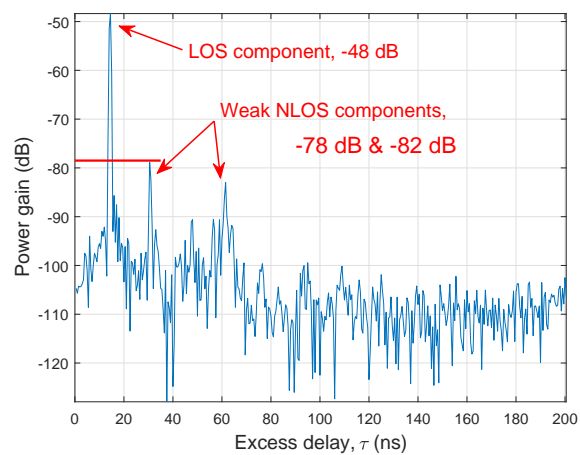


FIGURE 4.5: Three typical D-CIRs on the azimuth plane with 90° elevation angle based on the PPG levels in the LOS case.

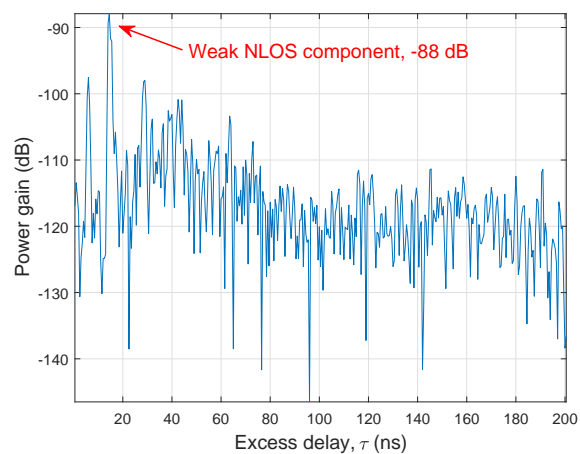
environment is significant. Anyway, the choice of ASL depends on the designed worse tolerance level of radio system as mentioned in Section 3.2.1 and [153], we do not further discuss it. Since the procedure of analysing channel properties is similar, we choose $ASL = 0.8$ in the rest of thesis.

We also estimate the RMS DSs, K-factors [77], and the PPGs based on measured directional mmWave channels/D-CIRs. The results on the azimuth plane with 90° elevation angle in LOS case are shown in Fig. 4.4a, Fig. 4.4b, and Fig. 4.5, respectively. Aligned those results together with the results of estimated ASRs, we can observe that where the ASRs are large, the corresponding RMS DSs are relatively small, but the K-factors and PPGs are high, vice versa. We also notice that in Fig. 4.5, the slopes in type 1, type 2, and type 3 within angle range $[127^\circ, 221^\circ]$ (one large area) change slower than those in type 3 within the angle range $[47^\circ, 72^\circ]$ and $[285^\circ, 312^\circ]$ (two small areas). This is because the measured D-CIRs in those two small areas in type 3 are in the transition from LOS class to Null class or vice versa. The channel environment changes greatly. However, for the slopes in all other areas (other angle ranges), the directional channels only change within one class (LOS class or NLOS class). The environment does not change as much as in the transition areas.

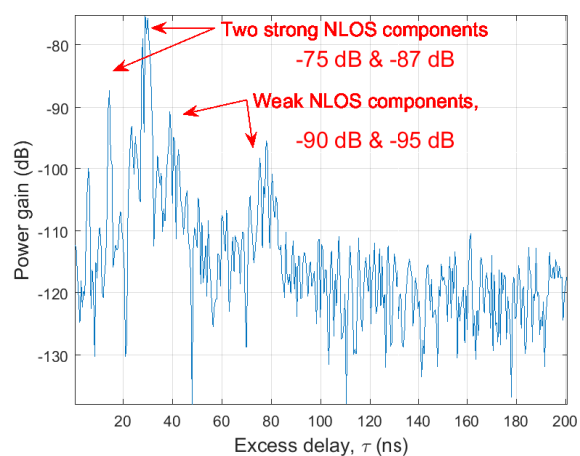
Similar phenomenon can be found in analysing the data on other azimuth planes (elevation angles from 30° to 150°). In order to reduce redundancy, we do not show



(a)



(b)



(c)

FIGURE 4.6: Three typical D-CIRs in the LOS case: (a) D-CIR of Type 1, (b) D-CIR of Type 2, and (c) D-CIR of Type 3.

those results.

Based on the analysis results, three typical D-CIRs were found:

- Type 1 D-CIRs: They all contain a strong LOS component as in Fig. 4.6a. We consider them within one large ASR.
- Type 2 D-CIRs: In the directions where the smallest ASRs are dominant. They normally contain weak NLOS components with very low power gains similar to that in Fig. 4.6b.
- Type 3 D-CIRs: The rest of them in the directions that the mediate ASRs are dominant. The power gains of them are similar to those in Fig. 4.6c. They may contain up to two strong NLOS components and a few weak NLOS components.

For the D-CIRs measured on the azimuth plane with 90° elevation angle in the LOS case, we can choose to use PPG levels to separate the three typical D-CIRs exactly as in Fig. 4.5:

- Type 1 D-CIRs: PPG levels are above -62 dB. The angular coverages are $\phi < 47^\circ$ and $\phi > 312^\circ$. they are all in one big group.
- Type 2 D-CIRs: PPG levels are below -80 dB. The angular coverages are $72^\circ < \phi < 127^\circ$ and $221^\circ < \phi < 285^\circ$. They are separated into two groups.
- Type 3 D-CIRs: PPG levels are smaller than -62 dB and larger than -80 dB. The angular coverages are $127^\circ < \phi < 221^\circ$, $47^\circ < \phi < 72^\circ$, and $285^\circ < \phi < 312^\circ$. They are separated into three groups.

Note that, in the following chapters, we will introduce the channel model and cluster evolution in the angular domain (azimuth angles) based on the properties of directional mmWave channels in the LOS case. For the simplicity of explaining the principles, we further narrow down our focus to directional mmWave channels on the azimuth plane with 90° elevation angle. Also note that the aforementioned measurements

can be used to mimic the indoor base station (i.e., Tx) and user (i.e., Rx) cases. We expect the similar results for the users in random positions in the indoor environment. However, we do not further study it at the moment.

4.2.4 Two Typical D-CIRs in the NLOS Case

We process the data of measured directional mmWave channels in the NLOS case in the similar manner. Two typical D-CIRs are observed, and they are with similar features as those Type 2 and Type 3 D-CIRs in the LOS case (Fig. 4.6b and Fig. 4.6c). We therefore consider these two types of D-CIRs as a subset of those three types of D-CIRs. Due to the similarity in the data processing, we do not show those results.

4.2.5 Study of Spatial Stationarity Based on Directional Mm-Wave Channels

The studies of spatial stationarity are more common that can be found in the literature [77], [176] compared with the studies of angular stationarity [70]. However, based on the current mmWave channel measurements in the literature, using rotating horn antenna or beamforming in plenty of measurements, it is straightforward to consider the angular domain in the data analysis. It is also true that the angular domain mm-Wave channel is a transformation of spatial domain mmWave channel. But design and perform the channel measurements aiming to directly study the channel environment in spatial domain can be much more complicated and time-consuming (for example, how to grid the whole environment and measure each of grids separately?). We leave it in the further at the moment.

The study of angular stationarity based on the directional mmWave channels can be considered as a special case of studying the spatial stationarity. In a Cartesian coordinates system, we can define the stationary distance $D_u(\phi)$, where u along y -axis, (within which the antenna position can be shifted and the statistical properties

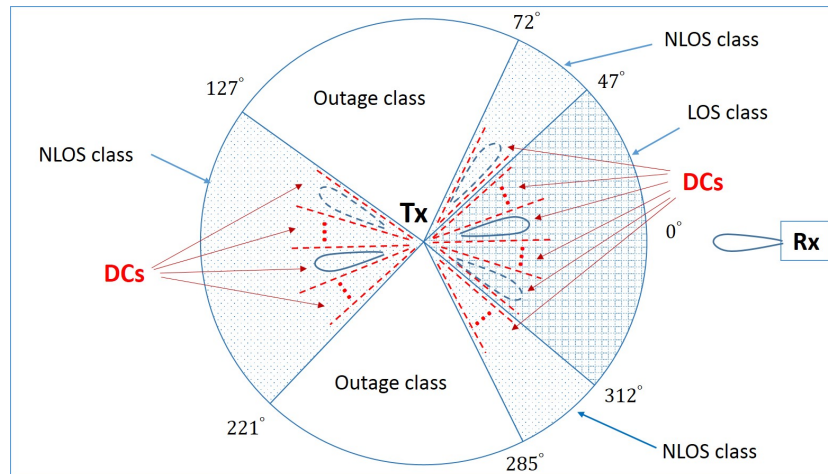


FIGURE 4.7: The DCs in the LOS and NLOS classes in the LOS case.

of measured channels won't change) as a function of the pointing direction of antenna pattern ϕ , which along x -axis, due to the inhomogeneity of channel environment.

In the following content, we will show that the stationary distance at a given radius can be simply calculated by trigonometric functions based on the estimated ASRs. However, since the focus is introducing the directional channel model based on the estimated ASRs, we do not further study the spatial stationarity based on the directional mmWave channels.

4.3 A New Modelling of Directional MmWave Channels

4.3.1 Three Classes of DCs

According to the aforementioned mmWave channel measurement in an office environment, we assume that the small-scale omni-directional wireless channel at Tx, with in a very-short-distance that are comparable with one wavelength [77], can be split into a few DCs based on the beamwidths of Tx beams, $F_i, i = 1, 2, \dots$, as shown in Fig. 4.7.

Generally speaking, there can be infinite number of DCs and modelling them individually become impossible. However, based on the three typical D-CIRs found in data analysis, we classify the DCs by three classes, namely LOS class $h^{\text{D,LOS}}(\tau)$, NLOS class $h^{\text{D,NLOS}}(\tau)$, and outage class Null as

$$h^{\text{D}}(\tau) = \begin{cases} h^{\text{D,LOS}}(\tau), & \text{LOS class} & \longleftarrow \text{based on Type 1 D-CIRs} \\ h^{\text{D,NLOS}}(\tau), & \text{NLOS class} & \longleftarrow \text{based on Type 3 D-CIRs} \\ \text{Null}, & \text{Outage class} & \longleftarrow \text{based on Type 2 D-CIRs.} \end{cases} \quad (4.4)$$

Similarly, for a D-CIR of DC in LOS class, we expect it consists of both LOS component and NLOS components. For a D-CIR of DC in NLOS class, we expect it consists of at least one strong NLOS component to maintain the communication between the Tx and Rx. While, for a D-CIR of DC in outage class, we consider the power of it is “zero”. In this case, we simplify model the DCs in those three classes instead of modelling each of them and we ignore the specific direction/angle information for each single DC in any one of the three classes.

We can classify the DCs in NLOS case by two classes, i.e., NLOS and outage classes. Since the two typical D-CIRs are a subset of those three typical D-CIRs in LOS case, the DCs in NLOS and outage classes are also considered as a subset of those three classes in LOS case. Due to the similarity in definitions, we do not repeat the details.

We choose to separate the D-CIRs by LOS and NLOS classes since the LOS component in the impulse response significantly affect the property of D-CIR (statistical parameters). Similar discussions about the property of channels with and without LOS component can also be found in most of standard channel models. We choose to add Null class for simplification purpose in the modelling of mmWave channels. We use “zero” to model the channels in Null class. Note that, in the rest of chapter, we only focus on the three classes of DCs in LOS case.

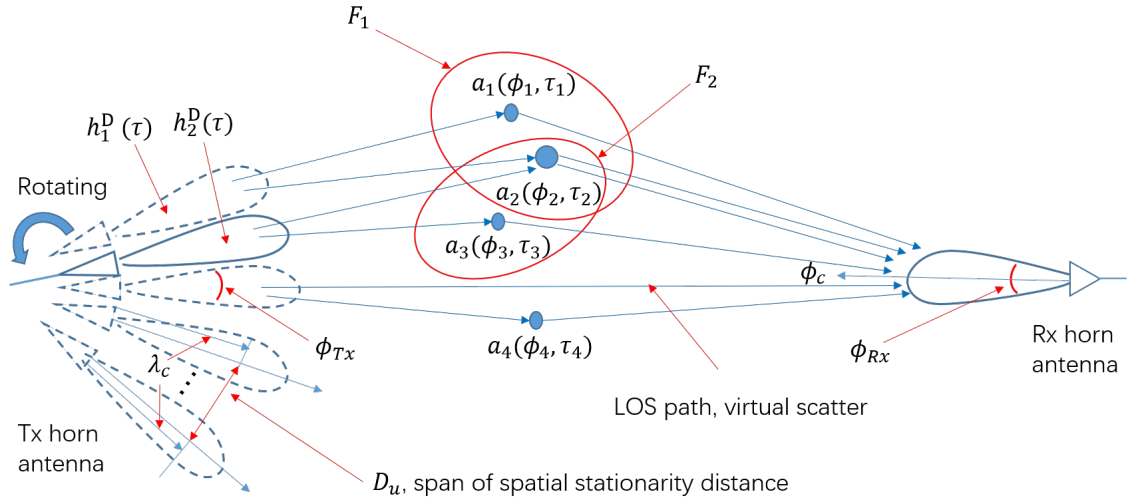


FIGURE 4.8: D-CIR $h^D(\tau)$ can be modelled as the sum of responses from the scatterers at (ϕ_l, τ_l) with amplitudes $a_l(\phi_l, \tau_l)$ in the angle range of a Rx beam.

4.3.2 Inhomogeneity of MmWave Channel Environment

The DCs in the LOS and NLOS classes can be described by Fig. 4.8. The beamwidths of Tx and Rx beams are denoted as ϕ_{Tx} and ϕ_{Rx} , the centre angle of beam is denoted as ϕ_c , and the response from the scatterer at (ϕ_l, τ_l) , $l = 1, 2, \dots$, with certain amplitude is denoted as $a_l(\phi_l, \tau_l)$, i.e., $a_l\delta(\phi - \phi_l)\delta(\tau - \tau_l)$ alternatively.

For the omni-directional CIR $h^{\text{Omni-d}}(\tau)$, it can be considered as the sum of the responses of scatterers in all the directions. Based on the HO channel assumption in [176], [214], it assumes the span of channel stationarity can be extended to several tens of the coherence distance (within which the channel parameters can be considered approximately the same [176]) in space and the responses from scatterers/clusters at different angles/directions are uncorrelated. However, in the study of D-CIR, the upper and lower limit of the sum of the responses of scatterers should be changed from $[-\pi, \pi)$ to $[-\phi_{Rx}/2 + \phi_c, \phi_{Rx}/2 + \phi_c]$ as below

$$h^{\text{Omni-d}}(\tau) = \sum_{-\pi}^{\pi} a_l(\phi_l, \tau_l) \longrightarrow h^D(\tau) = \sum_{-\phi_{Rx}/2 + \phi_c}^{\phi_{Rx}/2 + \phi_c} a_l(\phi_l, \tau_l). \quad (4.5)$$

A D-CIR $h^D(\tau)$ only reflects a part of the omni-directional channel in a certain direction. The D-CIRs in different directions can be very different and a response of

a scatterer can contribute to more than one adjacent D-CIRs. According to the estimated ASRs and three classified DCs previously, the statistical properties of DCs in different ASRs/classes are different due to the inhomogeneity of environment. It is also true that most of the environments are inhomogeneous in reality based on the measurements data available in the literature.

Given the estimated ASRs in Section 4.2.3, the stationary distance $D_u(\phi_i), \phi_i \in [0^\circ, 355^\circ]$ defined previously can be simply calculated by trigonometric functions with a given radius λ_c at the Tx as in Fig. 4.8, which is between $0.014\lambda_c$ and $0.2\lambda_c$. It is obvious that it can not be extended over the space occupied by a few DCs that belong to different ASRs.

4.3.3 Directional MmWave Channel Model

Based on the data, we can find that all the measured D-CIRs consist of a few multipath components (MPCs), i.e., the responses from scatterers. We can also observe that the power of LOS component in the measured D-CIRs spreads within a certain excess delay instead of only one sharp impulse at one excess delay point as shown in Fig. 4.6a with -48 dB power gain. If we considered the LOS signal arriving from one virtual scatterer, which consists of one LOS ray and a few rays with comparable high gains come very closely in time (delay), we can model the LOS component in the same way as other NLOS components.

We propose to model the D-CIRs of DCs in the LOS or in the NLOS class as the sum of l MPCs, $l = 1, 2, \dots, L$, within the angle range of Rx beam as in Fig. 4.8, i.e.,

$$h^D(\tau) = \sum_{l=1}^L a_l(\underbrace{\tau_l}_{\text{Resolved}}, \underbrace{\phi_l}_{\text{Suppressed}}), \quad -\phi_{Rx}/2 + \phi_c \leq \phi_i \leq \phi_{Rx}/2 + \phi_c \quad (4.6)$$

where a_l is the previously defined amplitude of scatterer, i.e., amplitude of cluster. We suppress the angle parameters ϕ_l in (4.6) for ignoring the slightly angle differences of the clusters within one DC and we further resolve the delay parameters based on

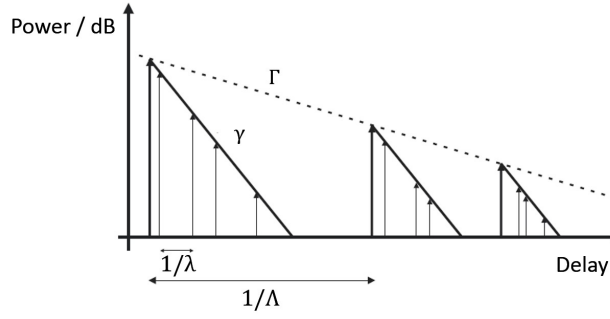


FIGURE 4.9: The modeling parameters of modified SV model.

the SV channel model [118], [119], i.e.,

$$h^D(\tau) = \sum_{l=1}^L \sum_{m=1}^M a_{l,m} \exp(j\beta_{l,m}) \delta(\tau - \tau_l - \tau_{l,m}). \quad (4.7)$$

We define M rays in each cluster, $m = 1, 2, \dots, M$. The inter-cluster delay is denoted as τ_l , and the amplitude and delay of intra-cluster rays are denoted as $a_{l,m}$ and $\tau_{l,m}$. Due to the effects of scattering, reflection, and etc., the random phase of each intra-cluster ray is denoted as $\exp(j\beta_{l,m})$, where $\beta_{l,m}$ is uniformly distributed, $\beta_{l,m} \sim \text{Uni}[-\pi, \pi]$.

Assume that the number of inter-cluster arrivals and the number of intra-cluster ray arrivals follow Poisson distributions for the fixed time intervals. The time lengths between each two consecutive arrivals follow exponential distributions. We define Λ as the inter-cluster arrival rate and λ as the intra-cluster ray arrival rate as those in the figure of SV model in Fig. 4.9 [77]. The inter-cluster arrival τ_l and the intra-cluster ray arrival $\tau_{l,m}$ can be written as

$$\text{pdf}(\tau_l | \tau_{l-1}) = \Lambda \exp[-\Lambda(\tau_l - \tau_{l-1})], l > 0 \quad (4.8)$$

$$\text{pdf}(\tau_{l,m} | \tau_{l,(m-1)}) = \lambda \exp[-\lambda(\tau_{l,m} - \tau_{l,(m-1)})], m > 0 \quad (4.9)$$

where the $\text{pdf}(\cdot)$ means the probability density function (PDF). We define Γ as the inter-cluster power decay rate and γ as the intra-cluster ray power decay rate. The exponential distributed inter-cluster powers and intra-cluster ray powers can be described as

$$a_l^2 \propto \exp\left(-\frac{\tau_l}{\Gamma}\right), \quad a_{l,m}^2 \propto \exp\left(-\frac{\tau_{l,m}}{\gamma}\right). \quad (4.10)$$

Note that this model is based on the D-CIRs without first component (which includes the LOS component), the details can be found in Section 4.3.6. The ray arrivals supposed to follow Rayleigh distribution as that described in SV model [118].

We also define the first cluster power ratio (FCPR) as

$$K_{c1} = 10 \log_{10} \left(\frac{\text{First cluster power}}{\text{Sum of all other cluster powers}} \right). \quad (4.11)$$

For the D-CIRs of DCs contain LOS component, it can be interpreted as the K-factor.

Note that, the exact angle for each generated DC can not be determined due to the stochastic nature of model and it must be within the angular range of LOS or NLOS class based on parameters used, see Fig. 4.7. Anyway, we can assign the angles to the generated DCs following the order of generating them in the cluster evolution. Also note that, the inter-cluster angle parameters were included in the super-resolved directional channel properties described in METIS [39]. However, we do not consider the inter-cluster angles within each DC since they are very close to each other and the model is less complex.

4.3.4 Cluster Evolution in The Angular Domain

In Fig. 4.8, the scatterer at (ϕ_2, τ_2) belongs to both the $F1$ and $F2$ sections of channel (environment) and it contributes to both neighbouring DC $h_1^D(\tau)$ and DC $h_2^D(\tau)$. Assume that $h_1^D(\tau)$ and $h_2^D(\tau)$ only consist of two paths, they can be written by the two-path models [77] as $h_1^D(\tau) = a_1\delta(\tau - \tau_1) + a_2\delta(\tau - \tau_2)$ and $h_2^D(\tau) = a_2\delta(\tau - \tau_2) + a_3\delta(\tau - \tau_3)$. Assume that the responses from every two clusters are uncorrelated, then we can calculate the correlation of $h_1(\tau)$ and $h_2(\tau)$ as

$$\frac{C[h_1^D(\tau), h_2^D(\tau)]}{\sqrt{V[h_1^D(\tau)]V[h_2^D(\tau)]}} = \frac{V[a_2]}{\sqrt{(V[a_1] + V[a_2])(V[a_2] + V[a_3])}} \quad (4.12)$$

where $C[\cdot]$ is covariance operator, and $V[\cdot]$ is variance operator. The variances of MPCs can be considered as the powers of MPCs and it is clear that the correlation of

those two neighbouring DCs is not zero. In the channel measurement, the Tx beam with certain beamwidth ϕ_{Tx} may receive the responses from the same clusters in the channel environment while it rotates from one direction to another neighbouring direction, those corresponding DCs are therefore highly correlated. Likewise, if there is no significant changes of the channel environment in the directions of neighbouring DCs, the DCs are highly correlated.

Based on the directional mmWave channel model described previously, we can generate the D-CIR of one DC first. Then, we propose to use a novel angular domain cluster evolution algorithm to generate the D-CIRs of neighbouring DCs. This algorithm maintains each two neighbouring DCs at a reasonable similarity level and ensures the consistency of the DCs. The algorithm is similar to the birth-death process in the cluster evolution used in [72], [73]. We simply use cluster survival rate instead of the cluster birth and death rates.

According to the modelling of DCs and the description in Fig. 4.8, we assume there are totally O DCs as the Tx rotates through a certain range of azimuth angles. If there is a cluster contributes to two neighbouring DCs, then we say this cluster evolves from one DC to another. Based on such assumption, the proposed algorithm includes following three items:

- Track the survival probability of each single cluster by

$$P_{\text{survival}} = \exp(-\lambda O') \quad (4.13)$$

when it evolves from one DC into another. The rate parameter is denoted by λ , and O' is the number of DCs one cluster survives.

- Pre-define the number of clusters for all DCs. When the clusters evolve to another DC, if the clusters are dead or the number of clusters increases, generate new clusters.

- The FCPRs and cluster decay rate are randomly generated in the procedure of generate each DC. They follow normal and log-normal distributions, respectively.

Note that we introduce the FCPR and cluster decay rate as variables are with the consent of inhomogeneity of mmWave channel environment. Such modification based on conventional SV model also makes the cluster evolution among DCs (in the angular domain) possible. Also note that the expected survival clusters after cluster evolution of O' sub-band channels can be calculated as: Initial cluster number $\times P_{\text{survival}}$, statistically [193]. However, we found that four (clusters) is the most suitable cluster number that used to estimate the statistical parameters from the measured DCs. Therefore, we pre-define cluster number in each DC in the cluster evolution algorithm. Furthermore, the cluster number can be environment-dependent. We suggest to analyse the measured data before determining the cluster number in different scenarios/environments.

4.3.5 No Cluster Drifts in Different DCs

In [215], [216], the drifting of clusters' parameters were observed in the massive MIMO channel measurements. Those were studied in the massive MIMO channel models in [72], [73], [185]. However, in the angular cluster evolution, when the clusters evolve to another DC and survive, there is no cluster drifting in the two consecutive DCs. Because the position of Tx/Rx does not change, only the Tx/Rx beam rotates according to the aforementioned channel measurements. If the rotated beam can receive the response from one cluster, then, this MPC will appear in the D-CIR of corresponding DC, otherwise not. Therefore, there is no delay and amplitude differences in the responses from the same clusters in different DCs. We do not need to consider the drift of cluster parameters in the cluster evolution based on such innate feature.

TABLE 4.1: Estimated Statistical Parameters in LOS Case.

Statistical parameters	Cluster arrival rate, $1/\Lambda$ (ns)	Ray arrival rate, $1/\lambda$ (ns)	Ray power decay rate
LOS class	4.4723 (1/0.2236)	1.0494 (1/0.9529)	-0.4147 (10.4725 ns)
NLOS class	4.1068 (1/0.2435)	0.9363 (1/1.068)	-0.5048 (8.6033 ns)

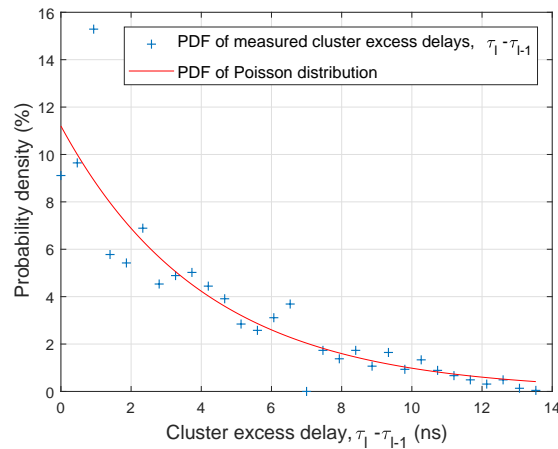
TABLE 4.2: Specific Statistical Parameters in LOS Case.

Parameters	Distribution	Mean, (dB)	μ_Γ/μ_k	Variance, (dB)	σ_Γ/σ_k
FCPR (LOS class)	Normal distributed	24.3459		2.07062	
Cluster decay (LOS class)	Log-normal distributed	10.9419		0.8875	
FCPR (NLOS class)	Normal distributed	-3.97446		7.41799	
Cluster decay (NLOS class)	Log-normal distributed	10.2335		1.1158	

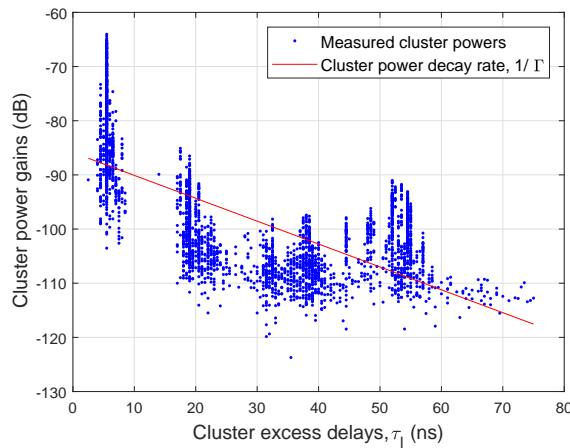
4.3.6 Estimation of Statistical Parameters

In the LOS case, there are overall 72×25 measured D-CIRs, which include 19×25 measured D-CIRs in the LOS class, and 31×25 measured D-CIRs in the NLOS class. The NLOS class contain 29×25 measured D-CIRs. In the data analysis, we use all the measured D-CIRs in each class for achieving accurate results. We use 40 dB dynamic range of them, which is considered large enough to include most of characteristics of the channel. We remove the first cluster (LOS component or first NLOS component) from each D-CIR and save them for the FCPR estimations according to (4.11). Then, we use the peak analysis to process the rest of D-CIRs in the estimation of the inter-/intra-cluster parameters. The 12 ns minimum inter-cluster interval is found suitable to separate the clusters and it enable us to capture the feature of D-CIRs in both the LOS and NLOS classes. We capture four clusters from each D-CIR and we also make sure the duration of each cluster is larger than 12 ns in the data processing.

Based on the data analysis, we can find three groups of DCs in the NLOS class. There are two small groups of DCs in the NLOS class separated by outage class as shown in Fig. 4.5. Though they reflect different parts of the channel environment, the DCs in different groups show similar feature as Section 4.2.3. Therefore, we only show the estimated statistical parameters based on the DCs in the largest groups in the simulation. Fig. 4.10, Fig. 4.11, Fig. 4.12 and Fig.4.13 are the estimated parameters



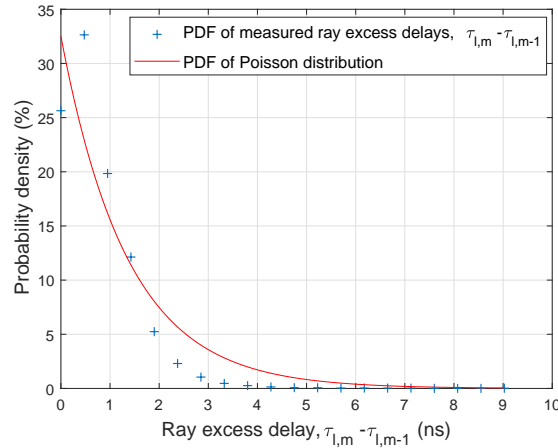
(a)



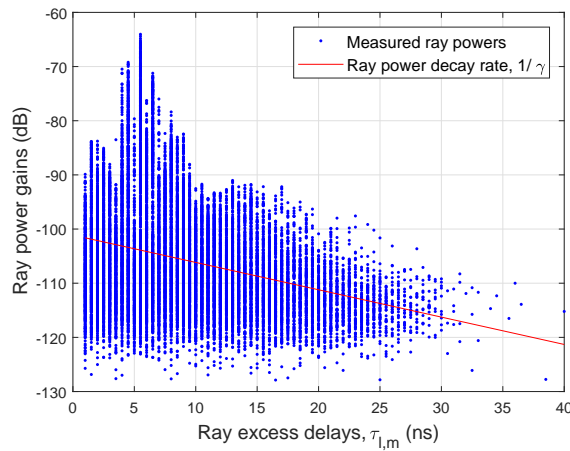
(b)

FIGURE 4.10: (a) PDF of cluster excess delay and (b) cluster power decay rate estimated based on the D-CIRs in the NLOS class in the LOS case.

based on the DCs in the NLOS class. Those red curves are good fits to the data. In Fig. 4.10b, we notice that the powers of the third clusters and the fourth clusters are comparable around -110 dB. However, they are the massive estimated cluster powers, not “noise” even with very low powers. We cannot remove them in the data fitting if the corresponding D-CIRs are valid for data analysis. The accuracy of the model is acceptable based on the results in the following content. In other figures, we can see that the estimated parameters can well fit the data. Since the data analysis in the LOS class is similar, we show it in the next chapter instead. Table 4.1 and Table 4.2 list all the estimated parameters in the LOS case.



(a)



(b)

FIGURE 4.11: (a) PDF of ray excess delay and (b) ray power decay rate estimated based on the D-CIRs in the NLOS class in the LOS case.

In the NLOS case, there are only D-CIRs in the NLOS and Outage classes, and the D-CIRs in NLOS class are the minority, i.e., less 10% based on the data. The D-CIRs in NLOS class are also separated into a few groups, and the correlation of D-CIRs within each group is high. Due to similarity of data processing, we do not show the results for the compact of context.

Note that the duration of minimum inter-cluster interval (12 ns) in the peak analysis significantly impacts the estimation results. The spatial dimension of 3.6m, i.e., roughly 12 ns, is reasonable for the separation of two clusters in the office environment. In the Table 4.1, the mean 12 ns is removed from the cluster arrival rates.

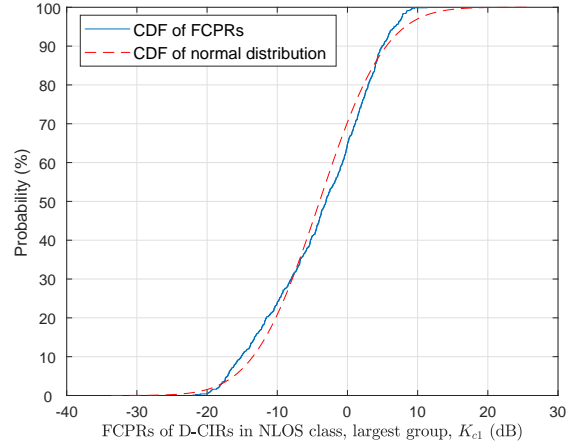


FIGURE 4.12: The normal distributed FCPRs estimated based on the D-CIRs in the NLOS class in the LOS case.

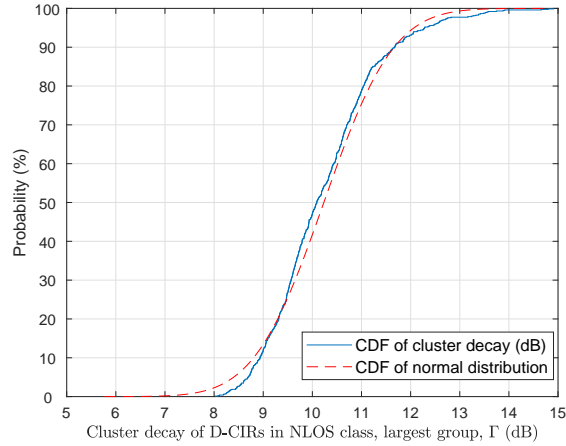


FIGURE 4.13: The log-normal distributed cluster decay rates (normal distributed values in dB) estimated based on the D-CIRs in the NLOS class in the LOS case.

Therefore, the arrival rate between two cluster are actually $4.4723 + 12 = 16.4723$ ns for LOS case and $4.1068 + 12 = 16.1068$ ns for NLOS case. The estimated cluster/ray power decay rates are the slopes as in Fig. 4.9. The equation to transfer the decay rate to decay in ns is: $\text{decay} = -1/\ln(10^{\text{decay rate}/10})$, by taking logarithm of $\exp^{-1/\text{decay}}$, which represents the relationship between the linear fitting and exponential fitting of the data. The ray decays calculated by this equation are 10.4725 in LOS case and 8.6033 ns in NLOS case. In Table 4.2, the cluster decays are show in dB. The corresponding linear values are: mean 12.6968 ns and standard deviation 2.8193 ns for LOS class; mean 10.9337 ns and standard deviation 3.2158 ns for NLOS class.

Another notice is that while the horn antenna rotates on one azimuth plane, the combination of antenna patterns in 360° azimuth angles can be seen as a near flat power response, i.e., a synthesized omni-directional CIR on such azimuth plane for removing the impact of antenna pattern [132], [133], [217]. Thus, such measurement data is often processed with simple peak search algorithm and the rotated angle is assumed to be the path angle of arrival/departure (AoA/D) in the literature [161]. However, we suppress the angle information and resolve the delay information in the data analysis as (4.6).

4.4 Generation of Channel Coefficients

4.4.1 Generation of First DC's Channel Coefficient/D-CIR

Step 1: Generate random cluster delays as

$$\tau'_l = \text{Poisson}(\Lambda) \quad (4.14)$$

based on the cluster arrival rate Λ in Table 4.1, where $\text{Poisson}(\cdot)$ is the Poisson distribution random number operator. We align them in descending order as

$$\Delta\tau_l = \text{sort}(\tau'_l - \min(\tau'_l)). \quad (4.15)$$

The final inter-cluster delay τ_l can be generated accordingly as

$$\tau_l = \begin{cases} 0, & l = 1 \\ \Delta\tau_{l-1} + 12 + \epsilon_{\tau_l}, & l = 2, 3, \dots, L \end{cases} \quad (4.16)$$

where the ϵ_{τ_l} is the compensation of delay interval between the first cluster and the rest of the clusters, and the minimum inter-cluster interval is 12 ns we found previously.

Step 2: We generate cluster powers as

$$a_l'^2 = \begin{cases} 1, & l = 1, \\ \exp(-\tau_l/10^{\frac{\mu_\Gamma + \sigma_\Gamma}{10}})/10^{\frac{\mu_k + \sigma_k}{10}}, & l = 2, 3, \dots, L \end{cases} \quad (4.17)$$

where μ_k and σ_k are the mean and variance of normal distributed FCPRs, and μ_Γ and σ_Γ are the mean and variance of log-normal distributed inter-cluster decay rates. The final inter-cluster power $a_l'^2$ can be achieved after normalising all the cluster powers as

$$a_l'^2 = \frac{a_l'^2}{\sum_{l=1}^L a_l'^2}. \quad (4.18)$$

Note that we do not estimate the shadowing parameter, because it is a LSP. We considered it as a scalar, which is not our focus in this model.

Step 3: Generating the intra-cluster ray delay $\tau_{l,m}$ and ray power $a_{l,m}'^2$ is similar to those in *Step 1* and *Step 2*, except that there is no FCPR for rays, and we fix the intra-cluster ray decay rate. We simply use intra-cluster parameters to substitute the corresponding inter-cluster parameters in (4.14), (4.15), and (4.18). We also use the following two equations instead of (4.16) and (4.17), i.e.,

$$\tau_{l,m} = \Delta\tau_{l,m}, \quad m = 1, 2, \dots, M \quad (4.19)$$

$$a_{l,m}'^2 = \exp\left(-\frac{\tau_{l,m}}{\gamma}\right), \quad m = 1, 2, \dots, M. \quad (4.20)$$

The rays in the LOS cluster and the first NLOS cluster are generated in the same way as those in the NLOS clusters for the simplification of model.

Step 4: We scale/shift the intra-cluster parameters based on inter-cluster parameters and sum up the ray powers that fall into the same delay bins, which depends on the bandwidth of the simulated mmWave channel.

Note that each final generated channel coefficient/D-CIR is the alignment of intra-cluster ray powers based on intra-cluster ray delays and those are shifted by inter-cluster delays according to (4.7). We keep each cluster consists of a certain number

of rays as in SV model. We do not sum up the rays within each cluster as one cluster power. This is designed in the concern of the large bandwidth of mmWave channels in latest 3GPP [95] and other standard models. The large bandwidth channels are modelled in ray level. It is not the same as those in the standard channel models used in 3G/4G systems, such as WINNER and 3GPP models.

4.4.2 Generate Other DCs' Channel Coefficients by Cluster Evolution

After generating the first DC's channel coefficient (we can assign an angle of such DC within the angle range of LOS class or NLOS class), we apply the angular domain cluster evolution in the generation of the rest of DCs' channel coefficients. Each cluster is tracked based on the survival rate when it evolved from one DC to another as in Section 4.3.4.

The procedures of cluster evolution used in the generations of channel coefficients of DCs in both LOS class and NLOS class are the same since we use the same model. However, we assume that the cluster survival rate and the statistical parameters used in the cluster evolution in LOS class are different from those used in NLOS class. When the clusters evolve from the DC in the LOS class to the DC in the NLOS class (or vice versa), we change all the statistical parameters used in the channel coefficient generation procedure in the LOS class to those in the NLOS class (or vice versa) and continue the cluster evolution.

4.4.3 Implementation Details of Channel Coefficient Generation

The pseudo-code to generate the channel coefficients can be written as follows.

- 1: Determine the inter-cluster and intra-cluster parameters (use Table 4.1 in our case), and the number of clusters (five clusters in our case);

```
2: % Comment: generate clusters %
3: if (first DC) then
4:     Generate the inter-cluster delay differences. Assume that the LOS cluster (or
       the first NLOS cluster) excess delay is 0, re-arrange all of them in descending
       order as the inter-cluster delays, and add the minimum cluster interval 12 ns as
       (4.16);
5:     Generate the inter-cluster powers. The FCPR and inter-cluster power decay
       rate should be generated randomly according to the corresponding distribution
       (use Table 4.2 in our case) in the generation of every channel coefficient. Assume
       that the LOS cluster (or the first NLOS cluster) power as 0 dB, and normalise all
       the cluster powers as inter-cluster powers;
6:     Save the delay, power of each cluster;
7: else
8:     while (not the last DC) do
9:         Track and calculate the cluster survival probability by (4.13) for each single
       cluster when it evolves to current DC;
10:        Update/re-generate FCPR and cluster decay rate parameters;
11:        Once one cluster dies or the cluster number increases, generate new clusters
       in the same manner based on the parameters for current DC;
12:        Normalise the cluster powers in current DC as new inter-cluster powers;
13:     end while
14: end if
15: % Comment: generate rays %
16: while (not the last DC) do
17:     Generate the ray for all the cluster in the current mmWave channel following
       Step 3;
18:     Scale the ray delays and powers by the cluster delays;
19:     Add up the ray powers within the same delay bin, which is determined by the
       bandwidth of the channel;
20:     Normalise all the intra-cluster powers;
21: end while
```


22: Re-arrange the ray powers as those in SV model.

4.4.4 Generate Omni-Directional Channel Coefficient

It is straightforward to continue the cluster evolution beyond one class by changing the class-dependent statistical parameters and generate all the DCs along with 360° azimuth angles. After that, the omni-directional channel coefficient of the whole channel, i.e., omni-CIR, can be synthesized by adding up the responses from each cluster in all DCs (adding up the ray powers of each cluster). However, the duplicate clusters that survive for several DCs in the cluster evolution need to be removed. Due to the similarity of generation procedure, we do not show them.

4.5 Simulation and Validation

In this section, we show both the simulation results of DCs in the LOS and NLOS classes and the simulated omni-CIRs. In the verification, we show the results of simulated DCs (D-CIRs) in two approximations at the same time. First, we use the simulated DCs to approximate the statistical RMS DSs based on all the DCs in the LOS/NLOS class. Second, we use simulated DCs to approximate the correlation coefficients of measured DCs (D-PDPs) in the LOS/NLOS class only on the azimuth plane with 90° elevation angle. In order to achieve smooth CDF curve, we use all the measured DCs in the LOS/NLOS class as the reference in the first approximation. However, we generate a same number of simulated DCs as the measured DCs on the azimuth plane with 90° elevation angle in both approximations.

4.5.1 Verification of DCs in the LOS Class

We generate 19 DCs in each trial, the same number as the measured DCs (D-CIRs) in the LOS class on the azimuth plane with 90° elevation angle in LOS case. We optimise

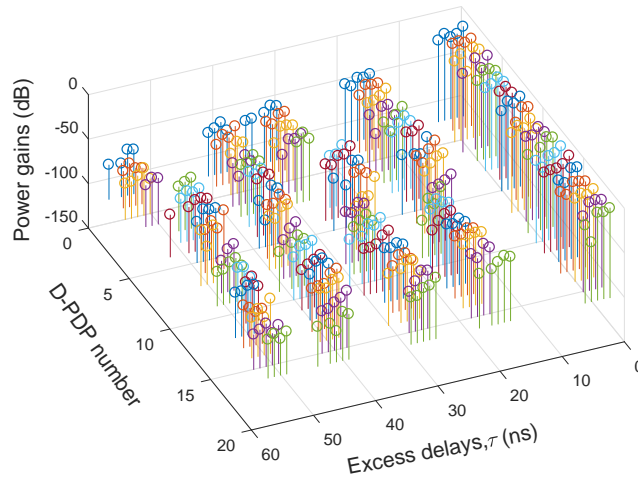
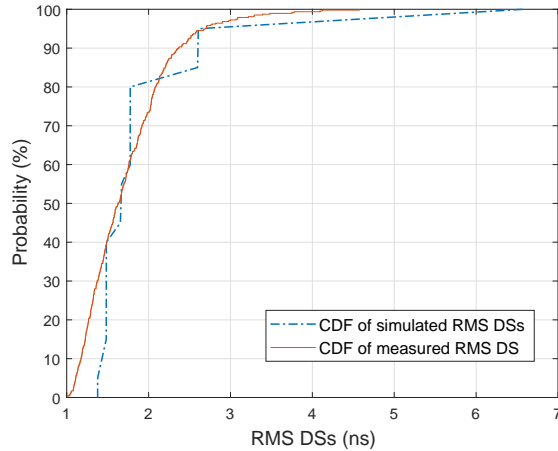


FIGURE 4.14: A group of simulated D-CIRs of DCs in the LOS class.

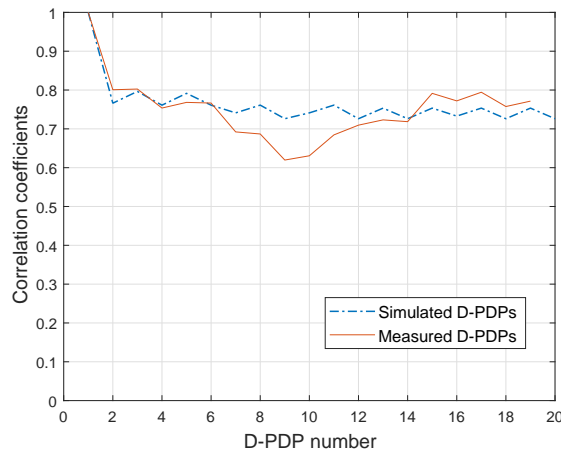
the trial until we find a group of 19 DCs can approximate both the RMS DSs of data and correlation of data at the same time. In the generation of each simulated D-CIR, we let the FCPR randomly generated according to the distribution, as well as the inter-cluster delay rate. We fixed the NLOS cluster number to 4 for all the DCs. A group of good-fit simulated DCs are shown in Fig. 4.14. The corresponding CDF of RMS DSs and correlation coefficients comparisons are shown in Fig. 4.15a and Fig. 4.15b, respectively. We can see that there are some deviation between simulated results and data at some points in the figures. However, the simulated RMS DSs and simulated correlation coefficients can be considered as good fits of the measurement data at the same time. In the approximation, the cluster survival rate λ used in the simulation is 0.1. There is no compensation of delay interval between the first cluster and the rest of the clusters.

4.5.2 Verification of DCs in the NLOS Class

We focus on the simulation of DCs in NLOS class on the azimuth plane with 90° elevation angle. In the generation of each simulated D-CIR, we also let the FCPR randomly generated according to the distribution, as well as the inter-cluster delay rate. We generate 20 DCs in each trial, the same number as the measured DCs in the largest group. We fixed the cluster number to 5 for all the DCs. We also optimise



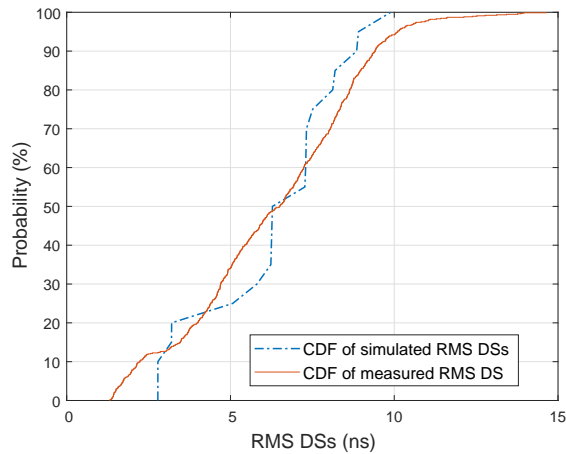
(a)



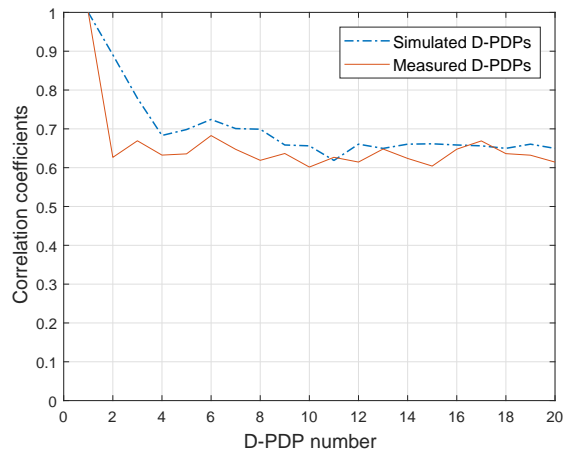
(b)

FIGURE 4.15: (a) Comparison of the CDF of RMS DSs between the simulated DCs and measured DCs and (b) comparison of the correlation coefficients between the simulated DCs and the measured DCs on the azimuth plane with 90° elevation angle in the LOS class in the LOS case.

the trial until we find a group of 20 DCs that can approximate the data. A group of good-fit simulated DCs are similar to those in Fig. 4.14, we do not show them due to redundancy. The corresponding CDF of RMS DSs and correlation coefficients comparisons are shown in Fig. 4.16a and Fig. 4.16b. Though there are some deviations, we can also consider that the simulated RMS DSs and simulated correlation coefficients can fit the measurement data at the same time. In the approximation, the compensation of delay interval between the first cluster and the rest of the clusters ϵ_{τ_1} is -3 ns and the cluster survival rate used in the simulation is 0.1 as well.



(a)



(b)

FIGURE 4.16: (a) Comparison of the CDF of RMS DSs between the simulated DCs and measured DCs and (b) comparison of the correlation coefficients between the simulated DCs and the measured DCs on the azimuth plane with 90° elevation angle in the largest group of NLOS class in the LOS case.

4.5.3 Verification of Omni-CIRs

We choose the first DC in LOS class and use angular cluster evolution to generate all other DCs along 360° azimuth angles in both LOS and NLOS classes. We remove the duplicated clusters that survive for more than one DC and add up all the rest of clusters (adding up the rays within each non-duplicated cluster according to the delay of them) in those DCs. Fig. 4.17 shows the comparison between one simulated omni-CIR and one measured omni-CIR. We can observe that the first cluster and second cluster can be well fitted by simulation, which most significantly affect the properties

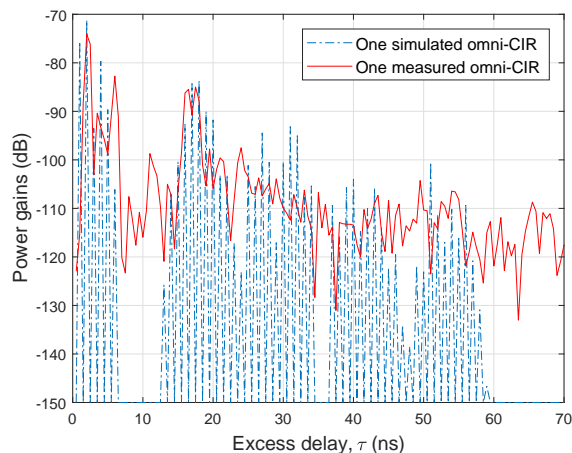


FIGURE 4.17: One simulated omni-CIR compared with one measured omni-CIR.

of channels. We can also observe that the trend of the simulated cluster power levels closely follows the data. We simulate 500 omni-CIRs in total. The compensation of delay interval ϵ_{τ_1} is 8 ns between the first cluster and the rest of the clusters in the modelling of DCs in NLOS class. The calculated mean RMS DSs based on the simulated omni-CIRs is 6.75 ns. This is very close to the estimated mean RMS DS based on the measured omni-CIRs, which is 6.89 ns.

4.6 Summary

An A-APDP method has been introduced to estimate the ASRs of channels and it has been applied in the data analysis of mmWave channel measurements performed in an office environment. Three typical D-CIRs have been found based on the estimated ASRs, RMS DSs, K-factors, and PPGs in the LOS case and two typical D-CIRs have been found, as a subset of those three typical D-CIRs, in the NLOS case.

We have defined the DCs based on the beamwidths of Tx/Rx beams used in the measurement. The LOS class, NLOS class, and outage class have been utilised to classify those DCs. A modified SV model has been proposed to model the DCs in both the LOS and NLOS classes. The normal distributed FCPRs and the log-normal distributed cluster decay rates are the key parameters in the model. The angular domain cluster evolution along the azimuth angles has been introduced to ensure the

consistency of simulated DCs. In the verification of proposed directional mmWave model, we have shown that both the root mean square RMS DSs and the correlation of simulated DCs can match the measurement data. We have also shown that the synthesised omni-CIR can match the measured omni-CIR.

Chapter 5

Spherical Angular Stationarity and Modelling Directional MmWave Channels by Markov States

5.1 Introduction

In this chapter, the focus is still the directional propagation feature of mmWave channels. In the former chapter, the directional mmWave channel model developed are based on the small-scale DCs that are defined by the beamwidths of Tx beams and the cluster evolution in azimuth domain was used to simulate all the DCs in the wireless environment. However, in the case that we do not need to clearly know which DC is used in the mmWave communication and the overall performance or the statistics of DCs between Tx and Rx is the focus, we can model the instantaneous directional mmWave channels by Markov states.

Based on the classification of general land mobile-satellite (LMS) fading environments and long-term variation of received signals, Markov chain channel models were utilised to model the time-variant characteristics of LMS channels [218]–[224]. There were also the modelling of received powers in vehicle-to-vehicle (V2V) and mobile-to-mobile (M2M) wireless communications based on Markov states for both below

6 GHz and mmWave frequencies [74], [225]–[227] and the studies of estimating the system level performances of mmWave communication systems, such as bit error rate (BER) and throughput, based on the finite state Markov channel [228]. Considering the diverse properties of directional mmWave channels between the Tx and Rx in different directions/angles due to the inhomogeneous channel environments, such as the indoor/outdoor scenarios, the Markov states can be utilised in the study of D-CIRs in mmWave frequency ranges as well. However, the studies of directional mmWave channels in this approach are rarely seen.

An A-APDP method used to estimate the ASRs of channels in azimuth angles was introduced and three typical D-CIRs were found in the data analysis in [70], [229]. In this chapter, we first extend the A-APDP method to estimate the spherical ASRs (S-ASRs) of channels in both azimuth and elevation angles. We apply this advanced A-APDP method to the data analysis of directional mmWave channel measurements. Similarly, three typical D-CIRs are found based on the estimated S-ASRs, RMS DSs, K-factors, and PPGs. Then, we propose to use a three-state Markov chain to model the directional mmWave channels and utilise joint channel models to simulate the instantaneous directional mmWave channels.

5.1.1 Contributions

The contributions of this chapter are as follows.

- An A-APDP method used to estimate the S-ASRs of the channels on both azimuth and elevation angles is introduced. It fully extends the APDP method used in former stationarity studies of channels from the time, frequency, and spatial domains [153] to the angular domain.
- In the data analysis of indoor time-invariant mmWave channel measurements, we find three typical D-CIRs in the LOS case and find two typical D-CIRs, as a subset of those three typical D-CIRs, in the NLOS case. Then, we propose to use a three-state Markov chain, namely the LOS, NLOS, and outage states,

according to those typical D-CIRs, to model the directional mmWave channels. The one-step transition matrix and the limiting distribution of Markov chain are estimated based on the measurement data.

- Joint channel models are proposed to simulate the instantaneous directional mmWave channels based on the limiting distribution of Markov chain. A stationary channel model is used to model the D-CIRs in the LOS state within one large S-ASR, a non-stationary channel model is used to model the D-CIRs in the NLOS states over a few small S-ASRs, while the powers of D-CIRs in the outage state are simply modelled as “zero”.
- We do not model the angular information of directional mmWave channel in the proposed stationary and non-stationary channel models. Therefore, they are much less complex compared with the former developed mmWave channel models.

The rest of this chapter is organized as follows. In Section 5.2, the A-APDP method based on both azimuth and elevation angles is introduced to study the S-ASRs of the channel. In Section 5.3, time-invariant mmWave channel measurements are described and three typical measured D-CIRs are found in the data analysis. Section 5.4 proposes a three-state Markov chain to model the directional mmWave channels. In Section 5.5, a stationary and non-stationary channel models are introduced and the joint channel models are developed to simulate the instantaneous directional mmWave channels. The validation of stationary and non-stationary channel models are shown in Section 5.6. Finally, conclusions are drawn in Section 5.7.

5.2 ASRs of Directional Channels

In the last chapter, the APDP method used to study the stationarity regions of channels in the time, frequency, and spatial domains has been extended to the angular domain (also in [70]). We consider the estimated ASRs in the last chapter as planar

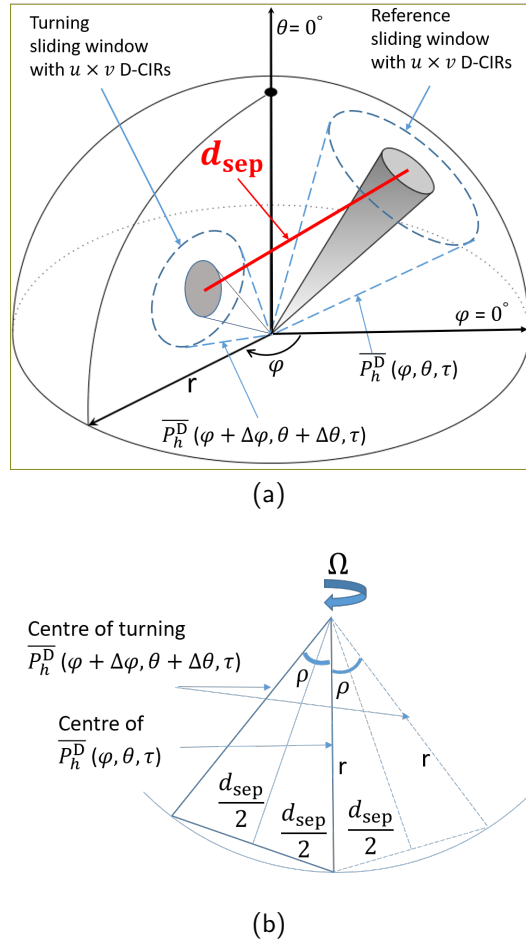


FIGURE 5.1: A-APDP method in the spherical coordinate system: (a) turning sliding windows and (b) apex angle and S-ASR.

ASRs (P-ASRs), which study the ASRs of channels along azimuth angles. In this chapter, we further develop the A-APDP method to study the S-ASRs of channels based on both azimuth and elevation angles.

5.2.1 S-ASRs of Directional Channel

As shown in Fig. 5.1a, there is a spherical coordinate system (r, ϕ, θ) , centred at the Tx (or Rx). The radius, azimuth angle, and elevation angle are denoted by r , ϕ , and θ , respectively. We define $h^D(\phi_i, \theta_j, \tau)$ as the D-CIR received in the direction denoted by (ϕ_i, θ_j) , $i = 1, 2, \dots, u$, $j = 1, 2, \dots, v$, and define the corresponding instantaneous directional power delay profile (D-PDP) as $P_h^D(\phi_i, \theta_j, \tau) = |h^D(\phi_i, \theta_j, \tau)|^2$. We assume there are $U \times V$ D-CIRs in total and the APDPs of $u \times v$ neighbouring D-CIRs

represent one sliding window ($u \times v \ll U \times V$) as

$$\overline{P}_h^{\text{D}}(\phi, \theta, \tau) = \frac{1}{U \times V} \sum_{i=1, j=1}^{U \times V} |h^{\text{D}}(\phi_i, \theta_j, \tau)|^2. \quad (5.1)$$

We let a sliding window $\overline{P}_h^{\text{D}}(\phi + \Delta\phi, \theta + \Delta\theta, \tau)$ turn around the reference sliding window $\overline{P}_h^{\text{D}}(\phi, \theta, \tau)$ with an angular separation interval d_{sep} ($d_{\text{sep}}^2 = \Delta\phi^2 + \Delta\theta^2$), which is the Euclidean distance between two sliding windows in the spherical coordinate system. Then, the angular correlation coefficient between those two APDPs is defined as

$$c(\phi, \theta, \Delta\phi, \Delta\theta) = \frac{\int \overline{P}_h^{\text{D}}(\phi, \theta, \tau) \overline{P}_h^{\text{D}}(\phi + \Delta\phi, \theta + \Delta\theta, \tau) d\tau}{\max\{\int \overline{P}_h^{\text{D}}(\phi, \theta, \tau)^2 d\tau, \int \overline{P}_h^{\text{D}}(\phi + \Delta\phi, \theta + \Delta\theta, \tau)^2 d\tau\}}. \quad (5.2)$$

If the angular correlation coefficients $c(\phi, \theta, \Delta\phi, \Delta\theta)$ between the APDPs are all higher than the ASL (for this step, the calculation is similar to those in the last chapters), we use the corresponding Euclidean distance between the centre of reference sliding window and the centre of turning-around sliding window to determine the apex angle ρ [230] in Fig. 5.1b as

$$\rho = 2 \times \arcsin\left(\frac{d_{\text{sep}}}{2r}\right). \quad (5.3)$$

Finally, the stationary solid angle is defined as Ω to represent the S-ASR of channel as in Fig. 5.1b, i.e.,

$$\Omega = 2\pi(1 - \cos\rho). \quad (5.4)$$

Note that the $u \times v$ D-CIRs used to calculate the APDPs are within a very small solid angle that we assume is much smaller than the stationary solid angle Ω . The total solid angle of a sphere is 4π steradian (sr).

5.3 Channel Measurements and Data Analysis

5.3.1 MmWave Channel Measurements

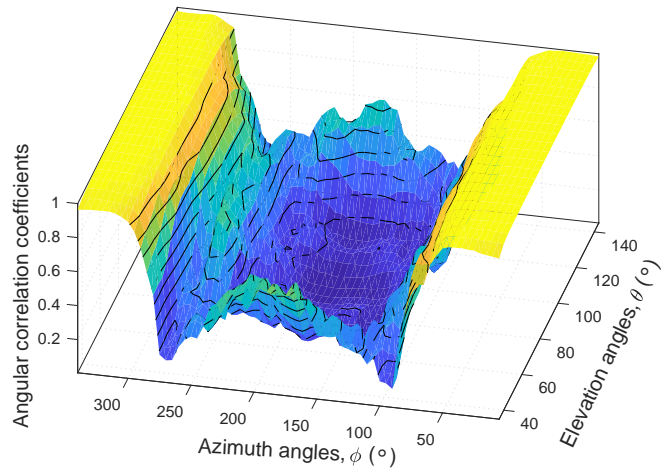
We still use the data from the mmWave channel measurements described in Section 4.2.2 in chapter 4. For the conciseness purposes, we do not repeat the details.

5.3.2 Data Analysis of LOS Case

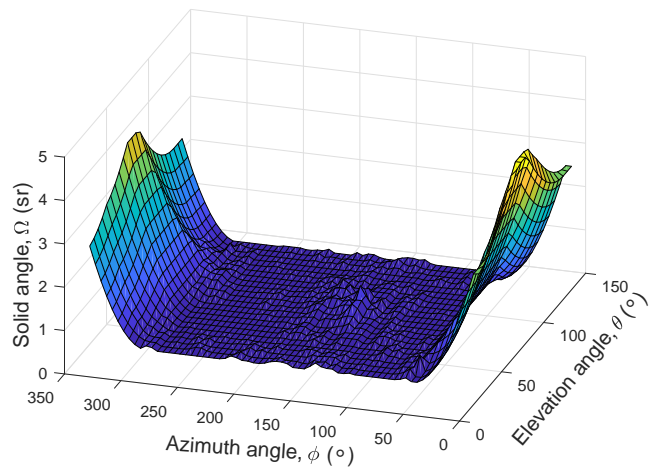
We apply the A-APDP method to the channel measurements. The S-ASRs are estimated based on the D-CIRs measured in all the directions (azimuth and elevation angles). Both the turning sliding windows and the reference sliding windows contain 5 D-CIRs in the calculations.

The spherical angular correlation coefficients between the APDP in the reference sliding window in the direction ($\phi = 0^\circ, \theta = 90^\circ$) and those in the turning sliding windows in all other directions are shown in Fig. 5.2a. For ASL = 0.8, the estimated S-ASR is about 3.62 sr (corresponds to $\rho \approx 64.5^\circ$). We also estimated all the S-ASRs in different directions as shown in Fig. 5.2b. We keep the ASL = 0.8 and we can observe that the S-ASRs are in the range between 0.023 (corresponds to $\rho \approx 5^\circ$) and 3.62 sr. It is obvious that the S-ASRs are the highest around the direction ($\phi = 0^\circ, \theta = 90^\circ$) and those measured D-CIRs are with high similarity due to the existence of LOS path between the Tx and Rx. While the estimated S-ASRs are much smaller in other directions, where the sounding signals are fully scattered, and the NLOS paths experience different parts of the channel environment.

We also estimate the PPGs, RMS DSs, and K-factors [77] based on corresponding D-CIRs as shown in Fig. 5.3, Fig. 5.4, and Fig. 5.5, respectively. Aligning the results, we can see that those parameters are similar along the elevation angles, while fluctuating along azimuth angles. In the directions where the S-ASRs are large, small RMS DSs, high K-factors, and high PPGs are found. While in the directions where the S-ASRs are small, large RMS DSs, high K-factors, and high PPGs are found.



(a)



(b)

FIGURE 5.2: (a) Spherical angular correlation coefficients against azimuth and elevation angles in the LOS case and (b) estimated S-ASRs of mmWave channels in all directions (ASL = 0.8).

Note that there is no unified criterion to determine the level of ASL as mentioned in last chapter.

5.3.3 Three Types of D-CIRs in the LOS Case

Based on the analysis in previous section, we find three typical D-CIRs, which are similar to those in [70].

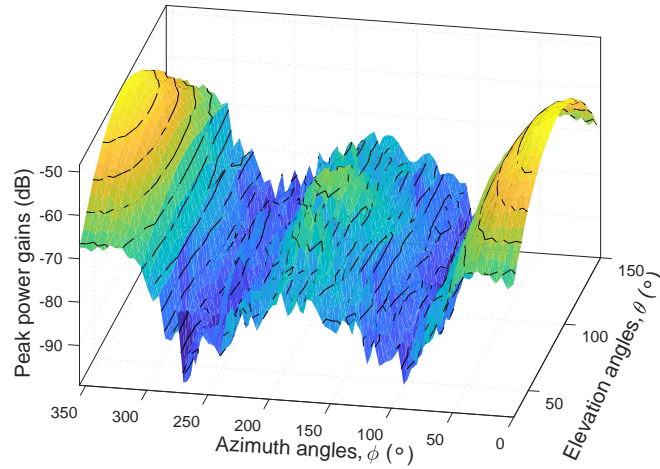


FIGURE 5.3: PPGs of D-CIRs in all directions in the LOS case.

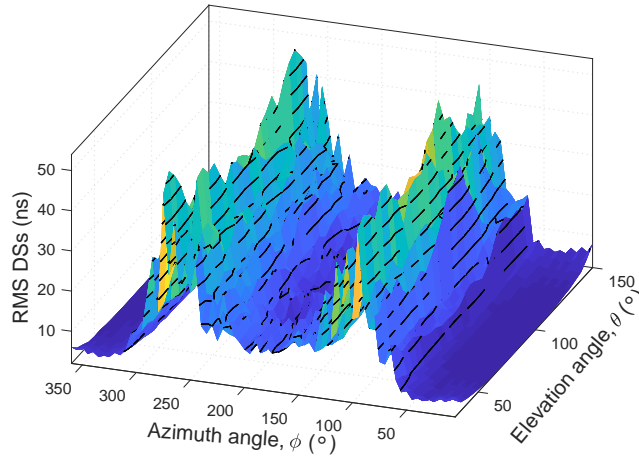


FIGURE 5.4: RMS DSs estimated by D-CIRs in all directions in the LOS case.

- Type 1 D-CIRs: In the directions around $(\phi = 0^\circ, \theta = 90^\circ)$. They all contain a strong LOS component and we consider them within one large S-ASR.
- Type 2 D-CIRs: In the directions where the smallest S-ASRs are dominant (close to 0.023 sr in Fig. 5.2b. They normally contain a weak NLOS component (or a few) with very low power gain. They account for the large DSs up to 40 ns and the low K-factors (the strongest NLOS component over the rest of D-CIR) mostly below 0 dB.
- Type 3 D-CIRs: The rest of them in the directions that the mediate S-ASRs are dominant. They may contain up to two strong NLOS components and a few

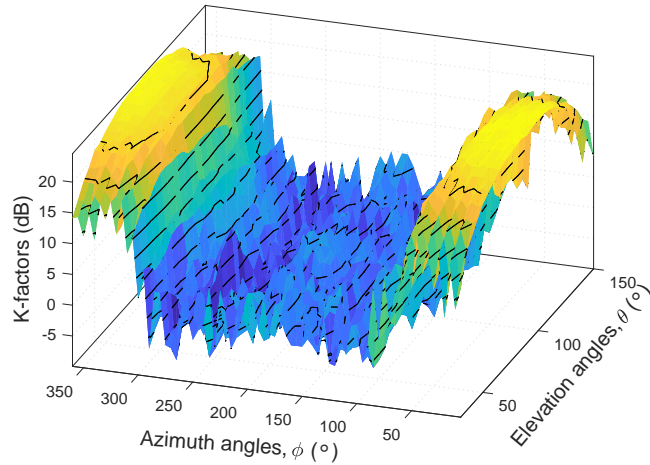


FIGURE 5.5: K-factors estimated by D-CIRs in all directions in the LOS case.

weak NLOS components. The K-factors are around 0 dB and the RMS DSs are about 5 to 10 ns.

Note that these results are similar to those in Section 4.2.3 Chapter 4. Similarly, on the horizontal plane ($\phi \in [0^\circ, 355^\circ], \theta = 90^\circ$), we also determine the three types of D-CIRs exactly by the PPG levels as shown in Fig. 4.5 in Chapter 4. We repeat it here for the convenience of readers.

- Type 1 D-CIRs: PPG levels are above -62 dB. The angular coverages are $\phi < 47^\circ$ and $\phi > 312^\circ$.
- Type 2 D-CIRs: PPG levels are below -80 dB. The angular coverages are $72^\circ < \phi < 127^\circ$ and $221^\circ < \phi < 285^\circ$.
- Type 3 D-CIRs: PPG levels are between -62 and -80 dB. The angular coverages are $127^\circ < \phi < 221^\circ$, $47^\circ < \phi < 72^\circ$, and $285^\circ < \phi < 312^\circ$.

Note that the peaks of S-ASRs in Fig. 5.2b are estimated based on the D-CIRs with most common characteristics compared with neighbouring D-CIRs. We can split the whole sphere (4π sr) into a few stationarity regions by the angular coverage areas of highest S-ASRs.

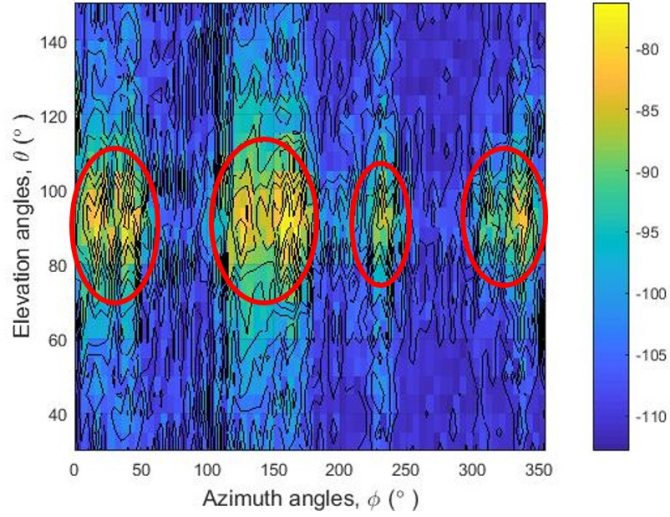


FIGURE 5.6: PPGs of D-CIRs in all directions in the NLOS case.

5.3.4 Two Types of D-CIRs in the NLOS Case

Similarly, the estimated S-ASRs, PPGs, RMS DSs, and K-factors for the mmWave channels in the NLOS case are estimated. We do not show all of them due to redundancy. From the results, the estimated S-ASRs in all the directions are smaller than 0.1 sr, and they are comparable to those small S-ASRs estimated in the LOS case. We find that the measured D-CIRs can be sorted into two types and they have similar features as those Type 2 and Type 3 D-CIRs in the LOS case. We still use the Type 3 D-CIRs to classify the D-CIRs with higher PPGs that are red-circled in Fig. 5.6. They account for the relatively smaller RMS DSs and relatively higher K-factors. The rest of D-CIRs are classified as the Type 2 D-CIRs. They account for the larger RMS DSs and lower K-factors. Therefore, these two types of D-CIRs are considered as a subset of the three types of D-CIRs in the LOS case.

Note that due to the high path loss of mmWave sounding signals, the power gain levels of D-CIRs received while Tx is in Tx2 position are different from those of D-CIRs received while Tx is in Tx1 position. Therefore, we adjust the power gain level threshold from -80 dB to -90 dB to separate those two types of D-CIRs. However, path loss is a large-scale parameter and we only focus on the small-scale parameters

in this chapter. In addition, we mainly focus on the three types of D-CIRs in the LOS case.

5.4 Three-State Markov Chain of Directional Mm-Wave Channels

5.4.1 Three Markov States of Directional MmWave Channels

Similar to the studies of LMS Markov channels in [220], [221], we propose to describe the measured directional mmWave channels in Section 5.3.1 by three Markov states, i.e.,

$$h^D(\tau) = \begin{cases} h^{D,\text{LOS}}(\tau), & \text{LOS state} \\ h^{D,\text{NLOS}}(\tau), & \text{NLOS state} \\ \text{Null}, & \text{Outage state.} \end{cases} \quad (5.5)$$

We define $h^{D,\text{LOS}}(\tau)$, $h^{D,\text{NLOS}}(\tau)$, and Null as the LOS state, NLOS state, and outage states, respectively, to describe the measured directional mmWave channel $h^D(\tau)$. If $h^D(\tau)$ falls to the LOS state, we expect it consists of both the LOS component and NLOS components. If $h^D(\tau)$ falls to the NLOS state, we expect it consists of only NLOS components and at least one NLOS component with high power can maintain the communication between the Tx and Rx. While, if $h^D(\tau)$ falls to the outage state, we simply consider the power of it as null (“zero”).

According to the descriptions of those three types of D-CIRs found in the LOS case in Section 5.3.3, we assign Type 1 D-CIRs to the LOS state, assign Type 3 D-CIRs to the NLOS state, and assign Type 2 D-CIRs to the outage state. Similarly for the NLOS case, we assign Type 3 D-CIRs to the NLOS state and assign Type 2 D-CIRs to the outage state.

Note that, in the standard models, such as 3GPP, the terms “LOS state” and “NLOS state” were also used. Those were determined by a LOS probability related to the propagation condition of simulated channel and the user terminal (UT) mobility.

However, those are not based on analysing channels by Markov states, which are different from the content in this chapter. Also note that the aforementioned channel measurements can be considered as one type of scenario that the Tx or Rx fixed in one position while the other end is rotating. For the scenario that both the Tx and Rx are moving, if we assume the Tx and Rx beams can be kept aligned by a tracing technique, we also expect to see the three typical D-CIRs since the DCs between Tx and Rx can be in different situations (LOS, NLOS, and "Null" cases, similarly) due to experiencing different parts of channel environment. For example, the different measured D-CIRs of DCs in vehicular communication scenarios [225]. However, this requires a lot of work in the design of channel sounder and the channel measurements. We do not further discuss those three types of D-CIRs in other scenarios in this chapter.

5.4.2 Transition Matrix and Limiting Distribution of Three-State Markov Chain

We define a stationary Markov chain (D-CIR sequence) $X_n, X_n \in (\text{LOS}, \text{outage}, \text{NLOS})$, and define $p_{j,i} = p(X_n = j | X_{n-1} = i)$ as state transition probability from the state i to the state j [193]. Here we re-define $j = 1, 2, 3$ and $i = 1, 2, 3$ to indicate the three Markov states. Then, the transition matrix of Markov chain can be written as

$$\mathbf{P} = \begin{pmatrix} p_{11} & p_{12} & p_{13} \\ p_{21} & p_{22} & p_{23} \\ p_{31} & p_{32} & p_{33} \end{pmatrix} \quad (5.6)$$

and the limiting distribution $\boldsymbol{\pi} = [\pi_1, \pi_2, \pi_3]$ satisfies

$$\boldsymbol{\pi} = \boldsymbol{\pi} \mathbf{P}, \quad \sum_{j=1}^3 \pi_j = 1. \quad (5.7)$$

TABLE 5.1: The numbers of state transitions in the LOS case.

Initial State \ Next State	LOS state	Outage state	NLOS state	Total transition number
LOS state	299	0	22	321
Outage state	0	546	119	665
NLOS state	22	119	648	789

5.4.3 State Transition Characteristics of Directional MmWave Channel in the LOS Case

Consider that there are transmission events as the channel measurements in the LOS case. We assume one D-CIR Rx received falls in a Markov state (random) as “initial state”. Then, the Tx rotates the horn antenna one angular step (5° as in the measurement) to the neighbouring direction that the azimuth angle always become larger, and we consider the D-CIR Rx received falls in another Markov state as “next state”. Note that the initial state and next state can be the same Markov state. We let the event repeats on every Tx rotating directions (azimuth and elevation angles, 71×25). The power levels of initial state and next state D-CIRs are measured, and their Markov states are determined according to the PPG levels listed in Section 5.3.3. The numbers of state transitions are listed in Table 5.1. The probability of one-step transition matrix is estimated as

$$P^1 = \begin{pmatrix} 0.9315 & 0 & 0.0685 \\ 0 & 0.8211 & 0.1789 \\ 0.0279 & 0.1508 & 0.8213 \end{pmatrix}. \quad (5.8)$$

We modify the event that we let the Tx rotate the horn antenna n angular steps randomly (in any random angle after rotating). Since the environment is kept unchanged, the Markov chain can be considered stationary. Then, after repeating the event for sufficient enough times, the limiting distribution of the Markov chain [193]

can be eventually reached. The limit of n -step transition matrix is estimated as

$$\lim_{n \rightarrow \infty} P^n = \begin{pmatrix} 0.1810 & 0.3746 & 0.4444 \\ 0.1810 & 0.3746 & 0.4444 \\ 0.1810 & 0.3746 & 0.4444 \end{pmatrix} \quad (5.9)$$

where $n = 1, 2, \dots, \infty$, and the limiting distribution is $\boldsymbol{\pi} = [0.1810, 0.3746, 0.4444]$ since the transition matrix is irreducible, aperiodic, and positive recurrent. We find that they are consistent with the ratio of that the number of D-CIRs in each state over the total number of measured D-CIRs (340 D-CIRs in the LOS state, 665 D-CIRs in the outage state, and 795 D-CIRs in the NLOS state).

5.4.4 State Transition Characteristics of Directional MmWave Channel in the NLOS Case

Similarly, the one-step transition matrix based on the measurement in the NLOS case is estimated as

$$P^1 = \begin{pmatrix} 0.6204 & 0.3796 \\ 0.0311 & 0.9689 \end{pmatrix} \quad (5.10)$$

and the limiting distribution is estimated as $\boldsymbol{\pi} = [0.0757, 0.9243]$. The limiting distribution is also consistent with the ratio of that the number of D-CIRs in each state over the total number of measured D-CIRs (138 D-CIRs in the NLOS state, and 1662 D-CIRs in the outage state).

Note that the averaged one-step transition probability of Markov chain acquired from different positions of a stationary environment should be used to estimate the limiting distribution. But we can not practically achieve it due to limited data. Also note that if a time-variant channel can be split into a few “quasi-stationary” channels, the Markov chain can be used within the limited duration of each “quasi-stationary” channel [77]. However, even within a stationary duration of time, the (averaged) one-step transition probability and limiting distribution are highly related to the channel environment, we do not recommend to use those results to predict the Markov-state

channels in other environments. Since a lot of work required and we focus on the modelling of directional mmWave channels in each Markov state in the following content, we leave them in the future at the moment.

5.5 Joint Channel Models

The channel models in the former studies [77], [81], [132], [133], and other related literature are based on the cluster model, which can be written as

$$h^D(\tau) = \sum_{l=1}^L a_l \delta(\tau - \tau_l) \underbrace{\delta(\phi - \phi_l) \delta(\theta - \theta_l)}_{\text{Substituted by Markov states}} \quad (5.11)$$

where we assume there are l clusters, $l = 1, 2, \dots, L$, and a_l is the amplitude of cluster.

Given the knowledge of directional mmWave channels in each Markov state, we can describe any D-CIR by one of the Markov states instead of describing them by exact directions in the angular domain (azimuth and elevation angles). Specifically, we can use the three Markov states to substitute the directional terms $\delta(\phi - \phi_l) \delta(\theta - \theta_l)$ in (5.11) (removing the angular information from model since the angular information of clusters is only within the -3dB angular range of each narrow beam) and a group of joint channel models can be used to model the directional mmWave channels in those Markov states. The complexity of channel models in each Markov state is much lesser compared with those of the current mmWave channel models mentioned in Section 5.1.

5.5.1 Procedure of Modelling Directional MmWave Channels

The procedure of modelling the instantaneous directional mmWave channels is illustrated in Fig. 5.7. We first distinguish the LOS case and NLOS case. Then we define three Markov states in the LOS case and two Markov states in the NLOS case. We assign each Markov state a channel model based on the candidate models with a

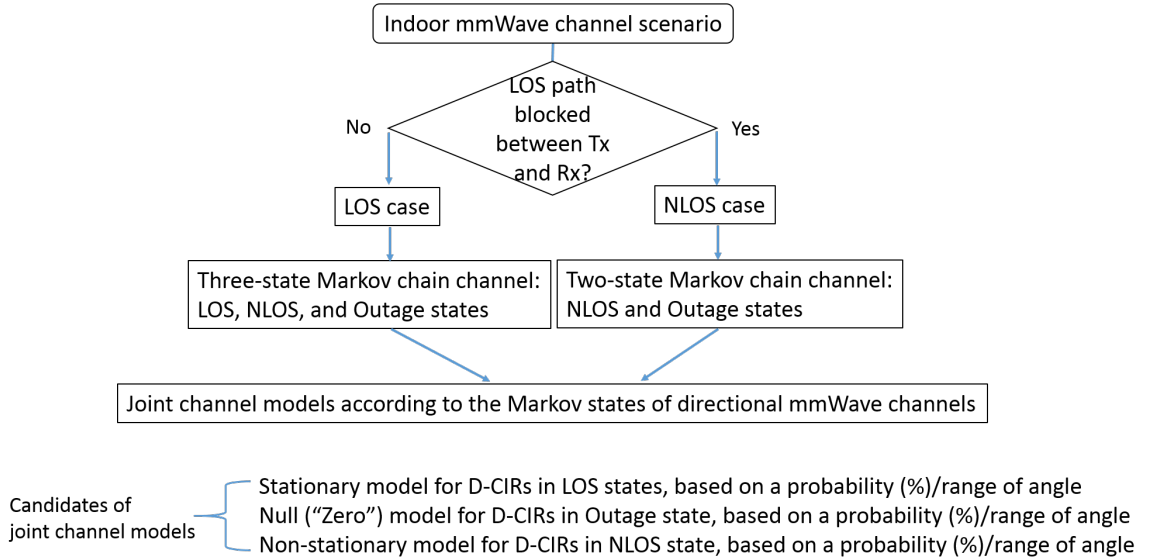


FIGURE 5.7: Procedure of modelling directional mmWave channels.

percentage. Finally, the joint channel models consisting of stationary/non-stationary model and Null model can be obtained.

For the LOS case, we consider the limiting distribution as the probability of each three Markov state and the joint channel models can be defined as

$$h^D(\tau) = \begin{cases} h^{D,LOS}(\tau), & p(X_n = \text{LOS state}) : \pi_1 \\ \text{Null}, & p(X_n = \text{Outage state}) : \pi_2 \\ h^{D,NLOS}(\tau), & p(X_n = \text{NLOS state}) : \pi_3 \end{cases} \quad (5.12)$$

where $p(\cdot)$ is the probability operator. Note that $h^{D,LOS}(\tau)$ and $h^{D,NLOS}(\tau)$ are location related (if measuring the D-CIRs in different locations other than Tx1 and Tx2 in Fig. 4.2a of Section 4.2.2). We may need to consider $h^{D,LOS}(\tau) = h_{\text{location}}^{D,LOS}(\tau) \times L_{\text{Scalar}}^{LOS}$ and $h^{D,NLOS}(\tau) = h_{\text{location}}^{D,NLOS}(\tau) \times L_{\text{Scalar}}^{NLOS}$. We define $h_{\text{location}}^{D,LOS}(\tau)$ and $h_{\text{location}}^{D,NLOS}(\tau)$ as location-dependent D-CIRs, and define L_{Scalar}^{LOS} and L_{Scalar}^{NLOS} as large-scale parameters, which can consist of path loss, diffraction loss, reflection loss, scattering loss, etc. [77], [95]. However, we do not further discuss the large-scale parameter in this thesis since the focus is the modelling of small-scale fading model.

For the NLOS case, there are only NLOS and outage Markov states, and the joint models only contain $h^{D,NLOS}(\tau)$ and Null. Since it is similar to process the data and

model the directional mmWave channels in the NLOS case, we only focus on the three Markov states in the LOS case in the rest of chapter. It is also reasonable that if the Tx is considered as a base station or relay, it is normally fixed in the position with high probability of establishing the LOS communication with the user/Rx.

Based on the data analysis results in Section 5.3.3, it is also possible to separate the D-CIRs in different Markov states by azimuth angles. However, the modelling based on the limiting distribution is considered more versatility for various channel scenarios. It enables us to model the instantaneous directional mmWave channels without considering the angles of directional mmWave channels. In the system level, if we only need to estimate the system performance based on massive mmWave signal transmissions and exactly angles/direction of each generated D-CIR does not significantly affect the simulation results, the proposed joint channel models are very suitable to serve the purposes and they are much less complex compared with the standard mmWave channel models.

5.5.2 Stationary and Non-Stationary Channel Models

Based on the data analysis, the D-CIRs in the LOS state belong to one large S-ASR. We assume the statistical parameters of those D-CIRs within the angular coverage of LOS state are constant, and we propose to use a stationary channel model to describe those D-CIRs. On the contrary, the D-CIRs in the NLOS state are over a few S-ASRs. We assume the statistical parameters of those D-CIRs within the angular coverage of NLOS state are variant, and we propose to use a non-stationary channel model to describe those D-CIRs. While we simply use “zero” to model the power of D-CIRs in the outage state.

5.5.2.1 LOS State Stationary Channel Model

The modelling of D-CIRs in the LOS state is also based on the SV channel model [118], [119]

$$h^{\text{D,LOS}}(\tau) = \sum_{l=1}^L \sum_{m=1}^M a_{l,m} \exp(j\beta_{l,m}) \delta(\tau - \tau_l - \tau_{l,m}). \quad (5.13)$$

We define L clusters and M rays in each cluster, $l = 1, 2, \dots, L$, $m = 1, 2, \dots, M$. The inter-cluster delay is denoted as τ_l , and the amplitude and delay of intra-cluster rays are denoted as $a_{l,m}$ and $\tau_{l,m}$, respectively. The random phase of each intra-cluster ray is denoted as $\exp(j\beta_{l,m})$, where $\beta_{l,m}$ is uniformly distributed $\beta_{l,m} \sim \text{Uni}[-\pi, \pi)$. We can see that this equation is very similar to (4.7) in Section 4.3.3.

We also assume that the number of inter-cluster arrivals and the number of intra-cluster ray arrivals follow Poisson distributions for the fixed time intervals. We model the inter-cluster arrival rate τ_l , the intra-cluster ray arrival rate $\tau_{l,m}$, The exponential distributed inter-cluster powers a_l^2 , intra-cluster ray powers $a_{l,m}^2$, and first cluster power ratio (FCPR) K_{c1} as (4.8)-(4.11) in Section 4.3.3.

5.5.2.2 NLOS State Non-Stationary Channel Model

The non-stationary model $h^{\text{D,NLOS}}(\tau)$ is similar to the stationary model $h^{\text{D,LOS}}(\tau)$. All the statistical parameters of channels are considered as constant, except the FCPR and inter-cluster decay rate are treated as variables.

We assume the inter-cluster power decay rate in (4.10) is log-normal distributed and we re-denote it as $\tilde{\Gamma}$, $\ln(\tilde{\Gamma}) \sim \text{N}(\mu_{\Gamma}, \sigma_{\Gamma})$. We assume the FCPR in (4.11) is normal distributed and we re-denote it as \tilde{K}_{c1} , $\tilde{K}_{c1} \sim \text{N}(\mu_k, \sigma_k)$.

Note that the random values are used in each simulation of the non-stationary model. However, each simulated D-CIR can be either stationary or non-stationary which depends on the situation of channels.

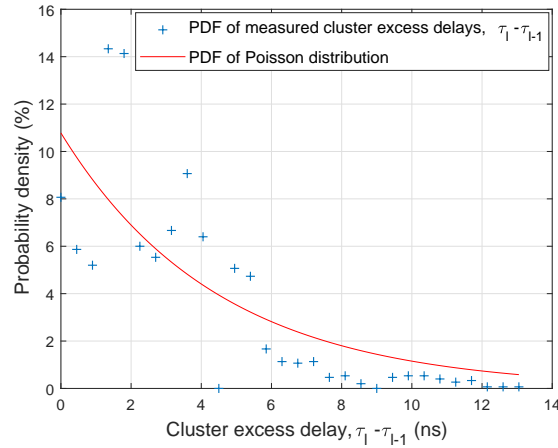
TABLE 5.2: Statistical parameters of both LOS state and NLOS state (LOS case).

D-CIRs in Markov states	Cluster arrival rate, $1/\Lambda$ (ns)	Cluster power decay rate	Ray arrival rate, $1/\lambda$ (ns)	Ray power decay rate	Mean FCPR, K_{c1} (dB)
LOS state	4.4723 (1/0.2236)	-0.3543 (12.2578 ns)	1.0494 (1/0.9529)	-0.4147 (10.4725 ns)	24.346
NLOS state	3.3400 (1/0.2994)	—	1.086 (1/0.9208)	-0.4321 (10.0508 ns)	—

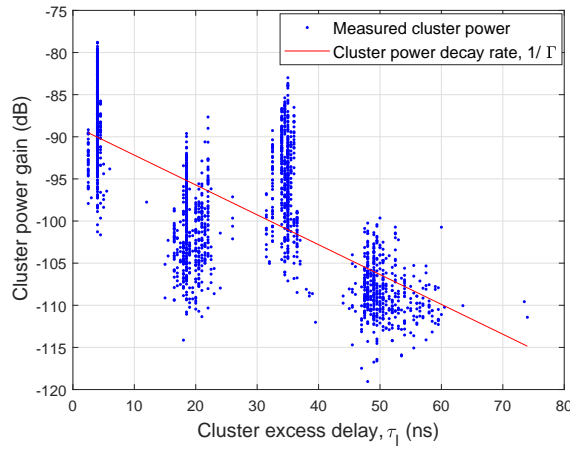
5.5.3 Estimation of Statistical Parameters

We use 40 dB dynamic ranges of the measured D-CIRs in the data analysis. The first cluster (the LOS component or the first NLOS component) from each D-CIR is removed and saved for the FCPR estimations according to (4.11), then the peak analysis is used to process the rest of D-CIRs in the estimation of inter-cluster and intra-cluster parameters. We find that the 12 ns minimum inter-cluster interval is suitable to separate the clusters (the spatial dimensions of 3.6 m, i.e., roughly 12 ns, is reasonable for the distance between two clusters in the office environment) and it enables us to capture the feature of D-CIRs in both the LOS and NLOS Markov states. We decide the border of each two consecutive clusters by one of the minimum peak power levels between them and make sure the duration of each cluster is larger than 12 ns. Four clusters are captured from each D-CIR and the inter-cluster and intra-cluster parameters are estimated based on them.

Note that the minimum inter-cluster interval used in the peak analysis significantly impacts the estimation results. It is similar to that in [132]. The arrival rate between two cluster are actually $4.4723 + 12 = 16.4723$ ns for LOS case and $3.34 + 12 = 15.34$ ns for NLOS case. The estimated cluster/ray power decay rates are the slopes in the SV model as in Fig. 4.9. The equation to transfer the decay rate to decay in ns is $\text{decay (ns)} = -1/\ln(10^{\text{decay rate}/10})$, which is the relationship between the linear fitting and exponential fitting of the data.



(a)



(b)

FIGURE 5.8: (a) PDF of inter-cluster excess delay and (b) inter-cluster power decay rate based on the D-CIRs in the LOS state in the LOS case.

5.5.3.1 Parameter Estimations

Based on the D-CIRs in the LOS state, the inter- and intra-cluster parameters are estimated. Fig. 5.8 shows the PDF of inter-cluster delays and Fig. 5.9 shows the inter-cluster power decay rate. We estimate those parameters based on the D-CIRs in the NLOS state in similar manner, except the FCPR and the inter-cluster power decay rate. We notice that there are two high probabilities above 14% that are far away from the simulated PDF of Poisson distribution (in red) in Fig. 5.8a. Based on the values shown in this figure (delay difference between two clusters, $\tau_l - \tau_{l-1}$) about 1.5–1.8 ns, we can calculate the corresponding distance of those two clusters:

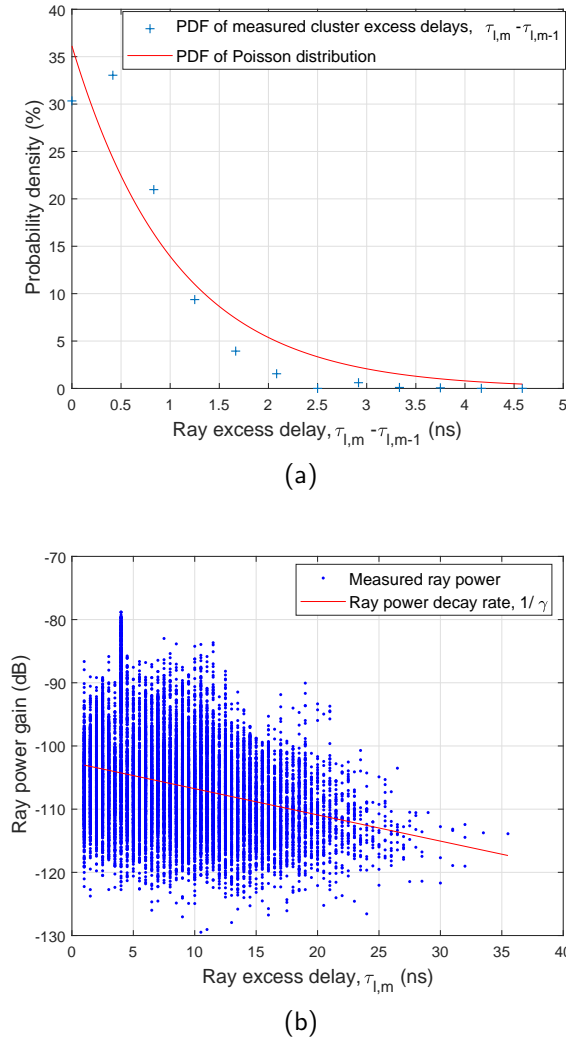


FIGURE 5.9: (a) PDF of intra-cluster/ray excess delay and (b) intra-cluster/ray power decay rate based on the D-CIRs in the LOS state in the LOS case.

about 0.5 metre away. We think this may due to the reflection/scattering of LOS component caused by big sounder testbed as shown in Fig. 4.2b. Since it is possible not to consider the sounder testbed as part of channel environment, we can leave it for now. However, we keep those two points for the integrity of data.

Then, a normal distribution is used to fit the statistics of FCPRs, $K_{cl}^{\tilde{}} \sim N(2.898, 13.67)$, as shown in Fig. 5.10 (CDF in the figures stands for cumulative distribution function). A log-normal distribution is used to fit the statistics of inter-cluster power decay rates, $\ln(\tilde{\Gamma}) \sim N(11.1077, 2.4291)$, as shown in Fig. 5.11. We may notice that the normal distributions seems not as good as the fitting in Fig. 4.12 and Fig. 4.13. This is

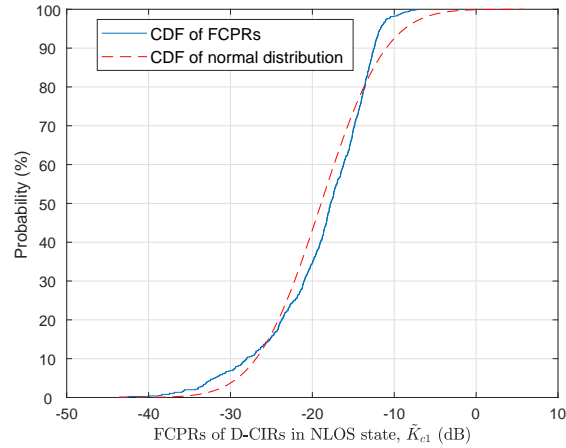


FIGURE 5.10: The normal distributed FCPRs estimated based on the D-CIRs in the NLOS state.

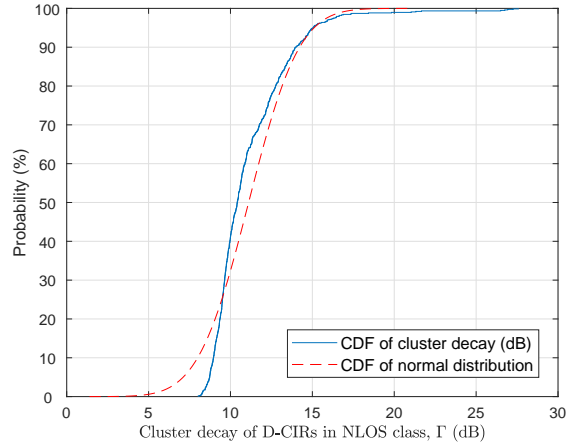


FIGURE 5.11: The log-normal distributed inter-cluster decay rates (data in dB follow normal distribution) estimated based on the D-CIRs in the NLOS state.

because the results in Fig. 5.10 and Fig. 5.11 are based on the D-CIRs in all three NLOS groups (one large group and two small groups mentioned in Section 4.3.6 of Chapter 4). The data contain the information of channels in different parts of channel environment (the objects are different, as well as channel properties). However, we keep using normal distributions to describe the channel properties as those in the last chapter, and normal distributions are still fairly good fit to the data. The accuracy is acceptable based on the results in the following content. All the estimated parameters (refer to SV model in Fig. 4.9), such as cluster/ray arrival rates, power decay rates, can be found in Table 5.2.

5.5.3.2 Implementation Details

Refer to [231], the details of the statistical parameter estimations based on the D-CIRs in the LOS state can be found in the pseudo-code below.

- 1: **while** (not the last of D-CIR in LOS state) **do**
 - 2: Separate the LOS cluster from the D-CIR. Estimate the FCPR and save the power of remaining D-CIR;
 - 3: Apply the peak analysis on the D-CIR without LOS cluster. Determine the border of each two consecutive clusters. Make sure the duration of each cluster \geq minimum inter-cluster interval;
 - 4: Save the delay and power level of each cluster, as well as those of each ray;
 - 5: **end while**
 - 6: Estimate the mean FCPR, the Poisson distributed inter-cluster and intra-cluster delay parameters, and the exponential distributed inter-cluster and intra-cluster power parameters.
-

The details of statistical parameter estimations based on the D-CIRs in the NLOS state are similar, except the separation of first cluster power, the estimation of FCPRs, and inter-cluster decay rates. We add a further step in the last line of above pseudo-code as below.

- Last line: Estimate the inter-cluster decay rates from each single D-CIR first, then, estimate the mean and standard deviation of both FCPRs and inter-cluster decay rates.
-

Note that while the horn antenna rotates on one azimuth plane, the combination of antenna patterns in 360° azimuth angles can be seen as a near flat power response, i.e., a synthesized omni-directional CIR for removing the impact of antenna pattern [132], [217]. Thus, such measurement data is often processed with simple peak search algorithm and the rotated angle is assumed to be the path angle of arrival/departure (AoA/D) in the literature [161]. However, we use the Markov states to substitute the angle information and resolve the delay information in the data analysis as (5.11) and (5.13).

5.5.4 Channel Coefficients Generation Based on Stationary Channel Model

Step 1: Generate random cluster delays by

$$\tau'_l = \text{Poisson}(\Lambda) \quad (5.14)$$

based on the cluster arrival rate Λ in Table 5.2. Align them in descending order as

$$\Delta\tau_l = \text{sort}(\tau'_l - \min(\tau'_l)). \quad (5.15)$$

Then, the final inter-cluster delay τ_l can be generated as

$$\tau_l = \begin{cases} 0, & l = 1 \\ \Delta\tau_{l-1} + 12 + \epsilon_{\tau_l}, & l = 2, 3, \dots, L \end{cases} \quad (5.16)$$

where the ϵ_{τ_l} is the compensation of delay interval between the first cluster and the rest of the clusters compared with the minimum inter-cluster interval (12 ns we found previously).

Step 2: The cluster powers are generated as

$$a'_l{}^2 = \begin{cases} 1, & l = 1, \\ \exp(-\frac{\tau_l}{\Gamma})/10^{\frac{\kappa_{cl}}{10}}, & l = 2, 3, \dots, L \end{cases} \quad (5.17)$$

where K_{c1} is the FCPR (K-factor). Then the final inter-cluster power a_l can be generated as

$$a_l^2 = \frac{a_l'^2}{\sum_{l=1}^L a_l'^2}. \quad (5.18)$$

Similarly, we do not consider shadowing since it is a large-scale parameters.

Step 3: Generation of the intra-cluster ray delay $\tau_{l,m}$ and ray power $a_{l,m}^2$. The sum of ray powers equal to the corresponding cluster power, i.e., $a_l^2 = \sum_{m=1}^M a_{l,m}^2$. The general procedure is similar to that used for generating the inter-cluster delays and powers in *Step 1* and *Step 2*. However, we use

$$\tau_{l,m} = \Delta\tau_{l,m}, \quad m = 1, 2, \dots, M \quad (5.19)$$

$$a_{l,m}^2 = \exp\left(-\frac{\tau_{l,m}}{\gamma}\right), \quad m = 1, 2, \dots, M \quad (5.20)$$

instead of (5.16) and (5.17), respectively. Then we simply use intra-cluster parameters to substitute the corresponding inter-cluster parameters in (5.14), (5.15), and (5.18). The rays in the LOS cluster are generated in the same way as those in NLOS clusters for the simplification of model. Note that we do not add any delay or compensation interval on each of ray delays.

Step 4: We scale/shift the intra-cluster parameters based on inter-cluster parameters, then, sum up the ray powers that fall into the same delay bins (depend on the bandwidth of the channel).

Each final generated channel coefficient (D-CIR) is the alignment of intra-cluster ray powers based on the intra-cluster ray delays according to (5.13). We keep each cluster consists of a certain number of rays as SV model. Because the very large bandwidth is the merit of mmWave channels, the WSS in the frequency domain may not be satisfied [153], and the neighbouring delay bins can be correlated. Therefore, the rays within each cluster are not summed up as one cluster power. It is not the same as those in WINNER and 3GPP models.

5.5.4.1 Implementation Details Based on Stationary Channel Model

The pseudo-code to generate the channel coefficients by LOS state stationary model can be written as follows.

- 1: Determine the FCPR, inter-cluster, and intra-cluster parameters (use Table 5.2 in our case), and the number of clusters (five clusters in our case);
 - 2: Generate the inter-cluster delay differences, and assume the LOS cluster excess delay is 0 ns. Re-arrange all of them in descending order as the inter-cluster delays, and add the minimum cluster interval 12 ns as (5.16). If needed, add the delay compensation ϵ_{τ_1} ;
 - 3: Generate the inter-cluster powers, and assume the LOS cluster power as 0 dB. Normalise all the inter-cluster powers;
 - 4: **while** ($l < \text{number of inter-clusters (4 + 1 in the simulation)}$) **do**
 - 5: Generate the intra-cluster delay differences, re-arrange them in descending order as intra-cluster excess delay;
 - 6: Generate the intra-cluster powers. Make sure the sum of intra-cluster ray powers equals to the current cluster power;
 - 7: **end while**
 - 8: Re-arrange all the intra-cluster ray powers in all the clusters together based on their delays. Determine the delay bin of final D-CIR and add up the intra-cluster ray powers if they fall into the same delay bin;
 - 9: Normalise all the delay bin powers and the final D-CIR obtained.
-

5.5.5 Channel Coefficients Generation Based on Non-Stationary Channel Model

The generation procedure is similar as that in the Subsection 5.5.4. However, in the *Step 2*, we use the log-normal distributed inter-cluster decay rate $\tilde{\Gamma}$ and normal

distributed FCPR \tilde{K}_{c1} . We rewrite (5.17) as

$$a_l'^2 = \begin{cases} 1, & l = 1, \\ \exp(-\tau_l/10^{\frac{\mu_\Gamma + \sigma_\Gamma}{10}})/10^{\frac{\mu_k + \sigma_k}{10}}, & l = 2, 3, \dots, L. \end{cases} \quad (5.21)$$

The rays in the first NLOS cluster are generated in the same way as those in other clusters.

5.5.5.1 Implementation Details Based on Non-Stationary Channel Model

The pseudo-code to generate the channel coefficients by NLOS state non-stationary model is generally the same as that in the Subsection 5.5.4.1, except two modifications:

- Modification 1: The FCPR and inter-cluster power decay rate should be generated randomly according to the corresponding distribution in the generation of every channel coefficient. The parameters to determine the distributions are fixed.
 - Modification 2: Substitute “LOS cluster” by “first NLOS cluster” in the pseudo-code.
-

5.6 Simulation and Validation of Stationary and Non-Stationary Models

In the studies of narrow-band channels by Markov states, the description of overall channel affect can be written in form of

$$\text{pdf}(h(t)) = \text{pdf}(h^{\text{LOS}}(t)) \times \pi_1 + \text{pdf}(\text{Null}) \times \pi_2 + \text{pdf}(h^{\text{NLOS}}(t)) \times \pi_3 \quad (5.22)$$

as that in [221]. Note that the notation of narrow-band channel is $h(t)$ instead of $h(\tau)$ since the channel affect is considered as powers presented by complex values along time axis t (no delay, because narrow-band channel can not distinguish the MPCs). However, in the study of wideband channels by Markov states, the channel affect is considered as an impulse response $h(\tau)$ (with delay) at one specific time (point) since the MPCs can be distinguished by delay bins. In this case, the overall channel affect can be written as (5.12). We need to study the Markov probability and each wideband channel model which representing the channel affect in each Markov state.

Since the Markov probability has been estimated from real measurement data in Section 5.4, we do not further discuss it. In this section, the focuses are the verification of stationary and non-stationary channel models. We directly simulate the models in the LOS case based on the parameters in Table 5.2 and those follow the normal/log-normal distributions. We compare the CDFs of RMS DSs estimated from the simulated D-CIRs and those estimated from the measured D-CIRs.

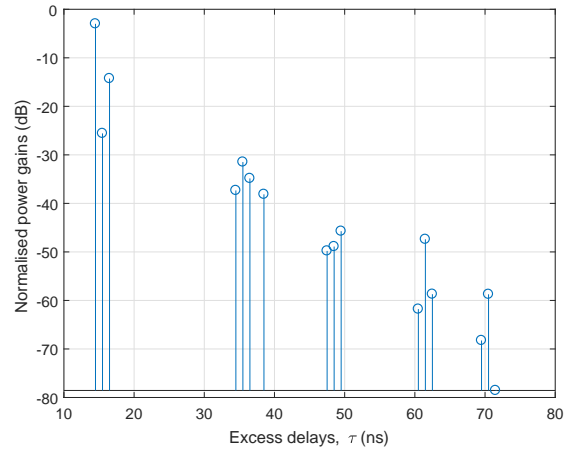
5.6.1 Verification of LOS State Stationary Model

We run the simulation of stationary channel model for 1000 times (more than the 340 measured D-CIRs in the LOS state, refer to Section 5.4.3). One simulated D-PDP is shown in Fig. 5.12a. The ϵ_{τ_1} is 5 ns. The comparison of the CDFs of RMS DSs between the simulated D-CIRs and the measured D-CIRs is shown in Fig. 5.12b. We can see that the statistics of simulated D-CIRs can fit the data.

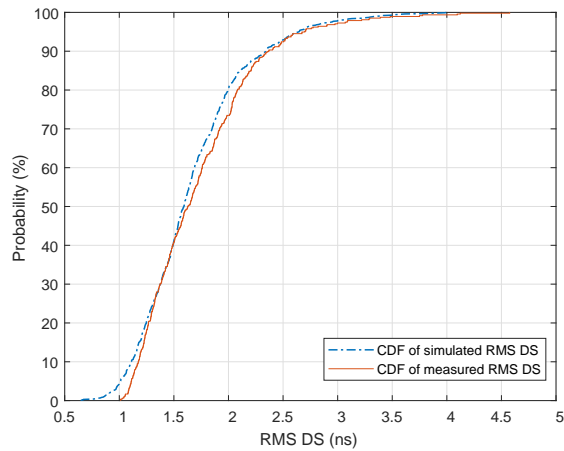
Note that the compensation of delay interval ϵ_{τ_1} in (5.16) is a very important factor in the data approximation shown in Fig. 5.12b.

5.6.2 Verification of NLOS State Non-Stationary Model

In each simulation run, we let the FCPR randomly generated according to the distribution, as well as the inter-cluster delay rate. One simulated D-PDP is shown in Fig. 5.13a. The ϵ_{τ_1} is -2 ns. We have run the simulation of non-stationary model



(a)



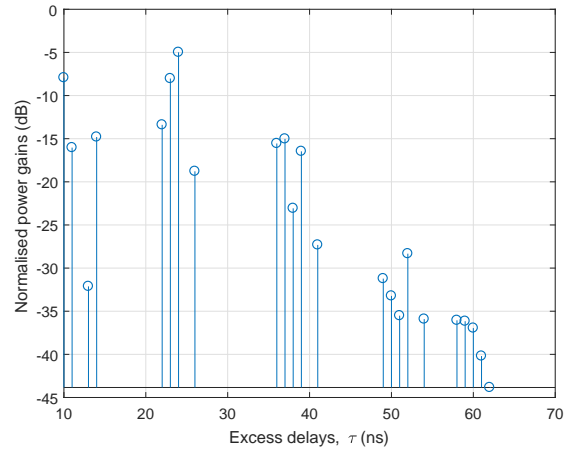
(b)

FIGURE 5.12: (a) One simulated LOS state D-PDP $h^{D,LOS}(\tau)$ and (b) the comparison of the CDFs of RMS DSs between the simulated D-CIRs and the measured D-CIRs, LOS state, LOS case

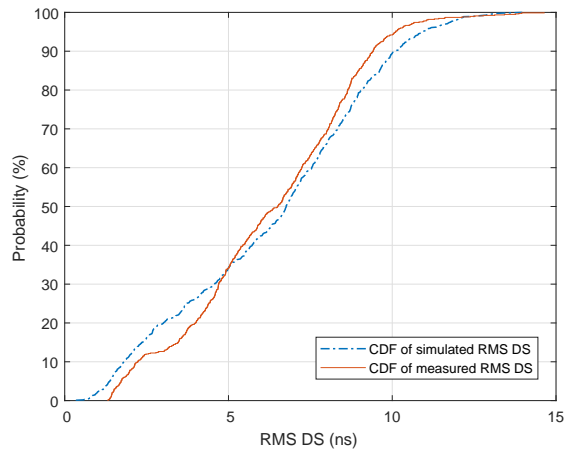
for 1000 times as well. The comparison of the CDFs of RMS DSs between the simulated D-CIRs and the measured D-CIRs is shown in Fig. 5.13b. We can see that the statistics of simulated D-CIRs can fit the data.

5.7 Summary

In this chapter, an A-APDP method based on both azimuth and elevation angles has been introduced to estimate the ASRs of channels. It has extended the former stationarity studies of channels from the time, frequency, and spatial domains to the



(a)



(b)

FIGURE 5.13: (a) One simulated NLOS state D-PDP $h^{\text{D,NLOS}}(\tau)$, and (b) the comparison of the CDFs of RMS DSs between the simulated D-CIRs and the measured D-CIRs, NLOS state, LOS case.

angular domain. In the data analysis of mmWave channel measurements, the S-ASRs, RMS DSs, K-factors, and PPGs based on the measured D-CIRs (in all azimuth and elevation angles) have been estimated. We have found three typical D-CIRs in the LOS case and two typical D-CIRs, as a subset of those three typical D-CIRs, in the NLOS case.

The LOS, NLOS, and outage Markov states have been defined based on those three typical D-CIRs and we have proposed a three-state Markov chain to model the directional mmWave channels. The one-step transition matrix and the limiting distribution

of Markov chain have been estimated based on the measurement data. We have developed the joint channel models based on the limiting distribution of Markov chain to simulate the instantaneous directional mmWave channels. A stationary channel model has been utilised to model the D-CIRs in the LOS state within one large S-ASR, a non-stationary channel model has been utilised to model the D-CIRs in the NLOS state over a few small S-ASRs, while the powers of D-CIRs in the outage state have been simply modelled as “zero”. We have simulated and verified the stationary and non-stationary channel models. The statistics of RMS DSs between the simulated D-CIRs and measured D-CIRs are well matched.

Chapter 6

Mobile-to-Mobile Directional MmWave Channels Based on A Novel Beamforming Scheme

6.1 Introduction

Beamforming technique is widely used in mmWave communication systems [55], and it is typical that both the Tx and Rx are casting beams to align with each other for transmitting information. If the Tx or Rx moves, the beams will be mis-aligned and the communication between Tx and Rx could be broken. There were studies about the impact of user mobility on mmWave communications in [138]. In previous chapters, the directional mmWave channels in the static environments were studied. For the Tx and Rx in motion scenarios, the mmWave technology is also widely adapted to greatly improve the data rate in the wireless communications. In this chapter, the studies of directional propagated mmWave channels when the Tx and Rx in motion is addressed.

To ensure the mmWave communications between the Tx and Rx in motion, a robust beam alignment scheme is required. The related state-of-the-art researches are mainly as follows: adaptive beamforming [61], [62], hybrid antenna array [63], two layers of

beam alignment [64], [65], beam switching [66], dual connectivity [67], beam training [68], intelligent beam search and tracking algorithms [69], etc.

6.1.1 Contributions

Those above mentioned schemes require the system level controls from protocol and application layers. They are relatively complicated to be implemented in the mobile to mobile (M2M) mmWave communication scenarios. In this chapter, we propose a simple physical layer double Gaussian beams (DGBs) scheme for M2M mmWave communications. It treats both the static and moving Tx and Rx scenarios in the same manner.

The rest of this chapter is organized as follows. Section 6.2 introduces the DGBs scheme. In Section 6.3, we model both the DGBs channels and measured mmWave channels by three Markov states. In Section 6.4, the connection ratios of three Markov states DGBs channels are estimated, and the connection ratios between the DGBs channels and measured mmWave channels are compared. Conclusions are finally drawn in Section 6.5.

6.2 Double Gaussian Beams Communication

In optical and visible light communication (VLC) [232]–[234], Tx transmits a Gaussian beam with a radiation pattern that gradually spreads as it propagates to further distance as shown in Fig. 6.1 [235]. In the figure, there is a beam from torch at upright corner. We call such beam as Gaussian beam because the transverse beam energy intensity is Gaussian distributed. Analogously, we can create a similar Gaussian beam with beamforming technology and use it to overcome the mis-alignment of Tx and Rx beams caused by the movement in mmWave communications.

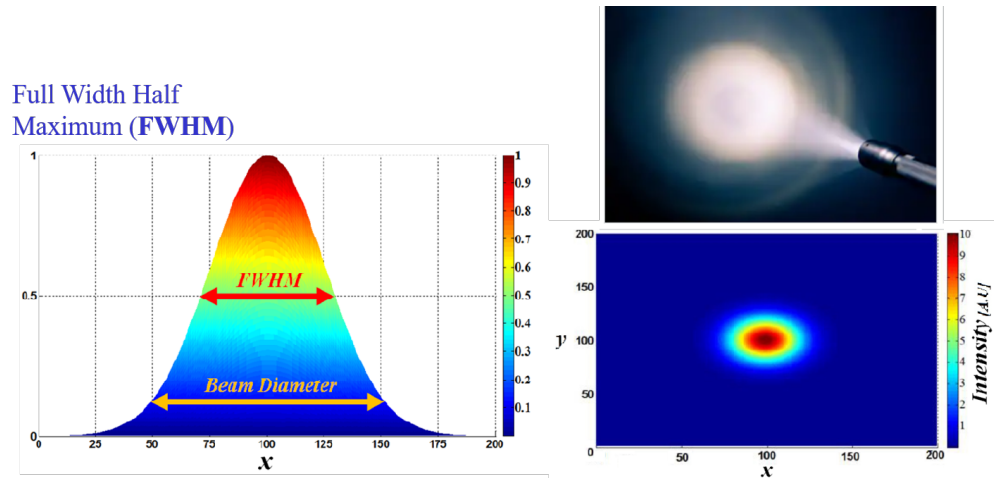


FIGURE 6.1: The transverse energy intensity of a beam follows Gaussian distribution. There is a torch at up-right corner, the transverse energy intensity at the down-right corner, and the transverse energy intensity profile at the left hand side.

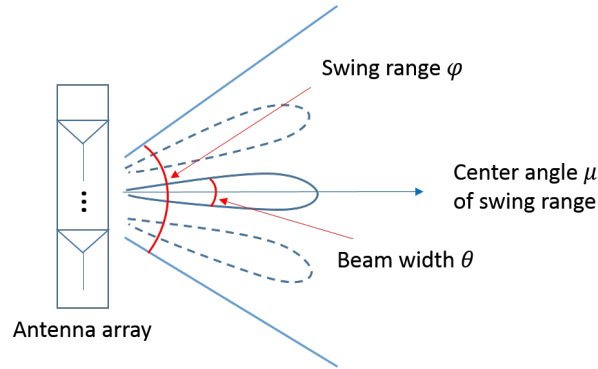


FIGURE 6.2: Construction of one Gaussian beam based on beamforming technology.

6.2.1 Gaussian Beam

Assume there is a radio system equipped with antenna arrays as in Fig. 6.2, and it uses beamforming technology during signal transmission/reception. We define a flashing rate γ as how many beams can be generated per second. All the generated beams have fixed beamwidth θ , and the pointing angles of them are limited within a swing range ψ ($\theta \ll \psi$). We assume μ is the centre angle of swing range and σ is the angular variation of the centre of beam. Statistically, the transverse power intensity in the swing range is Gaussian distributed $N(\mu, \sigma)$ along the propagation direction. The transverse energy intensity within such swing range is Gaussian distributed as that shown in Fig. 6.1. Based on [193], approximately 99.7 percent power lies within three standard deviations ($\mu \pm 3\sigma$) of the swing range, therefore, we define the relationship

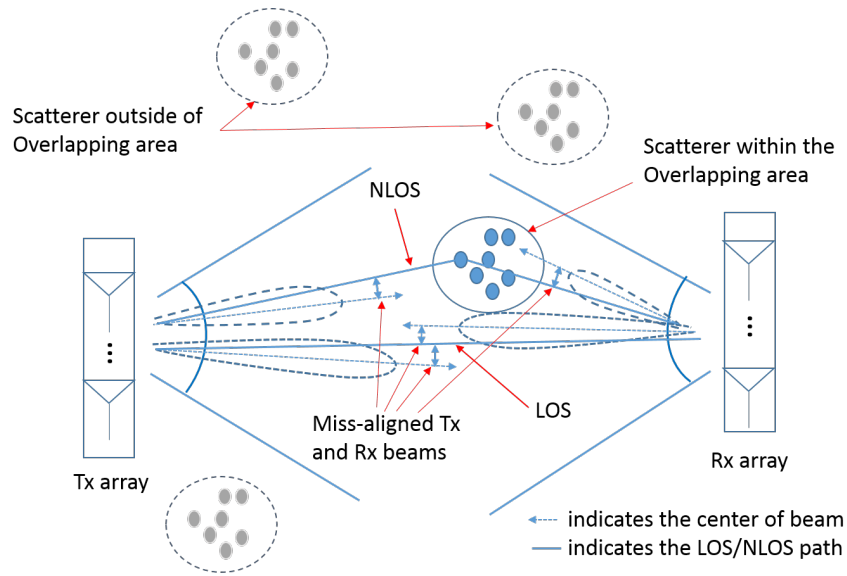


FIGURE 6.3: DGBs channels.

of ψ and σ as

$$\frac{\psi}{2} \approx +3\sigma \approx -3\sigma \text{ (i.e., } -3\sigma \leq \psi \leq +3\sigma \text{)}. \quad (6.1)$$

6.2.2 DGBs Communication Scheme

We apply the Gaussian beams to both Tx and Rx in channel scenario as in Fig 6.3. If we consider the instantaneous alignment of Tx and Rx beams as one connection, then, the communications between Tx and Rx are keeping connected and disconnected as long as there is an overlapping area of the Tx and Rx Gaussian beams. If the Tx and Rx can be connected (such as communicating with each other, transferring data, etc.) then we consider it a successful connection. We define a connecting ratio p as a metric to study the successful connections between the Tx and Rx.

$$p = \frac{\text{Successful connections per second}}{\gamma}. \quad (6.2)$$

The proposed communication scheme could be used for data packet transmissions as the Ethernet does. Each data packet is not guaranteed to be delivered to the receiver, but the Tx is trying the best to deliver them.

From implementing the DGBs scheme by hardware (printed circuit board and chips) point view, there are circuits connecting to each antenna element of an antenna array (beamforming technology requires antenna array). They are used to control the amplitude and the phase of signals feeding into antenna elements that generate the beams with beamwidth θ and make sure the pointing angles of them are limited within a swing range ψ . Based on that, it is possible to insert a high-speed radio frequency (RF) switch before the circuits connecting to the antenna elements. The switch is use for controlling flashing rate γ mentioned above. The speed of beam switching could be as short as a few nanoseconds [236], and the RF switches with such switching speed are widely used in the industry. In the rest of chapter, we assume that both Tx and Rx can generate 20 random beams per millisecond, i.e., $\gamma = 20,000$.

6.3 Markov States MmWave Channels

For the typical mmWave communications with beamforming technology, the directional wireless channels between Tx and Rx can be modelled by three Markov states. If the Tx and Rx beams are aligned with each other during communication, the channels can be considered in LOS state. When Tx/Rx moves or rotates, the beams become mis-aligned. If the communication could be maintained based on strong NLOS signals, the channels can be considered in NLOS state. Otherwise, it is in outage state. For the Rx side, the received D-CIRs $h^D(\tau)$ can be modelled as

$$h^D(\tau) = \begin{cases} h^{D,LOS}(\tau), & p_{LOS} \\ h^{D,NLOS}(\tau), & p_{NLOS} \\ \text{Null}, & 1 - p_{LOS} - p_{NLOS} \end{cases} \quad (6.3)$$

where $p_{[*]}$ is the percentage of D-CIRs in LOS state or NLOS state over the flash rate γ . The $h^{D,LOS}(\tau)$, $h^{D,NLOS}(\tau)$, and Null as the D-CIRs in LOS state, NLOS state, and outage states, respectively.

6.3.1 Three Markov States DGBs Channels

Assume that there is an object within the DGBs channel as in Fig. 6.3. The centre of this object is randomly located, and it is large enough to block the LOS path between Tx and Rx. In every instantaneous time, the Rx received D-CIR $h^D(\tau)$ falls into one of three Markov states. When the Tx and Rx beams are cast to each other directly within a tolerable mis-aligned angle, the DGBs channel is in LOS state. When the Tx and Rx all cast beams to the object within a tolerable mis-aligned angle and the scattered signals could maintain the communication between them, the DGBs channel is in NLOS state. In the cases that the object blocks the LOS path between the Tx and Rx and the angles of Tx and Rx beams are not inside of the tolerable mis-aligned angles, the DGBs channel is in the Outage state.

The one-step transition probabilities of Markov states are highly environmental dependent within the overlapping area. Due to the difficulty and high cost of implementing the DGBs scheme in the mmWave channel sounder, we are not able to perform the real measurement of a DGBs channel and estimated those parameters from the data at the moment (the channel measurement in the following subsection is not based on DGB scheme). However, compared with the high flashing rate of DGBs, we assume that the DGBs channel is stationary for a certain limited of time while the Tx and Rx move in relatively slow speed. We consider the limiting distribution of Markov states [193] in this case is related to p_{LOS} , p_{NLOS} , and $1 - p_{\text{LOS}} - p_{\text{NLOS}}$. The limiting distribution of Markov states is the key parameters to achieve the conclusion.

6.3.2 Channel Measurement and Three Markov States Measured Channels

The directional antennas were widely used in the mmWave channel measurements in the literature [81], [131], [161]. In this section, we choose one relatively simple and typical mmWave channel measurement mentioned as an example, and model the measured directional mmWave channels by three Markov states.

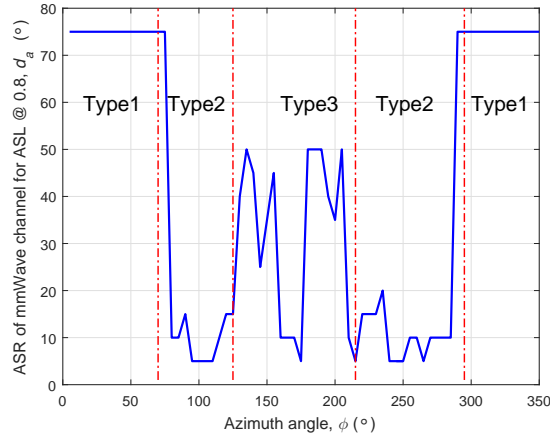


FIGURE 6.4: Estimated ASRs of mmWave channel from D-CIRs in different azimuth angles, ASL is 0.8.

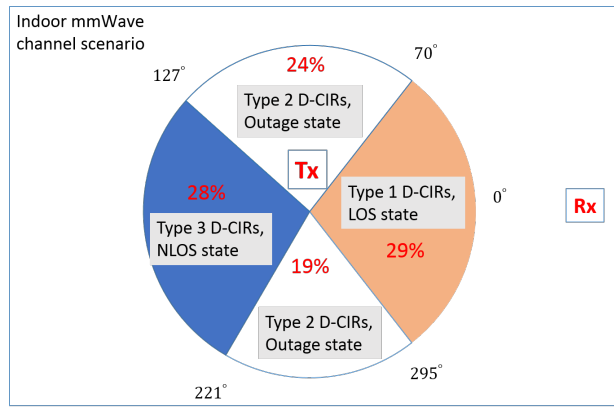


FIGURE 6.5: Angular separated three typical D-CIRs in three Markov states (Tx rotates and Rx hold still).

We still use the data from the mmWave channel measurements described in Section 4.2.2 of last chapter. For the conciseness purposes, we do not repeat the details. However, we only use the data in the azimuth plane with 90° elevation angle.

6.3.2.1 Three Markov States Measured Channels

In the data analysis, the estimated ASRs of the channel in the azimuth plane with 90° elevation angle, root mean square (RMS) delay spreads (DSs), K-factors, and three types of measured D-CIRs are the same as the Fig. 4.3b, Fig. 4.4a, Fig. 4.4b, and Fig. 4.6 in Section 4.2.3. We separate the D-CIRs based on three Markov states based

on the estimated ASRs as in Fig. 6.4. We can read the angular range of those three typical D-CIRs as (also in [70]):

- Type 1: D-CIRs measured at the azimuth angles smaller than 70° and larger than 295°
- Type 2: D-CIRs measured at the azimuth angles between 70° and 125° & between 215° and 295°
- Type 3: D-CIRs measured at the azimuth angles between 125° and 215°

We also consider those three typical D-CIRs as three Markov states as defined in Section 5.4.1. We consider the D-CIRs contain one strong LOS component and a few weak NLOS components are in the LOS state; those containing one relatively strong NLOS component and a few weak NLOS components are in the NLOS state; and those containing only weak NLOS components are in the Outage state. Fig. 6.5 shows both the locations and percentage of angular coverage areas of those three typical D-CIRs in each Markov state. They are: 29% in LOS state, 28% in NLOS state, and 43% in Outage state.

Note that the separation of three typical D-CIRs is not the same as those in Section 4.2.3 and Section 5.3.3 in last two Chapters that were based on PPG levels. It is due to history reasons of paper publication time chronologically. This also implies that there is no uniform verdict on how to determine three typical D-CIRs in the literature. It can depend on the situation of individual channel environment and personal judgement on the data.

6.4 Study and Comparison of Connection Ratios

The static and moving Tx/Rx scenarios are treated in the same manner as in DGBs scheme. For less confusing, we consider the Tx and Rx that are facing each other precisely in Fig. 6.6 as located case, and consider the Tx and Rx that are not facing

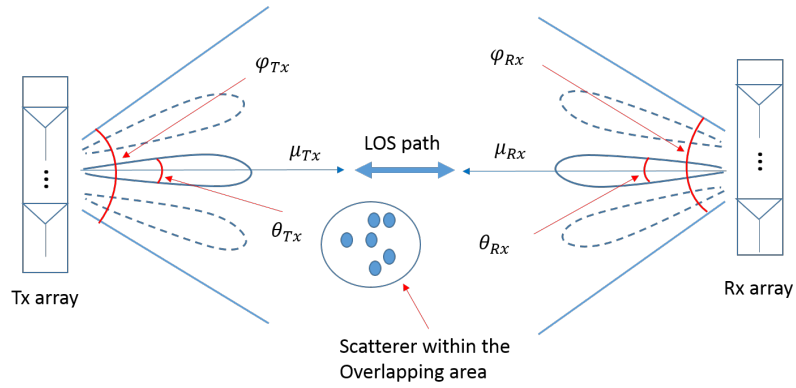


FIGURE 6.6: DGBs channels in the located case.

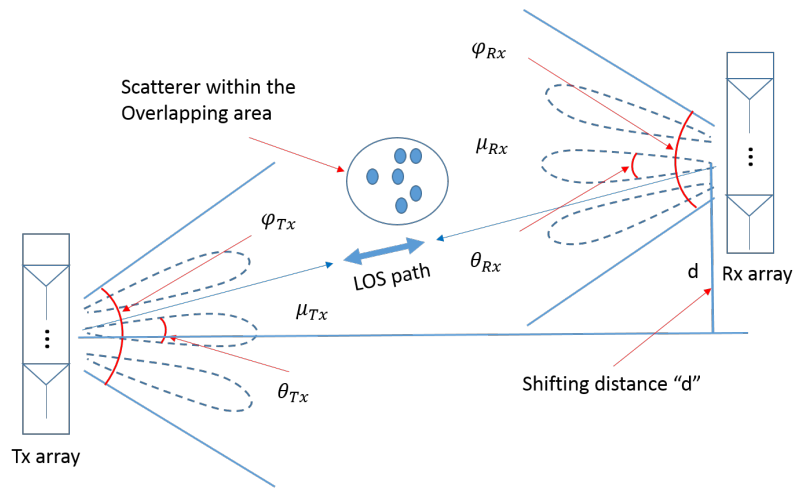


FIGURE 6.7: DGBs channels in the dislocated case (shifting distance is d).

each other precisely with a shifting distance in Fig. 6.7 as dislocated case. We assume those located and dislocate cases are independent of the movements of Tx and Rx.

The studies of DGBs channels are based on simulations in this chapter. However, we compare the connection ratios of DGBs channels with those estimated from the real mmWave channel measurement described previously.

6.4.1 Connection Ratios of Markov States DGBs Channels

LOS probability is one of the components in WINNER models [92] and other standard channel models. It estimates the probability that the communication between Tx and Rx is in the best situation which is based on the LOS path of channels. Similar idea

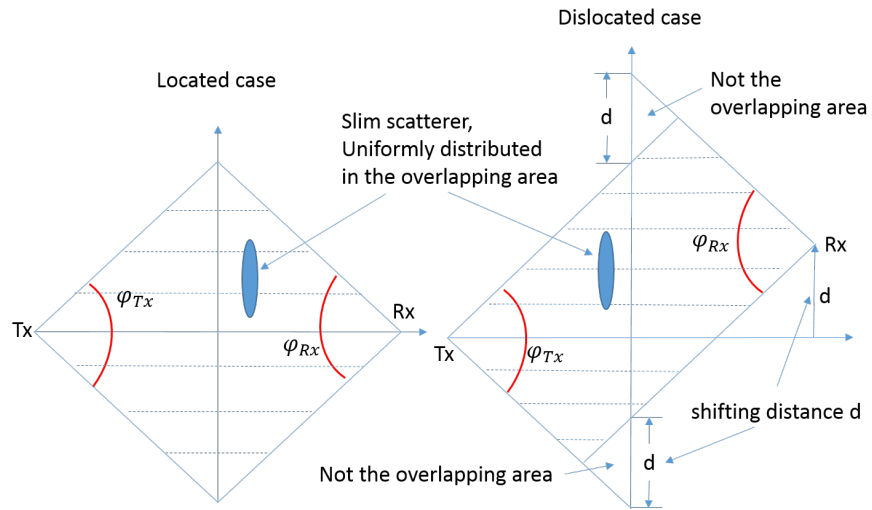


FIGURE 6.8: The DGBs overlapping area for both the located and dislocated cases.

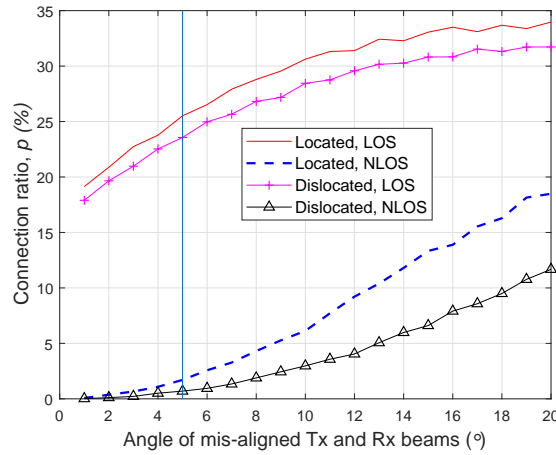


FIGURE 6.9: Synchronised DGBs channels (swing ranges $\psi_{Tx} = \psi_{Rx} = 60^\circ$, length of vertical positioned slim object is 1 m, distance between Tx and Rx is 10 m, and the shifting distance d is 2 m for the dislocated case).

can be used to check the probabilities of the directional mmWave channels in each Markov state.

6.4.1.1 Synchronised DGBs Channels

We assume that the Tx and Rx are casting γ beams per second to each other, and the timings of casting each simultaneous beam at both Tx and Rx sides are synchronised. In the simulation, we let the distance between the Tx and Rx is 10 m; the swing ranges of Tx and Rx Gaussian beams, ψ_{Tx} and ψ_{Rx} , are both 60° ; the variation of centre of

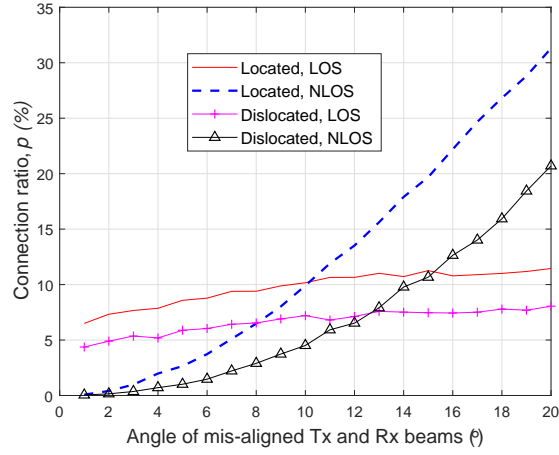


FIGURE 6.10: Synchronised DGBs channels (swing ranges $\psi_{Tx} = \psi_{Rx} = 60^\circ$, length of vertical positioned slim object is 3 m, distance between Tx and Rx is 10 m, and the shifting distance d is 2 m for the dislocated case).

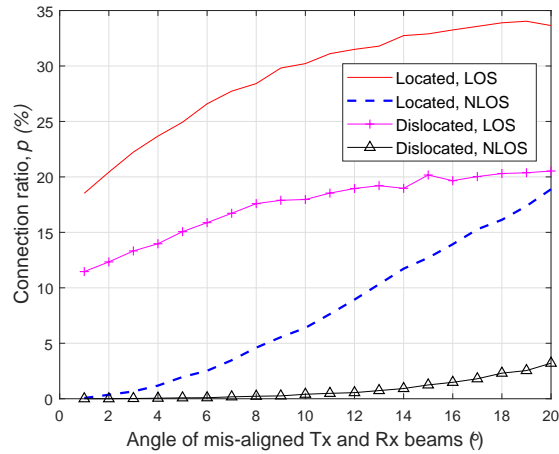


FIGURE 6.11: Synchronised DGBs channels (swing ranges $\psi_{Tx} = \psi_{Rx} = 60^\circ$, length of vertical positioned slim object is 1 m, distance between Tx and Rx is 10 m, and the shifting distance d is 4 m for the dislocated case).

Gaussian beam σ is 10° at both the Tx and Rx side; and the shifting distance d is 2 m for the dislocated case. We also assume that the object is slim, its width could be ignored and its length is 1 m (about 8.7% size of DGBs channel area in y -axis), which is long enough to block the LOS path between Tx and Rx. We position it vertically in the DGBs overlapping area as in Fig. 6.8 following the uniform distribution.

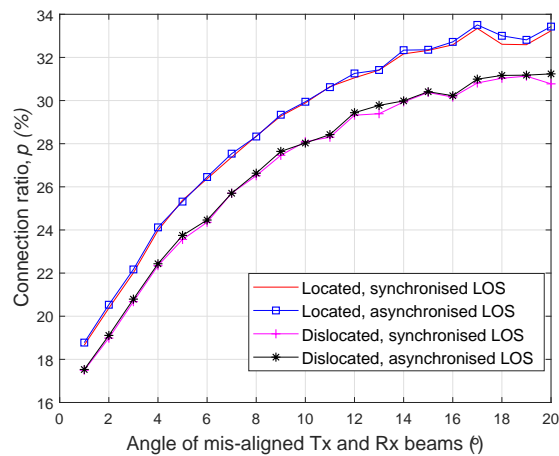
Note that we do not consider the beamwidths of Tx and Rx beams, θ_{Tx} and θ_{Rx} , in the simulation. Instead, we assume that the beamwidths are always suitable to obtain the simulation results (always be two times of each angle of mis-aligned beams for

example). We do not consider the frequencies of mmWave signals in the simulations neither. We let the distance between Tx and Rx is 10 m simply due to the high attenuation of mmWave signals.

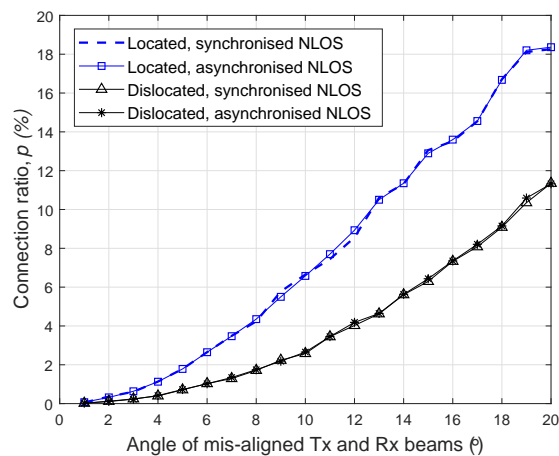
Fig. 6.9 shows the connection ratios of DGBs channels in LOS and NLOS Markov states vs. the angles of mis-aligned Tx and Rx beams from 1° to 20° . We can see that for both the located and dislocated cases, as we increase the angle of mis-aligned Tx and Rx beams, the connection ratios of both LOS and NLOS states become higher. The connection ratios of LOS states in the located case are from 18.92% to 33.79%, and are from 17.93% to 31.74% in the dislocated case with the shifting distance $d = 2$ m. The connection ratios of NLOS states in the located case are from 0.025% to 18.83%, and are from 0.025% to 11.7% in the dislocated case.

In Fig. 6.10, we increase the length of vertical positioned slim object to 3 m, and keep other settings as in Fig. 6.9. We can observe that for both the located and dislocated cases, the LOS state connection ratios decrease while the NLOS state connection ratios increase. It makes sense that as the length of slim objects increases, the chance that the LOS paths between the Tx and Rx are blocked increases, while the chance that the communication between Tx and Rx could be maintained based on the signals that are scattered by the slim object increases.

In Fig. 6.11, we let the shifting distance d be 4 m, and keep other settings the same as in Fig. 6.9. We can observe that the connection ratios of both LOS and NLOS states in the dislocated case decrease compared with those in Fig. 6.9. The reason is that when the shifting distance d increases, the size of DGBs overlapping area decreases, so as the connection ratios of DGBs channels in both LOS and NLOS states. We have found similar phenomena in the simulations with different swing ranges (120° and 60°), different distances between the Tx and Rx, and different lengths of the slim object. As the DGBs overlapping area decreases, the connection ratios of DGBs channels decrease accordingly.



(a)



(b)

FIGURE 6.12: Both synchronised and asynchronous DGBs channels (swing range $\psi_{Tx} = \psi_{Rx} = 60^\circ$, length of vertical positioned slim object is 1m, distance between Tx and Rx is 10 m, and the shifting distance d is 2 m for the dislocated case): (a) LOS states, and (b) NLOS states.

6.4.1.2 Asynchronised DGBs Channels

We assume that the Tx and Rx lost the synchronisation of timing to cast each simultaneous beam. We let the Tx casts each simultaneous beam earlier than Rx does (vice versa) with the time difference of 50% beam duration. We count the overall duration of connections in LOS or NLOS state over one second as connection ratio. From the results in Fig. 6.12, we can see that the synchronised and asynchronous connection ratios of LOS and NLOS states in both located and dislocated cases are almost the same. If we change the time difference to other values (time difference of 80% beam

duration, etc.), the connection ratios in asynchronous DGBs channels are also very close to those in synchronous DGBs channels. This indicates that the synchronisation of instantaneous Tx and Rx beams has no significant impact on the connection ratios of DGBs channels. The performance of DGBs scheme is very stable and it is possible to predict the connection ratio based on the size of overlapping area.

6.4.2 Connection Ratios of Markov States Measured mm-Wave Channels

In Section 6.3.2, we have estimated the percentage of angular coverage areas of three typical D-CIRs in each Markov state. If we consider the channel measurement as an unchanged environment, and the base station is kept casting one stable beam to the users without changing the beam angle. Then, we can assume that if one person is randomly walking in such a channel environment, she/he can connect to the base station when she/he is walking inside of the angular coverage areas of LOS and NLOS states. In this case, the percentages of angular coverage areas of Markov states can be considered as the limiting distribution of Markov states, which are also the connection ratios of directional mmWave channels in those Markov states. They are: 29% for the connection ratio of LOS state, 28% for the connection ratio of NLOS state, and 43% for the connection ratio of Outage state.

6.4.3 Comparison of Connection Ratios

Assume the beamwidths of Tx and Rx beams, θ_{Tx} and θ_{Rx} , used in DGBs communications are 10° , which are the same as those of the horn antennas used in the aforementioned channel measurement. In order to keep the connection between Tx and Rx in “good situation”, we let the aligned Tx and Rx beams are at least 50% overlapped in term of (-3 dB) beamwidth. Therefore, the mis-aligned angle of Tx and Rx beams should be limited to 5° , and we can find the corresponding connection ratios from Fig. 6.9. In the located case, the connection ratio of LOS state is 25.48%, and

the connection ratio of NLOS state is 1.66%. In the dislocated case, the connection ratio of LOS state is 23.65%, and the connection ratio of NLOS state is 0.84%.

Compared with the LOS state connection ratios estimated based on the channel measurement, the LOS state connection ratio of DGBs channels in the located case is 3.52% lower, and in the dislocated case, it is 5.35% lower. However, the NLOS state connection ratios of DGBs channels in both the located and dislocated cases are much lower compared with those estimated from the channel measurement. Because the NLOS state connection ratios are highly environment dependent, and the simulation assumption of DGBs channel is quite different from that in the measured channel (the objects, such as walls, ceiling, windows, and doors, etc., are all scatterers). According to the analysis in Section 6.4.1.1, if we can keep the overlapping area of DGBs channel as large as possible, the acceptable connection ratios as in Fig. 6.9 can be achieved in M2M mmWave communication under DGBs scheme.

6.5 Summary

We have proposed a simple DGBs scheme based on beamforming technology for M2M mmWave communications in this chapter. The Markov states have been utilised to model the DGBs channels, and to model the measured directional mmWave channels in an office environment for comparison purpose. The connection ratio of Markov state has been considered as the metric to study the performance of DGBs scheme from the channel point of view. It has shown that the DGBs channels have very similar LOS state connection ratios compared with those of the measured mmWave channels based on using the beams with 10° beamwidth. But the NLOS state connection ratios of DGBs channels are much lower, which is related to the environmental differences between the simulation assumption of DGBs channels and the measured mmWave channel. We have found that when the Tx and Rx are in the dislocated case, the connection ratios of both LOS and NLOS states decrease as the size of DGBs overlapping area decreases. We have also found that the synchronisation of Tx and Rx beams has no significant impact on the connection ratios of DGBs channels.

DGBs scheme is considered as a physical layer beam alignment technique. We expect that it requires less system level controls from the protocol and application layers. It is suitable for the communication scenarios that the Tx and Rx are moving all the time. It is also suitable for the mmWave communications at initiation stage, when the Tx and Rx have no knowledge of system configuration on the other side.

Conclusions and Future Work

7.1 Summary of Results

This thesis has presented a wealth of comprehensive research on wireless channel modelling and simulation for mmWave communication systems (i.e., a FnS channel model in Chapter 3, directional mmWave channel models in Chapter 4 and Chapter 5, and a novel beamforming scheme for mobile-to-mobile millimetre wave communications in Chapter 6). The importance of our research has been introduced and proved in detail. In this chapter, the key findings of my Ph.D. researches are summarized and several potential future research directions are proposed.

7.1.1 Frequency Non-Stationary MmWave Channel Models

The very broad bandwidth resource is the key merit of using mmWave communication. The absolute bandwidths of the mmWave channels are comparable to those of the UWB channels. The UWB channels are generally considered as FnS channels, within its bandwidth the estimated channel characteristics vary along with frequencies. Since the bandwidths of mmWave channels are comparable to those of UWB channels, the channel characteristics within the bandwidths of mmWave channels may vary along with frequencies as well. Therefore, the studies of frequency non-stationarity of

mmWave channels are needed. In order to improve the standard channel model, such as 3GPP model, the re-study of stationarity of mmWave channels is fundamental. We have introduced an APDP method to determine the stationarity regions of channels in the time, frequency, and spatial domains. We have used this method in the data analysis of channel measurements in a sub-6 GHz frequency band 2–4 GHz and two mmWave frequency bands 14–16 GHz and 28–30 GHz. The frequency non-stationarity of channels with very broad bandwidth (2 GHz in the measurement data) has been found in the data analysis. We have shown the FnS properties of channels in all the measured frequency bands.

UWB channel model [186], [202] is not similar to 3GPP model [95]. The methodology is totally different and it does not based on the estimation of FSRs. A FnS fading channel model that is similar to 3GPP model has been proposed in this thesis. It is suitable to model the channels in both the sub-6 GHz and mmWave frequency bands. In this model, the FnS channel is split into a few FS sub-band channels, modelled one by one, and combined as one FnS channel again. The cluster evolution in the frequency domain is the key to implement this model (if there are many sub-band channels) and it also ensures the frequency consistency of simulated sub-band channels. We have shown that the proposed channel model can well fit the measurement data. We suggest considering the proposed FnS channel model as an additional component of standard channel models, such as 3GPP, METIS, mMAGIC, etc.

7.1.2 Directional MmWave Channel Models

Directional propagation is another feature of mmWave, which due to using beamforming technology to obtain high gain to compensate for the high attenuation of mmWave signals. In the mmWave channel measurements, the rotating Tx/Rx beam based on horn antenna or beamforming technology is widely used. In this case, the statistics of obtained D-CIRs in different angles can be dramatically different due to the inhomogeneity of channel environment in different directions. Similarly, the re-study of stationarity of mmWave channels is fundamental. Based on the feature of directional

propagation of mmWave channels, the stationarity of channels in the angular domain is the focus. In Chapter 4 and 5, an A-APDP method has been developed as the metric to estimate the planar-ASR and spherical-ASR of directional mmWave channels (and measured D-CIRs in different angles). Then two directional models are proposed based on the three typical measured D-CIRs that are found in the data analysis.

In Chapter 4, we split small-scale omni-directional wireless channel into a few DCs based on the beamwidth of the Tx/Rx beams used in the measurement, and we have classified the DCs as LOS, NLOS, and outage classes to reduce the workload of modelling a large number of DCs. A modified SV model has been used to model the DCs in each class. The cluster evolution in the angular domain has been applied to correlate the consecutive DCs and to ensure the consistency of them. In the end, the omni-directional mmWave channel has been synthesised based on the generated DCs along with 360° azimuth angles. This model uses an inverted approach in the modelling of directional mmWave channels than those used in the standard channel models (modelling the omni-directional channel first, then acquiring the directional channels by adding antenna patterns at both Tx and Rx). We have shown that the simulation results can fit well the spatial correlation of measured directional mmWave channels and the statistical DSs. We have also shown that the simulation of omni-directional channel can also fit the measurement data. The accuracy of both the simulated directional mmWave channels and omni-directional channels can be maintained compared with measurement data. We can consider the proposed omni-directional channel model as an alternative of modelling the mmWave channels.

In Chapter 5, another model based on Markov chain has been proposed to model the instantaneous directional mmWave channels between Tx and Rx. The measured D-CIRs have been separated into three Markov states, i.e., LOS, NLOS, and outage states according to those three typical measured D-CIRs found in the data analysis. We have assigned modified SV-models to each of Markov states and joint channel models have been developed to simulate the instantaneous directional mmWave channels based on the estimated limiting distribution of Markov chain from the measurement data. The models do not include the angle information of each directional mmWave

channel (neither the property of omni-directional mmWave channel), they are much less complicated compared with those standard channel models. We have shown that both the proposed stationary and non-stationary channel models used to model the directional channels in LOS and NLOS Markov state, respectively, can well fit the data. However, we estimated the limiting distributions of Markov states from the data. We found that they are consistent with the ratio of that the number of D-CIRs in each state over the total number of measured D-CIRs. We suggest to consider the joint channel models as an alternative of mmWave channel modelling method in the system-level simulations, where the overall performance during a certain time period need to be estimated and the angular information of each directional mmWave channel does not significantly affect the simulation results. For example, the mobile-type mmWave channels according to different beam alignment schemes in Chapter 6.

7.1.3 A Novel Beamforming Scheme for Mobile-to-Mobile Millimetre Wave Communications

Due to using beamforming technology in both Tx and Rx for mmWave communications, a robust beam alignment scheme is required in mmWave communications in order to support the mobile Tx/Rx situations.

In Chapter 6, a simple DGBs scheme based on beamforming technology for M2M mmWave communications has been proposed. It treats both the stationary Tx/Rx and moving Tx/Rx scenarios in the same manner. The Markov states have been utilised to model the DGBs channels and the connection ratio of each Markov state is considered as the metric to study the channel behaviour when the DGBs scheme is applied. We have shown that the simulation results of connection ratios are acceptable compared with the angular coverage of D-CIRs in LOS, NLOS, and Outage states of a real measurement channel (analogous to the connection ratios). We expect that the DGBs scheme requires less system level controls from the protocol and application layers. It is suitable for the communication scenarios that the Tx and Rx are moving

all the time. It is also suitable for the mmWave communications at initiation stage when the Tx and Rx have no knowledge of system configuration from each other.

7.2 Future Research Directions

The models proposed in this thesis are based on the channel measurements in the static channel environments. Therefore, the mechanisms used in those models only focus on the time-invariant channels. For time-variant channels, we can consider it consists of a few snapshots and each snapshot is one time-invariant channel. Then we can apply the proposed models in this thesis snapshot by snapshot and combine the results. This can be considered as further research directions.

Apart from that, there are still several potential research directions based on the current development of models as follows:

7.2.1 Frequency non-Stationarity and Consistency of 5G Wireless Channels

Modification of 3GPP NR model

- In the current 3GPP NR channel model [95], the mmWave channels are all considered as FS channels at the moment. Since the very broad bandwidth is the main feature of mmWave channels and the frequency non-stationarity can be found based on the channel measurement data. The modification of 3GPP NR model is required to support the FnS properties of mmWave channels. The FnS model proposed in Chapter 3 can be modified and adapted as an additional component for 3GPP NR model.

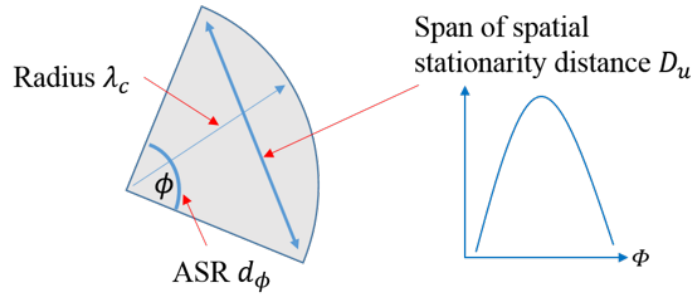


FIGURE 7.1: Directional dependent stationary distance for mmWave channels.

Frequency Consistency of Wireless Channels in Different Frequency Ranges

- The modelling and simulation of mmWave channels should be consistent in different scenarios/applications as well as in different frequency ranges. There is one application used in mmWave communication: dual connectivity, where Tx is using the frequencies below 6 GHz (3G/4G technologies) to establish the connection with Rx (allocate Rx), then, it transmits data to Rx in mmWave frequencies. In such scenario, the cluster evolution in the frequency domain can be used to model the channels in different frequency ranges, i.e., jumping between sub-6GHz and mmWave frequencies. It ensures the consistency of the same channel (same scenario) in different frequency ranges.

7.2.2 Modelling Directional MmWave Channels

Modelling Directional MmWave Channels by Cluster Evolution in Angular Domain

- After developing the joint channel models, the stationary and non-stationary models can be introduced in the modelling of DCs based on the cluster evolution in the angular domain as well. This could increase the accuracy of generating directional mmWave channels along with 360° azimuth angles as well as the accuracy of synthesized omni-directional channel.
- The spatial stationarity regions of channels may relate to the ASRs. We have calculated the spatial stationarity regions by trigonometric functions based on

ASRs, and the stationary distance can be directional dependent as Fig. 7.1. However, we can not fully study it within the limit of thesis and the limited measurement data. More channel measurements (e.g., directional mmWave channels between Tx and Rx in different positions in the channel environment) are required and the further studies of ASRs and spatial stationarity regions of the channels are needed.

Modelling Directional MmWave Channels by Markov States/Markov Chain

- Estimating the properties of mmWave mobile-type channels according to different beam alignment schemes are difficult. In this case, the joint channel models can be more tangible than other models in which the angular information of directional channel is an important factor in the modelling the mmWave channels. The complexity in the analysis of different mobile-type mmWave channels according to different beam alignment schemes can greatly reduced.
- At moment, we have only proposed to use homogeneous Markov chain in the modelling of indoor static environment. The statistical parameters used in the description of Markov chain, e.g., the limiting distribution, are fixed values. However, for the time-variant channel scenarios, the description of Markov chain can be time/spacial dependent. In this case, we can use inhomogeneous Markov chain to model the time-variant scenarios. This maybe less complex than the formerly mentioned approach that splitting the time-variant scenario to a few time-invariant snapshots, then use the proposed Markov chain and joint channel models to model the channel snapshot by snapshot.
- The study of large scale parameters is required in order to verify the overall performance if $h^D(\tau)$ in (5.12) according to Section 5.5.1. Further studies need to be done and the higher layer performance based on $h^D(\tau)$ need to be verified from the comparison between the simulation and measurement data.
- Instead of using the modified SV channel models proposed in this thesis to model the D-CIRs in different Markov states, we can consider using correlation-based

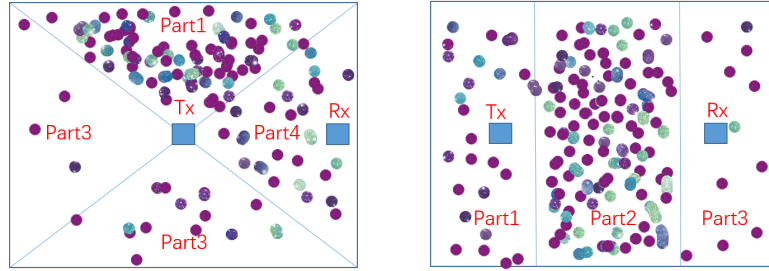


FIGURE 7.2: Split the channel environment into parts.

models (CBMs) to further lower the complexity of system level simulations. For example, the model for LOS state can be considered as AWGN model and the model for NLOS state can be modified according to the correlation-based double-directional stochastic channel model in [237], [238].

Modification of 3GPP NR model¹

- In the current 3GPP NR channel model [95], the parameters used in the system-level simulation of the whole channel is fixed, which does not reflect the variation of the channel properties in different directions/angles, the channel environments are considered homogeneous. In the study of ASRs based on the measurement data, the inhomogeneity of the channel environment is revealed and it is more realistic if the channel environments are considered inhomogeneous. In order to mimic the inhomogeneous channel environment in 3GPP fast fading model, we can split the whole (omni-directional) channel into parts (3-5 parts for the indoor environment, for examples) in the angular/spatial domain, Fig. 7.2. We can generate cluster-map of each part separately by using slightly different statistical parameters (reflect different channel properties in different parts). Then, we combine the cluster map generated in each part as the overall cluster map of the environments. After that, the rest of procedure in generating channel coefficients is the same as those in 3GPP NR. With such modification, the properties of generated D-CIRs by system-level model can be angular dependent.

¹Note that the modification of 3GPP model with the concern of inhomogeneous environment is cooperated with Nokia Networks in Oulu Finland. The contact person in Nokia: Kinnunen, Pasi Et. (Nokia - FI/Oulu), pasi.et.kinnunen@nokia-bell-labs.com

7.2.3 Double Gaussian Beams MmWave Communication Scheme

- This work needs to be continued. The overall duration/time of connected Tx and Rx per second need to be studied when the Gaussian beams of Tx and Rx are not asynchronised.
- The DGBs scheme needs to be realised in practical M2M mmWave communications by designing the related protocol layer tracking algorithm and the corresponding Tx and Rx hardware. The performance of DGBs scheme applied in the M2M mmWave communication in system level need to be verified by real measurement data.

Appendix A

Usage of Stationarity Regions of Wireless Channels

A.1 Data of Measured Channels Over a Few Stationarity Regions

Fig. A.1 is an example of channel measurements and parameters estimations based on a time-variant scenario. On the left-hand side, there is a car moving in one channel environment. The Tx is the tower and it is keeping sending the sounding signals to the Rx, the car. While the car in two different positions, it measures the channel and the CIRs obtained are $h(t_1, \tau)$ and $h(t_2, \tau)$, which can be considered as two different snapshots of the channel.

Assume the two snapshots are in different stationarity regions (either in two temporal stationarity regions or two spatial stationarity regions), the estimated statistical properties of channels within that two snapshots can be quite different.

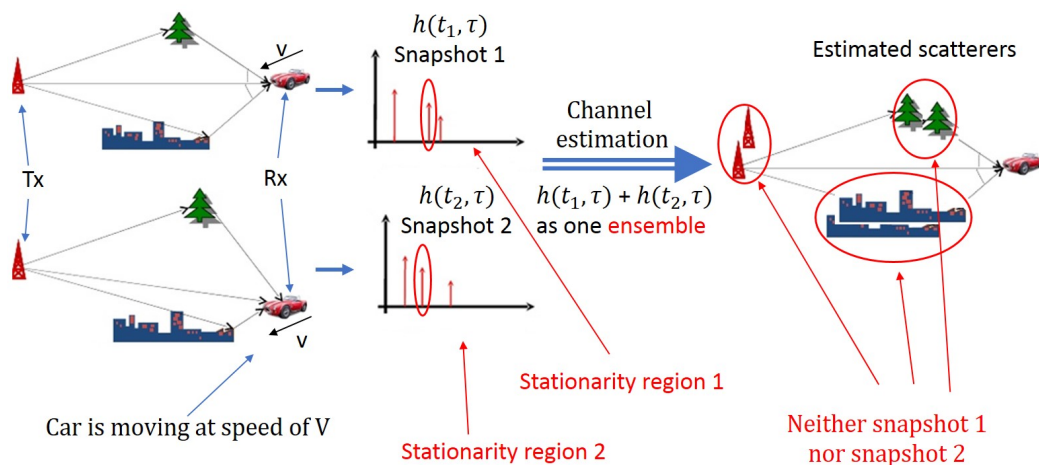


FIGURE A.1: The distorted estimation of channel.

A.2 Only Use Data Within One Stationarity Region

If we do not have the knowledge of the size of stationarity regions and we estimate the statistical parameters of channel based on the data of two snapshots, then the estimated parameters are not correct. Because such estimation mixes the data from two stationarity regions, the estimated results can neither reflect the real property of channel in the first snapshot nor that in the second snapshot. For example, the estimated objects in the right-hand side of Fig. A.1, which is not exact snapshot1, neither snapshot2.

Therefore, we should only use the data within one stationarity region (highly similarity of data) in the channel parameter estimation, or the estimated results will be distorted and blurred.

A.3 Stationarity in the time, frequency, spatial, and angular domains

In this thesis, the stationarity studies of mmWave channels relate to that in the frequency and angular domains. The overview stationarities of mmWave channel

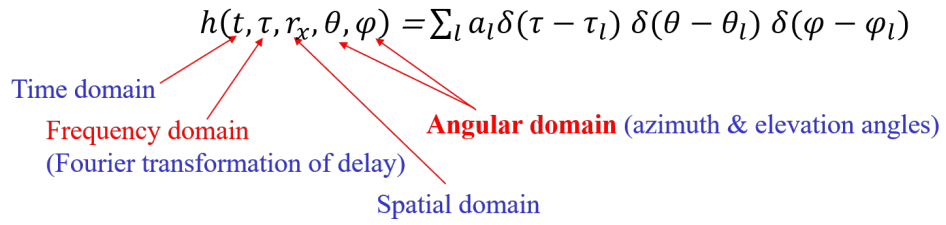


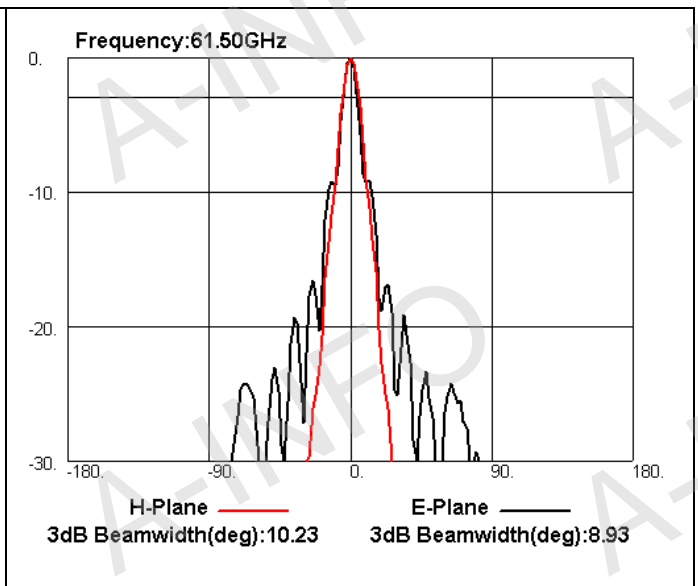
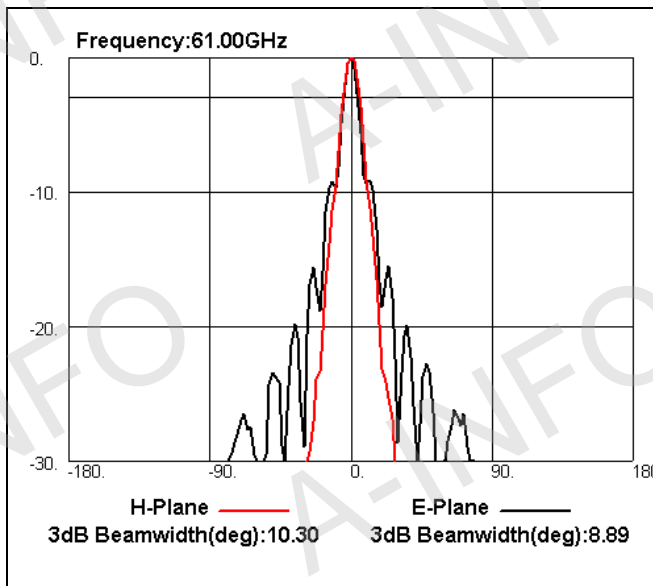
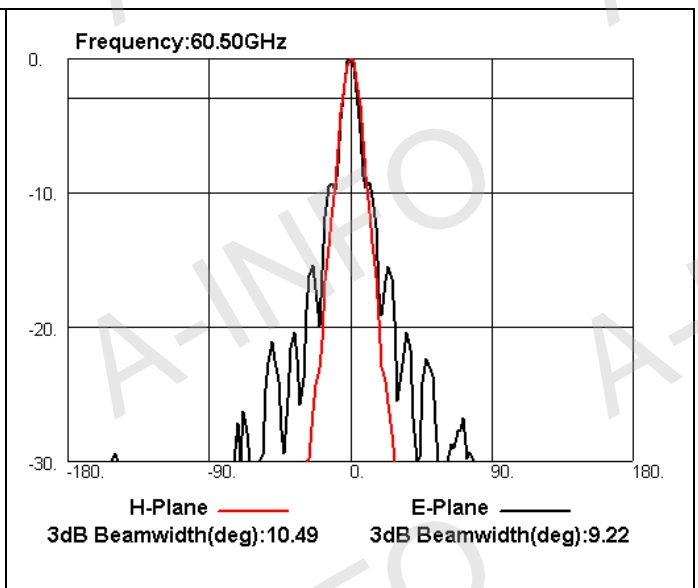
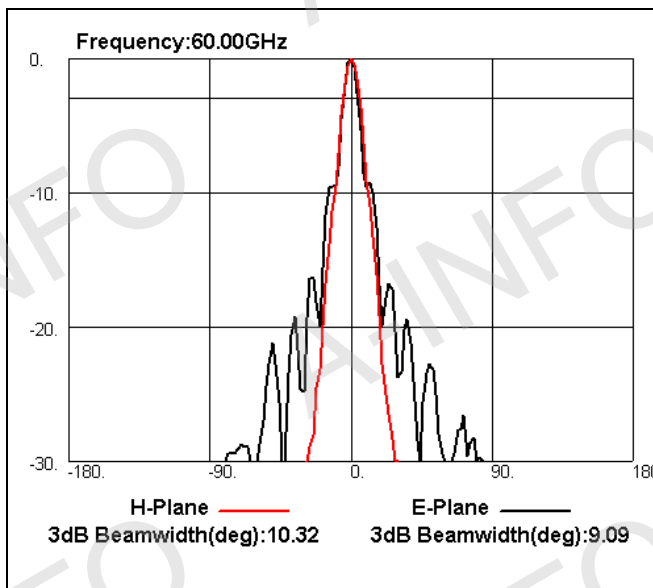
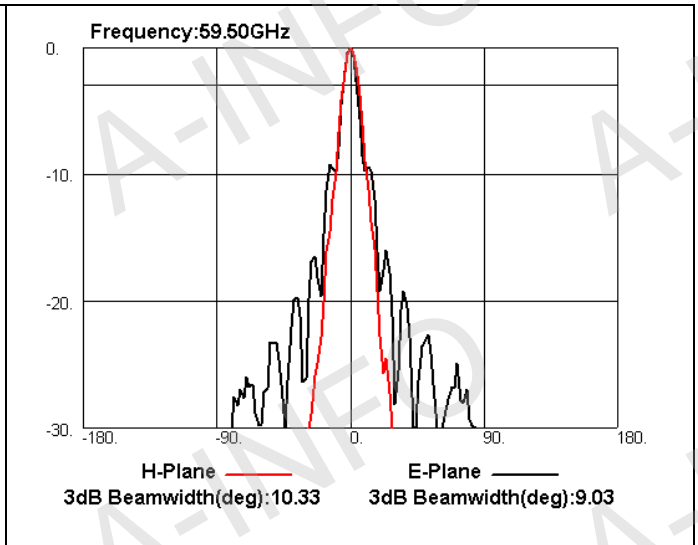
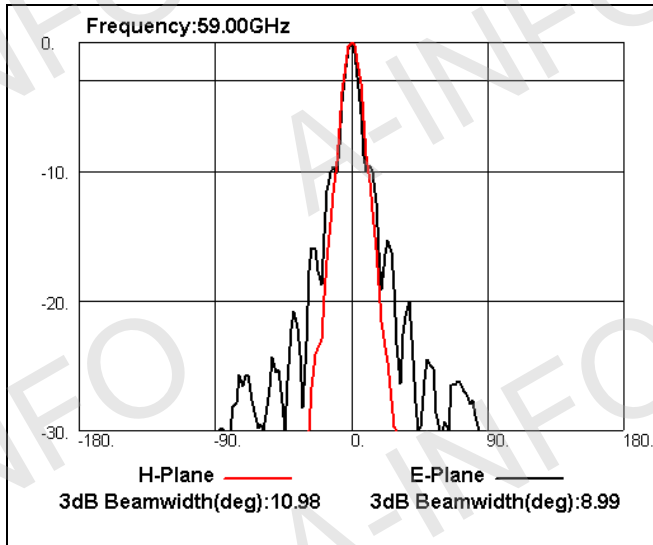
FIGURE A.2: Stationarity studies of mmWave channels.

modelling in the time, frequency, spatial, and angular domains can be illustrated in Fig. A.2. The stationarities of channels in the frequency and angular domains are in red colour.

Appendix **B**

Radiation Pattern of Commercial Standard Horn Antenna

There is an one-page excerpt from the specification of commercial standard horn antenna found from the website: http://www.ainfoinc.com/en/p_ant_h_std.asp. It is the radiation pattern of standard horn antennas used in the channel measurements in Chapter 4, 5, and 6.



References

- [1] White paper on “5G Channel Model for bands up to 100 GHz,” ver 2.0, Mar. 2016. Available: <http://www.5gworkshops.com/5GCM.html>.
- [2] C.-X. Wang, F. Haider, X. Gao, X.-H. You, Y. Yang, D. Yuan, H. Aggoune, H. Haas, S. Fletcher, and E. Hepsaydir, “Cellular architecture and key technologies for 5G wireless communication networks,” *IEEE Commun. Mag.*, vol. 52, no. 2, pp. 122–130, Feb. 2014.
- [3] K. Mallinson, “The path to 5G: as much evolution as revolution,” May 10, 2016. Available: http://www.3gpp.org/news-events/3gpp-news/1774-5g_wisearbour.
- [4] S. Kavanagh, “What is 5G New Radio (5G NR).” Available: <https://5g.co.uk/guides/what-is-5g-new-radio/>.
- [5] P. Nikolich, C.-L. I, J. Korhonen, R. Marks, B. Tye, G. Li, J. Ni, and S. Zhang, “Standards for 5G and beyond: their use cases and applications,” *IEEE 5G Tech Focus*, vol. 1, no. 2, Jun. 2017. Available: <https://5g.ieee.org/tech-focus/june-2017/standards-for-5g-and-beyond>.
- [6] D. Kim and M. Zarri, “Road to 5G introduction and migration final,” Apr. 2018. Available: https://www.gsma.com/futurenetworks/wp-content/uploads/2018/04/Road-to-5G-Introduction-and-Migration_FINAL.pdf.
- [7] 3GPP TR 37.864-11-22, “E-UTRA (Evolved Universal Terrestrial Radio Access) - NR Dual Connectivity (EN-DC) of LTE 1 Down Link (DL) / 1 Up Link (UL) and inter-/intra-band NR 2 Down Link (DL) / 2 Up Link (UL) bands (Frequency Range 1 (FR1) + Frequency Range 2 (FR2)) (Release 15).” V15.0.0, Jun. 2018.

- [8] B. Bertenyi, “Webinar - Working towards full 5G in Rel-16.” Available: https://www.3gpp.org/news-events/1966-webinar2_ran.
- [9] E. G. Larsson, F. Tufvesson, O. Edfors, and T. L. Marzetta, “Massive MIMO for next generation wireless systems”, *IEEE Commun. Mag.*, vol.52, no. 2, pp.186–195, Feb. 2014.
- [10] “An introduction to network slicing,” GSMA Association. Available: <https://www.gsma.com/futurenetworks/wp-content/uploads/2017/11/GSMA-An-Introduction-to-Network-Slicing.pdf>.
- [11] T. Chen and N. Nikaein, “Towards software defined 5G radio access networks,” *IEEE Softwarization*, Mar. 2016. Available: <https://sdn.ieee.org/newsletter/march-2016/towards-software-defined-5g-radio-access-networks>.
- [12] A. Sabharwal, P. Schniter, D. Guo, D. W. Bliss, S. Rangarajan, and R. Wichman. “In-band full-duplex wireless: challenges and opportunities,” *IEEE J. Sel. Areas Commun.*, vol.32, no.9, pp.1637–1652, Sept. 2014.
- [13] M. Di Renzo, H. Haas, and P. M. Grant, “Spatial modulation for multiple-antenna wireless systems - a survey,” *IEEE Commun. Mag.*, Vol. 49, No. 12, pp. 182–191, Dec. 2011.
- [14] L. Wang and E. Şaşıoğlu, “Polar coding for interference networks,” in *Proc. IEEE ISIT’14*, Honolulu, HI, 2014, pp. 311–315.
- [15] G. R. Al-Juboori, A. Doufexi, and A. R. Nix, “System level 5G evaluation of GFDM waveforms in an LTE-A platform,” in *Proc. IEEE ISWCS’16*, Poznan, Poland, Sept. 2016, pp. 335–340.
- [16] J. Zhang and P. Elia, “Fundamental limits of cache-aided wireless BC: interplay of coded-caching and CSIT feedback,” *IEEE Trans. Inf. Theory*, vol. 63, no. 5, pp. 3142–3160, May 2017.
- [17] “Intel Introduces Portfolio of Commercial 5G New Radio Modems,” Intel Newsroom, Nov. 2017. Available: <https://newsroom.intel.com/news/intel-introduces-portfolio-new-commercial-5g-new-radio-modem-family/>.

- [18] “Our 5G vision is closer to reality than ever,” Qualcomm News & Media. Available: <https://www.qualcomm.com/news/onq/2018/02/14/our-5g-vision-closer-reality-ever>.
- [19] “Lenovo sets eye on 5G smartphone leadership,” Mobile world live, Devices, News. Available: <https://www.mobileworldlive.com/devices/news-devices/lenovo-sets-eye-on-5g-smartphone-leadership/>.
- [20] G. Mascot, “Unleashing the potential of 5G - ITU,” Nokia, 2018. Available: <https://networks.nokia.com/5g>.
- [21] “5G is now,” www.huawei.com, spotlight. Available: <https://www.huawei.com/en/industry-insights/outlook/mobile-broadband/5g>.
- [22] “5G open for business,” www.ericsson.com. Available: <https://www.ericsson.com/en/5g>.
- [23] “5G vision,” Samsung, Aug. 2015. Available: <http://images.samsung.com/is/content/samsung/p5/global/business/networks/insights/5g/global-networks-insight-samsung-5g-vision-2.pdf>.
- [24] “5G,” Wikipedia. Available: https://en.wikipedia.org/wiki/5G#cite_note-newsroom.intel.com-17.
- [25] K. Chamberlain, “EE to launch first commercial 5G network in U.K.” www.fiercewireless.com. Available: <https://www.fiercewireless.com/5g/ee-to-launch-first-commercial-5g-network-u-k-may-30>.
- [26] “China issues 5G licences,” www.thestar.com. Available: <https://www.thestar.com.my/business/business-news/2019/06/07/china-issues-5g-licences/>.
- [27] “Call for papers,” 6G Wireless Summit, Levi, Finland, Mar. 2019. Available: <http://www.6gsummit.com/call-for-papers/>.
- [28] “Cisco visual networking index: global mobile data traffic forecast update, 2017–2022, white Paper,” www.cisco.com, Feb. 2019. Available: <http://www.cisco.com/c/en/us/solutions/collateral/service-provider/visual-networking-index-vni/mobile-white-paper-c11-520862.html>.

- [29] M. Peter, et al., “Measurement campaigns and initial channel models for preferred suitable frequency ranges,” H2020-ICT-671650-mmMAGIC/D2.1, Deliverable D2.1, Mar. 2016.
- [30] ITU-R M2290, “Future spectrum requirements estimate for terrestrial IMT,” Dec. 2013.
- [31] A. F. Molisch and F. Tufvesson, “Propagation channel models for next-Generation wireless communications systems,” *IEICE Trans. Commun.*, vol. E97-B, no.10, pp. 2022–2034, Oct. 2014.
- [32] T. S. Rappaport, S. Sun, R. Mayzus, H. Zhao, Y. Azar, K. Wang, G. N. Wong, J. K. Schulz, M. Samimi, and F. Gutierrez, “Millimeter wave mobile communications for 5G cellular: It will work!” *IEEE Access*, vol. 1, pp. 335–349, 2013.
- [33] S. Rangan, T. S. Rappaport, and E. Erkip, “Millimeter-wave cellular wireless networks: potentials and challenges,” in *Proc. IEEE*, vol. 102, no. 3, pp. 366–385, 2014.
- [34] K. Sakaguchi, G.K. Tran, H. Shimodaira, S. nanba, T. Sakurai, K. Takinami, I. Siaud, E.C. Strinati, A. Capone, I. Karls, R. Arefi, and T. Haustein, “Millimeter-wave evolution for 5G cellular networks,” *IEICE Trans. Commun.*, vol.98, no.3, pp.388–402, Mar. 2015.
- [35] ITU-R M.2376, “Technical feasibility of IMT in bands above 6GHz,” Jul. 2015.
- [36] Resolution 238 (WRC-15), “Studies on frequency-related matters for international mobile telecommunications identification including possible additional allocations to the mobile services on a primary basis in portion(s) of the frequency range between 24.25 and 86 GHz for the future development of International Mobile Telecommunications for 2020 and beyond,” in *Proc. IUT WRC’15*, Geneva; 2015. p. 424–426.
- [37] ITU-R M.2083, “Framework and overall objectives of the future development of IMT for 2020 and beyond,” Sept. 2015.
- [38] 3GPP TR 38.913, “Scenarios and requirements for next generation access technologies,” V0.2.0, Feb. 2016.
- [39] V. Nurmela, et al., “METIS Channel Models,” ICT-317669-METIS, Deliverable D1.4, Feb. 2015.

- [40] T. S. Rappaport, Y. Xing, G. R. MacCartney, A. F. Molisch, E. Mellios, and J. Zhang, “Overview of millimeter wave communications for fifth-generation (5G) wireless networks—with a focus on propagation models,” *IEEE Transactions on Antennas and Propagation*, vol. 65, no. 12, pp. 6213–6230, Dec. 2017.
- [41] A. Papathanassiou and A. Khoryaev, “Cellular V2X as the essential enabler of superior global connected transportation services,” *IEEE 5G tech focus*, vol. 1, no 2, Jun. 2017. Available: <https://5g.ieee.org/tech-focus/june-2017/cellular-v2x>.
- [42] R. W. Heath Jr., “Vehicle-to-X communication for 5G – a killer application of millimeter wave,” IEEE 5G summit, 2017. Available: http://www.5gsummit.org/hawaii/docs/slides/D2_%234_Heath_V2X%20mmWave%205G.pdf.
- [43] N. Bahadori, N. Namvar, B. Kelley, and A. Homaifar, “Device-to-device communications in the millimeter wave band: A novel distributed mechanism,” in *Proc. IEEE WTS’18*, pp. 1–6, Apr. 2018.
- [44] Y. Zeng, R. Zhang, and T. Lim, “Wireless communications with unmanned aerial vehicles: opportunities and challenges,” *IEEE Commun. Mag.*, vol. 54, pp. 36–42, May 2016.
- [45] G.i Li, B. Ai, D. He, Z. Zhong, B. Hui, and J. Kim, “On the feasibility of high speed railway mmWave channels in tunnel scenario,” *Wirel. Commun. Mob. com.*, vol. 2017, Article ID 7135896, 17 pages, 2017.
- [46] E. Calvanese Strinati, et al. “5G champion–disruptive 5G technologies for roll-out in 2018,” *ETRI Journal*, vol. 40. no. 1, pp. 10–25, Feb. 2018.
- [47] F. Lemic, et al., “Localization as a feature of mmWave communication,” in *Proc. IWCMC’16*, Paphos, Cyprus, Sept. 2016, pp. 1033–1038.
- [48] T. Wu, T. S. Rappaport, and C. M. Collins, “The human body and millimeter-wave wireless communication systems: interactions and implications,” in *Proc. IEEE ICC15*, London, U.K. Jun. 2015, pp. 2423–2429.
- [49] J. C. Lin, “Human exposure to RF, microwave, and millimeter-wave electromagnetic radiation [Health Effects],” *IEEE Microw. Mag.*, vol. 17, no. 6, pp. 32–36, Jun. 2016.

- [50] K. Sakaguchi, T. Haustein, S. Barbarossa, E. C. Strinati, A. Clemente, G. Destino, A. Pärssinen, I. Kim, H. Chung, J. Kim, and W. Keusgen, “Where, when, and how mmWave is used in 5G and beyond,” *IEICE Trans. Electron.*, 100(10), pp.790–808. Oct. 2017.
- [51] E. Björnson, E. G. Larsson, and T. L. Marzetta, “Massive MIMO: ten myths and one critical question,” *IEEE Commun. Mag.*, vol. 54, no. 2, pp. 114–123, Feb. 2016.
- [52] F. Boccardi, R. W. Heath, A. Lozano, T. L. Marzetta, and P. Popovski, “Five disruptive technology directions for 5G,” *IEEE Commun. Mag.*, vol. 52, no. 2, pp. 74–80, Feb. 2014.
- [53] F. W. Vook, E. Visotsky, T. A. Thomas, and A. Ghosh, “Performance characteristics of 5G mmWave wireless-to-the-home,” in *Proc. Asilomar’16*, Pacific Grove, CA, 2016, pp. 1181–1185.
- [54] M. Xiao, et al., “Millimeter wave communications for future mobile networks,” *IEEE J. Sel. Areas Commun.*, vol. 35, no. 9, pp. 1909–1935, Sept. 2017.
- [55] W. Roh, et al., “Millimeter-wave beamforming as an enabling technology for 5G cellular communications: theoretical feasibility and prototype results,” *IEEE Commun. Mag.*, vol. 52, no. 2, pp. 106–113, Feb. 2014.
- [56] G. R. MacCartney, Jr., et al., “Millimeter wave wireless communications: new results for rural connectivity,” in *Proc. AllThingsCelluar’16 Workshop*, in conjunction with ACM MobiCom, Oct. 7, 2016.
- [57] R. W. Heath, N. Gonzalez-Prelcic, S. Rangan, W. Roh, and A. Sayeed, “An overview of signal processing techniques for millimeter wave MIMO systems,” *IEEE J. Sel. Top. Signal Process.*, vol. 10, no. 3, pp. 436–453, Apr. 2016.
- [58] A. Ghosh, “The 5G mmWave radio revolution,” *Microwave J.*, vol. 59, no. 9, pp. 22–36, Sept. 2016.
- [59] S. Sun, T. S. Rappaport, R. W. Heath, Jr., A. Nix, and S. Rangan, “MIMO for millimeter-wave wireless communications: Beamforming, spatial multiplexing, or both?” *IEEE Commun. Mag.*, vol. 52, no. 12, pp. 110–121, Dec. 2014.

- [60] K. Haneda, "Channel models and beamforming at millimeterwave frequency bands," *IEICE Trans. Commun.*, vol. 98, no. 5, pp. 755–772, May 2015.
- [61] A. Alkhateeb, O. Ayach, G. Leus, and R. Heath, "Channel estimation and hybrid precoding for millimeter wave cellular systems," *IEEE Trans. Signal Process.*, vol. 8, no. 5, pp. 831–846, Oct. 2014.
- [62] H. Huang, K. Liu, R. Wen, Y. Wang, and G. J. Wang, "Joint channel estimation and beamforming design for wide band millimeter wave cellular system," in *Proc. IEEE Globecom'15 Workshop*, San Diego, USA, Dec. 2015, pp. 1–6.
- [63] J. A. Zhang, X. Huang, V. Dyadyuk, and Y. J. Guo, "Massive hybrid antenna array for millimeter-wave cellular communications," *IEEE Wireless Commun. Mag.*, vol. 22, no. 1, pp. 79–87, Feb. 2015.
- [64] T. Nitsche, C. Cordeiro, A. B. Flores, E. W. Knightly, E. Perahia, and J. C. Widmer, "IEEE 802.11ad: Directional 60 GHz communication for multi-gigabit-per-second Wi-Fi," *IEEE Commun. Mag.*, pp. 132–141, Dec. 2014.
- [65] Y. Wang, Z. Shi, K. Zeng, and P. Zhu, "Two layers of beam alignment for millimeter-wave communications," in *Proc. DIPDMWC'16*, Moscow, Russia, Jul. 2016, pp. 262–267.
- [66] V. Va, T. Shimizu, G. Bansal, and R. W. Heath, "Beam design for beam switching based millimeter wave vehicle-to-infrastructure communications," in *Proc. IEEE ICC'16*, Kuala Lumpur, Malaysia, May 2016, pp. 1–6.
- [67] M. Polese, M. Giordani, M. Mezzavilla, S. Rangan, and M. Zorzi, "Improved handover through dual connectivity in 5G mmWave mobile networks," *IEEE J. Sel. Areas Commun.*, vol. 35, no. 9, pp. 2069–2084, Sept. 2017.
- [68] J. Palacios, D. Donno, and J. Widmer, "Tracking mm-Wave channel dynamics: fast beam training strategies under mobility," in *Proc. IEEE INFOCOM'17*, Atlanta, GA, USA, May 2017, pp. 1–9.
- [69] G. Brown, O. Koymen, and M. Branda, "The promise of 5G mmWave - how do we make it mobile?" *Light Reading Webinar*, Jun. 2016.

- [70] Y. Tan, J. Huang, R. Feng, and C.-X. Wang, "A study of angular stationarity of 5G millimeter wave channels," in *Proc. ISWCS'18 Workshop*, Bologna, Italy, Aug. 2017.
- [71] S. Jaeckel, L. Raschkowski, K. Börner, and L. Thiele, "QuaDRiGa: A 3-D multi-cell channel model with time evolution for enabling virtual field trials," *IEEE Trans. Antennas Propag.*, vol. 62, no. 6, pp. 3242–3256, Jun. 2014.
- [72] S. Wu, C.-X. Wang, H. Aggoune, M. M. Alwakeel, and Y. He, "A non-stationary 3D wideband twin-cluster model for 5G massive MIMO channels," *IEEE J. Sel. Areas Commun.*, vol. 32, no. 6, pp. 1207–1218, Jun. 2014.
- [73] S. Wu, C.-X. Wang, H. Haas, H. Aggoune, M. M. Alwakeel, and B. Ai, "A non-stationary wideband channel model for massive MIMO communication systems," *IEEE Trans. Wireless Commun.*, vol. 14, no. 3, pp. 1434–1446, Mar. 2015.
- [74] Y. Tan, C. -X. Wang, Q. Zhu, Z. Zhang, Z. Wang, J. Huang, and R. Feng, "A novel beamforming scheme for mobile-to-mobile millimeter wave communications," in *Proc. WSA '18*, Bochum, Germany, Mar. 2018.
- [75] C.-X. Wang, J. Bian, J. Sun, W. Zhang, and M. Zhang, "A survey of 5G channel measurements and models," *IEEE Commun. Surveys Tuts.*, vol. 20, no. 4, pp. 3142–3168, Aug. 2018.
- [76] I. A. Hemadeh, K. Satyanarayana, M. El-Hajjar, and L. Hanzo, "Millimeter-wave communications: physical channel models, design considerations, antenna constructions, and link-budget," *IEEE Commun. Surveys Tuts.*, vol. 20, no. 2, pp. 870–913, 2nd Quart. 2018.
- [77] A. F. Molisch, *Wireless Communications, Second Edition*. John Wiley & Sons, 2011.
- [78] S. Baek, Y. Chang, H. Kim, and A. Agiwal, "Comparison analysis of outdoor channel characteristics at 28 GHz and 2 GHz using 3D ray-tracing technique," in *Proc. IEEE VTC'14-Fall*, Vancouver, BC, 2014, pp. 1–5.
- [79] N. F. Abdullah, et al., "Channel parameters and throughput predictions for mm-Wave and LTE-A networks in urban environments," in *Proc. IEEE VTC'15-Spring*, Glasgow, 2015, pp. 1–5.

- [80] Z. Zhang, J. Ryu, S. Subramanian, and A. Sampath, “Coverage and channel characteristics of millimeter wave band using ray tracing,” in *IEEE ICC’15*, London, 2015, pp. 1380–1385.
- [81] T. S. Rappaport, G. R. MacCartney, M. K. Samini, and S. Sun, “Wideband millimeter-wave propagation measurements and channel models for future wireless communication system design,” *IEEE Trans. Commun.*, vol. 63, no. 9, pp. 3029–3056, Sept. 2015.
- [82] H. C. Nguyen, G. R. MacCartney, T. Thomas, T. S. Rappaport, B. Vejlgaard, and P. Mogensen, “Evaluation of empirical ray-tracing model for an urban outdoor scenario at 73 GHz E-band,” in *Proc IEEE VTC’14-Fall*, Vancouver, BC, 2014, pp. 1–6.
- [83] S.-K. Yong, et al., “TG3c channel modeling subcommittee final report.” IEEE 802.15-07-0584-01-003c, 2007.
- [84] A. Maltsev, et al., “Channel models for 60 GHz WLAN systems,” IEEE doc. 802.11-09/0334r8, May, 2010.
- [85] A. Maltsev, et al., “Channel modeling and characterization,” Deliverable D5.1, Jun., 2014.
- [86] H. Özcelik, N. Czink, and E. Bonek, “What makes a good MIMO channel model,” in *Proc. VTC’05*, Stockholm, Sweden, May 2005, pp. 156–160.
- [87] R. H. Clarke, “A statistical theory of mobile radio reception,” *Bell Sys. Tech. J.*, vol. 47, no. 6, Jul./Aug. 1968, pp. 957–1000.
- [88] M. Pätzold, *Mobile Radio Channels, Second Edition*. John Wiley & Sons, 2011.
- [89] S. Wu, C.-X. Wang, H. Aggoune, M. M. Alwakeel, and X. You, “A general 3D non-stationary 5G wireless channel model,” *IEEE Trans. Commun.*, vol. 66, no. 7, pp. 3065–3078, Jul. 2018.
- [90] C.-X. Wang, A. Ghazal, B. Ai, P. Fan, and Y. Liu, “Channel measurements and models for high-speed train communication systems: a survey,” *IEEE Commun. Surveys Tuts.*, vol. 18, no. 2, pp. 974–987, 2nd Quart., 2016.

- [91] C.-X. Wang, S. Wu, L. Bai, X. You, J. Wang, and C.-L. I, “Recent advances and future challenges for massive MIMO channel measurements and models,” *Sci. China Inf. Sci.*, Invited Paper, vol. 59, no. 2, pp. 1–16, Feb. 2016.
- [92] K. Pekka, J. Meinilä, L. Hentilä, X. Zhao, T. Jämsä, C. Schneider, and M. Narandzic, et al., “WINNER II channel models,” D1.1.2 V1.2, IST-4-027756 WINNER II Deliverable, 4 Feb. 2008.
- [93] P. Heino, et al., “WINNER+ final channel models”, ver 1.0, Jun. 2010. Available: <http://projects.celticinitiative.org/winner+/WINNER+Deliverables/D5.3v1.0.pdf>.
- [94] R. Verdone and A. Zanella, *Pervasive Mobile and Ambient Wireless Communications: COST Action 2100*. Springer Science & Business Media, 2012.
- [95] 3GPP T.R. 38.901, “Study on channel model for frequencies from 0.5 to 100 GHz,” V15.0.0, Jun. 2018.
- [96] L. Liu, C. Oestges, J. Poutanen, K. Haneda, P. Vainikainen, F. Quitin, F. Tufveson, and P. D. Doncker, “The COST 2100 MIMO channel model,” *IEEE Wireless Commun.*, vol. 19, no. 6, pp. 92–99, Dec. 2012.
- [97] 3GPP TR 25.996, “Spatial channel model for multiple input multiple output (MIMO) simulations,” V15.0.0, Jun. 2018.
- [98] 3GPP TR 36.873, “Study on 3D channel model for LTE,” V2.0.0, Mar. 2014.
- [99] M. Peter and K. Sakaguchi, “White Paper: W2.1, 6 – 100 GHz channel modelling for 5G: measurement and modelling plans in mmMAGIC,” H2020-ICT-671650-mmMAGIC/D2.1.
- [100] 5G Infrastructure Public Private Partnership (5G PPP). Available: <https://5g-ppp.eu/>.
- [101] A. Maltsev, “Channel Models for IEEE 802.11ay,” IEEE 802.11-15/1150r9, May 2016. Available: http://www.ieee802.org/11/Reports/tgay_update.htm.
- [102] ITU-R WP5D Contribution 459, “Proposal on IMT-2020 channel model,” Feb. 2017. Available: https://www.itu.int/md/R15-WP5D-C-0459/_page.print.

- [103] “MmWave channel modeling,” NYU Wireless. Available: <http://wireless.engineering.nyu.edu/mmwave-channel-modeling/>.
- [104] G. R. Maccartney, T. S. Rappaport, S. Sun, and S. Deng, “Indoor office wideband millimeter-wave propagation measurements and channel models at 28 and 73 GHz for ultra-dense 5G wireless networks,” *IEEE Access*, vol. 3, pp. 2388–2424, 2015.
- [105] G. R. MacCartney, S. Deng, and T. S. Rappaport, “Indoor office plan environment and layout-based mmWave path loss models for 28 GHz and 73 GHz,” in *Proc. IEEE VTC’16-Spring*, Nanjing, 2016, pp. 1–6.
- [106] S. Sun, et al., “Investigation of prediction accuracy, sensitivity, and parameter stability of large-scale propagation path loss models for 5G wireless communications,” *IEEE Trans. Veh. Technol.*, vol. 65, no. 5, pp. 2843–2860, May 2016.
- [107] C. Gustafson, K. Haneda, S. Wyne, and F. Tufvesson, “On mm-wave multipath clustering and channel modeling,” *IEEE Trans. Antennas Propag.*, vol. 62, no. 3, pp. 1445–1455, Mar. 2014.
- [108] T. Bai, V. Desai, and R. W. Heath, “Millimeter wave cellular channel models for system evaluation,” in *Proc. ICNC’14*, Honolulu, HI, 2014, pp. 178–182.
- [109] J. Lee, Y. Song, E. Choi, and J. Park, “MmWave cellular mobile communication for giga Korea 5G project,” in *Proc. APCC’15*, Kyoto, 2015, pp. 179–183.
- [110] T. Mavridis, L. Petrillo, J. Sarrazin, D. Lautru, A. Benlarbi-Delaï, and P. De Doncker, “Theoretical and experimental investigation of a 60-GHz off-body propagation model,” *IEEE Trans. Antennas Propag.*, vol. 62, no. 1, pp. 393–402, Jan. 2014.
- [111] X. Wu, Y. Zhang, C. X. Wang, G. Goussetis, e. M. Aggoune, and M. M. Alwakeel, “28 GHz indoor channel measurements and modelling in laboratory environment using directional antennas,” in *Proc. EuCAP’15*, Lisbon, 2015, pp. 1–5.
- [112] L. Wei, R. Q. Hu, Y. Qian, and G. Wu, “Key elements to enable millimeter wave communications for 5G wireless systems,” *IEEE Wireless Commun.*, vol. 21, no. 6, pp. 136–143, Dec. 2014.
- [113] Q. Li, et al., “Validation of a geometry-based statistical mmWave channel model using ray-tracing simulation,” in *Proc. IEEE VTC’15-Spring*, Glasgow, 2015, pp. 1–5.

- [114] Q. Li, H. Shirani-Mehr, T. Balercia, H. Niu, A. Papathanassiou, and G. Wu, “Millimeter wave channel model and system design considerations,” in *Proc. IEEE ICCW’15*, London, 2015, pp. 1214–1219.
- [115] Q. C. Li, G. Wu, and T. S. Rappaport, “Channel model for millimeter-wave communications based on geometry statistics,” in *Proc. IEEE GC’14 Wkshps*, Austin, TX, 2014, pp. 427–432.
- [116] Y. Wang, L. Huang, Z. Shi, K. Liu, and X. Zou, “A millimeter wave channel model with variant angles under 3GPP SCM framework,” in *Proc. IEEE PIMRC’15*, Hong Kong, 2015, pp. 2249–2254.
- [117] C.-X. Wang, “Channel characterization and modeling of 5G wireless communication systems ,” in *ICCC’16*, Tutorial 4, Chengdu, China, 27 Jul. 2016.
- [118] A. A. M. Saleh and R. Valenzuela, “A statistical model for indoor multipath propagation,” *IEEE J. Sel. Areas Commun.*, vol. 5, no. 2, pp. 128–137, Feb. 1987.
- [119] Q. H. Spencer, B. D. Jeffs, M. A. Jensen, and A. L. Swindlehurst, “Modeling the statistical time and angle of arrival characteristics of an indoor multipath channel,” *IEEE J. Sel. Areas Commun.*, vol. 18, no. 3, pp. 347–360, Mar. 2000.
- [120] A. Maltsev, A. Puduev, I. Karls, I. Bolotin, G. Morozov , R.J. Weiler, M. Peter, and W. Keusgen “Quasi-deterministic approach to mmWave channel modeling in a mon-stationary environment”, in *Proc. IEEE Globecom’14*, Austin, Texas, USA.
- [121] A. Ali, N. González-Prelcic, and R. W. Heath, “Millimeter Wave Beam-Selection Using Out-of-Band Spatial Information,” *IEEE Trans. Wireless Comm.*, vol. 17, no. 2, pp. 1038–1052, Feb. 2018.
- [122] C. Kourogiorgas, S. Sagkriotis, and A. D. Panagopoulos, “Coverage and outage capacity evaluation in 5G millimeter wave cellular systems: Impact of rain attenuation,” in *Proc. EuCAP’15*, Lisbon, Apr. 2015, pp. 1–5.
- [123] Y.-P. Zhang, P. Wang, and A. Goldsmith, “Rainfall effect on the performance of millimeter-wave MIMO systems,” *IEEE Trans. Wireless Commun.*, vol. 14, no. 9, pp. 4857–4866, Sept. 2015.

- [124] “Millimeter waves: How we got here, the physical challenges, and 5G opportunities,” www.nutaq.com. Available: <https://www.nutaq.com/blog/millimeter-waves-how-we-got-here-physical-challenges-and-5g-opportunities>.
- [125] E. Kampert, P. A. Jennings, and M. D. Higgins, “Investigating the V2V millimeter-wave channel near a vehicular headlight in an engine bay,” *IEEE Commun. Lett.*, vol. 22, no. 7, pp. 1506–1509, Jul. 2018.
- [126] W. Qi, J. Huang, J. Sun, Y. Tan, C.-X. Wang, and X. Ge, “Measurements and modeling of human blockage effects for multiple millimeter wave bands,” in *Proc. IWCMC’17*, Valencia, Spain, Jun. 2017.
- [127] J. Huang, C.-X. Wang, R. Feng, J. Sun, W. Zhang, and Y. Yang, “Multi-frequency mmWave massive MIMO channel measurements and characterization for 5G wireless communication systems,” *IEEE J. Sel. Areas Commun.*, vol. 35, no. 7, pp. 1591–1605, Jul. 2017.
- [128] J. Huang, C.-X. Wang, Y. Liu, J. Sun, and W. Zhang, “A novel 3D GBSM for mmWave MIMO channels,” *Sci. China Inf. Sci.*, vol. 6, no. 10, Oct. 2018.
- [129] Q. Zhu, H. Li, Y. Fu, C.-X. Wang, Y. Tan, X. Chen, and Q. Wu, “A novel 3D non-stationary MIMO channel simulator and hardware emulator,” *IEEE Trans. Commun.*, vol. 66, no. 9, pp. 3865–3878, Sept. 2018.
- [130] A. I. Sulyman, A. Alwarafy, G. R. MacCartney, T. S. Rappaport, and A. Alsanie, “Directional radio propagation path loss models for millimeter-wave wireless networks in the 28-, 60-, and 73-GHz bands,” *IEEE Trans. Wireless Commun.*, vol. 15, no. 10, pp. 6939–6947, Oct. 2016.
- [131] G. R. MacCartney Jr., M. K. Samimi, and T. S. Rappaport, “Exploiting directionality for millimeter-wave wireless system improvement,” in *Proc. IEEE ICC’15*, London, U.K., Jun. 2015, pp. 1–7.
- [132] M. K. Samimi and T. S. Rappaport, “3-D millimeter-wave statistical channel model for 5G wireless system design,” *IEEE Trans. Microw. Theory Techn.*, vol. 64, no. 7, pp. 2207–2225, Jul. 2016.

- [133] M. K. Samimi and T. S. Rappaport, “3-D statistical channel model for millimeter-wave outdoor mobile broadband communications,” in *Proc. IEEE ICC’15*, London, U.K., Jun. 2015, pp. 8–12.
- [134] M. K. Samimi and T. S. Rappaport, “Ultra-wideband statistical channel model for non line of sight millimeter-wave urban channels,” in *Proc. IEEE Globecom’14*, Austin, TX USA, Dec. 2014, pp. 3483–3489.
- [135] M. K. Samimi and T. S. Rappaport, “Local multipath model parameters for generating 5G millimeter-wave 3GPP-like channel impulse response,” in *Proc. EuCAP’16*, Davos, Switzerland, Apr. 2016, pp. 1–5.
- [136] M. K. Samimi and T. S. Rappaport, “Statistical channel model with multi-frequency and arbitrary antenna beamwidth for millimeterwave outdoor communications,” in *Proc. IEEE GC’15 Workshops*, Dec. 2015, pp. 1–7.
- [137] Robert W. Heath Jr., “Millimeter wave communication: from origins to disruptive applications.” Available: http://users.ece.utexas.edu/~rheath/presentations/2017/MmWaveOriginsDisruptiveApplications_Lytle_Washington_2017.pdf.
- [138] A. Maltsev, I. Bolotin, A. Lomayev, A. Pudeyev, and M. Danchenko, “User mobility impact on millimeter-wave system performance,” in *Proc. EuCAP’16*, Davos, Switzerland, Apr. 2016, pp. 1–5.
- [139] E. Ben-Dor, T. S. Rappaport, Y. Qiao, and S. J. Lauffenburger, “Millimeter-wave 60 GHz outdoor and vehicle AOA propagation measurements using a broadband channel sounder,” in *Proc. IEEE Globecom’11*, Dec. 2011, pp. 1–6.
- [140] A. Tassi, M. Egan, R. J. Piechocki, and A. Nix, “Modeling and design of millimeter-wave networks for highway vehicular communication,” *IEEE Trans. Veh. Technol.*, vol. 66, no. 12, pp. 10676–10691, Dec. 2017.
- [141] V. Va, J. Choi, and R. W. Heath, “The Impact of beamwidth on temporal channel variation in vehicular channels and its implications,” *IEEE Trans. Veh. Technol.*, vol. 66, no. 6, pp. 5014–5029, Jun. 2017.
- [142] V. Va, J. Choi, T. Shimizu, G. Bansal, and R. W. Heath, “Inverse multipath fingerprinting for millimeter wave V2I beam alignment,” *IEEE Trans. Veh. Technol.*, vol. 67, no. 5, pp. 4042–4058, May 2018.

- [143] A. Ali, N. González-Prelcic, and R. W. Heath, “Millimeter wave beam-selection using out-of-band spatial information,” *IEEE Trans. Wireless Commun.*, vol. 17, no. 2, pp. 1038–1052, Feb. 2018.
- [144] C. Zhang, J. Zhang, Y. Huang, and L. Yang, “Location-aided channel tracking and downlink transmission for HST massive MIMO systems,” *IET Commun.*, vol. 11, no. 13, pp. 2082–2088, Oct. 2017.
- [145] X. Song, S. Haghghatshoar, and G. Caire, “A scalable and statistically robust beam alignment technique for millimeter-wave systems,” *IEEE Trans. Wireless Commun.*, vol. 17, no. 7, pp. 4792–4805, Jul. 2018.
- [146] A. V. Oppenheim, A. S. Willsky, and S. H. Nawab. *Signals and Systems, 2nd ed.* Prentice-Hall, 1, 997, 2014.
- [147] V. P. G. Jiménez, et al., “A MIMO-OFDM testbed, channel measurements, and system considerations for outdoor-indoor WiMAX,” in *Proc. EURASIP’09, J. Wireless Commun. Netw.*, pp. 1–13, Dec. 2009.
- [148] R. Müller, et al., “Ultra-wideband channel sounder for measurements at 70 GHz,” in *Proc. IEEE VTC’15-Spring*, Glasgow, 2015, pp. 1–5.
- [149] R. Müller, D. A. Dupleich, C. Schneider, R. Herrmann, and R. S. Thomä, “Ultrawideband 3D mmWave channel sounding for 5G,” in *Proc. URSI GASS’14*, Beijing, 2014, pp. 1–4.
- [150] R. J. Weiler, M. Peter, T. Kühne, M. Wisotzki, and W. Keusgen, “Simultaneous millimeter-wave multi-band channel sounding in an urban access scenario,” in *Proc. EuCAP’15*, Lisbon, Apr. 2015, pp. 1–5.
- [151] H. K. Kwon, M. D. Kim, and Y. j. Chong, “Implementation and performance evaluation of mmWave channel sounding system,” in *Proc. APS/URSI’15*, Vancouver, BC, 2015, pp. 1011–1012.
- [152] Z. Wen and H. Kong, “MmWave MIMO channel sounding for 5G,” in *Proc 5GU’14*, Akaslompolo, 2014, pp. 192–197.
- [153] Y. Tan, C.-X. Wang, J. Ø. Nielsen, and G. F. Pedersen, “Comparison of stationarity regions for wireless channels from 2 GHz to 30 GHz,” in *Proc. IWCMC’17*, Invited Paper, Valencia, Spain, Jun. 2017.

- [154] S. Hur, N.-G. Kang, J. Park, J. Lee, Y.-J. Cho, and M. Nekovee, "Millimeter-wave channel modeling on 28 GHz," in *Proc. EURO-COST'14*, IC1004 TD(14)09033, Ferrara, Italy, Feb., 2014.
- [155] S. Hur, et al., "Wideband spatial channel model in an urban cellular environments at 28 GHz," in *Proc. EuCAP'15*, Lisbon, Apr. 2015, pp. 1–5.
- [156] S. Hur, et al., "Proposal on millimeter-wave channel modeling for 5G cellular system," *IEEE J. Sel. Topics Signal Process.*, vol. 10, no. 3, pp. 454–469, Apr. 2016.
- [157] T. S. Rappaport, F. Gutierrez, Jr., E. Ben-Dor, J. N. Murdock, Y. Qiao, and J. I. Tamir, "Broadband millimeter-wave propagation measurements and models using adaptive-beam antennas for outdoor urban cellular communications," *IEEE Trans. Antennas Propag.*, vol. 61, no. 4, pp. 1850–1859, Apr. 2013.
- [158] I. Rodriguez, H. C. Nguyen, T. B. Sorensen, J. Elling, J. A. Holm, P. Mogensen, P. Mogensen, and B. Vejlggaard, "Analysis of 38 GHz mmWave propagation characteristics of urban scenarios," in *Proc. EW'15*, Budapest, Hungary, May 2015.
- [159] S. Rajagopal, S. Abu-Surra, and M. Malmirchegini, "Channel feasibility for outdoor non-line-of-sight mmWave mobile communication," in *Proc. IEEE VTC'12 Fall*, Sept. 2012, pp. 1–6.
- [160] J. Zhu, H. Wang, and W. Hong, "Large-scale fading characteristics of indoor environments channel at 45 GHz," *IEEE Antennas Wireless Propag. Lett.*, vol. pp, no. 99, Dec. 2014.
- [161] X. Wu, C. X. Wang, J. Sun, J. Huang, R. Feng, Y. Yang, and X. Ge, "60-GHz millimeter-wave channel measurements and modeling for indoor office environments," *IEEE Trans. Antennas Propag.*, vol. 65, no. 4, pp. 1912–1924, Apr. 2017.
- [162] S. Salous, S.M. Feeney, X. Raimundo, and A. A. Cheema, "Wideband MIMO channel sounder for radio measurements in the 60 GHz band," *IEEE Trans. Wireless Comm.*, vol.15, no.4, pp.2825–2832, 2016.
- [163] R. J. Weiler, M. Peter, W. Keusgen, and M. Wisotzki, "Measuring the busy urban 60 GHz outdoor access radio channel," in *Proc. IEEE ICUWB'14*, Paris, 2014, pp. 166–170.

- [164] M. Kyro, et al., “Measurement based path loss and delay spread modeling in hospital environments at 60 GHz,” *IEEE Trans. Wireless Commun.*, vol. 10, no. 8, pp. 2423–2427, Aug. 2011.
- [165] H. Sawada, H. Nakase, S. Kato, M. Umehira, K. Sato, and H. Harada, “ Impulse response model and parameters for indoor channel modeling at 60GHz,” in *Proc. IEEE VTC’10-Spring* , Taipei, Taiwan. May 2010.
- [166] N. Zhang, X. Yin, X. Lu, M. Du, and X. Cai, “Measurement-based angular characterization for 72 GHz propagation channels in indoor environments,” in *Proc. IEEE Globecom’14*, Austin, TX, Dec. 2014, pp. 370–376.
- [167] M. Kyrä, S. Ranvier, V.-M. Kolmonen, K. Haneda, and P. Vainikainen, “Long range wideband channel measurements at 81–86 GHz frequency range,” in *Proc. EuCAP’10*, 2010, pp. 1–5.
- [168] J. Medbo, et al., “Channel modelling for the fifth generation mobile communications,” in *Proc. EuCAP’14*, The Hague, Netherlands, Apr. 2014, pp. 219–223.
- [169] A. F. Molisch, “Ultra-wide-band propagation channels,” *Proc. IEEE*, vol. 97, no. 2, pp. 353–371, Feb. 2009.
- [170] N. A. Muhammad, P. Wang, Y. Li, and B. Vucetic, “Analytical model for outdoor millimeter wave channels using geometry-based stochastic approach,” *IEEE Trans. Veh. Technol.*, vol. 66, no. 2, pp. 912–926, Feb. 2017.
- [171] J. Yang, et al., “A geometry-based stochastic channel model for the millimeter-wave band in a 3GPP high-speed train scenario,” *IEEE Trans. Veh. Technol.*, vol. 67, no. 5, pp. 3853–3865, May 2018.
- [172] R. He, B. Ai, G. L. Stüber, G. Wang, and Z. Zhong, “Geometrical-based modeling for millimeter-wave MIMO mobile-to-mobile channels,” *IEEE Trans. Veh. Technol.*, vol. 67, no. 4, pp. 2848–2863, Apr. 2018.
- [173] Q. Zou, A. Tarighat, and A. H. Sayed, “Performance analysis of multiband OFDM UWB communications with application to range improvement,” *IEEE Trans. Veh. Technol.*, vol. 56, no. 6, pp. 3864–3878, Nov. 2007.

- [174] K. Guan, et al., “On millimeter wave and THz mobile radio channel for smart rail mobility,” *IEEE Trans. Veh. Technol.*, vol. 66, no. 7, pp. 5658–5674, Jul. 2017.
- [175] P. Bello, “Characterization of randomly time-variant linear channels,” *IEEE Trans. Commun.*, vol. 11, no. 4, pp. 360–393, Dec. 1963.
- [176] A. Paulraj, R. Nabar, and D. Gore, *Introduction to Space-Time Wireless Communications*. Cambridge University Press, 2003.
- [177] Report ITU-R M.2135-1 “Guidelines for evaluation of radio interface technologies for IMT-Advanced”, Dec. 2009.
- [178] J. Bian, J. Sun, C.-X. Wang, R. Feng, J. Huang, Y. Yang, and M. Zhang, “A WINNER+ based 3D non-stationary wideband MIMO channel model,” *IEEE Trans. Wireless Commun.*, vol. 17, no. 3, pp. 1755–1767, Mar. 2018.
- [179] Y. Yuan, C.-X. Wang, Y. He, M. M. Alwakeel, and H. Aggoune, “3D wideband non-stationary geometry-based stochastic models for non-isotropic MIMO vehicle-to-vehicle channels,” *IEEE Trans. Wireless Commun.*, vol. 14, no. 12, pp. 6883–6895, Dec. 2015.
- [180] Y. Liu, C.-X. Wang, C. F. Lopez, and X. Ge, “3D non-stationary wideband circular tunnel channel models for high-speed train wireless communication systems,” *Sci. China Inf. Sci.*, vol. 60, no. 8, doi: 10.1007/s11432-016-9004-4, Aug. 2017.
- [181] Y. Liu, C.-X. Wang, J. Huang, J. Sun, and W. Zhang, “Novel 3-D nonstationary mmWave massive MIMO channel models for 5G high-speed train wireless communications,” *IEEE Trans. Veh. Technol.*, vol. 68, no. 3, pp. 2077–2086, Mar. 2019.
- [182] Y. Liu, A. Ghazal, C.-X. Wang, X. Ge, Y. Yang, and Y. Zhang, “Channel measurements and models for high-speed train wireless communication systems in tunnel scenarios: a survey,” *Sci. China Inf. Sci.*, vol. 60, no. 8, doi: 10.1007/s11432-016-9014-3, Oct. 2017.
- [183] X. Gao, O. Edfors, F. Tufvesson, and E. G. Larsson, “Massive MIMO in real propagation environments: do all antennas contribute equally?” *IEEE Trans. Commun.*, vol. 63, no. 11, pp. 3917–3928, Nov. 2015.

- [184] X. Gao, F. Tufvesson, and O. Edfors, “Massive MIMO channels- measurements and models,” in *Proc. Asilomar’13*, Pacific Grove, CA, 2013, pp. 280–284.
- [185] C. F. Lopez and C.-X. Wang, “Novel 3D non-stationary wideband models for massive MIMO channels,” *IEEE Trans. Wireless Commun.*, vol. 17, no. 5, pp. 2893–2905, May 2018.
- [186] K. Haneda, A. Richter, and A. F. Molisch, “Modeling the frequency dependence of ultra-wideband spatio-temporal indoor radio channels,” *IEEE Trans. Antennas Propag.*, vol. 60, no. 6, pp. 2940–2950, Jun. 2012.
- [187] Y. F. Chen and V. K. Dubey, “Dynamic simulation model of indoor wideband directional channels,” *IEEE Trans. Veh. Technol.*, vol. 55, no. 2, pp. 417–430, Mar. 2006.
- [188] J. Turkka, P. Kela, and M. Costa, “On the spatial consistency of stochastic and map-based 5G channel models,” in *Proc. IEEE CSCN’16*, Berlin, Germany, 31 Oct.–2 Dec. 2016, pp. 1–7.
- [189] A. Gehring, M. Steinbauer, I. Gaspard, and M. Grigat, “Empirical channel stationarity in urban environments,” in *Proc. EPMCC’01*, Vienna, Austria, Feb. 2001.
- [190] M. Herdin and E. Bonek, “A MIMO correlation matrix based metric for characterizing non-stationarity,” in *Proc. IST’04 Summit*, Lyon, France, Jun. 2004, 5 pages.
- [191] M. Herdin, N. Czink, H. Ozcelik, and E. Bonek, “Correlation matrix distance, a meaningful measure for evaluation of non-stationary MIMO channels,” in *Proc. IEEE VTC’05-Spring*, Stockholm, Sweden, Jan. 2005, vol. 1, pp. 136–140.
- [192] O. Renaudin, V. Kolmonen, P. Vainikainen, and C. Oestges, “Impact of correlation matrix estimation accuracy on the computation of stationarity intervals,” in *Proc. EuCAP’10*, Barcelona, Spain, Apr. 2010, pp. 1–5.
- [193] A. Papoulis and S. U. Pillai, *Probability, Random Variables, and Stochastic Processes*. Tata McGraw-Hill Education, 2002.
- [194] A. F. Molisch, “6.8.1 Appendix 6.A: Validity of WSSUS in Mobile Radio Channels,” *Supplementary Material for Second Edition*, John Wiley & Sons. Available: <http://www.wiley.com/go/molisch>.

- [195] W. Q. Malik, D. J. Edwards, and C. J. Stevens, "Frequency dependence of fading statistics for ultrawideband systems," *IEEE Trans. Wireless Commun.*, vol. 6, no. 3, pp. 800–804, Mar. 2007.
- [196] A. Maltsev, A. Pudeyev, R. Weiler, M. Peter, W. Keusgen, and I. Bolotin, "Virtual antenna array methodology for outdoor millimeter-wave channel measurements," in *Proc. IEEE GC'16 Workshops*, Washington, DC, 2016, pp. 1–6.
- [197] Y. Tan, J. Ø. Nielsen, and G. Pedersen, "Spatial stationarity of ultrawideband and millimeter wave radio channels," *Int J Antennas Propag.*, vol. 2016, Article ID 3212864, 7 pages, 2016.
- [198] W. Q. Malik and A. F. Molish, "Ultra-wide band antenna arrays and directional propagation channels," in *Proc. EuCAP'06*, Nice, France. Nov. 2006.
- [199] B. H. Fleury, M. Tschudin, R. Heddergott, D. Dahlhaus, and K. I. Pedersen, "Channel parameter estimation in mobile radio environments using the SAGE algorithm," *IEEE J. Sel. Areas Commun.*, vol. 17, no. 3, pp. 434–450, Mar. 1999.
- [200] R. Feng, J. Huang, J. Sun, and C.-X. Wang, "A novel 3D frequency domain SAGE algorithm with applications to parameter estimation in mmWave massive MIMO indoor channels," *Sci. China Inf. Sci.*, vol. 60, no. 8, doi: 10.1007/s11432-017-9139-4, Aug. 2017.
- [201] K. Haneda, C. Gustafson, and S. Wyne, "60 GHz spatial radio transmission: multiplexing or beamforming?" *IEEE Trans. Antennas Propag.*, vol. 61, no. 11, pp. 5735–5743, Nov. 2013.
- [202] A.F. Molisch, et al., "IEEE802.15.4a channel model subgroup final report," IEEE P802.15, pp. 943–968, 2004.
- [203] N. Czink, P. Cera, J. Salo, E. Bonek, J.-P. Nuutinen, and J. Ylitalo, "A framework for automatic clustering of parametric MIMO channel data including path powers," in *Proc. IEEE VTC'06-Fall*, Quebec, Canada, Sept. 2006, pp. 1–5.
- [204] J. Salmi and A. F. Molisch, "Propagation parameter estimation, modeling and measurements for ultra-wide band MIMO radar," *IEEE Trans. Antennas Propag.*, vol. 59, no. 11, pp. 4257–4267, Nov. 2011.

- [205] Y. S. Yoon, L. M. Kaplan, and J. H. McClellan, "TOPS: new DOA estimator for wideband signals," *IEEE Trans. Signal Process.*, vol. 54, no. 6, pp. 1977–1989, Jun. 2006.
- [206] N. C. Beaulieu and C. Cheng, "Efficient Nakagami-m fading channel simulation," *IEEE Trans. Veh. Technol.*, vol. 54, no. 2, pp. 413–424, Mar. 2005.
- [207] Q. Zhu, X. Dang, D. Xu, and X. Chen, "High efficient rejection method for generating Nakagami-m sequences," *Electron. Lett.*, vol. 47, no. 19, pp. 1100–1101, Sept. 2011.
- [208] G. stüber, *Principles of Mobile Communication*. Kluwer, Norwell, MA, 1996.
- [209] C. Sun, X. Gao, S. Jin, M. Matthaiou, Z. Ding, and C. Xiao, "Beam division multiple access transmission for massive MIMO communications," *IEEE Trans. Commun.*, vol. 63, no. 6, pp. 2170–2184, Jun. 2015.
- [210] L. You, X. Gao, G. Y. Li, X. Xia, and N. Ma, "BDMA for millimeter-wave/trahertz massive MIMO transmission with per-beam synchronization," *IEEE J. Sel. Areas Commun.*, vol. 35, no. 7, pp. 1550–1563, Jul. 2017.
- [211] S. Sun, T. Rappaport, M. Shafi, P. Tang, J. Zhang, and P. J. Smith, "Propagation models and performance evaluation for 5G millimeter-wave bands," *IEEE Trans. Veh. Technol.*, vol. 67, no. 9, pp. 8422–8439, Sept. 2018.
- [212] Wireless world research forum, future mobile communication forum. White Paper 5: "Wireless communication using higher frequency bands," Outlook 23, Nov. 2017.
- [213] M. K. Samimi, T. S. Rappaport, and G. R. MacCartney, "Probabilistic omnidirectional path loss models for millimeter-wave outdoor communications," *IEEE Wireless Commun. Lett.*, vol. 4, no. 4, pp. 357–360, Aug. 2015.
- [214] G. D. Durgin, "Theory of stochastic local area channel modeling for wireless communications," PhD diss., Virginia Tech, 2000.
- [215] S. Payami and F. Tufvesson, "Channel measurements and analysis for very large array systems at 2.6 GHz," in *Proc. EUCAP'12*, Prague, Czech Republic, Mar. 2012, pp. 433–437.

- [216] W. Li, L. Liu, C. Tao, Y. Lu, J. Xiao, and P. Liu, "Channel measurements and angle estimation for massive mimo systems in a stadium," in *Proc. IEEE, ICACT'17*, Seoul, South Korea, Jul. 2015, pp. 105–108.
- [217] X. Yin, C. Ling, and M. D. Kim, "Experimental multipath-cluster characteristics of 28-GHz propagation channel," *IEEE Access*, vol. 3, pp. 3138–3150, 2015.
- [218] E. Lutz, D. Cygan, M. Dippold, F. Dolainsky, and W. Papke, "The land mobile satellite communication channel-recording, statistics and channel model," *IEEE Trans. Veh. Technol.*, vol. 40, no. 2, pp. 375–386, May 1991.
- [219] E. Lutz, "A Markov model for correlated land mobile satellite channel," *Int. J. Satell. Commun.*, vol. 14, no. 4, pp. 333–339, Jul. 1996.
- [220] Y. Karasawa, K. Kimura, and K. Minamisono, "Analysis of availability improvement in LMSS by means of satellite diversity based on three-state propagation channel model," *IEEE Trans. Veh. Technol.*, vol. 46, no. 4, pp. 1047–1056, Nov. 1997.
- [221] F. P. Fontan, M. Vazquez-Castro, C. E. Cabado, J. P. Garcia, and E. Kubista, "Statistical modeling of the LMS channel," *IEEE Trans. Veh. Technol.*, vol. 50, no. 6, pp. 1549–1567, Nov. 2001.
- [222] F. P. Fontan, et al., "A versatile framework for a narrow- and wide-band statistical propagation model for the LMS channel," *IEEE Trans. Broadcast.*, vol. 43, no. 4, pp. 431–458, Dec. 1997.
- [223] P. Petropoulou, E. T. Michailidis, A. D. Panagopoulos, and A. G. Kanatas, "Radio propagation channel measurements for multi-antenna satellite communication systems: a survey," *IEEE Antennas Propag. Mag.*, vol. 56, no. 6, pp. 102–122, Dec. 2014.
- [224] M. Hui, D. Shen, Y. Cui, J. Xu, and C. Zhao, "Theoretical analysis and simulation of the outage probability for six-state Markov model on land-mobile satellite channels," in *Proc. ISAPE'08*, Kunming, Nov. 2008, pp. 1516–1519.
- [225] W. Schafer, "Channel modelling of short-range radio links at 60 GHz for mobile intervehicle communication," in *Proc. IEEE VTC'91*, St. Louis, MO, USA, May 1991, pp. 314–319.

- [226] D. W. Matolak and Q. Wu, “Vehicle-to-vehicle channels: are we done yet?” in *Proc. IEEE Globecom’09 Workshops*, Honolulu, HI, Nov. – Dec. 2009, pp. 1–6.
- [227] C.-X. Wang, X. Cheng, and D. I. Laurenson, “Vehicle-to-vehicle channel modeling and measurements: recent advances and future challenges,” *IEEE Commun. Mag.*, vol. 47, no. 11, pp. 96–103, Nov. 2009.
- [228] R. Ford, S. Rangan, E. Mellios, D. Kong, and A. Nix, “Markov channel-based performance analysis for millimeter wave mobile networks,” in *Proc. IEEE WCNC’17*, San Francisco, CA, Mar. 2017, pp. 1–6.
- [229] Y. Tan, C.-X. Wang, Q. Zhu, J. Huang, R. Feng, and J. Bian, “A novel GBSM for wireless directional mmWave channels,” *IEEE Trans. Commun.*, submitted for publication.
- [230] C. A. Balanis, *Antenna Theory: Analysis and Design*. John Wiley & Sons, 2016.
- [231] A. Davydov, A. Maltsev, and A. Sadri “Saleh-Valenzuela channel model parameters for library environment,” IEEE 802.15-06-0302-02-003c, Channel Modeling for 60 GHz WLAN Systems - IEEE Mentor, Jul. 2006.
- [232] R. E. Fischer, B. Tadic-Galeb, P. R. Yoder, and R. Galeb, *Optical system design*. New York: McGraw Hill, 2000.
- [233] Z. Ghassemlooy, W. Popoola, and S. Rajbhandari, *Optical wireless communications: system and channel modelling with Matlab*, CRC Press, 2012.
- [234] H. Burchardt, N. Serafimovski, D. Tsonev, S. Videv, and H. Haas, “VLC: Beyond point-to-point communication,” *IEEE Commun. Mag.*, vol. 52, no. 7, pp. 98–105, Jul. 2014.
- [235] Available: https://en.wikipedia.org/wiki/Gaussian_beam.
- [236] G. Li, S. Yang, Y. Chen, and Z. P. Nie, “A novel electronic beam steering technique in time modulated antenna array,” *Progress In Electromagnetics Research (PIER)*, vol. 97, pp. 391–405, 2009.
- [237] X. Hong, C.-X. Wang, B. Allen, and W. Malik, “A correlation based double-directional stochastic channel model for multiple-antenna UWB systems,” *IET Micro. Antenna. P.*, vol. 1, no. 6, pp. 1182–1191, Dec. 2007.

- [238] F. Talebi and T. Pratt, "Channel sounding and parameter estimation for a wideband correlation-based MIMO model," *IEEE Trans. Veh. Technol.*, vol. 65, no. 2, pp. 499–508, Feb. 2016.